USING INFRARED OBSERVATIONS OF CIRCUMSTELLAR DUST AROUND EVOLVED STARS TO TEST DUST FORMATION HYPOTHESES

A Dissertation presented to
the Faculty of the Graduate School
at the University of Missouri

In Partial Fulfillment
of the Requirements for the Degree
Doctor of Philosophy

---

by
SUKLIMA GUHA NIYOGI
Dr. Angela Speck, Dissertation Supervisor
DECEMBER 2011

The undersigned, appointed by the Dean of the Graduate School, have examined the dissertation entitled:

USING INFRARED OBSERVATIONS OF
CIRCUMSTELLAR DUST AROUND EVOLVED STARS
TO TEST DUST FORMATION HYPOTHESES

presented by Suklima Guha Niyogi,

a candidate for the degree of Doctor of Philosophy and hereby certify that, in their opinion, it is worthy of acceptance.

Dr. Angela K. Speck

Dr. Bahram Mashhoon

Dr. Paul F. Miceli

Dr. Carsten Ullrich

Dr. Steven W. Keller

To Babu & Ma, the guiding stars of my life.

ACKNOWLEDGMENTS

I would like to take this opportunity to sincerely thank my advisor Professor Angela K. Speck for her wonderful guidance, support and encouragement in making this thesis possible. Her immense patience and excellent teaching skills have always made it a joyful experience to learn Astronomy from her. She has being a wonderful mentor and always provide me all the possible opportunities to explore my research area. I must also add here that Professor Alan Whittington, too, deserves special thanks for his warmth and kindness.

I would like to thank Professor Bahram Mashhoon, Professor Paul F. Miceli, Professor Carsten Ullrich and Professor Steven Keller for agreeing to be my defense committee members and being extremely understanding and helpful, and special thanks to Professor Carsten Ullrich for giving me his valuable time whenever I approached him. Professor H. R. Chandrasekhar for being an excellent Graduate advisor during my first year of graduate school and help me to choose the right path of my academic career, and all the other professors in the Physics & Astronomy department (MU) from whom I had gained valuable knowledge during my graduate career. I would also like to thank Dr. Kevin Volk (STScI) for putting up with me and guiding me in all respect for the observing trip in Hawaii. My heartfelt gratitude to Professor Varun Sahni (IUCAA) for always being a tremendous inspiration in my life.

Thanks to the former members of the stardust group: Dr. Catharinus (Rien) Dijkstra, Dr. Adrian Corman, Dan Caputo for helping me with all the difficulties during my early days in the stardust group; Menzi Mchunu, David Arrant, Nelson Desouza for being amazing colleagues and friends.

My heartfelt gratitude goes to the most important people in my life, my incredible and loving parents. Without their enduring love and support I would not have come this far. Thank you Babu and Ma! My affectionate sister and brother-in-law and my little niece have also been extremely caring and supportive. Thank you O, Dipen and Boni!

And last but not least, my heartfelt thanks to Rien, for his unconditional love and support. He has been a constant source of motivation for the past two and half years and always provided fruitful ideas for this thesis. I cannot thank him enough for being so tremendously supportive and for being there whenever I needed him.

TABLE OF CONTENTS

LIST OF TABLES

LIST OF FIGURES

Figure Page

ABSTRACT

Asymptotic Giant Branch (AGB) stars are evolved, low to intermediate mass (0.8–8$M_\odot$) stars. These stars lose a significant fraction of their mass through stellar pulsation. As a result, they are surrounded by gaseous, dusty circumstellar envelopes. They are major contributors of material to the interstellar medium (ISM), new stars, planets and also produce the majority of the dust complement of galaxies. Consequently, understanding the dust around AGB stars is critical to our understanding of the contribution of dust to many aspects of astrophysics.

This thesis aims to study how the mineralogy and morphology of circumstellar dust varies with the pulsation cycle of the star and how the variation in spectral dust features (temporally and spatially) can be explained by different competing dust formation hypotheses. In the circumstellar envelopes of oxygen-rich (O-rich) AGB stars, all carbon (C) atoms from the gas are locked into carbon-monoxide (CO), leaving a surplus of oxygen (O) atoms to dominate the chemistry and form silicate dust particles (among other dust species). Consequently, AGB stars are divided into two main categories: oxygen-rich (O-rich) and carbon-rich (C-rich). In this thesis I consider only O-rich AGB stars where silicate dust is expected to dominate. The silicate dust may be present in either crystalline or amorphous form, where the crystalline silicates exhibit sharp and narrow spectral features throughout the infrared (IR) spectral region, while the amorphous silicates show two broad spectral features at 10 and 18 μm.

Circumstellar dust should vary both temporally as these stars pulsate; and spatially as dust flows away from the star and physical conditions change. My research on the temporal variation of the spectral dust features with pulsation cycle for single, O-rich Mira variable, T Cep, suggests that its spectral features cannot be explained in terms of the "classic" dust formation hypothesis. Instead, it suggests that the dust

is crystalline in nature and iron-rich silicates, neither of which is expected around low mass-loss rate O-rich AGB stars. This scenario may be consistent with the so-called “chaotic solids” hypothesis.

My research on spatial variation of spectral dust features investigates seven O-rich AGB stars for which I have acquired spatially resolved spectra using Gemini/MICHELLE spectrometer. In most cases, the observational data show that the spectral features vary significantly but without any spatial trend. These scenarios may also be consistent with the “chaotic solids” hypothesis. These results also suggest that the turbulent dynamics, pulsation shocks in the dust-forming zones around O-rich AGB stars lead to inhomogeneous dust formation, producing fine scale structure in the density of the dust envelope. In this O-rich environment, there are many potential minerals can be formed but their stability is very sensitive to the precise local conditions.

In this thesis, I have also explored different parameter space of the IR laboratory spectra of crystalline olivine minerals. The spectral feature parameters (peak, width and amplitude) can be strongly affected by composition, temperature and grain shape and that can create degeneracy, such that a given spectral feature can have more than one explanation. In order to disentangle these effects, I have developed a database, which will allow to study the IR spectral features of crystalline olivine as a combined function of composition and temperature. For future work, I propose tools for mapping and breaking this degeneracy, which will help us in order to have a better understanding on astromineralogy around O-rich AGB stars.

This thesis provides a significant contribution to our understanding of dust formation process around O-rich AGB stars, which is considered to be a complicated process and not well understood.

Chapter 1

Introduction

“Where do we come from? What are we? Where are we going?” - Paul Gauguin

1.1 Why do we care about cosmic dust?

The main goal of science is to understand the world around us. From the beginning of history of mankind, people have always tried to predict and control the future and thus their lives, based on their current knowledge. One of the fundamental question in science is: “Where do we come from, and where are we going to?” Astronomy is no exception to this rule. By looking at many different stars in different evolutionary phases astronomy tries to answer this fundamental question (at least partly). In this thesis, I will try to unveil a small part of that answer, by studying cosmic dust.

At the beginning of the Universe, all matter was in the form of hydrogen and helium, with tiny traces of lithium, beryllium, and boron, carbon, oxygen; all heavier elements form through nuclear fusion in stars. Newly-formed elements are ejected from stars either explosively (in the case of supernovae) or more gently over a few hundred thousand years for lower mass stars like the Sun. These new elements form dust grains which play an essential role in many astrophysical environments (e.g. Videen & Kocifaj 2002, Draine 2003, Krishna Swamy 2005) [146, 34, 82]. It plays an essential role in star formation processes, and contributes to several aspects of interstellar processes such as gas heating and molecule formation (Krugel 2008) [83], as well as mass loss from evolved stars (Woitke 2006) [154]. Furthermore, dust has been observed at higher redshifts (i.e., earlier in cosmic history) than expected, and understanding this phenomenon is vital to our understanding of the cosmos at large and its evolution (e.g. Sloan et al. 2009, Bussmann et al. 2009) [126, 12]. Moreover, the detection of dust at high redshift raises concerns about the use of standard candles (e.g. Type 1a Supernovae) as accurate distance indicators (Jain & Ralston 2006) [70]. Thus understanding the dust at high redshift is vital to cosmological models and dark energy studies (Corasaniti 2006, Jain & Ralston 2006) [25, 70]. Dust needs to be well understood in its own right, if we are to understand how it contributes to many aspects of astrophysics.

One of the important sites of dust formation is in the atmosphere of Asymptotic Giant Branch (AGB) stars. These are intermediate mass (0.8–8$M_\odot$) aging stars, with low effective temperature ($T_{\mathrm{eff}}\approx$3000 K), high luminosity ($L_\star\approx10^4$ $L_\odot$) and large radius ($R_\star\approx$1 AU). During the AGB phase, these stars lose mass at a high rate. The mass loss leads to the formation of a circumstellar shell of (molecular) gas and dust. The dust is formed from as the gas drifts away from the star and cools. The dust and gas eventually drift off into the interstellar medium (ISM), from which new stars and planets can be formed. AGB stars produce the majority of the dust complement in galaxies and are major contributors to galactic chemical evolution (Kwok et al. 2004) [84].

The dust grains are heated by absorbing starlight and subsequently reemit photons at infrared (IR) wavelengths. The composition, lattice structure, size, shape and mass fraction of the dust grains all affect the resulting IR spectrum, as do the temperature and density distribution of the dust within the circumstellar envelope. Using IR spectroscopy, we study the IR spectral features produced by the dust in order to identify the physical properties of the dust grains. In particular, this thesis aims to provide a good understanding of how the mineralogy and morphology of circumstellar dust varies with the pulsation cycle of the star and how the variation in spectral dust features (temporally and spatially) can be explained by different competing dust formation hypotheses.

1.2 Organization of the thesis

In this thesis, I study the dust formation hypotheses and dust properties in the circumstellar environments of O-rich AGB stars. The work presented in this thesis is a combination of: 1. analyzing temporal variation of dust spectra of a pulsating variable O- rich AGB star using Space based telescope (*Infrared Space Observatory*) data; 2. observing and analyzing spatial variation of dust spectra of seven O-rich AGB stars using ground based telescope (*Gemini Observatory*) data; 3. analyzing the compositional-temperature effects on the laboratory IR spectra of crystalline olivine minerals and developing a database for mapping the degeneracy space created by the compositional-temperature effects.

In Chapter 2, I discuss the stellar evolution of sun like stars, particularly concentrating on the internal structure and atmosphere of AGB stars.

In order to determine the precise nature of cosmic dust, we have to know how it interacts with radiation (i.e. its optical properties). By the term optical properties we refer to the scattering and absorption properties of a particle at arbitrary wavelengths. In Chapter 3, I discuss the basic principles of the optical properties of solids.

Chapter 4 gives an introduction of dust mineralogy (composition and lattice structure) and morphology (grain shape and size) around O-rich AGB stars and how the AGB stars are classified based on their spectral dust features.

In Chapter 5, I present a temporal study of O-rich AGB star T Cep, a long-period Mira variable. The spectral dust features suggest that the dust is crystalline in nature and iron-rich silicates. These findings contradict the currently favored “classic” dust formation hypotheses.

In Chapter 6, I present spatially resolved spectra of seven O-rich AGB stars, using Gemini/MICHELLE spectrometer. These data provide a better understanding of how the variation in spectral dust features with the different distances from the star, can be explained by different dust formation hypotheses.

In chapter 7, I develop a database and associated tools by using existing laboratory spectra for crystalline olivine minerals in order to disentangle the effects of composition and temperature on observable spectral features.

The work in this thesis will help to understand the cosmos at large.

Chapter 2

Stellar evolution and Asymptotic Giant Branch (AGB) stars

2.1 Introduction

In this chapter, I will discuss the fate of solar-type stars by addressing the future evolution of the Sun itself. In order to understand the stellar evolution process, first we need to learn the Hertzsprung-Russell diagram.

2.2 Hertzsprung-Russell diagram and evolution of solar type stars

In the early 20-th century Hertzsprung (1905) and Russell (1914) independently discovered that when they compared the absolute magnitudes (or luminosities) with the surface temperature (or spectral classes) observed from stars, there were many patterns that emerged. In recognition of the originators, the plot of luminosity (L) of a star against its effective surface temperature (T_{eff}) is called Hertzsprung - Russell (HR) diagram (see Figure 2.1: left panel).

The majority of stars lie on a diagonal band that extends from hot stars of high luminosity in the upper left corner to cool stars of low luminosity in the lower right corner. This band is called the Main Sequence (MS) where stars spend most of their lives; during this phase hydrogen (H) is fused into helium (He) in the core of the star. Our Sun is currently a main sequence star. There are also stars which are abnormally faint for their white-hot surface temperatures, they lie sparsely scattered on the lower left corner in the HR diagram and they are called white dwarfs (WD) (see Figure 2.1: left panel). And the giant stars, which are of great luminosity (L) and size (R), form a thick, approximately horizontal band that joins the main sequence near the middle of the diagonal band. Above the giant stars, there is another sparse horizontal band consisting of the supergiant stars. The stars in the lower right corner of the main sequence are frequently called red dwarfs, and the stars between the main sequence and the giant branch are called subgiants (see Figure 2.1: left panel).

The significance of the HR diagram is that stars are concentrated in certain distinct regions instead of being distributed at random. This regularity is an indication that definite laws govern stellar structure. Therefore the existence of fundamentally different types (groups) of stars in the HR diagram is the most important tool in understanding the stars. The HR diagram suggests that stars should change in luminosity (L) and temperature (T_{eff}) through out their lives as they evolve. This means that the stars within the same group share essentially the same characteristics and as they evolve something must have caused changes in temperature (T_{eff}) and luminosity (L) for the star to move from one group to another in HR diagram. Thus the evolution of stars can be tracked through the HR diagram since it represents stars at different stages of their evolution. The expected evolutionary path of a $1\,M_{\odot}$ is shown in Figure 2.1: right panel.

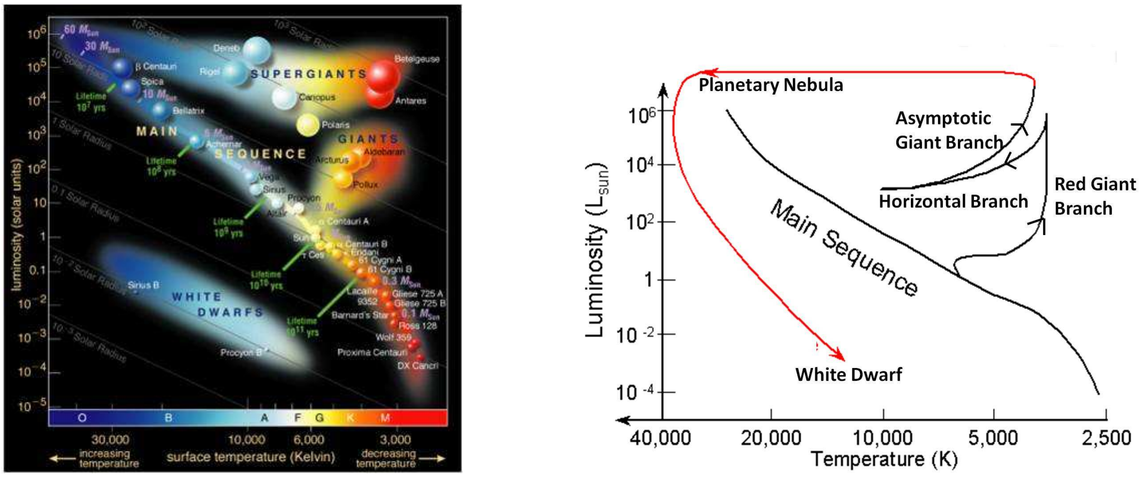

Figure 2.1: Left: Hertzsprung-Russell Diagram. Right: Schematic diagram showing the post-main-sequence evolutionary track of Sun like stars.

A star with an initial mass of $1\,M_{\odot}$ starts its life on the main sequence (MS), where it burns hydrogen (H) in its core, and fuses it into helium (He):

$$4H_1^1 \rightarrow He_2^4 + energy \tag{2.1}$$

This produces tremendous amount of energy, which helps to maintain the state of hydrostatic equilibrium; the tendency of the star to collapse due to its own gravitational pull is exactly balanced by the gas and radiation pressure outwards. Once the H in the core is exhausted, the star ascends the Red Giant Branch (RGB; see Figure 2.1: right panel). During this phase, the core of the star begins to collapse because there is no longer an energy source to provide heat to the gas, and its resistance to the gravitational pull of the star's mass dwindles. This heats up the material in the center of the star, causing a shell of H surrounding the now dormant He core to begin fusion. The rate of fusion in this shell is much higher than the previous core H fusion, so more energy is produced. This will make the star increases the luminosity (L), which expands to many times its original size, and decreases the effective temperature ($T_{\rm eff}$).

The dormant He core of RGB, does not produce energy by nuclear burning. The evolution of low-to-intermediate mass (LIMS; 0.8–8M$_\odot$) red giant stars vary slightly depending on their mass. The core of these red giant stars of mass below 2.5M$_\odot$ cannot continue shrinking forever, because eventually its volume will have decreased to the point where it becomes degenerate matter (i.e.the pressure due to quantum mechanical interactions between the electrons in the core dominates the pressure due to the temperature). Because the core of a red giant becomes degenerate, the core stops collapsing (the gravitational force due to the core is not strong enough to overcome the degeneracy pressure). Eventually, the He core will continue to collapse until it finally gains enough thermal energy to begin fusing He into carbon (C) and oxygen (O) by triple α process:

$$3He_2^4 \rightarrow C_6^{12} + energy \tag{2.2}$$

This stage is called Horizontal Branch (HB) (see Figure 2.1: right panel), which is analogous to the MS stage, except that helium is fusing in the core instead of hydrogen. Eventually, the helium will become exhausted and the core of the star will once again begin to collapse until it becomes degenerate. LIMS are not massive enough for C fusion to occur in the core; however, as the collapse continues the material surrounding the core will start fusion, producing concentric shells of He and H around the inert core. This is the Asymptotic giant branch (AGB) phase of the star's evolution, where again effective temperature ($T_{\rm eff}$) decreases and luminosity (L) and radius (R) increases (see Figure 2.1: right panel). During this AGB phase that stars produce copious quantities of dust, escaping at a few tens of kilometers per second.

Early in the AGB phase, the internal structure of all stars are qualitatively similar, irrespective of their initial mass. As a star ascends the AGB phase, it starts losing significant fraction of its original mass through slow, massive winds at a rate of

$10^{-8} < \dot{M} < 10^{-4}\,\mathrm{M}_{\odot}\,\mathrm{yr}^{-1}$ (vanLoon et al. 2005) [142]. This mass loss occurs as a result of stellar pulsation (Habing 1996) [51] followed by acceleration of dust grains by radiation pressure (e.g. Gehrz & Woolf 1971, Hofner et al. 2007) [44, 63]. Mass loss increases with the pulsation period, and starts to dominate the evolution of the star. Eventually, it ends up with extremely high mass-loss rate, the so-called superwind (SW) phase[1] in which $\dot{M} > 10^{-5} M_{\odot}\, yr^{-1}$.

When the SW phase is over, the star starts to collapse in size but at constant luminosity, getting hotter over time. The star is now in post-AGB phase. Mass loss still occurs, but at a substantially lower rate. Depending on the rate at which the central star evolves and the speed at which the envelope moves outwards, the star may eventually start to photo-ionize the material that was ejected during the AGB phase, when $T_{\rm eff} \geq 30000\,\mathrm{K}$, creating a planetary nebula (PN; see Figure 2.1: right panel). In this case the phase between the end of the AGB and birth of the PN is called proto-planetary nebula (proto-PN) phase. Finally, the star starts to decrease rapidly in luminosity, and eventually becomes a cool white dwarf (WD) (see Figure 2.1: right panel), while the remains of the circumstellar envelope disperse into the Interstellar Medium (ISM). Depending on the initial mass of the star, it will experience different mass-loss rates during the AGB phase, and will evolve through the AGB, post-AGB and planetary nebula phases on different time scale.

2.3 Asymptotic Giant Branch (AGB) stars

This thesis concentrates on exploring the dust production of the AGB phase of the stellar evolution. Now it is appropriate to discuss the AGB stars in detail.

---

[1] A SW phase is a hypothesis, because the mass loss rate of a $1\mathrm{M}_{\odot}$ star will never exceed $10^{-7} M_{\odot}\, yr^{-1}$ (Blocker 1995) [6]

2.3.1 Internal structure of an AGB star

Figure 2.2 shows schematically an internal structure of an AGB star. It consists of a degenerate C and O core surrounded by a He and H-burning shells respectively. Due to the degeneracy of the core, there is no carbon burning occurs. A large convective envelope is surrounded by the core and the shells. During most of the time, the H-shell burns H to He and provides the stellar luminosity. However, when temperature and density are favorable, He can be fused in the He-shell, causing a thermonuclear runaway. This phenomenon (a He-flash) is called a thermal pulse (TP). During such thermal pulses, the convective layers in the mantle may reach the region between the H and He-burning shells (see Figure 2.2) and transport new materials (mainly C, N and O) to the surface of the star. This is called a *dredge-up*. The timescales between consecutive pulses range from $10^4 - 10^5$ years, depending on the luminosity of the AGB star.

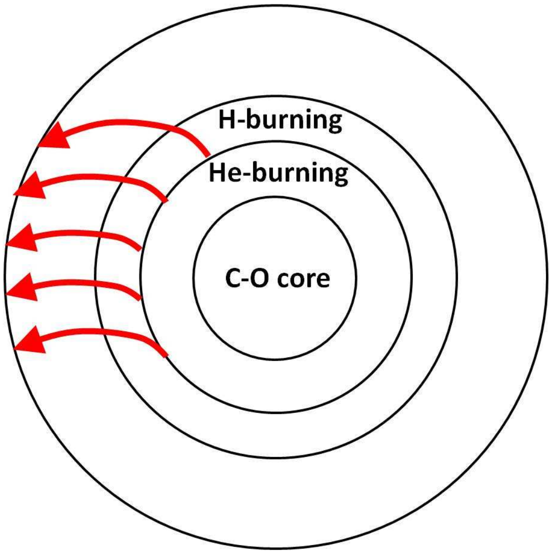

Figure 2.2: The internal structure of an AGB star (not to scale).

2.3.2 Structure of the circumstellar envelope of an AGB star

Figure 2.3 represents a typical structure of a circumstellar envelope of an AGB star. The envelope is created by mass loss from the central star due to stellar pulsation in combination with radiation pressure on molecules and dust. During an outward pulse, gas moves away from the star and gradually cools down. Below $\approx 3000\,K$, outside the photosphere of the star molecules start to form within the gas, resulting a warm molecular layer around the star. At some distance from the central star solids can exist; dust particles begin to form ($\approx 1000\,K$). The dust grains are driven outwards by radiation pressure from stellar photon, and drag the gas along with them, creating a dusty circumstellar envelope.

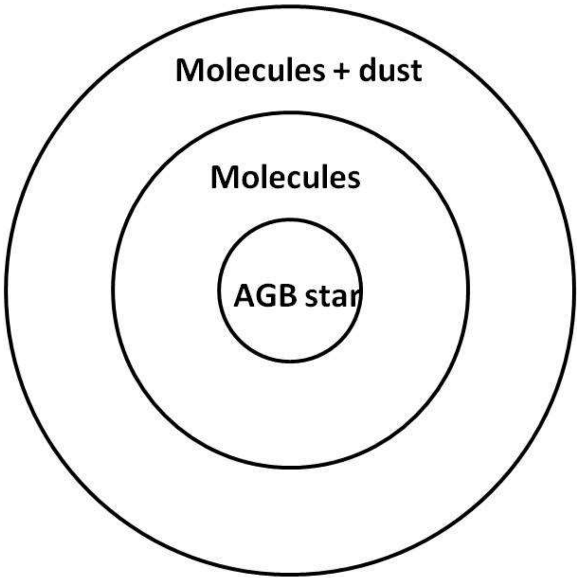

Figure 2.3: The circumstellar envelope of an AGB star.

2.3.3 Different types of AGB star

The formation of dust depends largely on the availability of atoms and molecules. The most abundant elements used for the formation of dust are C and O. However, the carbon monoxide (CO) molecule is very stable and already forms at high temperatures in the stellar atmosphere. This leads to a clear separation of the type of dust present around AGB stars. If more oxygen than carbon is available, i.e. the number density ratio of carbon-to-oxygen (C/O) is smaller than unity, all the C will be trapped in CO and only O atoms will dominate the chemistry. In this case oxygen-rich (O-rich, also known as M-type) dust will form, for instance (simple) oxides and silicates (see Figure 2.4: left panel). This is the initial situation for all stars. The material in the ISM from which stars form is O-rich (C/O ≈ 0.4; Asplund et al. 2009) [1].

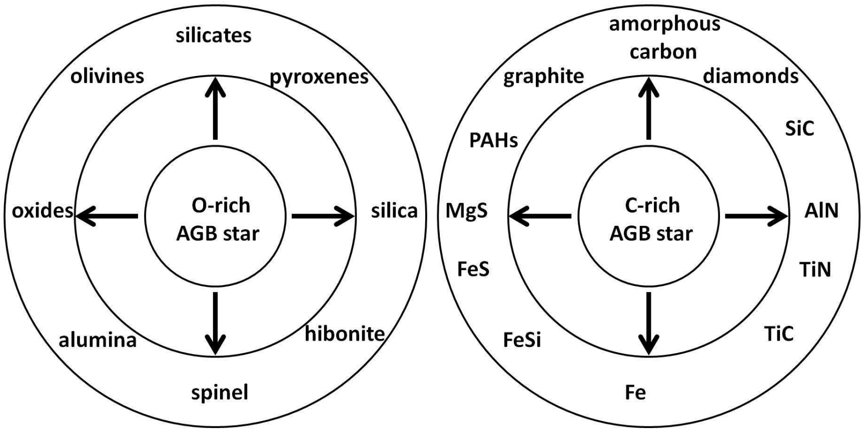

Figure 2.4: The circumstellar dust envelope of Oxygen-rich (left panel) and Carbon-rich (right panel) AGB star.

As the AGB stars evolve, newly-formed elements are transported to the surface via convection current (see Figure 2.2), which changes the C/O of the stellar atmosphere. If dredge-up of carbon is sufficient it can raise C/O above unity to form carbon-rich (C-rich) stars (see Figure 2.4: right panel). In these C-rich envelope most of the oxygen is trapped in CO, so that carbon is left to dominate the chemistry. Carbon-rich dust species include silicon carbide (SiC) and graphite and polycyclic aromatic hydrocarbons (PAHs). During the carbon dredge up atmospheric C/O increases, so that some stars have C/O ≈ 1[2]. Thus, the atomic abundances in the wind strongly determine what kind of dust is formed. The physical and chemical processes leading

---

[2] these stars are referred as S-stars

to dust formation are still poorly understood. This thesis concentrate on studying the dust properties around O-rich AGB stars.

2.3.4 Mechanism behind pulsation of AGB stars and their light curves

From observations, we know that the AGB stars are pulsating variable stars. They change in brightness in a more or less regular pattern with a period of ~ 1 year. They fall into two groups according to the mode of pulsation. The first group contains Long Period Mira variable stars, having regular pulsation with large amplitude (visual magnitude > 2.5) and periods longer than 60 days. The second group contains semiregular variable stars, having less regular pulsation and smaller amplitude (visual magnitude < 2.5). In this thesis, I have analyzed the spectral dust features of both Mira and semiregular variable AGB stars (see Chapter 5 & 6).

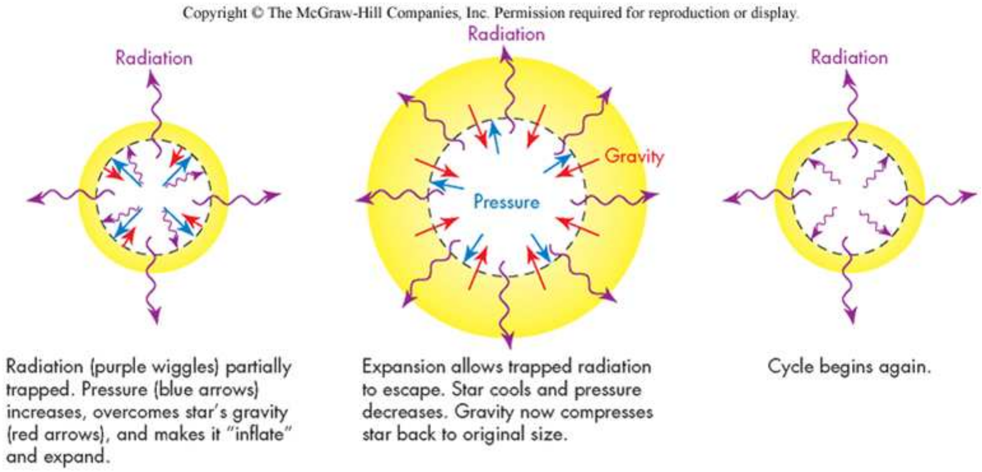

Figure 2.5: A schematic diagram of pulsating AGB stars.

The mechanism behind pulsation is governed by: outward radiation pressure, omnidirectional gas pressure and inward gravitational pressure (see Figure 2.5). Opacity of the gas inside the star traps energy (i.e., radiation is absorbed and converted to thermal energy). That increases the gas pressure, which in turn overcomes gravity and leads to expansion of the star. But this expansion decreases the density of the gas, which allows radiation to escape and the gas to cool down radiatively. As a result gas pressure drops and gravity dominates, and the star to shrinks again. This produces an increase in the density of the gas and thus the opacity increases and the cycle begins again.

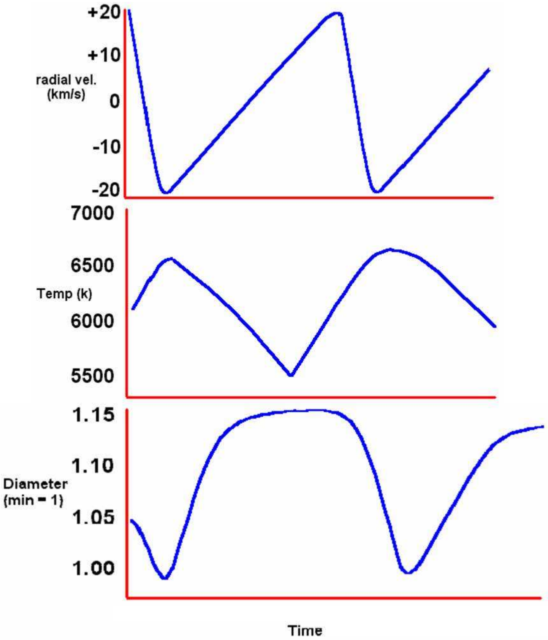

Figure 2.6: A schematic cartoon shows the effect of stellar pulsation.

To study the cycle-to-cycle changes of the pulsating variable stars, astronomers use a very simple but valuable tool, known as "light curve". A light curve is a plot which shows the change in apparent visual magnitude (brightness) of a star over time. Figure 2.6 shows an example of how the size, surface temperature of the star and radial velocity of the gas change over the course of time. The observations are generally taken by amateur astronomers using ground-based telescopes and the observational data are available from one of the most popular worldwide database maintained by the American Association of Variable Star Observers (AAVSO). The light curve observations provide a great opportunity to test the hypotheses that link pulsation, stellar variability and dust formation.

2.3.5 Mass loss and dust formation around AGB stars

During the AGB phase, stars lose 40-80% of their original mass. This mass loss is crucial for LIMS stars evolution since it leads to the formation of stellar remnants below the Chandrasekhar limit, and prevents these stars from exploding as supernovae. Furthermore, LIMS are the major contributors of newly-formed elements and dust to the ISM.

As a star loses mass, gas drifts away from the star and cools; at some distance from the star dust forms leading to a circumstellar shell of gas and dust. The dust gains momentum by absorbing stellar photons (radiation pressure) and accelerates away from the star. Momentum is transferred to the gas by collisions with the dust, and thus the gas is dragged away from the star. This creates a low pressure zone in the atmosphere into which gas will flow (from the star's surface). In this way, dust formation drives mass loss. As the refractory dust and gas moves outwards it cools further and more dust can form which will also be acted upon by radiation pressure. Thus mass-loss rate increases.

The efficiency of capture of momentum by the dust grains depends on their absorption properties, and thus, on the precise nature (composition, lattice structure, grain size, grain shape, temperature and mass fraction) of the dust grains. This thesis aims to study these properties of dust grains around oxygen-rich AGB stars.

2.4 Using infrared spectroscopy to study AGB stars

AGB stars are bright and numerous enough to observe and explore a statistically significant number of stars. There are estimated to be $\approx 10^5$ AGB stars in our galaxy out of a total population of $\approx 10^{11}$ stars, or a frequency of 1 in 1 million (Habing & Whitelock 2003) [52]. Most of their light is emitted in the IR spectral region. Infrared spectroscopy of (circumstellar) dust provides a powerful diagnostic tool to determine their properties (chemical composition, lattice structure size and shape, temperature, mass fraction). A significant part of this thesis deals with the analysis and identification of these dust properties by using IR spectroscopy. The infrared is particularly suitable for this since dust grains absorb starlight and reemit photons according to their temperature and optical properties, typically in IR range. In this regime, dust shows many spectral features, which are sensitive to the above mentioned dust properties. Early all-sky surveys such as the *InfraRed Astronomical Satellite* (Neugebauer et al. 1984) [105] and subsequent satellite IR telescopes along with ground-based IR spectroscopy have provided us with tens of thousands of spectra of dusty AGB stars with a wide range of dust properties. While in principle each spectrum provides a diagnostic view of the dust properties of individual stars, the spectra of AGB stars are observed to vary substantially from object to object (Speck et al. 2000, Sloan et al. 2003) [131, 123], as well as temporally (e.g. Guha Niyogi et al. 2011, Monnier et al. 1998) [49, 102] and spatially (Sloan & Egan 1995, Guha Niyogi et al. 2011-b) [122, 50] for a given object.

2.4.1 Recent developments in Telescopes era

The availability of space-based observatories have opened a new era in IR astronomy. For the last two decades, the mostly used observational data are available from the following Telescopes: *InfraRed Astronomical Satelite* (IRAS; Neugebauer et al. 1984) [105], *Infrared Space Observatory* (ISO; Kessler et al. 1996) [74], *Spitzer Space Telescope* (Werner et al. 2004) [151], *Herschel Space Observatory* (Doyle et al. 2009) [33]. Space-borne observations opened way for spectroscopic studies in the IR wavelength regions which were inaccessible from the ground (only narrow window in the IR are available from the ground).

IRAS was the space-based observatory (launched in 1983) to perform a survey of the entire sky at IR wavelengths (12, 25, 60, and 100 μm). This telescope was a joint project of the United States (NASA), the Netherlands (NIVR), and the United Kingdom (SERC). The European Space Agency's *ISO* was operational between 1995–1998 (see Figure 2.7: left panel). The two spectrometers (SWS and LWS), a camera (ISO-CAM) and an imaging photo-polarimeter (ISOPHOT) jointly covered wavelengths from 2.5 to around 240 μm. This made it possible to obtain a continuous flux spectrum extending from visual to the far-IR wavelengths for many observations and compare with theoretical models. The *Spitzer Space Telescope* was launched in 2003 and operating at IR wavelength region from 3–180 μm and has multiple imaging abilities. The most recent European Space Agency's *Herschel Space Observatory* (launched in 2009) has the largest single mirror ever built for a space telescope. It is the only space observatory to cover a spectral range from the far infrared to sub-millimeter (60–670 μm).

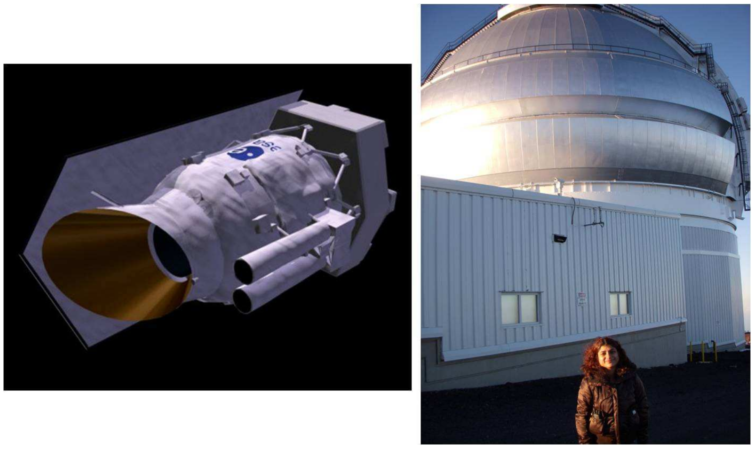

Figure 2.7: Left: Space borne telescope ISO; Right: Ground based Gemini Observatory at Mauna Kea.

Along with the space based telescopes, the recent advances in ground-based telescopes for visible and infrared wavelength regions, have spurred extraordinary advances in our understanding in many astronomical areas. The most noted ground based telescopes operated in IR wavelength region are James Clerk Maxwell Telescope (*JCMT*), United Kingdom Infra-Red Telescope (*UKIRT*), Gemini Observatory (see

Figure 2.7: right panel), European Southern Observatory (*ESO*), South African Astronomical Observatory (*SAAO*), and Australian Astronomical Observatory (*AAT*). The first three are situated close to the summit of Mauna Kea, Hawaii, at an altitude around 4100 m, whereas, *ESO* operates in Chile, *SAAO* in South Africa and *AAT* in Australia . There are some disadvantages of ground based IR observations. As an example, both the telescopes and our atmosphere emit infrared radiation which creates background radiation. Infrared telescopes are designed to limit the amount of this thermal emission from reaching the detectors. But this problem is generally solved by taking proper measurement of both the emission from atmosphere and from the observing object and then by subtracting the atmospheric emission from the infrared emission of a celestial object.

In this thesis, I have explored the observational data taken by *ISO*, *IRAS* and *Gemini observatory.*

Chapter 3

Optical properties of solid dust grains

3.1 The interaction of radiation with dust grains

In order to determine the precise nature of the cosmic dust, we need to know how the dust grains interact with the radiation (i.e. their optical properties). When a dust particle is placed in a beam of light, it absorbs some of the light and scatters part of them. The light then we receive from the dust particle is attenuated. The total amount of energy by scattering and absorption is called extinction. Extinction depends on the precise nature (composition, lattice structure, grain size, grain shape, temperature and mass fraction) of the dust grains. In this chapter I will give an outline of how dust particle interacts with light and how it helps us to determine the optical properties of the light.

3.2 Thermal emission

Any object with a temperature greater than absolute zero emits thermal radiation. The spectrum of the emitted radiation is determined by the characteristics of the emitting body as well as by its temperature. A perfect blackbody, which absorbs all radiation that is incident on it, will thermally re-emit radiation in a distribution over wavelength, as given by the Planck function. The maximum of this function shifts towards shorter wavelengths when the temperature of the body increases (see Appendix § A).

Dust grains are not perfect blackbodies. The radiation emitted by a non-perfect blackbody is a Planck curve multiplied by the emission efficiency of the emitting object (for further discussion see § 4.2). Therefore, to compute the thermal emission of a dust grain we need to compute its emission efficiency. A particle in thermal equilibrium emits the same amount of energy as it absorbs. Kirchhoff's law states that at any wavelength the emission efficiency is equal to the absorption efficiency.

As discussed in § 2.3.2, below $\approx 3000\,K$, outside the photosphere of the star molecules start to form within the gas, resulting a warm molecular layer around the star. At some distance from the central star, dust particles form in the range from $\approx 1000 - 1500\,K$. Above this temperature the grains will evaporate. This corresponds to an emission spectrum peaking at wavelengths longwards of $\approx 2\,\mu$m. In most cases, the bulk of the dust grains will have much lower temperatures, peaking at even longer wavelengths. Thus the thermal emission by dust grains dominate at IR wavelength region (see Figure 3.1).

3.3 Extinction

When a parallel beam of light meets a dust particle, then the light is absorbed and scattered by the particle. The total amount of energy removed from the incident

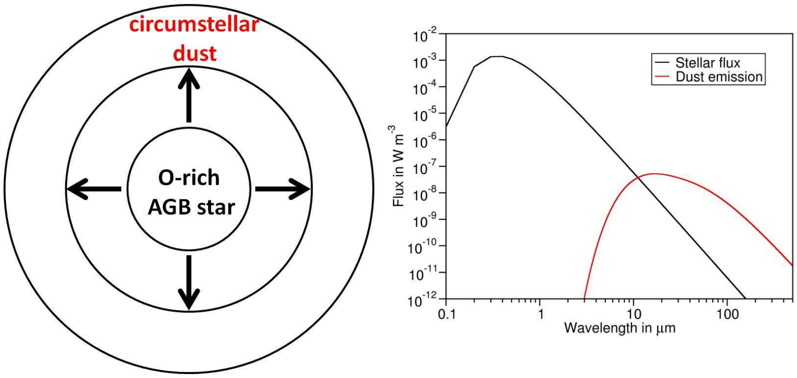

Figure 3.1: A schematic presentation of stellar emission and dust emission in IR region.

light beam by scattering and absorption is referred to as extinction. The wavelength dependence of the extinction provides precise information about the dust particle.

3.3.1 Scattering and absorption of small particle compare to their wavelength

In this section, I reproduce the derivation from Speck 1998 [129], in order to explain the ideas of scattering and absorption of small particle compare to their wavelength.

Let's consider a small particle placed in a beam of light (see Figure 3.2). The intensity of the electromagnetic radiation incident on the particle is I_0, at a point a large distance r from the particle and the intensity of the scattered light is I. The scattered intensity (I) is directly proportional to I_0 and given by,

$$I(\theta, \phi) = \frac{I_0 F(\theta, \phi)}{k^2 r^2} \tag{3.1}$$

where, $k = \frac{2\pi}{\lambda}$ is the wavenumber, and $F(\theta, \phi)$ is an orientation dependent, dimensionless function of the direction but does not depend on the distance of the particle.

The total energy scattered by the particle in all directions is defined as being equal

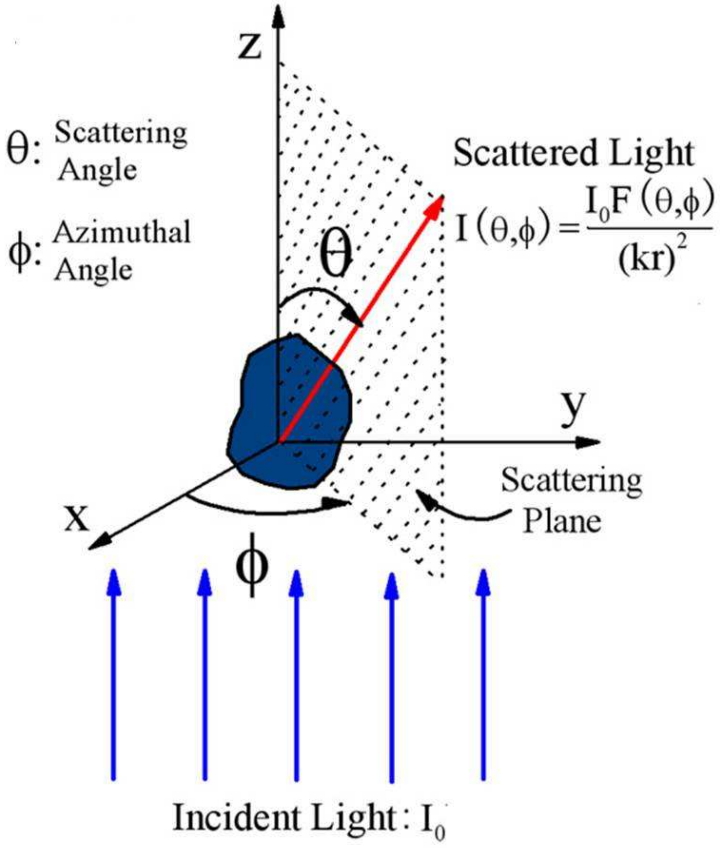

Figure 3.2: A schematic representation of scattering geometry of a dust grain (taken from Bohren & Huffman 1983 [8]).

to the energy of the incident light falling on the scattering cross-sectional area (C_{sca}).

If the function $F(\theta, \phi)$ is divided by $k^2 C_{sca}$ the phase function is obtained, which has no dimensions and whose integral overall direction is 1. Therefore,

$$C_{sca} = \frac{1}{k^2} \int F(\theta, \phi) d\omega \tag{3.2}$$

where $d\omega = \sin\theta d\theta d\phi$ is the element of solid angle and the integral is taken over all directions.

Similarly, the energy absorbed by the particle is equal to the energy incident on the area of absorption cross-section (C_{abs}). So, the total energy depleted from the original beam can be put equal to the incident energy on the area of extinction cross-section

(C_{ext}). The law of conservation of energy requires that,

$$C_{ext} = C_{abs} + C_{sca} \tag{3.3}$$

The efficiency of a particle to absorb, scatter and extinction are given by the Q factors, where,

$$C_{ext} = Q_{ext} \times \text{geometrical} - \text{area} \tag{3.4}$$

$$C_{abs} = Q_{abs} \times \text{geometrical} - \text{area} \tag{3.5}$$

$$C_{sca} = Q_{sca} \times \text{geometrical} - \text{area} \tag{3.6}$$

$$\tag{3.7}$$

3.4 Computing the optical properties of dust grains

To study the optical properties of the dust grains, first we need to discuss about the optical constants and how they are interrelated. The first set is real and imaginary parts of the complex refractive index (m) and the second set is real and imaginary parts of complex dielectric function (ϵ). They are defined as,

$$m = n - ik \tag{3.8}$$

$$\epsilon = \epsilon_1 - i\epsilon_2 \tag{3.9}$$

And they are related by,

$$\epsilon_1 = n^2 - k^2 \tag{3.10}$$

$$\epsilon_2 = 2nk \tag{3.11}$$

The media with which we are concerned, have complex refractive indices that depend on wavelength. These parameters need to be computed in accurate manner. The computation of the optical properties of dust grains requires that the Maxwell equations for the interaction of the incident light with the particle to be solved. This is in general not a trivial exercise. For this reason, in most cases the shape of the cosmic dust particles are assumed to be simple and symmetrical.

There are two extreme ways to approach the problem of light scattering and absorption by small particles. The first approach is to assume that the dust grains can be approximated by homogeneous spheres. In this way the optical properties can be obtained from Mie theory. The second approach is to model the dust grains in the most exact way possible. In both of these approaches have their advantages and disadvantages and are discussed below:

3.4.1 For spherical particles: Mie theory

In 1908 Gustav Mie published an exact solution for the interaction of light with a homogeneous sphere of arbitrary composition and radius. Certain assumptions are made about these particles in order to simplify the situation.

These assumptions are:

1)Only the interactions of a single particle with light of arbitrary wavelength are considered.

2)The optical properties of the particle are completely described by frequency dependent optical constants (i.e. the complex refractive index or the complex dielectric function).

3)Scattering is elastic, i.e. frequency of the scattered light is identical to the incident light.

4)The medium is considered to be linear, homogeneous and isotropic.

Calculations of scattering and absorption cross sections of homogenous spherical particle can be done very accurately using Mie theory. In Rayleigh limit, we consider the limiting case of particles very small compared to the wavelength of radiation inside and outside the particle (i.e. $2\pi a/\lambda \ll 1$).

For a spherical particle of radius a, C_{abs} and is given by,

$$C_{abs} = kVIm(3\alpha), \tag{3.12}$$

where,

$$\begin{aligned} k &= \frac{2\pi}{\lambda}, \\ V &= \frac{4}{3}\pi a^3, \\ m &= n - ik, \\ Im(\alpha) &= \frac{m^2-1}{m^2+2}. \end{aligned} \tag{3.13}$$

Therefore, for spherical particle (SPH)

$$C_{abs} = \frac{8\pi^2 a^3}{\lambda} Im\left(\frac{m^2-1}{m^2+2}\right) \tag{3.14}$$

This approach is fast and easy and also provides useful insights in the physical processes and general trends (see e.g. van de Hulst 1957) [141]. However, in reality, cosmic dust grains are not homogeneous spheres, and therefore we need to consider the alternative approaches.

3.4.2 For non-spherical particles

Since solid particles in astrophysical environments are expected to be very irregular in shape, it is very difficult to characterize the shape of the particles in a simple way. Traditionally, cosmic dust grains have been assumed to be spherical for simplicity, however, it is becoming increasingly obvious that the use of spherical grains leads to unrealistic spectral features (see e.g. Min et al. 2003, DePew et al. 2006, Pitman et al. 2008, Corman 2010) [95, 31, 115, 26]. There are several possible approaches to addressing the grain shape effect, which I will compare here.

Fabian et al. (2001) [37] used their optical constants of crystalline olivine minerals to calculate mass absorption coefficients for IR region for a variety of grain shapes. These authors primarily chose: spherical grains, ellipsoids elongated along the z-axis, and distributions of ellipsoids; based on the assumption that mineral forms crystalline ellipsoids elongated along the z-axis, when condensing from the gas phase at high temperature. Whether there should be a preferred growth axis for a grain shape or not, will be discussed below. These authors compared their calculated mass absorption coefficients data directly with *ISO* SWS observational data of evolved stars. They concluded that the spectral features are shifted in wavelength by grain shape effects and this effect is prominent in mid-IR region, whereas, the spectral features in far-IR region remain practically unaffected by the particle shape.

Recent experimental studies by Takigawa et al. (2009) [135] on the evaporation of single crystals of forsterite show that this mineral evaporates anisotropically, which may lead to distinct grain shape distributions (e.g. disk-shaped dust grain, flattened along the y or z axes). They showed that forsterite always evaporates anisotropically, but the details of the anisotropy (i.e. which axis is elongated) depends on the experimental conditions (total gas pressure and temperature). They concluded that the precise shape of forsterite grains depends on the formation conditions in space. Because the peak positions and relative strengths of dust spectral features are expected to depend on grain shape, these spectral parameters may be diagnostic of the formation and heating conditions for the dust grains.

Another recent study by Koike et al. (2010) [77] investigated how the spectral features of forsterite are affected by grain shape. They measured the IR mass absorption coefficients of forsterite grains of a variety of shapes including irregular, plate-like with no sharp edges, elliptical, cauliflower and spherical. They concluded that spectral features of forsterite in mid-IR region (at 11, 19, 23, 33 μm) are extremely sensitive to particle shape, whereas, the features in far-IR region (at 49, 69 μm) remained unchanged despite the different grain shapes (cf. Fabian et al. 2001) [37].

Min et al. (2003) [95] adopted statistical approach (following Bohren & Huffman 1983) [8] in order to understand the effect of grain shape on IR dust features of forsterite. They considered the limiting case, where the particles are very small compared to the wavelength of radiation (Rayleigh domain). In this statistical approach, the scattering and absorption properties of irregularly shaped particles can be simulated by the average properties of a distribution of simple shapes (such as ellipsoids, spheroids, and hollow spheres). They calculated the absorption and scattering cross sections of different grain shapes and concluded that there is a strong similarity between the absorption spectra of distributions of various non-spherical homogeneous particles (e.g. ellipsoid, spheroids) and a distribution of hollow spheres in Rayleigh domain, but that homogenous spherical particles show a markedly different spectrum. (for further reference see Figure 5.14). In general, the cross section for absorption by an arbitrary particle in this approximation, averaged over all orientations is given by,

$$C_{abs} = kVIm(\alpha_{ave}), \tag{3.15}$$

where, $k = \frac{2\pi}{\lambda}$,

V = volume of the particle,

α_{ave} = the polarizabilities per unit volume of the shape distribution.

For Continuous Distribution of Ellipsoids (CDE),

$$Im(\alpha_{ave}) = 2\frac{m^2}{m^2-1}\ln(m^2) - 2, \tag{3.16}$$

where, m = n - ik.

For Continuous Distribution of Spheroids (CDS),

$$Im(\alpha_{ave}) = \frac{1}{3}\ln(m^2) + \frac{4}{3}\ln\left(\frac{m^2+1}{2}\right) \tag{3.17}$$

For Distribution of Hollow Sphere (DHS),

$$Im(\alpha_{ave}) = \frac{6m^2+3}{2m^2-2}\ln\left(\frac{(2m^2+1)(m^2+2)}{9m^2}\right) \tag{3.18}$$

By using the real and imaginary parts of refractive index of the materials, I have evaluated C_{abs} for different grain shapes (some examples are shown in § 4.5).

3.5 Introducing different terminologies and relation among them

In § 3.3.1 & 3.4, we have used different terminologies in order to explain the optical properties of solid dust grains. Because laboratory optical properties of solids are produced for a variety of applications, the various laboratory data are published in several different types of units (e.g. absorbance, mass absorption coefficient, complex refractive index etc.; also see Figure 3.3). In this section I will reproduce the derivations from Speck et al. 2011 [132], in order to discuss different terminologies and establish relationship among them.

Transmittance (T; which is also referred to as *transmissivity*) is defined as the ratio of the intensity of transmitted (I_{trans}) and incident (I_0) light, i.e. I_{trans}/I_0. Similarly reflectivity, R and absorptivity, A are the ratios of absorbed to incident light and

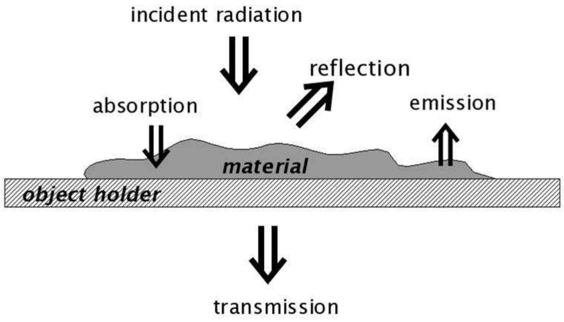

Figure 3.3: A schematic presentation of various phenomenon while the radiation is incident on a material.

reflected to incident light, respectively.

$$I_0 = I_{\mathrm{abs}} + I_{\mathrm{trans}} + I_{\mathrm{refl}}$$

$$\frac{I_{\mathrm{trans}}}{I_0} = 1 - \frac{I_{\mathrm{abs}}}{I_0} - \frac{I_{\mathrm{refl}}}{I_0}$$

$$T = 1 - R - A$$

For simplicity we will assume the reflectivity is negligible or has been accounted for. Then,

$$T = 1 - A \tag{3.19}$$

When light passes through a solid the absorption can be expressed as:

$$I_x = I_0 e^{-\alpha L} \tag{3.20}$$

where L is pathlength or thickness of the solid sample and α is usually called the absorption coefficient, but sometimes it is called as opacity. In addition $\alpha = \kappa\rho$, where κ is the mass absorption coefficient, and ρ is the mass density.

$$T = e^{-\alpha L} = e^{-a} \tag{3.21}$$

Absorbance, (a), is the exponent in the decay of light due to absorption: $a = \alpha L = \kappa\rho L$. Optical depth τ_λ of an absorbing material is defined by:

$$I_x = I_0 e^{-\tau_\lambda} \tag{3.22}$$

From equations 3.20, 3.21 and 3.22 we see that the absorbance (a) is similar to optical depth (τ_λ). In order to compare astronomical data in which we have a wavelength-dependent optical depth we can use absorbance. Now we can relate the absorbance (a) and absorptivity (A) via equation 3.21:

$$A = 1 - e^{-a}$$

To compare with some astronomical observations we still need to extract a version of the laboratory data that is comparable to the absorption efficiency, Q-values. To get this we need to consider how Q-values are defined. For a non-blackbody dust grain we define an absorption cross-section C_{abs} as the effective geometrical cross-section of the particle once we account for it not being a blackbody:

$$C_{\text{abs}} = Q_{\text{abs}} \times \Upsilon$$

where Υ is the geometrical cross-sectional area of a dust grain. Now if we consider how the absorption cross section gives rise to absorption we get:

$$\frac{I_{\rm abs}}{I_0} = A = C_{\rm abs} n L \tag{3.23}$$

where n is the number density of absorbing particles and L is the pathlength or thickness of the absorbing zone.

$$n = \frac{\rho}{M_{\rm mol} \times m_H} \tag{3.24}$$

where $M_{\rm mol}$ is the molar mass of the solid and m_H is the mass of a hydrogen atom. Combining equations 3.23 and 3.24 we get:

$$Q_{\rm abs} = \frac{A \times M_{\rm mol} \times m_H}{\Upsilon \rho L} \tag{3.25}$$

It is clear from equation 3.25 that Q-values $\propto$ absorptivity such that:

$$Q_{\rm abs} = \zeta A$$

where,

$$\zeta = \frac{M_{\rm mol} \times m_H}{\Upsilon \rho L}$$

Consequently, the spectral feature parameters shown in Q-values will be identical to those for A, the absolute values depend on the pathlength and on the cross-section areas of a given grain distribution.

3.6 Introducing various laboratory data sets

There are several laboratories that have measured optical properties of various solid minerals for a variety of applications. In this thesis, I will use the IR spectral data from three most noted laboratory groups. They are: 1. WashU (e.g. Hofmeister et al. 2007, Pitman et al. 2010) [60, 114], 2. Kyoto (e.g. Chihara et al. 2002, Koike et al. 2003, Koike et al. 2006, Murata et al. 2009, Koike et al. 2010) [23, 76, 78, 104, 77] and 3. Jena (e.g. Fabian et al. 2001, Jaeger et al. 1998) [37, 69] groups.

The WashU & Kyoto groups provide opacity measurements (absorbance & mass absorption coefficient respectively) for a good sampling over several composition ratios of various minerals. But they do not measure the complex indices of refraction or dielectric constants for all these compositions. On the other hand, Jena group supplies complex refractive indices of several minerals, but does not measure the over various composition ratios. The advantages and limitations of both of these measurements will be further discussed in Chapter 5 & 7. Now, it is important to remember that, when we use different data sets from different laboratory groups (with different units), we need to use appropriate conversion factors (as discussed in § 3.5) in order to be consistent.

Chapter 4

An introduction of dust mineralogy and morphology around O-rich AGB stars

4.1 Introduction

As discussed in § 1.1, dust is very important in many astrophysical environments. In particular, due to the interplay between dust and stellar photons in driving mass loss, it is necessary to understand the nature of the dust around O-rich AGB stars. Dust grains absorb starlight and reemit photons according to their temperature and optical properties, typically in IR region. Composition, lattice structure, grain size, and morphology all affect the resulting IR spectrum, as do the temperature and density distribution in the dust shell (as also discussed in § 2.4). We can compare laboratory spectra of different dust species to astronomical observations in order to identify the dust species present in circumstellar envelopes. To understand the dust spectral features, first we need to understand what contributes to an observed spectrum.

4.2 What is a spectrum?

In order to understand the dust spectral features, we need to consider what contributes to the observed spectra. A spectrum, F_λ, can be interpreted as a product of the underlying continuum and an extinction efficiency factor (Q_λ) for the entire spectrum,

$$F_\lambda = C \times Q_\lambda \times B_\lambda(T) \tag{4.1}$$

where $B_\lambda(T)$ is the Planck function for a black body of temperature T, Q_λ is a composite value including contributions from all dust grains of various sizes, shapes, crystallinities and compositions, and C is a scale factor that depends on the number of dust particles, their geometric cross section and the distance to the star. In reality the spectrum should be represented by:

$$F_\lambda = \sum_{i=1,j=1}^{n,m} C_j \times Q_{\lambda,j} \times B_{\lambda,i}(T_i) = \sum_{i=1,j=1}^{n,m} C_j \times Q_j \times B_i \tag{4.2}$$

where each B_i represents a single dust (or stellar) temperature black body (of which there are n in total), each Q_j represents the extinction efficiency for a single grain type as defined by its size, shape, composition and crystal structure, and each C_j represents the scale factor for a single grain type (of which there are m in total).

An example of a spectral dust features of O-rich AGB star RX Lac is shown in Figure 4.1. In order to identify the dust composition of RX Lac, the spectral dust feature parameters (e.g. peak positions, widths and amplitudes) are compared with the laboratory spectra of two crystalline silicate minerals (fayalite: Fe_2SiO_4, forsterite: Mg_2SiO_4).

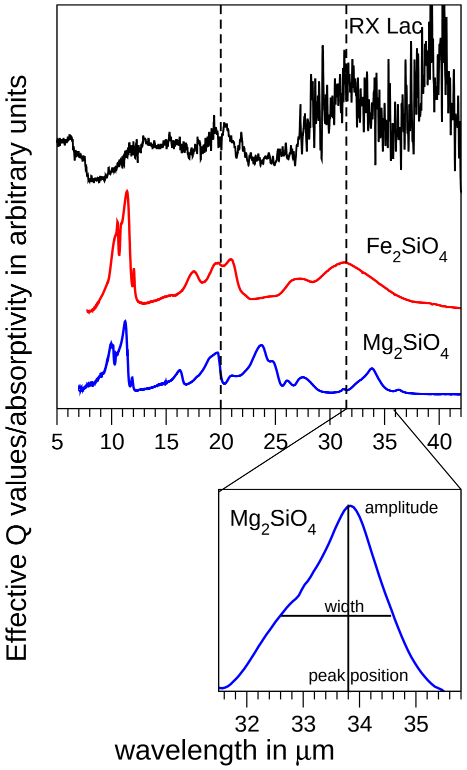

Figure 4.1: Top panel: Comparison of spectral dust features of RX Lac with end member of crystalline olivine minerals. For further reference see Pitman et al. (2010) [114]. Bottom panel: Three spectral parameters (position, width and amplitude) of a well-separated spectral feature of forsterite (Mg_2SiO_4) are shown.

4.3 Previous observations of dust in space

In the late 1960s, while investigating deviations of stellar energy distributions from blackbodies, Gillett et al. (1968) [46] discovered a peak near 10 μm in the spectra of four late-type, evolved, variable stars. Shortly thereafter a 10 μm absorption feature was discovered in the interstellar medium (ISM; Knacke et al. 1969, Hackwell et al. 1970) [75, 53]. Since then, it has been found to be almost ubiquitous, occurring in many astrophysical environments including the solar system and extrasolar planetary systems (e.g., Mann et al. 2006, and references therein) [89], the circumstellar regions of both young stellar objects, AGB stars, and planetary nebulae (e.g. Speck et al. 2000, Casassus et al. 2001, and references therein) [131, 18]; many lines of sight through the interstellar medium in our own galaxy (e.g. Chiar et al. 2007) [21]; in nearby and distant galaxies (e.g. Hao et al. 2005) [54].

Initially this feature was attributed to silicate minerals (Woolf & Ney 1969) [157], based on spectra of mixtures of crystalline silicate species predicted to form by theoretical models (Gaustad 1963, Gilman 1969) [43, 47]. However, laboratory spectra of crystalline silicate minerals showed more structure within the feature than observed in the astronomical spectra (see Woolf 1973, Huffman & Stapp 1973) [156, 66]. Subsequent comparison with natural glasses (obsidian and basaltic glasses from, e.g., Pollack et al. 1973) [116] and with artificially disordered silicates (Day 1979, Kraetschmer & Huffman 1979) [28, 81] showed that "amorphous" silicate was a better candidate for the 10 μm feature than any crystalline silicate mineral.

Following the discovery of the 10 μm silicate feature, the spectra of O-rich AGB stars have been found to show a diverse range of spectral features, which are interpreted in terms of dust condensation hypotheses. In order to understand how IR spectra are classified and the features are interpreted we now need to discuss the currently-favored dust formation hypotheses.

4.4 Dust formation hypotheses

While there are many dust formation hypotheses for AGB circumstellar environments, these can be broken down into three main ideas: (i) thermodynamic equilibrium condensation (Lodders & Fegley 1999) [87]; (ii) formation of chaotic solids in a supersaturated gas followed by annealing (Stencel et al. 1990) [133]; (iii) formation of seed nuclei in a supersaturated gas, followed by mantle growth (Gail & Sedlmayr 1999) [42]. The latter should follow thermodynamic equilibrium as long as density is high enough for gas-grain reactions to occur. Several observational studies support this thermodynamic condensation sequence (Dijkstra et al. 2005, Blommaert et al. 2007)

[32, 7], however, the interpretation of the observational data is, in part, dictated by the condensation sequence. In (ii), chaotic grains form with the bulk composition of the gas, and then anneal if the temperature is high enough (Stencel et al. 1990) [133].

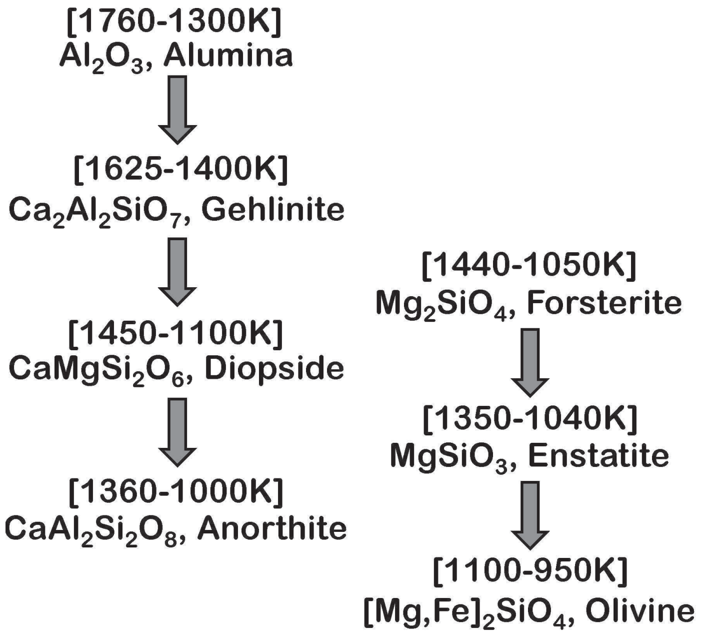

Figure 4.2: Predicted dust condensation sequence for O-rich environments from Tielens (1990) [137]; after Grossman (1972) [48].

The thermodynamic condensation sequence for a gas cooling down from a high temperature is shown in Figure 4.2 (following Tielens 1990, Grossman 1972) [137, 48]. The condensation sequence starts with the formation of refractory oxides (e.g. Al_2O_3) which, upon cooling, react with gaseous SiO, Ca and Mg to form spinel ($MgAl_2O_4$, not shown in the figure), then to melilite (ranging from gehlenite [$Ca_2Al_2SiO_7$] to åkermanite [$Ca_2MgSi_2O_7$]) and then to diopside ($CaMgSi_2O_6$). The conversion of diopside to anorthite ($CaAl_2Si_2O_8$) involves a solid-solid reaction, and is therefore kinetically unlikely.

In this sequence, the more abundant Mg/Fe-rich silicates form as mantles on the more refractory grains. Because of the relative abundance of Mg and Fe when compared to Ca and Al, most of the silicon atoms condense as the Mg-rich end member of the olivine family (forsterite: Mg_2SiO_4). As the gas cools, the gaseous SiO converts forsterite into the Mg-rich end member of the pyroxene family (enstatite: $MgSiO_3$). Consequently, the $MgSiO_3/Mg_2SiO_4$ ratio increases with the decreasing temperature. At the pressure relevant for stellar outflows, gaseous Fe, may react with enstatite to form olivine with some iron ($[Mg, Fe]_2SiO_4$). It is also predicted that Fe condense into metallic iron grains, but it is not predicted that the Fe-rich end members of the olivine (fayalite: Fe_2SiO_4) or pyroxene series (ferrosilite: $FeSiO_3$) will form. Regardless of the precise mineral into which it condenses, iron is expected to be in solid phase because it is strongly depleted from the gas phase (Okada et al. 2009) [108].

For solar metallicity[1], Mg and Fe are approximately equally abundant in O-rich circumstellar environment (Lodders & Fegley 1999) [87]. In these dust condensation sequences, the condensation temperatures are dependent on the gas pressure. However, for the pressures relevant to the typical AGB outflow, the silicate formation temperatures are above the assumed glass transition temperature of 1000 K, implying that crystalline dust should form.

4.5 Dust mineralogy and morphology around O-rich evolved stars

According to the classical dust condensation sequence, Al_2O_3 is expected to form closer to the star since it is a high temperature condensate and with increasing distance from the central star, silicates minerals are expected to form. A schematic presentation of dust shells around O-rich AGB stars is shown in Figure 4.3.

In this section I will provide a list of all the astrominerals that are predicted to be present according to the condensation sequence, along with their chemical formulae, lattice structures, spectral features, formation conditions and astronomical

---

[1] In astronomy, all elements with atomic number greater than 2 are called metals. The metallicity is a measure of the amount of these elements present in a star.

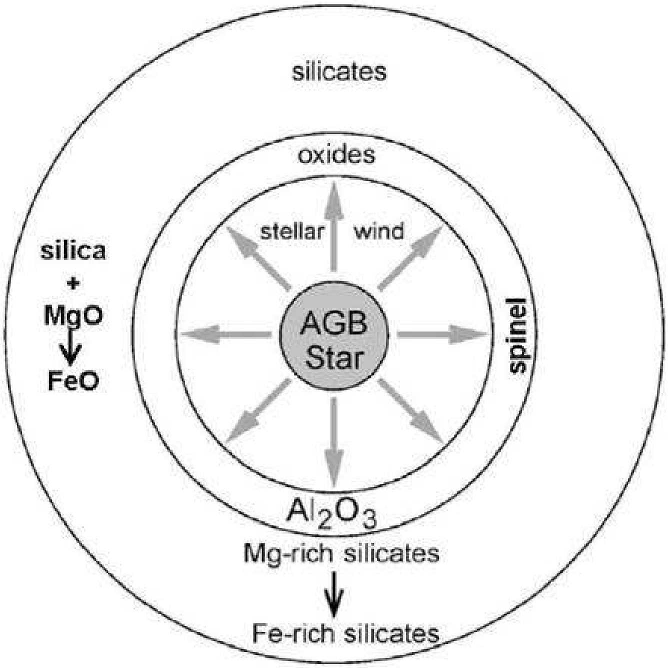

Figure 4.3: A schematic presentation of dust shells around O-rich AGB stars based on the classical dust condensation sequence (e.g. Tielens (1990) [137]).

evidences. It is also important to understand that the spectral feature parameters (position, width and amplitude; also shown in Figure 4.1: bottom panel) are significantly influenced by three parameters (composition, temperature and grain shape of the dust grains). By following the method discussed in § 3.4.1 and 3.4.2, I have computed the absorption cross section (C_{abs}) for four different grain shape distribution: Spherical (SPH), Continuous distribution of ellipsoid (CDE), Continuous distribution of spheroid (CDS) and Distribution of hollow spheres (DHS)[2] from their optical constants[3] for various minerals. The effect of grain shapes on the IR spectral features of some of the minerals are shown below.

---

[2] Hollow spheres are meant to simulate fluffy grains

[3] optical constants are available at http://www.astro.uni-jena-de/Laboratory/Database/databases.html

4.5.1 Silicates

Since silicates are most abundant mineral in O-rich environment, I'll first discuss them.

Olivines and pyroxenes

Chemical formula: Different types of silicate species can exist depending on the number of shared oxygen atoms and the precise cations. For example, olivine minerals, which have isolated tetrahedra, and have the general formula: $Mg_{2x}Fe_{(2-2x)}SiO_4$. Endmembers of mineral series are those with x close to 0 or 1. For example, Forsterite (Mg_2SiO_4) is the Mg-rich endmember and Fayalite (Fe_2SiO_4) is the Fe-rich endmember of olivine minerals. Another example of silicate mineral is Pyroxene. This mineral consists of chains of tetrahedra and is usually written as $Mg_xFe_{(1-x)}SiO_3$ but can also contain Ca^{2+} (in case of diopside). The endmembers of pyroxene family members are known as Enstatite ($MgSiO_3$) and Ferrosilite ($FeSiO_3$) respectively.

Lattice structure: Silicates consist of silica tetrahedra (SiO_4^{4-}) which can either be isolated or share oxygen atoms with other tetrahedra (see Figure 4.4[4]). Unless all oxygen atoms are shared there are also metal cations (e.g. Mg^{2+}, Fe^{2+}, Ca^{2+}). These tetrahedra can either be arranged in an orderly manner, giving rise to crystalline lattice structures, or they can be randomly oriented with respect to one another, in which case the solid is amorphous. Whether dust grains will be amorphous or crystalline depends on their formation conditions and subsequent processing.

Spectral features: Spectroscopically, all silicates, amorphous and crystalline alike, show spectral features at ~10 and ~20 μm in the mid-IR, due to the Si–O stretching and the O–Si–O bending modes. Alignment of the tetrahedra may cause sharp peaked resonances, whereas amorphous silicates will show broad features which can be seen as a blend of such sharp resonances. Furthermore, crystalline silicates exhibit far-IR lattice modes at $\lambda > 25\,\mu$m which are not evident for amorphous silicates (see

---

[4] from http://www4.nau.edu/meteorite/Meteorite/Book-GlossaryS.html

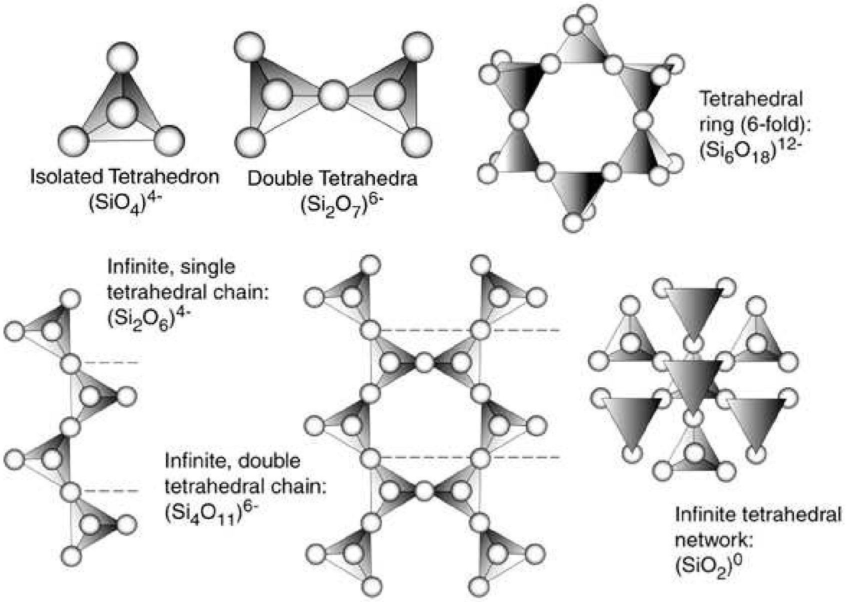

Figure 4.4: Structure of silicate minerals.

Figure 4.5).

Silicate grains show many spectral features whose peak positions, widths and amplitudes are dependent on the Si/O ratio and Fe/[Mg+Fe] ratio of the silicate as well as the temperature and the shapes of dust grains (for further discussion see Chapter 7).

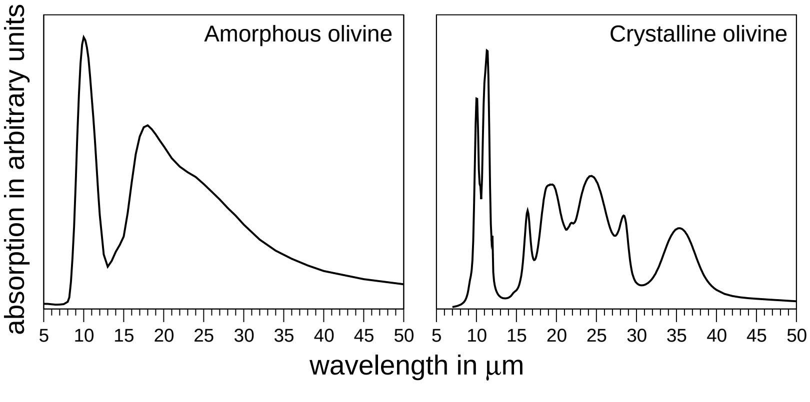

Figure 4.5: The laboratory IR spectra of amorphous (left) and crystalline (right) silicates. x-axis is wavelength (in μm), y-axis is absorption in arbitrary units.

Formation condition: Amorphous silicates can form below the glass transition temperature. Molecules that stick to the surface of the grain, immediately freeze out without having sufficient energy to find energetically favorable lattice positions. Thus an amorphous structure can be formed.

Crystalline silicates can be possibly formed by two mechanisms. If the gas temperature is higher than the glass temperature then the crystalline structure can form by direct condensation. The second mechanism to form crystalline silicates is by annealing the amorphous silicates. In this mechanism, all silicates are formed at temperature below the glass temperature. But if the grains are heated by some mechanisms, that may allow the atoms to re-arrange in a crystal structure.

Astronomical evidence: Amorphous silicates were found to be almost ubiquitous being found in observations of evolved stars (e.g. Speck et al. 2000, Casassus et al. 2001) [131, 18]; many lines of sight through the interstellar medium in our own galaxy (e.g. Chiar et al. 2007) [21]; and in nearby and distant galaxies (e.g. Hao et al. 2005) [54].

However, after discovery by *ISO*, evidence for crystalline silicates has been found in the circumstellar environment of evolved stars and young stars as well (e.g. Waters et al. 1996, Waelkens et al. 1996, Molster et al. 2002-a, Pitman et al. 2010, Guha Niyogi et al. 2011) [149, 148, 99, 114, 49].

Diopside

Chemical formula: $CaMgSi_2O_6$.

Lattice Structure: Monoclinic pyroxene; see Figure 4.6: Left Panel[5].

Spectral features: Crystalline diopside shows several strong narrow features around 10 and 20 μm region, due to the Si-O stretching and Si-O-Si bending modes. Strong spectral features are found at 9.3, 10.3, 11.4, 19.5, 20.6, 25.1, 29.6, 33.9 μm (see Figure 4.6: Right Panel; data taken from Koike et al. (2000) [79].

---

[5] from http://www.chem.ox.ac.uk/icl/heyes/structure_of_solids/Lecture4/Lec4.html

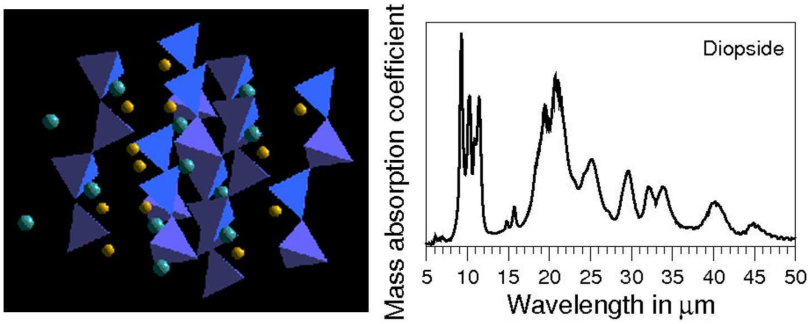

Figure 4.6: Left: The lattice structure of diopside. Its a chain of tetrahedra, containing Mg^{2+}, and Ca^{2+}. Right: The IR laboratory spectrum of diopside.

Formation condition: As melilite cools down, diopside can form (Grossman 1972) [48].

Astronomical evidence: The spectral features of RX Lac has been attributed to crystalline diopside by Hony et al. (2009) [64], whereas, by crystalline fayalite by Pitman et al. (2010) [114]. Diopside had identified in some post-AGB stars and planetary nebulae (e.g. NGC 6302; Koike et al. 2000, Molster et al. 2002-a, Kemper et al. 2002-b) [79, 99, 73].

Melilite Series

Chemical formula: Ranging from Gehlenite [$Ca_2Al_2SiO_7$] to Åkermanite [$Ca_2MgSi_2O_7$].

Lattice Structure: Sorosilicates, isolated, double tetrahedral groups; see Figure 4.7: Left panel.

Spectral features: The laboratory IR spectral features of two crystalline Melilite family members (Gehlenite and Åkermanite) are shown in Figure 4.7: right panel; data taken from WashU lab[6]. Here we see a variation in the spectral parameters with variation in chemical composition (also see Chihara et al. 2007) [22]. Gehlenite shows a strong 10–12 μm broad feature with structure, along with week features at 14, 17, 19 μm. Åkermanite shows a broad 9–12 μm feature with prominent structure along with 16, 17.5 and 21 μm.

---

[6] http://galena.wustl.edu/ dustspec/idals.html

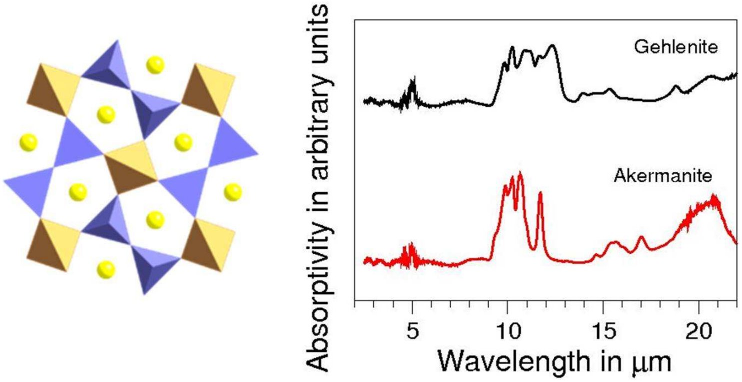

Figure 4.7: Left: The lattice structure of melilite. It has a general formula $A_2B(T_2O_7)$, where A-position is a large 8-coordinated yellow sites and can be occupied by by Ca or Na; and B (pale orange) and T-positions are blue tetrahedral. B-position can by taken by Al, Mg; and T-position by Si or Si and Al. Oxygen atoms (not shown) are on the corners of the tetrahedra. The resulting Si:O ratio is 2:7. Right: The IR spectra of crystalline Gehlenite and Åkermanite are shown.

Formation condition: As spinel cools down, melilite can form (Grossman 1972) [48].

Astronomical evidence: A broad far-IR feature was detected $\approx 63\,\mu$m in some O-rich evolved stars; such as AFGL4106, NGC 6302 and HD 161796 (e.g. Molster et al. 1999, Molster et al. 2001, Molster et al. 2002-b) [101, 97, 98]. Originally, this far-IR feature has been attributed to various crystalline minerals: water ice (Molster et al. 1999) [101], diopside: $CaMgSi_2O_6$ (Koike et al. 2000, Chihara et al. 2002) [79, 23]. and dolomite: $(Ca,Mg)CO_3$ (Kemper et al. 2002-a) [72]. After the optical properties of melilite were measured, it is also included as a potential carrier of this feature (Chihara et al. 2007) [22].

Silica

Chemical formula SiO_2

Lattice Structure: Various lattice structure depending on the pressure and temperature. It consists of SiO_4 tetrahedra which share all their oxygen atoms with other tetrahedra. There are three main polytypes for crystalline SiO_2: quartz, tridymite and cristobalite; see Figure 4.8[7].

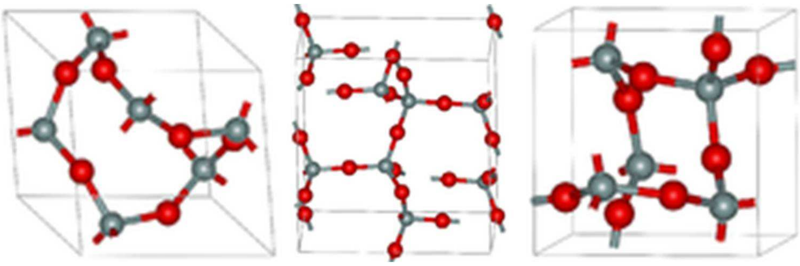

Figure 4.8: The lattice structure of silica. Three main polytypes of silica (e.g. quartz, tridymite and cristobalite) are shown.

Spectral features: The IR spectral features of silica for four different grain shape distribution[8]: Spherical (SPH), Continuous distribution of ellipsoid (CDE), Continuous distribution of spheroid (CDS), Distribution of hollow spheres (DHS) are shown in Figure 4.9. Here we see an example of how the spectral features change with the variation of dust grain shapes. Silica shows spectral features at 9.7, 13 and 21.5 μm.

Formation condition: It has been predicted that quartz can condense directly in the O-rich outflow (Gail & Sedlmayr 1999) [42]. Experimental evidence showed that the annealing of silicates lead to the production of silica, in the form of tridymite or cristobalite (Fabian et al. 2000) [38].

Astronomical evidence: Silica is identified to be the carrier of the 13 μm feature (Speck et al. 2000, DePew et al. 2006) [131, 31]. Trace of silica has also been found in Herbig Ae/Be system (Bouwman et al. 2001) [11].

4.5.2 Oxides

In this section I'll discuss the various predicted refractory oxides in O-rich dusty envelope.

---

[7] taken from http://en.wikipedia.org/wiki/Silicon_dioxide

[8] the absorption cross sections are calculated from optical constants using the statistical approach as discussed in § 3.4.1 and 3.4.2; optical constants are available at http://www.astro.uni-jena-de/Laboratory/Database/databases.html.

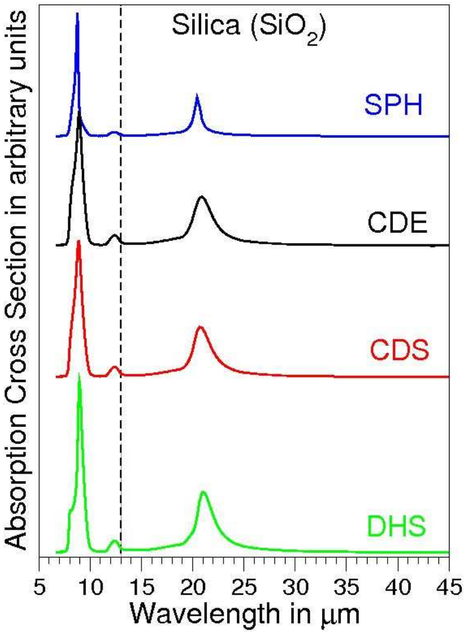

Figure 4.9: The IR spectral features of silica for four different grain shape distribution: Spherical (SPH), Continuous distribution of ellipsoid (CDE), Continuous distribution of spheroid (CDS), Distribution of hollow spheres (DHS).

Corundum

Chemical formula: Al_2O_3.

Lattice Structure: Hexagonal; see Figure 4.10: Left panel[9].

Spectral features: The IR spectral features of corundum for four different grain shape distribution[10]: Spherical (SPH), Continuous distribution of ellipsoid (CDE), Continuous distribution of spheroid (CDS), Distribution of hollow spheres (DHS) are shown in Figure 4.10: Right panel. The spherical grain shows a strong feature at 13 μm, due to the Al-O vibrational band (e.g. Sloan et al. 2003, DePew et al. 2006) [123, 31]. For other shape distribution (CDE, CDS, DHS), we see a broader feature centered at 15 μm, accompanied by another IR feature at 21 μm (Begemann et al. 1997) [3].

Formation condition: It is predicted to be the first major condensate closest to

---

[9] from http://wapedia.mobi/en/Sapphire

[10] optical constants are taken from http://www.astro.uni-jena-de/Laboratory/Database/databases.html

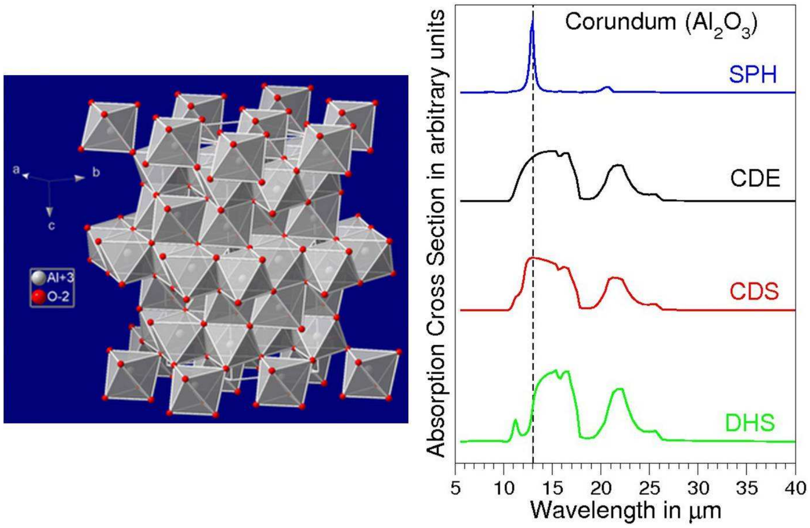

Figure 4.10: Left: The lattice structure of corundum. The positions of Al^{+3} and O^{-2} are shown by grey and red circles; Right: The IR spectral features of corundum for four different grain shape distribution: Spherical (SPH), Continuous distribution of ellipsoid (CDE), Continuous distribution of spheroid (CDS), Distribution of hollow spheres (DHS).

the central star and serves as a condensation core for the subsequent formation of silicates (Salpeter 1974) [119].

Astronomical evidence: Approximately 50% of O-rich AGB stars exhibit a "13 μm" feature (for detail discussion see § 4.6) and also this feature is associated with semiregular variable stars (SRs; Sloan et al. 1996, Speck et al 2000) [124, 131]. Spherical corundum is one of the proposed mineral as carrier of this feature (e.g. Sloan et al. 2003) [123]; whereas, DePew et al. (2006) [31] proposed silica as a carrier of the 13 μm feature. There are also evidence of refractory oxides (corundum, spinel) presolar grains[11] from meteorites (Nittler et al. 1994, Huss et al. 1995) [106, 67], which indicate that the most likely stellar source of these grains are AGB stars.

Spinel

Chemical formula: $MgAl_2O_4$.

---

[11] presolar grains are tiny dust particles that are literally bits of stars we can study in the laboratory. They condensed from the gas phase in the cooling outflows of stars billions of years ago

Lattice Structure: Cubic (isometric), octahedral; see Figure 4.11: Left panel[12].

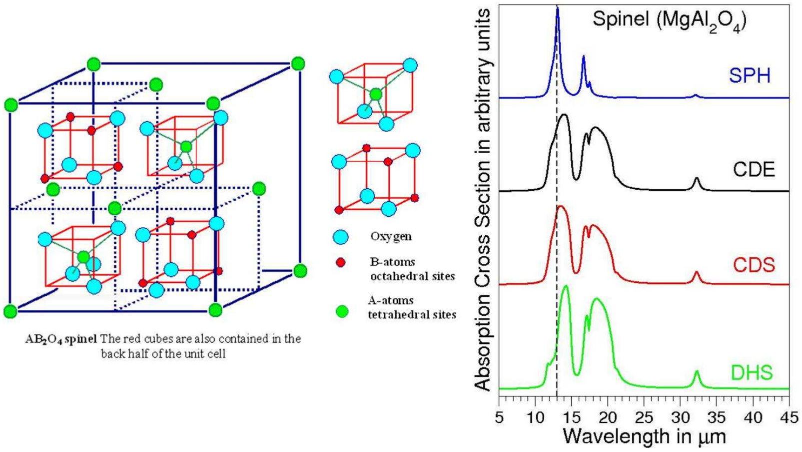

Figure 4.11: Left: The lattice structure of spinel. It has a general formula AB_2O_4, where A-positions can be occupied by by Mg^{+2}, Fe^{+2}, Zn^{+2}, Mn^{+2}; and the B-positions by Al^{+3}, Fe^{+3}, Cr^{+3}; Right: The IR spectral features of corundum for four different grain shape distribution: Spherical (SPH), Continuous distribution of ellipsoid (CDE), Continuous distribution of spheroid (CDS), Distribution of hollow spheres (DHS).

Spectral features: Spinel shows strong mid-IR spectral features at 13 and 17 μm (DePew et al. 2006) [31], both due to Al-O vibrational modes and a weaker feature at 32 μm (Fabian et al. 2001; also see Figure 4.11: Right panel) [37]. These features shift in peak position, width and amplitude as the grain shape changes.

Formation condition: When corundum cools down, it reacts with gaseous SiO, Al and Mg to form spinel (Grossman 1972) [48].

Astronomical evidence: Spinel is also one of the proposed carrier of the 13 μm feature (e.g. Posch et al. 1999, Cami 2002) [118, 13]. However, spinel has been ruled out as the carrier of the 13 μm feature because it also shows a strong feature at 17 μm (as also shown in Figure 4.11: Right panel), and this feature does not occur in the spectra of AGB stars that exhibit the 13 μm (e.g. Sloan et al. 2003, Heras & Hony 2005, DePew et al. 2006) [123, 57, 31].

Magnesium Iron Oxides

---

[12] from http://www.tf.uni-kiel.de/matwis/amat/def_en/kap_2/basics/b2_1_6.html

Chemical formula Periclase (MgO), Wustite (FeO).

Lattice Structure: Cubic; see Figure 4.12[13].

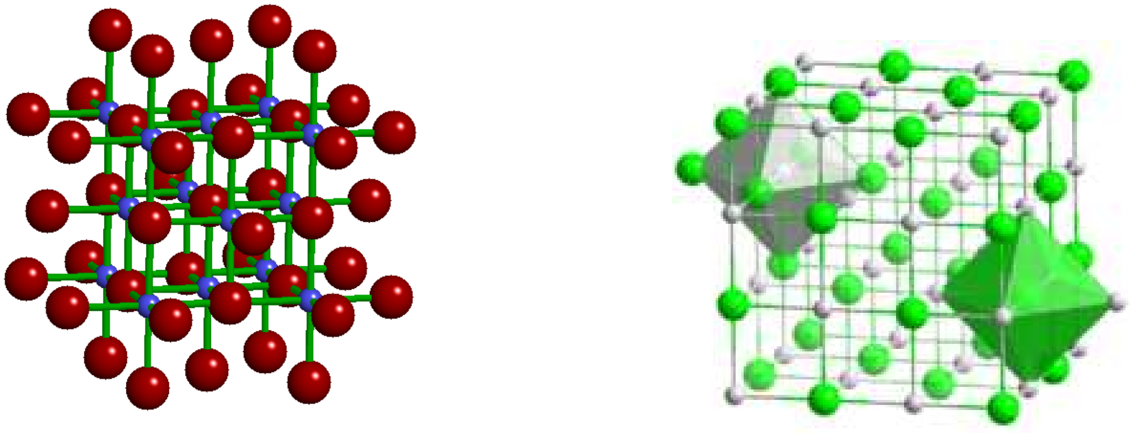

Figure 4.12: The lattice structure of Periclase and Wustite. The red/green circles represent the oxygen atoms, whereas the blue/white one are magnesium/iron atoms.

Spectral features: Periclase has a broad feature at 15 μm (e.g. Henning et al. 1995, Begemann et al. 1995) [56, 4] and Wustite shows a strong feature at 20 μm (Henning et al. 1995) [56].

Formation condition: Gail & Sedlmayr (1999) [42] have considered periclase as one of the possible condensates in O-rich outflows and wustite can form when periclase react with SiO.

Astronomical evidence: MgO has not been identified in evolved stars. But $\mathrm{Mg_{0.1}Fe_{0.9}O}$ is independently identified for the 19.5 μm feature by Posch et al. (2002) [117] and Cami (2003) [14] in several evolved stars with low mass-loss rate. A recent study on globular cluster evolved stars also suggested that FeO is a good candidate for this ∼20 μm (McDonald et al. 2010-a) [93].

---

[13] from http://ruby.colorado.edu/ smyth/min/periclase.html and http://www.thefullwiki.org/Wustite

4.5.3 Metallic iron

Chemical formula Fe.

Lattice Structure: Isometric; see Figure 4.13[14].

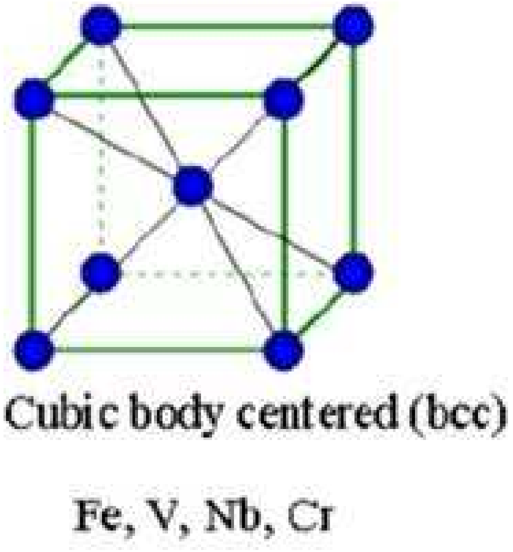

Figure 4.13: The lattice structure of Metallic iron.

Spectral features: Metallic iron produces a smooth continuum. Since its a conducting mineral, it has a high absorptivity in visible and near-IR.

Formation condition: It is predicted that Fe can condense into metallic iron grains in dust condensation sequence (Grossman 1972) [48].

Astronomical evidence: The evidence of metallic iron has been found in OH/IR star OH 127.8+0.0 (Kemper et al. 2002-c) [71] and red supergiant VY CMa (Harwit et al. 2001) [55]. A recent *Spitzer Space Telescope* study on globular cluster evolved stars also suggested that metallic iron grains are present around O-rich AGB stars, where it is observationally manifested as a featureless mid-IR excess (McDonald et al. 2010-b) [94].

Stellar winds are commonly assumed to be dust-driven in circumstellar environ-

---

[14] from http://www.substech.com/dokuwiki/doku.php?id=metals_crystal_structure

ments of evolved stars (Ferrarotti & Gail 2006) [41]. Opacity of dusty materials is an important parameter for the wind-driving mechanism. If iron is absent from dust, a stellar wind cannot be driven because of the transparency of Mg-rich silicates. Iron has often been included in dust grains in order to increase the near-IR absorption efficiency (Tielens et al. 1998) [138]. However, the precise effect of the iron depends on how it is incorporated, i.e. as an integral part of the silicate (e.g. in amorphous $[Mg,Fe]_2SiO_4$ silicate) or as metallic inclusions. For Mg-rich silicates with metallic iron inclusions, their absorption efficiency is so high that radiative heating leads to grain evaporation and only a limited amount of dust can survive (Woitke 2006) [154].

4.6 Spectral classification of O-rich AGB stars based on dust spectral features

Now it is appropriate to discuss the classification of O-rich AGB stars based on their spectral dust features. Various attempts have been made to classify the observed dust features of O-rich evolved stars (Little-Marenin et al. 1990, Sloan & Price 1995, Speck et al. 2000) [86, 127, 131]. All these authors have classified the observed spectra into groups according to the shape of the dust feature, which reflects a progression from a broad feature to the classic narrow 10 μm silicate feature. This progression of the spectral features is expected to represent the evolution of the dust from the early forming refractory amorphous oxides (the broad feature) to the dominance of magnesium-rich amorphous silicates (the narrow 10 μm feature).

The study of dust properties around O-rich AGB stars had been greatly advanced after using *IRAS* LRS IR spectra. Onaka et al. (1989) [109] fitted successfully the *IRAS* LRS spectra of 109 Mira variables, by assuming the dust shell is spherical and optically thin, the dust grain consist of aluminium oxide and amorphous magnesium silicate, and dust temperatures of 200–500 K. They concluded that these low temperatures could not be understood in the framework of homogeneous nucleation theories, and proposed that mantle growth on pre-existing aluminium grains was the major process of silicate formation. Sloan & Price (1995) [127], investigated the *IRAS*/LRS spectra of 635 oxygen-rich variables and showed a smoothly varying sequence of spectral shapes, from the broad features to the typical silicate feature. They called this the silicate dust sequence. Their classification was achieved by comparing the flux ratios at 10, 11 and 12 μm. They divided the sequence into eight segments, labeled SE1-SE8 (SE = silicate emission). Classes SE1-SE3 are expected to correspond to low-contrast alumina-rich amorphous dust seen in evolved stars losing mass at low rates and have optically thinner shells. Moving up the sequence, classes SE3-SE6 show structured silicate emission, with features at 10 and 11 μm. The upper end of the silicate dust sequence (SE6-SE8) consists of sources with the classic silicate emission feature believed to be produced by amorphous silicate grains (see Figure 4.14).

Egan & Sloan (2001) [35] made radiative transfer models of the LRS spectra of oxygen rich circumstellar shells, and concluded that optically thin shells dominated by amorphous silicate grains, which reproduce the classic narrow silicate feature at 10 μm. Spectra with broad, low-contrast emission features peaking at wavelengths longer than 11 μm, originated from optically thin shells composed of amorphous alumina. Speck et al. (2000) [131] analyzed UKIRT CGS3 spectra of 80 oxygen-rich AGB stars and concurred with Sloan & Price (1995, 1998) [127, 128] that here is a smoothly varying sequence of spectral shapes. However, they found that the broad 9–12 μm could not be explained using only amorphous alumina grains, but rather that some amorphous silicate was always needed to explain the blue side of the feature.

In 1995 the Infrared Space Observatory (*ISO*) was launched which opened the possibility of studying mass-losing stars at IR wavelengths with unprecedented wavelength coverage and spectral resolution. It observed over 900 objects with the Short Wavelength Spectrometer (SWS; de Graauw et al. 1996) [29] in full grating scan

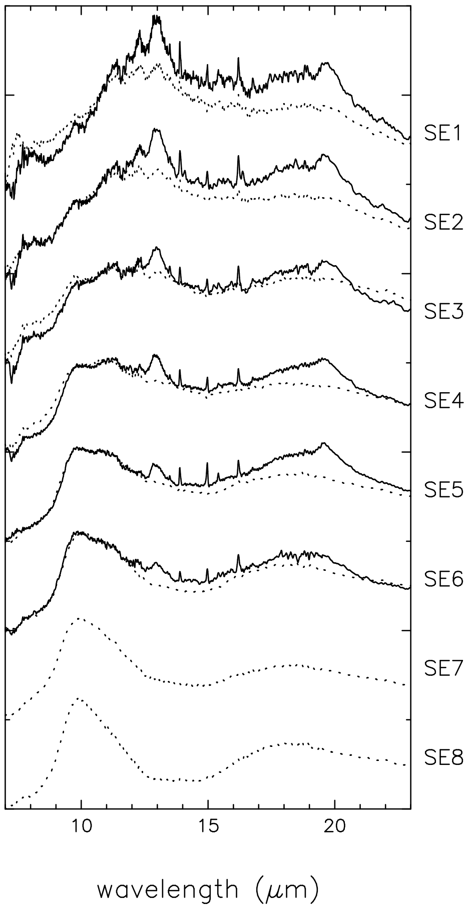

Figure 4.14: Comparison of dust spectra based on silicate emission (Sloan et al. 2003) [123].

mode (2.38–45.2 μm). The SWS was better suited for the study of dust than previous instruments because of its higher spectral resolution and its broader wavelength coverage.

Kraemer et al. (2002) [80] classified the *ISO* SWS spectra in seven groups. This classification was well correlated with Sloan & Price (1995) and Sloan & Price (1998) [127, 128] silicate dust sequence. Cami (2002) [13] studied the *ISO* SWS spectra of twenty-four AGB stars with low mass-loss rates, modeled the observed molecular bands and made a qualitative analysis of the composition of the dust in the shells. He suggested that low mass-loss rate stars do not produce silicates, but instead produce large amounts of Al_2O_3, spinel ($MgAl_2O_4$) and MgFeO, a result that obviously conflicts with Speck et al. (2000) [131]. As we will see below, spinel has since been discredited as a major contributor to dust spectral features around AGB stars. Based on these results, Cami (2002) [13] suggested a correlation of the different spectral appearance of the SWS spectra with the silicate dust condensation sequence. In another study of the SWS spectra of low mass-loss AGB stars that showed the broad emission plateau between 11–15 μm, Posch et al. (2002) [117] suggested that the dominant components of the dust are oxides instead of silicates. These authors suggested that aluminium, magnesium and iron oxides represent the first spectroscopically detectable dust species to condense in O-rich circumstellar envelopes. However, these oxides alone cannot explain the blue side of the broad spectral feature (Speck et al. 2000) [131].

Sloan et al. (2003) [123] revisited and revised the IRAS classification of Sloan & Price (1995) [127] using ISO SWS spectra. In addition to the SE# classification, based on the features in the 9–12 μm range, another mid-IR feature at $\sim$13 μm is sometimes present. Approximately 50% of O-rich AGB stars exhibit this feature and it is the cause of some controversy. The so-called "13 μm feature" was discovered in the IRAS LRS spectra (Vardya et al. 1986) [144] and does not lend itself to the standard IR feature classification system. It is found in all SE classes (Sloan et al. 2003, Speck et al. 2000) [123, 131]. Furthermore, the 13 μm feature is associated with semiregular variables (SRs) rather than Miras or red supergiants (Sloan et al. 1996, Speck et al. 2000) [124, 131]. Many minerals have been proposed as the likely carrier of this feature (as discussed in § 4.5), including corundum (crystalline form of Al_2O_3), spinel ($MgAl_2O_4$) and silica (SiO_2; Speck et al. 2000, Sloan et al. 2003, DePew et al. 2006) [131, 123, 31]. The strongest sources of 13 μm features occur in the SE3-SE6 classes. Furthermore, DePew et al. (2006) [31] showed that only spherical grains of spinel or corundum give rise to a narrow 13 μm feature; other grainshape distributions exhibit broader features at longer wavelengths.

One of the most exciting recent findings in cosmic dust studies was the discovery of crystalline silicate dust by the *ISO* SWS. These crystalline silicates were first observed around evolved stars with very high mass-loss rates, leading to the inference that crystal formation requires such conditions (e.g. Cami et al. 1998) [15]. However, recent studies on occurrence of crystalline silicates and their distribution with evolution suggest that crystalline silicates preferentially occur around less-evolved, low mass-loss rate evolved stars (e.g. Sloan et al. 2010, McDonald et al. 2011) [125, 92].

The classical amorphous silicates have broad, smooth spectral features at $\sim$10 and 18 μm, with no diagnostic features at longer wavelengths; that is not true for crystalline silicates. A crystalline mineralogy would manifest itself more clearly at long IR wavelengths. Molster et al. 2002-a, Molster et al. 2002-b, Molster et al. 2002-c [99, 98, 100] in their series of three papers studied dust mineralogy of several oxygen-rich (post-)AGB stars using *ISO* SWS data. By comparing the observational spectra with laboratory data, these authors concluded presence of Mg-rich crystalline silicates (both olivines and pyroxenes).

Various authors (e.g. Begemann et al. 1996, and references therein) [2] pointed to some connection between iron-rich (and possibly Mg-rich) oxide and an excess emission in the 19–20 μm range. Shortly thereafter, the 19.5 μm feature was attributed to $Mg_{0.1}Fe_{0.9}O$ independently by Posch et al. (2002) [117] and Cami (2003) [14]. Following this study, Lebzelter et al. (2006) [85] also attributed the same mineral for 20 μm feature, while studying the mid-IR dust features of AGB stars in the globular clusters 47 Tuc. However, the occurrence of circumstellar $Mg_{0.1}Fe_{0.9}O$ is not expected from thermodynamic models (e.g. Lodders & Fegley 1999) [87] and the low stability temperature of Mg-Fe oxides suggests that these minerals should not form directly from the gas phase. Consequently a large abundance of $Mg_{0.1}Fe_{0.9}O$ is unlikely. Confirmation of this attribution is further hampered by the fact that Mg-Fe oxides exhibit only one resonance vibrational band in the IR region, which precludes verification of this composition by matching further features.

A recent *Spitzer Space Telescope* Infrared Spectrograph (IRS; Houck et al. 2004) [65] study on globular cluster evolved stars also suggested that FeO is a good candidate for this $\sim 20\,\mu$m feature (McDonald et al. 2010-a) [93]. In addition their modeling suggests that metallic iron grains are present around O-rich AGB stars, where it is observationally manifested as a featureless mid-IR excess. Another interesting far-IR feature at $\sim 32\,\mu$m was studied by Molster (2000) [96], and tentatively attributed to crystalline diopside ($CaMgSi_2O_6$, a pyroxene).

Furthermore, recent re-analysis of *ISO* SWS spectra have also suggested iron-rich crystalline silicates provides better fits to observed spectra than that previous mentioned attributions. For example, two recent independent studies of the spectra of the AGB star RX Lac attribute the same spectral feature to two different minerals: diopside (Hony et al. 2009) [64] and fayalite (Pitman et al. 2010) [114]. The diopside does not give as good a match as fayalite. Pitman et al. (2010) [114] studied the dust features of 4 oxygen-rich AGB stars from SE1 class (RX Lac, T Cep, T Cet, R Hya) and Guha Niyogi et al. (2011) [49] studied T Cep, using *ISO* SWS data. They claimed not to see any evidence of Mg-rich silicate (Mg_2SiO_4), rather these authors found that the peak positions and width of the spectral features of these 4 stars match better with non-endmember iron-rich silicate ($Mg_{0.18}Fe_{1.82}SiO_4$). The authors concluded that this result is unexpected, but not entirely out of the question, since it has been long assumed that silicates in space include iron in order to account for their opacities. Moreover, Tielens et al. (1998) [138] found iron-bearing dust to be more refractory than typical silicates, and therefore more likely to survive, which may explain the Pitman et al. (2010) [114] result. In addition to these spectroscopic studies, recent work on presolar silicate grains from meteorites also suggests that there is more iron in AGB star silicate grains that our current models allow (e.g. Stroud et al. 2008, Bose et al. 2010) [134, 10].

Chapter 5

Investigating the dust properties of O-rich AGB star: T Cep

5.1 Introduction

We have learned in § 2.3.2 that pulsation is believed to be the leading cause of dusty mass loss from AGB stars. Now, in this chapter I present a temporal study of T Cep, a long-period Mira variable[1], using seven *ISO* SWS spectra, covering a 16-month period over a single pulsation cycle. The observed spectral dust features change over the pulsation cycle of this Mira. In general, the overall apparent changes in spectral features can be attributed to changes in the dust temperature, resulting from the intrinsic pulsation cycle of the central star. However, not all feature changes are so easily explained. Based on direct comparison with laboratory spectra of several potential minerals, the dust is best explained by crystalline iron-rich silicates. These findings contradict the currently favored classic dust condensation hypotheses.

---

[1] Mira variables are defined in § 2.3.4

5.2 Observations of T Cep

The O-rich AGB star T Cep was discovered by Ceraski in 1878, has been classified as spectral type M7IIIe (SIMBAD Astronomical Database)[2] or M5.5e - M8.8e (Onaka et al. 1999) [111] and infrared spectral class of SE1 (i.e. low-contrast broad dust feature/low mass-loss rate) with a 13 μm feature (Sloan et al. 2003) [123]. Its estimated distance is 210 pc from the HIPPARCOS catalogue (Perryman et al. 1997) [113].

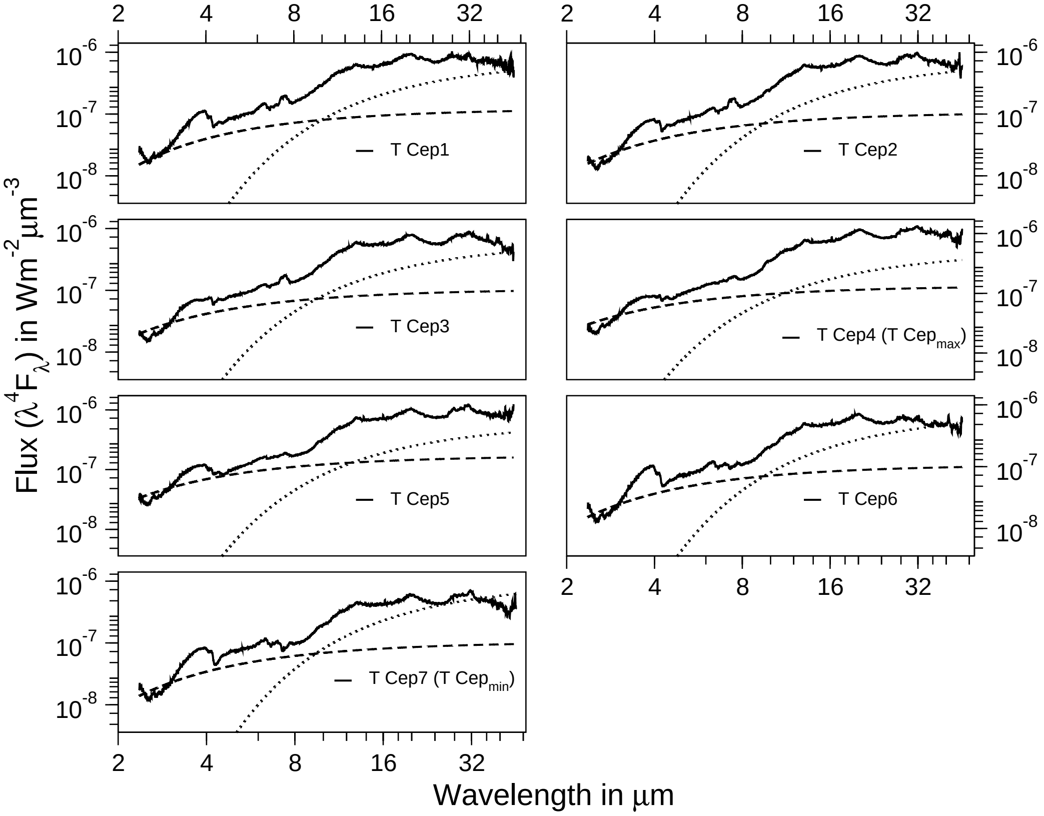

Figure 5.1: *ISO* SWS spectra of T Cep together with both stellar and dust continua. x-axis is wavelength (in μm) y-axis is flux ($\lambda^4 F_\lambda$) (in $Wm^{-2}\mu m^{-3}$) in log-scale. *solid lines* are the observed spectra; *dashed lines* are fitted stellar blackbody continua; *dotted lines* are dust blackbody continua (see text for details). The estimated temperatures of the stellar blackbodies (T_{eff}) and the fitted temperatures for the dust blackbodies (T_{dust}) are listed in Table 5.1.

---

[2] http://simbad.u-strasbg.fr/simbad/

Table 5.1: Information regarding observational data and blackbody curves.

Observation Number	TDT Number	Observation Date	Visual magnitude	T_{eff} (K)	T_{dust} (K)
T Cep1	26300141	08/05/1996	9.7	2703	575
T Cep2	34601646	10/27/1996	9.8	2683	550
T Cep3	42602251	01/15/1997	8.0	3035	600
T Cep4	51401256	04/13/1997	6.4	3347	650
T Cep5	57501031	06/16/1997	7.7	3093	600
T Cep6	66101436	09/07/1997	10.0	2644	550
T Cep7	74602101	12/01/1997	10.4	2566	500

T Cep was observed using *ISO* SWS seven times in a 16-month period (from August 1996 to December 1997) covering one full stellar variability period. The fully processed post-pipeline spectral data were acquired from an online atlas associated with Sloan et al. (2003) [123]. Detailed data reduction information is available from the atlas webpages[3]. Dates of the observations and TDT numbers are listed in Table 5.1, and all seven flux-calibrated spectra are shown in Figure 5.1 (seven observations are designated by sequential numbers).

In addition to the IR spectral data, we have also acquired light curve data for T Cep from American Association of Variable Star Observers (AAVSO) database[4], which is shown in Figure 5.2. The positions in the lightcurve at which *ISO* SWS data was taken, are indicated by dashed straight lines. The apparent visual magnitudes at each *ISO* SWS observation are listed in Table 5.1. According to these light curve data from AAVSO, the estimated pulsation period of T Cep is 388 days, but the period shows evidence of variation. Castelaz et al. (2000) [19] reported the pulsation period is of 398 days, whereas, Weigelt et al. (2003) [150] showed the period is of 382 days. These variation of mean pulsation period of T Cep is confirmed to be real by Isles & Saw (1989) [68] and these authors also reported that T Cep varies slowly in amplitude over the time. Also, an unusual secondary variation in T Cep

---

[3] http://isc.astro.cornell.edu/ sloan/library/swsatlas/atlas.html

[4] http://www.aavso.org/

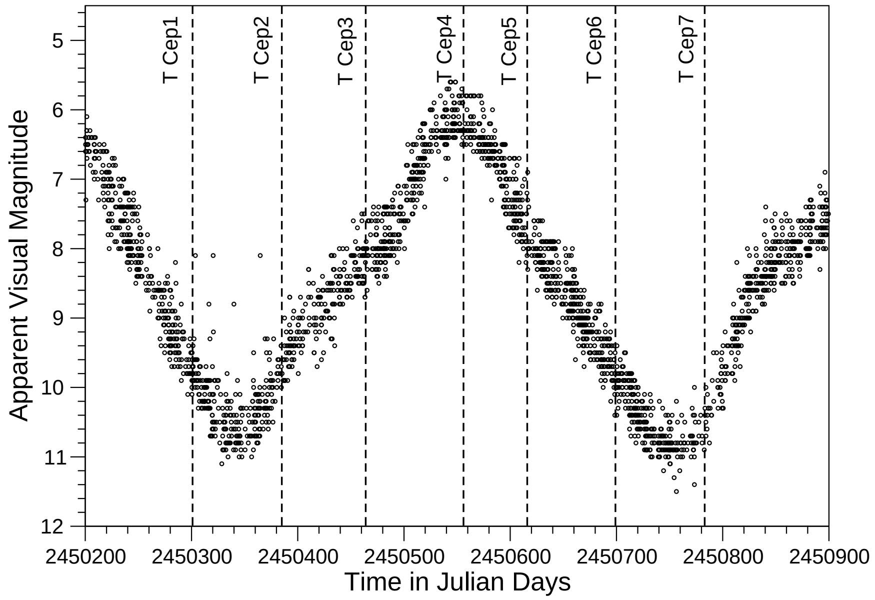

Figure 5.2: Light curve of T Cep over a 16 month period. x-axis is the date in Julian Days; y-axis is apparent visual magnitude. The seven *ISO* SWS observations are indicated by dashed straight lines.

had been reported by Marsakova & Andronov (2000) [90], using the observation from AFOEV[5] and VSOLJ[6] databases (Schweitzer 1990, Nogami 1998) [120, 107], obtained over 75-years. These authors also reported significant variation of amplitude and asymmetry over the pulsation cycle, and they indicated the possibility of interference of pulsations with two periods to explain this unusual variation. Similar findings for other several long period Mira variables are also reported by several authors (e.g. Wood & Zarro 1981, Zijlstra & Bedding 2002, Benitez & Vargas 2002, Zijlstra et al. 2004) [155, 160, 5, 161].

5.3 Analysing the dust spectral features of T Cep

In order to investigate the potential effects of the pulsation cycle on dust formation, we need to consider what contributes to the observed spectra. As discussed in § 4.2,

---

[5] ftp://cdsarc.u-strasbg.fr/pub/afoev

[6] http://www.kusastro.kyoto-u.ac.jp

the spectrum F_λ can be interpreted as a product of the underlying continuum and an extinction efficiency factor (Q_λ) for the entire spectrum.

For T Cep, which is a low mass-loss rate AGB star and exhibits low-contrast spectral features, the spectrum is dominated by stellar photons. Furthermore, since T Cep has an optically thin dust shell (see e.g. Onaka et al. 1999, Sloan et al. 2003) [111, 123], its dust spectrum should be dominated by the hottest and densest part of the dust shell, which is essentially the inner dust radius. Therefore we can simplify Eq. 4.2 (for reference see § 4.2) as:

$$F_\lambda = B_{stellar}(\lambda, T) + B_{dust} Q_{dust} \tag{5.1}$$

where B_{dust} is the Planck curve for the inner dust temperature (T_{dust}), and Q_{dust} is the emission efficiency for the innermost dust grains. This assumption is an approximation to the dust continuum, but the exact continuum does not significantly alter the subsequent analysis.

Following Eq. 5.1 we can subtract the stellar contribution as approximated by an appropriate blackbody, leaving only the contribution from the dust shell. The stellar spectral energy distribution (SED) is assumed to be reasonably well simulated by a blackbody in the 2500–3500 K range. The precise temperature used in our analysis, was estimated from the spectral type and its variability over time. For the spectral observation closest to maximum light (T Cep4; hereafter T $\mathrm{Cep}_{\mathrm{max}}$), we use a temperature of 3347 K, determined from the spectral type of M5.5 (Perrin et al. 1998) [112]; similarly at minimum light (T Cep7; hereafter T $\mathrm{Cep}_{\mathrm{min}}$) we used a temperature of 2566 K, determined from the spectral type of M8.8, by extrapolating the data from Perrin et al. (1998) [112]. For the intermediate observations we linearly interpolated between these minimum and maximum temperatures, relating to their apparent changes in visual magnitude. Table 5.1 lists the estimated stellar blackbody temperatures (T_{eff}) for all the seven observations. Figure 5.1 includes the original

ISO spectra (in solid lines) together with the assumed stellar blackbodies (in dashed lines) in logarithmic scale (normalized at 3.0 μm, averaging over the range from 2.98–3.02 μm)[7].

In reality, these spectra contain contributions of the stellar photosphere, the extended atmosphere, and the circumstellar dust shell. In particular, stellar atmospheric water (H_2O) molecules are major absorbers in the near-and-mid-IR range. If the stellar emission is dominated by the (cooler) water layer (∼2000 K), the temperatures estimated from spectral type are too high. However, we have repeated our analysis using stellar temperatures in range 2000–3500 K (including ignoring the variation with pulsation phases) and found that the effect on spectral feature position, strength ratios and fitted dust temperature is negligible.

Having subtracted the starlight from our spectra, we are left with the emission from dust (i.e. $B_{dust}Q_{dust}$; Eq. 5.1), which still contains a temperature factor. Therefore, we have fitted each starlight-subtracted spectrum with a blackbody representative of the inner dust temperature (T_{dust}). The estimated dust blackbody temperatures (T_{dust}) are listed in Table 5.1 and dust blackbodies are shown in Figure 5.1 (in dotted lines), together with the observed spectra and stellar continua.

Dividing each starlight-subtracted spectrum by the best-fitted dust blackbody curve (normalized at 10.0 μm, averaging over the range from 9.98–10.02 μm) leaves only the intrinsic absorption/emission properties of the dust "Q_{dust}" (shown in Figure 5.3), by assuming all dust species have the same blackbody temperature. In this case, we effectively construct a composite emission efficiency spectrum which can be compared directly with absorptivity or mass absorption coefficient measurements of minerals in the laboratory (as discussed in § 3.5). Hereafter, we refer to the

---

[7] while there may be molecular spectral features due to water within this range, visual inspection of the spectra shows these to be negligible, and the averaging over a range of wavelengths mitigates any potential problem. Furthermore since we are simply scaling a blackbody whose temperature is determined independent of the spectrum, small errors in scaling factor do not effect our results.

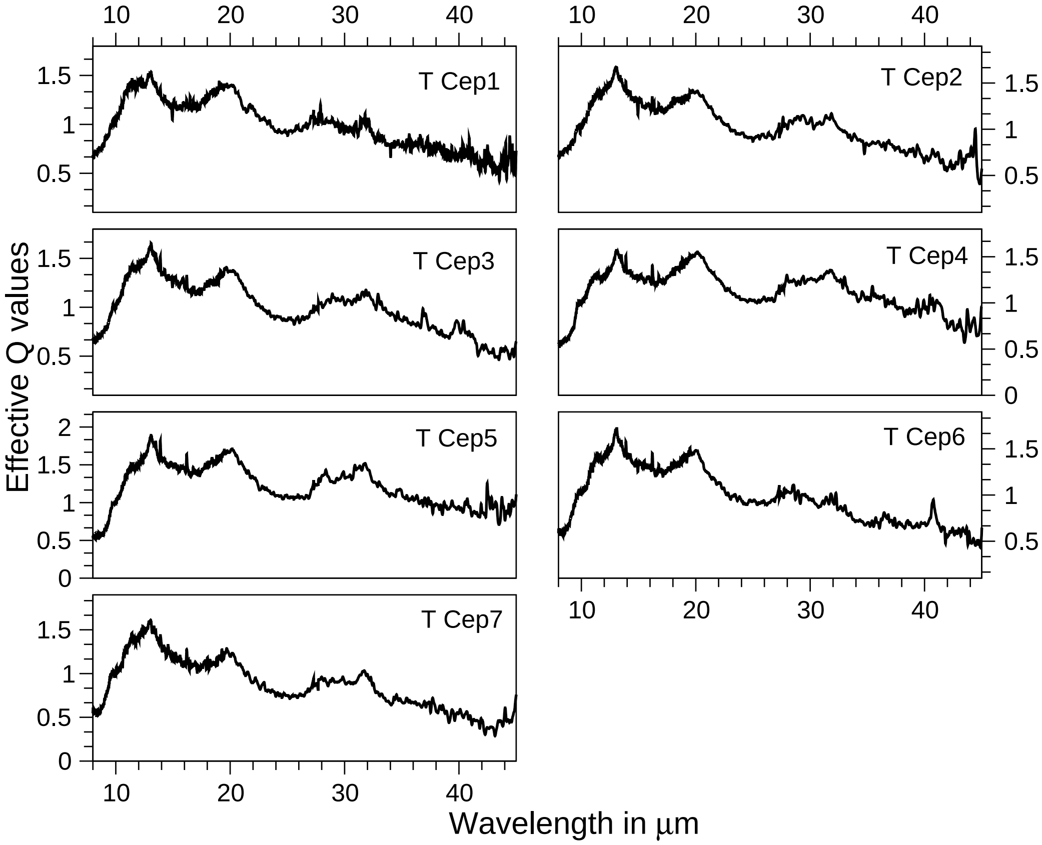

Figure 5.3: Starlight subtracted, dust-continuum-divided spectra (continuum-eliminated spectra). x-axis is wavelength (in μm) y-axis is effective Q values.

starlight-subtracted, dust-continuum-divided spectra as continuum-eliminated spectra for simplicity.

Since, T Cep has an optically thin dust shell and its dust spectrum is dominated by the innermost dust, we can apply this simple modeling method, rather than the more complex radiative transfer modeling method. Radiative transfer modeling is known to be degenerate because it actually models optical depth (τ), which convolves geometrical shell thickness, opacity and density. Furthermore, most radiative transfer models use optical constants (n & k) from laboratory experiments (or, worse, artificially derived optical constants), which are then applied usually using Mie theory to calculate the opacities/absorption cross sections of spherical grains. Recent studies (see e.g. Min et al. 2003, DePew et al. 2006, Pitman et al. 2008, Corman

2010) [95, 31, 115, 26] show that the use of spherical grains leads to unrealistic spectral features (as also discussed in § 3.4.2). In addition, mineral data in the form of optical constants (complex refractive index, n & k) only exist for a limited set of compositions. Available complex refractive indices are limited to the end-members of the olivine series (forsterite, fayalite), and for pyroxenes the situation is worse (only enstatite is available). Consequently, using radiative transfer modeling we cannot explore the mineralogical parameter space so thoroughly. Although, our simple modeling approach does not account for different sizes, shapes and/or temperatures within the dust grain population (see Thompson et al. 2006 for more discussion) [136], it does allow us to explore the mineralogical parameter space comprehensively.

5.4 Results from analysis of T Cep's spectrum

Table 5.1 shows that our modeled inner dust temperature (T_{dust}) changes with pulsation cycle of the star. This result is not dependent on the precise temperature of the subtracted stellar black body. It is unexpected because it is usually assumed that dust forms at minimum light and the dust formation temperature is rather constant. However, the temperature at which dust can be formed depends on the mass-loss rate, which should vary through the stellar pulsation cycle. Thus the changing inner dust temperature may reflect the stability temperature at that moment in the pulsation cycle. Consequently, our simple model suggests that dust may not be formed constantly; rather it is sporadic. This finding is similar to that for another M-type variable star Z Cyg (Onaka et al. 2002) [110].

We have calculated the linear correlation coefficients between the estimated stellar temperature (T_{eff}, which is derived from the visual magnitude and is thus a measure of the phase of pulsation) and the fitted dust temperature (T_{dust}). There is a strong cor-

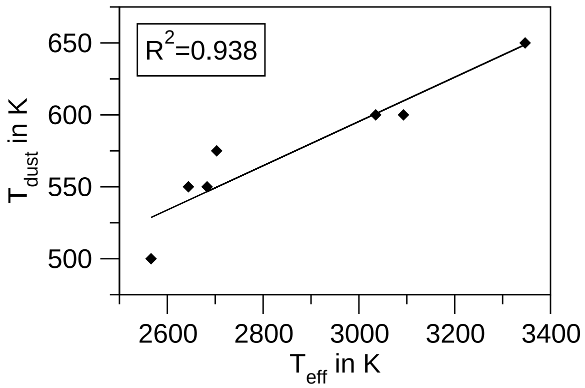

Figure 5.4: Correlation between assumed stellar temperature ($T_{\rm eff}$) and fitted inner dust temperature (T_{dust}), along with the linear correlation coefficient.

relation[8] between them as shown in Figure 5.4, suggesting that the apparent change in dust temperature is dictated by the stellar variations, rather than the dust formation. This variation in inner dust temperature will be discussed further in § 5.5.2.

In order to study the dust properties (e.g. grain mineralogy, morphology) of T Cep, we concentrate on the continuum-eliminated spectra for the entire 8–45 μm, all seven of which are shown in Figure 5.5: top panel. Since, the effect of dust temperature has been removed in our analysis (as discussed in § 5.3), there is no apparent change in overall underlying slope over the course of the pulsation period. However, in all cases there are clear spectral features that peak at 9.7, 11.3, 13.1, 20 and 32 μm, indicated by dashed straight lines (see Figure 5.5: top panel). The sub-peak features within the broad 8–14 μm complex emission features (at 9.7, 11.3, 13.1 μm) are explicitly shown in Figure 5.5: bottom panel. These sub-peak features are subtle, but we are confident that they are real because they do not occur at any known artifact wavelength of the SWS according to the SWS handbook[9].

Previous studies of the *ISO* SWS spectra of T Cep discovered sharp molecular bands at 2.5, 7.3, 16.2 μm, which are attributed to molecular H_2O, SO_2 and CO_2

---

[8] The linear regression coefficient is R, but using the determination coefficient, $R^2 > 0.5$ is a better criterion for whether a correlation exists (Thompson et al. 2006) [136]

[9] http://iso.esac.esa.int/manuals/HANDBOOK/sws_hb/

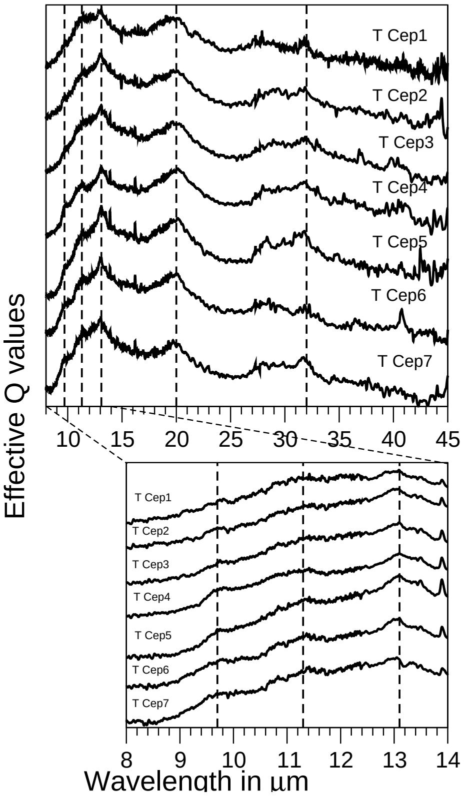

Figure 5.5: Continuum-eliminated spectra of T Cep in mid-IR region. x-axis is wavelength (in μm); y-axis is Effective Q values. The position of the spectral features (at 9.7, 11.3, 13.1, 20, 32 μm) are indicated by dashed straight lines in the top panel. The sub-peak features within the broad 8–14 μm emission (at 9.7, 11.3, 13.1 μm) are explicitly shown in the bottom panel.

gas respectively (e.g. Yamamura et al. 1999, Cami et al. 1999, Matsuura et al. 2002, Van Malderen 2003) [158, 17, 91, 143]. The attribution of the 7.3 μm feature has been further refined to be a combination of H_2O emission and SiO absorption (Verhoelst et al. 2006) [145]. Figure 5.1 shows that these molecular emission features change substantially with the pulsation cycle of T Cep, whereas the dust production shows only slight change. Molecular emission is affected more strongly than the dust emission by the stellar temperature, which changes with the pulsation cycle. The SpectraFactory database (Cami et al. 2010) [16] shows that molecular H_2O and OH exhibit several spectral bands at $\lambda > 20\,\mu$m. However, the molecular features are beyond the scope of the thesis.

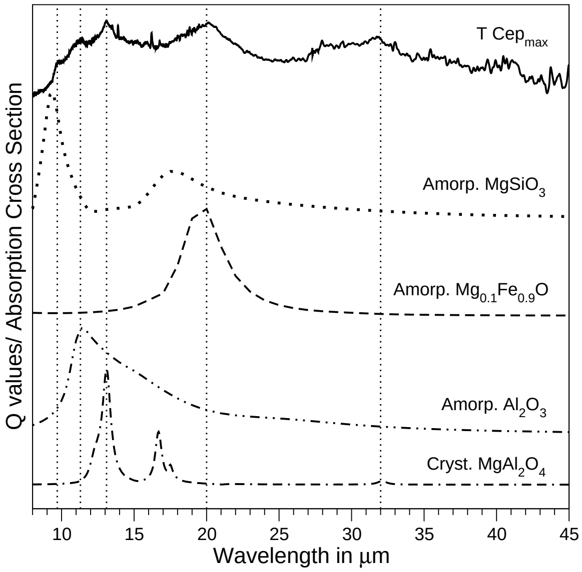

Figure 5.6: Comparison of continuum-eliminated spectra of T Cep4 (T Cep$_{\mathrm{max}}$) with several amorphous minerals suggested by Van Malderen (2003). The dotted straight lines indicate the positions of dust spectral features at 9.7, 11.3, 13.1, 20, 32 μm. x-axis is wavelength (in μm); y-axis is Effective Q values/Absorption Cross Section.

In addition to studying the molecular features, Van Malderen (2003) [143] also studied the dust features of T Cep, using the same *ISO* SWS spectra presented here. He concurred that the dust spectra of T Cep are characterized by 9.7, 11.0, 13.0 and 19.5 μm features, but his interpretation of the carriers of these features is different from our present analysis; he used amorphous silicate ($MgSiO_3$), amorphous alumina (Al_2O_3), spinel ($MgAl_2O_4$) and amorphous magnesium-iron oxides ($Mg_{0.1}Fe_{0.9}O$) respectively. However, as discussed in § 4.5, spinel is no longer considered the likely carrier of the 13 μm feature, while $Mg_{0.1}Fe_{0.9}O$ as the carrier of the 19.5 μm feature also has some difficulties. Furthermore, using the same optical constants (see Table 5.3) used by Van Malderen, it is not possible to produce sharp enough features to explain those observed in the spectrum of T Cep (see Figure 5.6).

In order to understand the lattice structure and the composition of the dust around T Cep, we have sought linear correlations amongst five prominent spectral features at 9.7, 11.3, 13.1, 20 and 32 μm. To ensure that the measure of relative strength of

Table 5.2: Correlations between flux ratios for the observed spectral features.

Continuum measured at →		8.2μm	40μm
Peak Position		R^2	
$F_{9.7}$	$F_{11.3}$	**0.913**	**0.958**
$F_{9.7}$	$F_{13.1}$	0.489	**0.899**
$F_{9.7}$	$F_{20.0}$	**0.576**	**0.863**
$F_{9.7}$	$F_{32.0}$	0.439	**0.579**
$F_{11.3}$	$F_{13.1}$	0.334	**0.797**
$F_{11.3}$	$F_{20.0}$	**0.633**	**0.826**
$F_{11.3}$	$F_{32.0}$	**0.504**	**0.537**
$F_{13.1}$	$F_{20.0}$	**0.545**	**0.869**
$F_{13.1}$	$F_{32.0}$	**0.567**	**0.530**
$F_{20.0}$	$F_{32.0}$	0.215	0.323

Coefficients of determination (R^2) > 0.5 constitutes a correlation;
bold designates to which there are strong/significant correlation.

the features is independent of the choice of continuum fitting technique, we define the relative intensity as the ratio of the flux measured at a peak position ($F_{peak}(\lambda_1)$) to that measured at a continuum point ($F_{cont.}(\lambda_2)$). In particular the relative intensity ($F_{peak}(\lambda_1)/F_{cont.}(\lambda_2)$) is less likely to be affected by overlapping molecular absorption bands than any fitted continuum (especially from SiO absorption; Tsuji et al. 1997, Speck et al. 2000) [139, 131]. The peak flux intensities are measured at $\lambda_1 = 9.7$, 11.3, 13.1, 20, 32 μm from each original flux-calibrated spectra. We used two separate continuum points (at $\lambda_2 = 8.2$ and 40 μm) to verify our results. Towards the long wavelength end of the spectra the signal-to-noise deteriorates. The increased noise could affect our correlations. Consequently, we take the average flux in a wavelength bin covering the range of 39.9–40.1 μm which contains 20 points.

Table 5.2 lists the determination coefficients (R^2) for the flux ratios at peak positions ($\lambda_1 = 9.7$, 11.3, 13.1, 20, 32 μm) with respect to the continuum points at ($\lambda_2 =$ 8.2 μm and 40 μm). This table shows that not all the features have strengths which are strongly/significantly correlated if the continuum reference is at 8.2 μm. However, if the reference continuum point of 40 μm is used, almost all of the features have strongly/significantly correlated strengths. The discrepancy between these results for the different continuum points can be explained by the effect of SiO molecular absorption band, which may overlap with the 8.2 μm region and make this wavelength point not truly continuum. If the SiO absorption is very strong, then the FWHM of the feature will be affected, but not necessarily the peak positions.

The strong correlations amongst all the peak features with respect to the 40 μm continuum point (see Table 5.2) demonstrate that the 32 μm is a real feature, rather than an artifact in these spectra, as suggested by Sloan et al. (2003) [123]. The strong correlation between 9.7 and 11.3 μm features strongly suggests that the carrier is a crystalline olivine, rather than a combination of two separate minerals (i.e. amorphous silicate and amorphous alumina, as suggested by Van Malderen (2003) [143]). Furthermore the strong correlations between the 9–12 μm complex features and the far-IR features at (20 and 32 μm) provide evidence that these far-IR features probably arise from the same carrier (i.e. crystalline olivine). Moreover, some previous studies suggest the 13 μm feature is carried by a different dust species from the rest of the "broad" feature (as discussed in § 4.6), the correlation of the 13 μm feature with the numerous other features supports the hypothesis that this feature is due to some form of silicate (see Begemann et al. 1997, Speck et al. 2000) [3, 131]. This will be further discussed in § 5.5.1. The positions of the spectral features and correlations amongst all these features together, suggests a crystalline silicate origin.

Having determined that the apparent broad spectral feature appears to be composed of overlapping features at 9.7, 11.3, 13.1, 20, 32 μm, we must now consider the implications for the mineralogy of the dust around T Cep.

5.5 Mineralogy and morphology of dust grains around T Cep

5.5.1 Comparing T Cep spectrum with laboratory data of crystalline silicates

As discussed above, the *ISO* SWS spectra of T Cep, a low mass-loss rate O-rich AGB star, provide the evidence of crystalline silicates in its circumstellar environment, which call the current dust condensation sequences into question. From the strong correlations among the spectral features (as discussed in § 5.4) the features at 9.7, 11.3, 20 and 32 μm may be indicative of crystalline silicate minerals (as also mentioned by the following authors: Waters et al. 1996, Molster et al. 2002-a, Pitman et al. 2010) [149, 99, 114]. While the correlations discussed in § 5.4 suggest that the carrier of the 13 μm feature is a silicate, we do not have an exhaustive database of silicate mineral spectra to investigate this idea. In fact, silica-rich minerals can show a 13 μm feature and future work to find spectra of silica-rich minerals may be fruitful. Meanwhile, whereas the 20 μm feature has been attributed to $Mg_{0.1}Fe_{0.9}O$ (e.g. Posch et al. 2002, Cami 2003) [117, 14], our analysis suggests a silicate origin because of the correlations amongst the features.

In order to match and identify the dust species present in the circumstellar envelope of T Cep, we compare the spectral features of the laboratory data from Pitman et al. (2010) [114] and Hofmeister et al. (2007) [60] (from WashU Group) of different crystalline dust species to the *ISO* spectra of T Cep. In Figure 5.7, we compare the continuum-eliminated spectra of T Cep$_{\text{max}}$ and T Cep$_{\text{min}}$ with the laboratory absorptivity data for a selection of crystalline olivine samples of varying composition (data taken from Pitman et al. (2010) [114]). Likewise, Figure 5.8 compares the same two T Cep spectra together with laboratory absorptivity data for a selection of crystalline pyroxene samples of varying composition (data taken from Hofmeister et

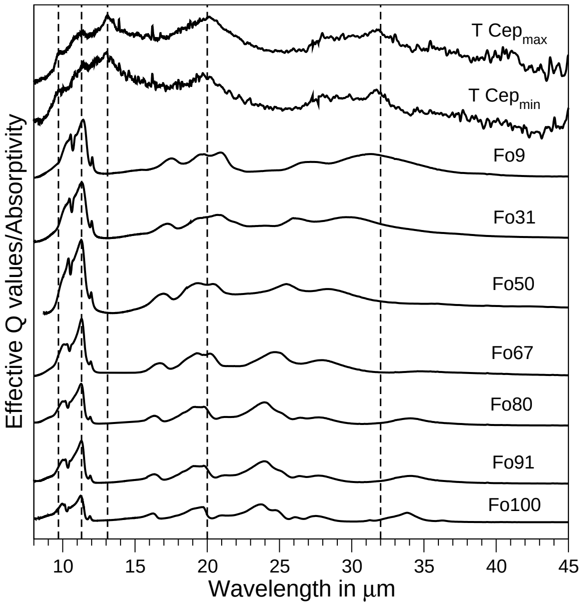

Figure 5.7: Comparison of continuum-eliminated spectra at maximum (T Cep$_{\rm max}$) and minimum (T Cep$_{\rm min}$) light with the laboratory absorptivity data for the olivine solid solution with varying Fe/(Mg+Fe) ratios. FoX (X=9, 31, 50, 67, 80, 91, 100) defines the composition such that each olivine has the composition $\mathrm{Mg}_{2X/100}\mathrm{Fe}_{2-2(X/100)}\mathrm{SiO}_4$. x-axis is wavelength (in μm); y-axis is Effective Q values/ Absorptivity. The dotted straight lines indicate the positions of dust spectral features at 9.7, 11.3, 13.1, 20, 32 μm.

al. in prep.)[10]

For the olivine data, FoX is an indication of the composition such that each olivine has the composition $\mathrm{Mg}_{2X/100}\mathrm{Fe}_{2-2(X/100)}\mathrm{SiO}_4$ (dataset ranging from Fo9 to Fo100 are shown in Figure 5.7); for the pyroxene data, EnX gives the composition via $\mathrm{Mg}_{X/100}\mathrm{Fe}_{1-(X/100)}\mathrm{SiO}_3$ (dataset ranging from En1 to En99 are shown in Figure 5.8). Since we have compiled laboratory mineral spectral data from a number of sources, these sources, along with other relevant sample/experimental information are listed in Table 5.3.

---

[10] We have a longstanding collaboration with Anne Hofmeister at WashU and can access new laboratory data through: http://galena.wustl.edu/∼dustspec/info.html, even before publication. These crystalline olivine and pyroxene series spectra agree well with the laboratory data from Kyoto group (e.g. Koike et al. 2003, Chihara et al. 2002) [76, 23] but provide fine grid spacing in composition space. Comparison among the data from several laboratory groups will be further discussed in Chapter 7.

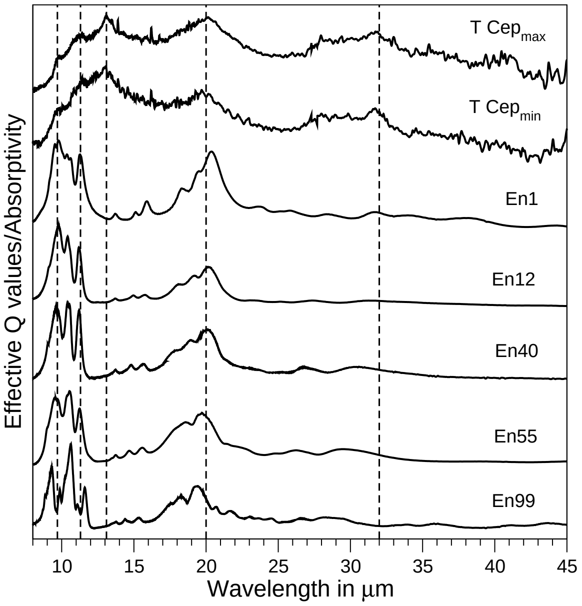

Figure 5.8: Comparison of continuum-eliminated spectra at maximum (T Cep$_{\rm max}$) and minimum (T Cep$_{\rm min}$) light with the laboratory absorptivity data for a pyroxene solid solution with varying Fe/(Mg+Fe) ratios. EnX (X=1, 12, 40, 55, 99) defines the composition such that that each pyroxene has the composition $\mathrm{Mg}_{X/100}\mathrm{Fe}_{1-(X/100)}\mathrm{SiO}_3$. x-axis is wavelength (in μm); y-axis is Effective Q values/ Absorptivity. The dotted straight lines indicate the positions of dust spectra features at 9.7, 11.3, 13.1, 20, 32 μm.

The WashU laboratory spectra are in the form of absorbance (a), which is proportional to the optical depth, whereas we need to compare to the absorption efficiency ($Q_{\rm abs}$). In order to convert the laboratory data to an appropriate form we use absorbance (a) is proportional to the log of the absorptivity (A), i.e. $a \propto \ln(A)$.

In general, we compare the spectral features of the laboratory spectra of different dust species to the astronomical observational data in order to match and identify the dust species present in circumstellar envelopes. However, the spectral feature parameters (positions, strengths and widths) are significantly influenced by three parameters (composition, temperature and grain shape of the dust grains; as mentioned in § 4.5). The effect of these three parameters are discussed below.

It is clear from both Figures 5.7 (for the olivine family members) and 5.8 (for the pyroxene family members) that positions and strengths of the spectral features change

Table 5.3: Sources of laboratory mineral data.

Sample	Chemical Composition	Designated by	Original form of lab data	References
Amorp. enstatite	$MgSiO_3$	-	optical constants (n, k)	Jäger et al. (1994)
Amorp. alumina	Al_2O_3	-	optical constants (n, k)	Begemann et al. (1997)
Cryst. spinel	$MgAl_2O_4$	-	optical constants (n, k)	Fabian et al. (2001)
Amorp. Mg-Fe oxides	$Mg_{0.1}Fe_{0.9}O$	-	optical constants (n, k)	Henning et al. (1995)
Cryst. Olivine	$(Mg, Fe)_2SiO_4$	FoX	absorbance (a)	Pitman et al. (2010)
Cryst. Pyroxene	$(Mg, Fe)SiO_3$	EnX	absorbance (a)	Hofmeister et al. in prep.
Cryst. alumina	Al_2O_3	Cor	optical constants (n, k)	Gervais (1991)
Cryst. Forsterite	Mg_2SiO_4	Fo100	optical constants (n, k)	Mukai & Koike (1990)
Cryst. Mg-rich Olivine	$Mg_{1.9}Fe_{0.1}SiO_4$	Fo90	optical constants (n, k)	Fabian et al. (2001)
Cryst. Fayalite	Fe_2SiO_4	Fo0	optical constants (n, k)	Fabian et al. (2001)

with varying Fe/[Mg+Fe] ratio. The positions of peak features shift towards longer wavelength as the Fe/[Mg+Fe] ratio increases. For T Cep, the spectral features are more closely matched to Fe-rich silicate dust (Fo9 and En1), rather than expected Mg-rich silicate dust (Fo100 or En99; see Figure 5.7 and 5.8), which calls the conventional wisdom regarding the dust condensation sequence into question. These laboratory data compared to the observational spectra of T Cep, preclude the possibility of large abundances of the conventional Mg-rich silicates (Fo100, En99) to explain the dust features, unless grain shape or temperature effects can be invoked.

Koike et al. (2006) [78] performed laboratory experiments to determine the effect of temperature on crystalline olivines (for further discussion see § 7.3.2). In general increasing temperature moves spectral features redwards as well as broadening and diminishing the heights of the features. This effect is most marked for far-IR features (at 49 and 69 μm for forsterite), and is much less effective in the mid-IR (8-45 μm) region (for further discussion see § 7.3.2). The experiments covered a wide range of sub-room temperatures (8–292 K), and even this large change in temperature has little effect on the mid-IR features. Consequently, extrapolation of the effects to higher temperature still suggests that temperature is an insignificant factor in determining the positions of the spectral features with which we are concerned.

The third parameter often invoked to shift spectral features is grain shape (see e.g. Fabian et al. 2001, DePew et al. 2006, Sloan et al. 2006) [37, 31, 121]. This will be discussed further in § 7.3.3.

5.5.2 Investigation of mineralogy of dust around T Cep: Compositional mixtures

It is clear from the qualitative comparisons in Figures 5.7 and 5.8 that Fe-rich crystalline silicates (Fo9, En1) are promising constituents for the dust around T Cep.

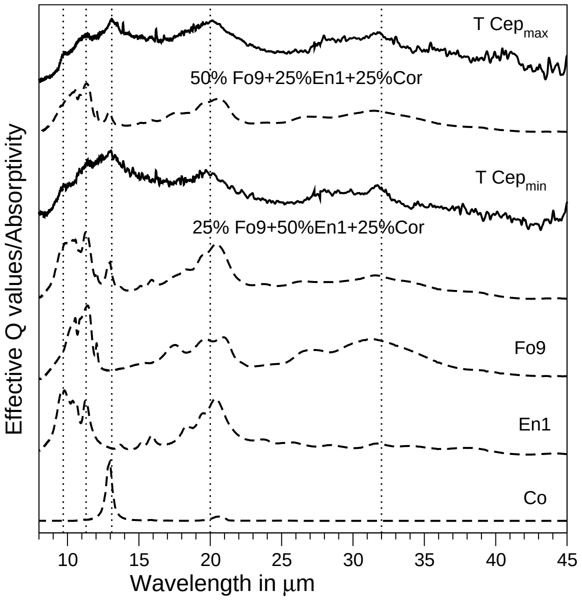

Figure 5.9: Comparisons of continuum-eliminated spectra at maximum (T Cep$_{\rm max}$) and minimum (T Cep$_{\rm min}$) light (solid lines) along with the best fit model (dashed lines) of mixtures of different potential crystalline minerals with different ratios. The laboratory data of individual crystalline minerals (Fo9, En1, Cor) are also included. x-axis is wavelength (in μm); y-axis is Effective Q values/ Absorptivity. The dotted straight lines indicate the positions of dust spectra features as shown in Figure 5.5.

Figure 5.9 shows comparison of continuum-eliminated spectra of T Cep$_{\rm max}$ and T Cep$_{\rm min}$ with mixture of these potential Fe-rich crystalline silicates minerals in different ratios. To account for the 13 μm feature, we have also included spherical corundum (Al_2O_3) grains. We use this mineral simply to give a feature, and not because we necessarily believe the carrier to be corundum. The source of the laboratory data of corundum (Cor) and its chemical composition are listed in Table 5.3.

The best fit models from our calculations are mixtures of crystalline fayalite (Fo9; not-quite-endmember of olivine family), ferrosilite (En1) and corundum (Cor) in varying proportion (with the error-bars of 10% for each constituent). Although the models are not a perfect fit, there appears to be a variation from T $\mathrm{Cep_{max}}$ to T $\mathrm{Cep_{min}}$. This variation is best explained by changing the ratio of Fo9 to En1. This is demonstrated in Figure 5.9, which shows the best fit models with T $\mathrm{Cep_{max}}$ and T $\mathrm{Cep_{min}}$ along with the laboratory data of each constituent separately.

As discussed in § 3.5, the laboratory optical properties of solids are produced for a variety of applications, the various laboratory data are published in several different types of units (e.g. absorbance, mass absorption coefficient, complex refractive index etc.) Using the appropriate conversion factors, all are converted to absorptivity (A) before attempting to make mixtures for spectral fitting.

For Fo9 and En1 the original spectra were in absorbance (a) units (e.g., A. M. Hofmeister et al. 2011, in preparation; Pitman et al. 2010), [59, 114], which were converted to absorptivity (A), using $A \propto e^a$. And for Cor, we used the Min et al. (2003) [95] method to calculate the absorption cross section (C_{abs}) for spherical grains of size 0.1 μm using its optical constants (data taken from Gervais 1991) [45]. Absorptivity (A) is directly proportional to the absorption efficiency Q_{abs} of a grain, which, in turn, is directly proportional to the absorption cross section (C_{abs}).

We use the following linear conversion equation to convert C_{abs} to A for corundum:

$$A = C_{abs} \times n \times d \tag{5.2}$$

where n is the number of particle per unit volume of the material used, and d is the path length. For thin film, d is taken as 1 μm. And to calculate n, we use

$$n = \frac{\rho}{M_{mol} \times m_{H_2}} \tag{5.3}$$

where ρ is the density of corundum (4.02 gm/cm^3), m_{H_2} is 1.672×10^{-24} gm. And M_{mol} for Al_2O_3 is (27×2+16×3=102). Using these values in Eq 5.3, we get $n = 2.35\times10^{22}$ cm^{-3}. Knowing C_{abs}, n and d, we calculated A for Al_2O_3 by using Eq 5.2.

Figure 5.9 demonstrates that these mixtures produce a reasonably good match to the detailed shape and as well as overall shape of the spectrum for both T Cep$_{\mathrm{max}}$ and T Cep$_{\mathrm{min}}$. Consequently, we can conclude that the compositions of the individual dust constituents remain the same in both spectra, while the relative amounts of these constituents may change, but are consistent with no variations at all. The spectra are consistent with a variation in the ratio of Fo9/En1 such that it is doubled at maximum light (T Cep$_{\mathrm{max}}$) and the ratio is halved at minimum light (T Cep$_{\mathrm{min}}$), while the relative abundance of Cor remains unchanged. This suggests that the olivine grains are slightly favored at maximum light.

The apparent subtle changes in mineralogy with pulsation cycle may be entirely due to statistical effects. However, in the classic condensation sequence (shown in Figure 4.2), Mg-rich olivine exists at higher temperatures than Mg-rich pyroxene. Furthermore the Mg-rich olivine reacts with SiO gas to form Mg-rich pyroxene. If a similar reactive process exists for the iron-rich endmembers, the occurrence of higher olivine/pyroxene compositions at maximum light, may be a temperature effect. In this case, the Fe-rich pyroxene (En1) is more easily destroyed than the Fe-rich olivine (Fo9) at maximum light; while at minimum light the reaction with SiO gas is promoted. Essentially, the change in stellar radiation field causes selective destruction/processing of the inner most grains.

From our analysis, the most striking result is that we need Fe-rich crystalline silicates in order to explain the spectral features. This result is unexpected, but supported by recent studies of silicate presolar grains from meteorites which show that silicate grains from AGB stars have nano-crystalline structures and some are very iron-rich, indicative of non-equilibrium formation processes (e.g. Stroud et al. 2008, Vollmer et al. 2008, Bose et al. 2010) [134, 147, 10].

5.5.3 Investigation of morphology of dust around T Cep: Grain shape effects

Our analysis on dust compositions around T Cep strongly suggest that the crystalline silicates are almost completely Fe-rich, with little evidence of Mg-rich silicates. This result conflicts with both current dust formation hypotheses, and studies of cosmic crystalline silicates to date. However, as mentioned in § 5.5.1, it is possible that grain shape effects may allow Mg-rich silicates to match the positions and strengths of the observed dust features of T Cep. Previous studies show that the position of spectral features of dust grains depend on their grain shapes (as discussed in § 3.4.2; and for reference see Bohren & Huffman 1983, Bohren et al. 1983, Fabian et al. 2001, Min et al. 2003, Sloan et al. 2006, DePew et al. 2006, Koike et al. 2010) [8, 9, 37, 95, 121, 31, 77]. Here we investigate the grain shape effects of crystalline silicates.

The spectral features of crystalline silicate grains exhibit wide variety in the positions, widths and strengths of their peaks. For a given series, these are dependent on the composition (Fe/[Mg+Fe] ratio) of the silicates, as well as the temperatures (as discussed in § 5.5.1) and shapes of dust grains. Disentangling these competing effects is difficult because we do not have the data to test both grain shape and compositional effects simultaneously. There are several laboratories that have produced spectral data for crystalline silicates in the olivine and pyroxene series. As introduced in § 3.6, here we will only consider the laboratory data from WashU (e.g. Hofmeister et al. 2007, Pitman et al. 2010) [60, 114], Kyoto (e.g. Chihara et al. 2002, Koike et al. 2003, Koike et al. 2006, Murata et al. 2009, Koike et al. 2010) and

[23, 76, 78, 104, 77] and Jena (e.g. Fabian et al. 2001, Jaeger et al. 1998) [37, 69] group.

A series of opacity (mass absorption coefficients) measurements for the olivine series, covering several Fe/[Mg+Fe] ratios from forsterite (Fo100) to fayalite (Fo0) has been published by the Kyoto group (Koike et al. 2003) [76]. A finer grid of compositions across the olivine series was published by the WashU group (Hofmeister et al. 2007, Pitman et al. 2010) [60, 114], which agree with the Kyoto data. Here we use the finer grid of Pitman et al. (2010) [114]. A similar series of measurements for pyroxene from enstatite (En100) to ferrosilite (En1) has been also published by the Kyoto group (Chihara et al. 2002) [23]. Here, we use currently unpublished pyroxene data from the WashU group (Hofmeister et al. in prep.), which also agree with the Kyoto data.

While the data from WashU and Kyoto groups provide a good sampling over several Fe/[Mg+Fe] ratios for both olivines and pyroxenes, they do not measure the complex indices of refraction or dielectric constants for all these compositions. As a consequence we cannot use them to analyze the effect of grain shape on dust spectra. Thus we cannot fit both the compositional effect (Fe/[Mg+Fe] ratio) and the shape distribution simultaneously. For this reason, extensive studies of grain shape effects have generally been limited to a single composition: forsterite (Fo100), supplied by the Jena group.

The complex refractive indices for the end-member compositions of olivine (Mg-rich olivine: Fo90[11], fayalite: Fo0) and Mg-rich pyroxene (enstatite: En100) are provided by the Jena group[12] (e.g. Fabian et al. 2001, Jaeger et al. 1998) [37, 69]. The refractive indices are provided for the vibrational directions parallel to the three crystallographic axes x, y, z. Meanwhile, Mukai et al. (1990) [103] provided optical constants for forsterite (Fo100), but this data was for unoriented samples and therefore

---

[11] Technically Fo90 is still called forsterite and most natural samples are closer to Fo90 than Fo100

[12] optical constants available at http://www.astro.uni-jena-de/Laboratory/Database/databases.html

represents an average of the three axial directions. A list of all the sources of these laboratory data used, can be found in Table 5.3.

We have already discussed in § 3.4.2, there are several possible approaches to addressing the grain shape effect (e.g. Fabian et al. 2001, Min et al. 2003, Takigawa et al. 2009, Koike et al. 2010) [37, 95, 135, 77]. Here we adopt the statistical approach by Min et al. (2003) [95] and assume that there is no tendency for a certain axis to be elongated. We have calculated the absorption cross-sections ($C_{\rm abs}$) for three compositions of olivine (Fo100, Fo90 and Fo0; see Table 5.3 for sources of complex refractive indices). For each composition, we calculate $C_{\rm abs}$ for four grain shape distributions: Spherical particle (SPH), Continuous distribution of ellipsoids (CDE), Continuous distribution of spheroids (CDS), and Distribution of hollow spheres (DHS) as described in § 3.4.1 and § 3.4.2. The grain size is defined by the grain volume being equivalent to a sphere of radius 0.1 μm (for further justification see Speck et al. 1997) [130]. When data is available for the individual crystallographic axes, we calculate the $C_{\rm abs}$ separately and then average the three axial absorption cross sections ($\langle C_{\rm abs}\rangle$). The final $\langle C_{\rm abs}\rangle$ spectra are shown in Figures 5.10–5.14.

For all three compositions (Fo100, Fo90 and Fo0), the spectral feature parameters (e.g. peak positions and strengths) are similar for both ellipsoids (CDE) and spheroids (CDS). For the hollow spheres (DHS) the peak positions are similar to both CDE and CDS, but the spectral features are stronger. The spectral features of spherical (SPH) particles are significantly different in both position and strength from those of CDE, CDS and DHS.

Figure 5.14 compares the positions of the spectral features in the derived absorption cross-sections with those observed for T Cep. It is clear that fayalite (Fo0) provides a better match with the observed peak positions (at 20, 32 μm) of T Cep, than does forsterite (Fo100). Following the work of Takigawa et al. (2009) [135], it

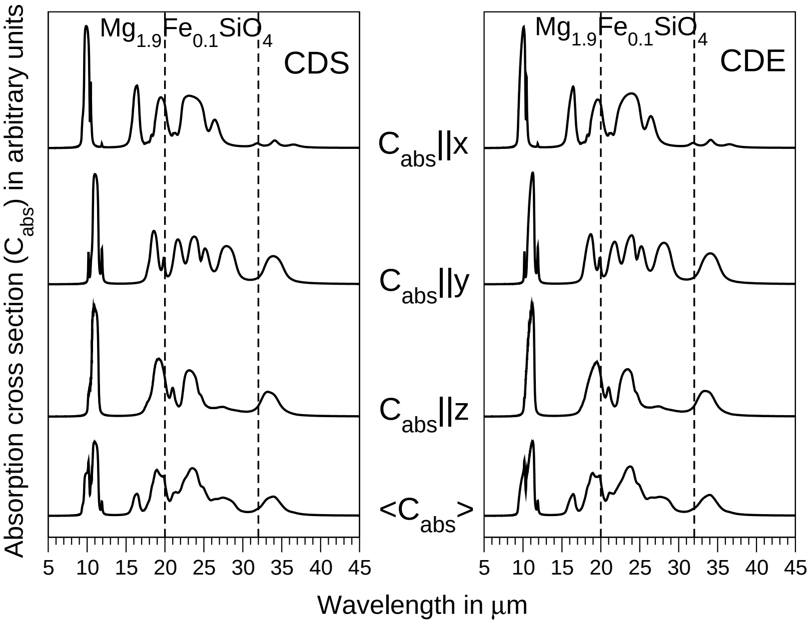

Figure 5.10: Absorption cross section of very Mg-rich Olivine ($Mg_{1.9}Fe_{0.1}SiO_4$) for spheroid (CDS: left panel) and ellipsoid (CDE: right panel). The upper three plots correspond to calculated C_{abs} parallel to the x, y and z axes. The bottom plots correspond to average ($\langle C_{\text{abs}} \rangle$). x-axis is wavelength (in μm) y-axis is absorption cross-section in arbitrary units. Vertical dashed lines show positions of observed spectral features of T Cep at long wavelength (20 and 32 μm).

is possible that a single growth axis is elongated. However, Figure 5.14 shows that even using only a single crystallographic axis does not produce an Mg-rich olivine with features that match T Cep.

5.6 Discussion

Our analysis of the spectra of T Cep strongly suggest that the dust forming around this Mira is both highly crystalline and iron-rich. This has implications for not only for other stars exhibiting these crystalline features, but also for conventionally Mg-rich condensation sequence observed for amorphous circumstellar silicates.

Woitke (2006) [154] showed that while carbon dust around an AGB star could drive a radiation-pressured wind, oxygen-rich dust (silicate) was too transparent.

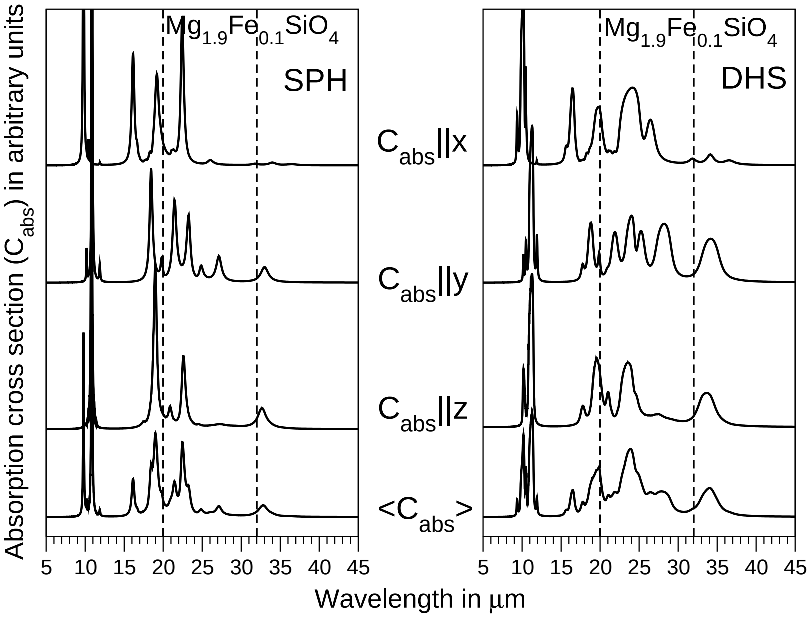

Figure 5.11: Absorption cross section of very Mg-rich Olivine ($Mg_{1.9}Fe_{0.1}SiO_4$) for spherical (SPH: left panel) and hollow sphere (DHS: right panel). The upper three plots correspond to calculated $C_{\rm abs}$ parallel to the x, y and z axes. The bottom plots correspond to average ($\langle C_{\rm abs} \rangle$). x-axis is wavelength (in μm) y-axis is absorption cross-section in arbitrary units. Vertical dashed lines show positions of observed spectral features of T Cep at long wavelength (20 and 32 μm).

However, this result assumes the silicates are Mg-rich. Iron-rich silicate grains tend to have higher optical/near-IR opacities which facilitate the capture of momentum from the star through radiation pressure. The inclusion of iron-rich silicate grains may solve this problem.

Woitke (2006) [154] also showed that the dynamics in the dust-forming zones around carbon-rich AGB stars lead to inhomogeneous dust formation, producing fine scale structure in the density of the dust envelope. In these models the only condensate considered is amorphous carbon. In an oxygen-rich environment, there are many potential minerals that can be formed and their stability is sensitive to the precise conditions.

In addition to the turbulent/hydrodynamic density inhomogeneities predicted by Woitke (2006) [154], pulsation shocks are expected to have a strong effects on local

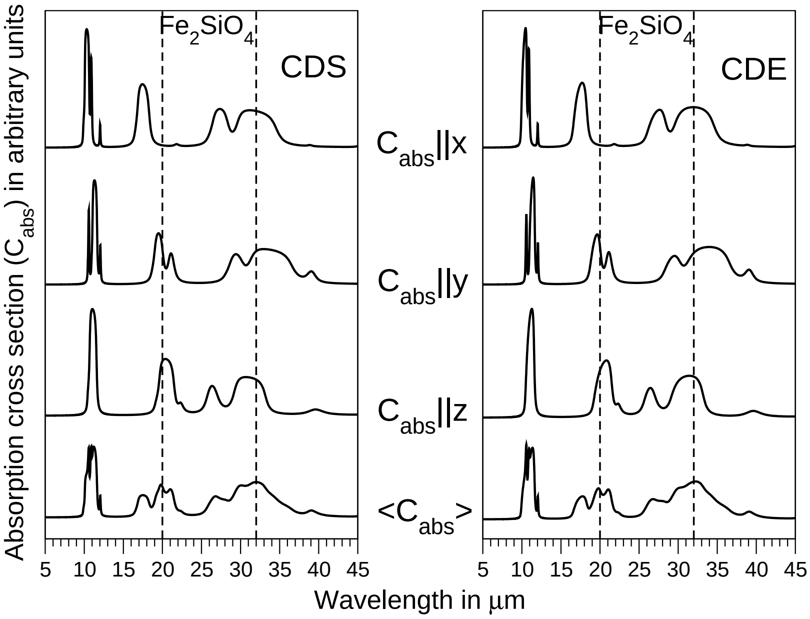

Figure 5.12: Plot of Absorption cross section of fayalite (Fe_2SiO_4) for spheroid (CDS: left panel) and ellipsoid (CDE: right panel). The upper three plots correspond to calculated $C_{\rm abs}$ parallel to the x, y and z axes. The bottom plots correspond to average ($\langle C_{\rm abs}\rangle$) of them. x-axis is wavelength (in μm) y-axis is absorption cross-section in arbitrary units. Vertical dashed lines show positions of observed spectral features of T Cep at long wavelength (20 and 32 μm).

conditions (e.g. Cherchneff 2006) [20]. This combination of physical effects should lead to non-equilibrium dust formation and may lead to unexpected dust-forming conditions. Therefore we suggest that even at low mass-loss rates the density structure in the outflows of AGB stars is such that crystalline silicates may form, though it is not clear why iron-rich silicates are apparently favored. This scenario may be consistent with the chaotic grain formation hypothesis (ii), as suggested by Stencel et al. (1990; for reference see § 4.4) [133]. In terms of chaotic grains, in low-mass loss rate objects dust only forms close to the star where the density is high; higher temperature allow the chaotic grains to be annealed.

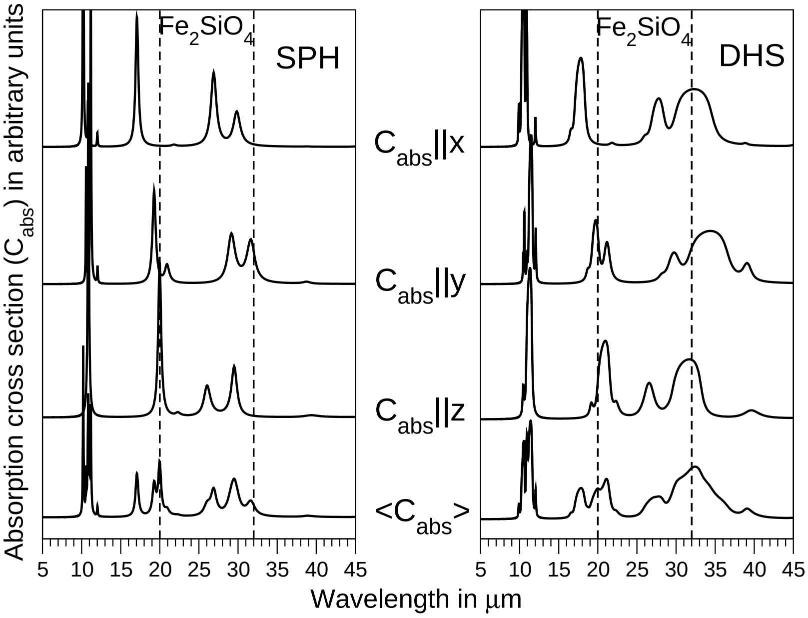

Figure 5.13: Plot of Absorption cross section of fayalite (Fe_2SiO_4) for spherical (SPH: left panel) and hollow sphere (DHS: right panel). The upper three plots correspond to calculated C_{abs} parallel to the x, y and z axes. The bottom plots correspond to average ($\langle C_{\mathrm{abs}} \rangle$). x-axis is wavelength (in μm) y-axis is absorption cross-section in arbitrary units. Vertical dashed lines show positions of observed spectral features of T Cep at long wavelength (20 and 32 μm).

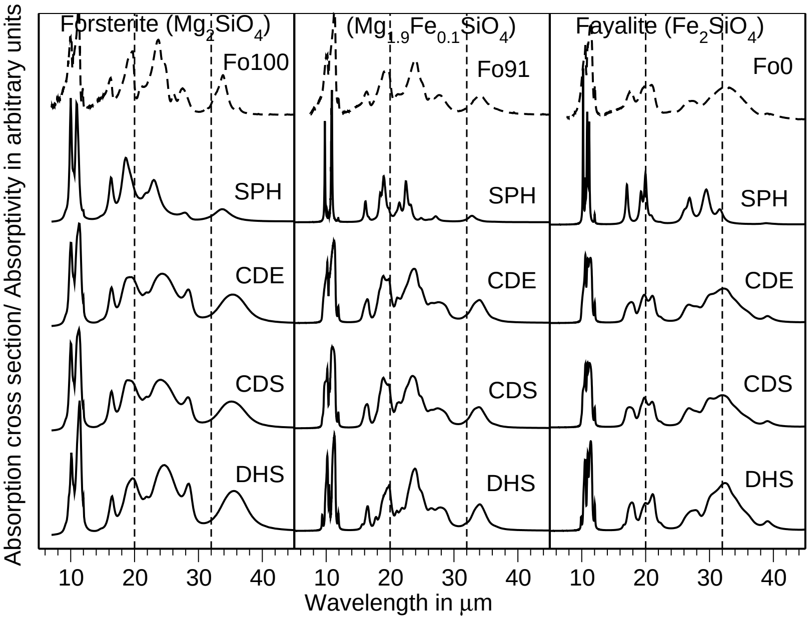

Figure 5.14: Calculated absorption cross section (C_{abs}) for four shape distributions (SPH, CDE, CDS, DHS) of 0.1 μm-sized grains of three different members of olivine family along with the directly-measured laboratory absorption spectrum. *Right panel*: forsterite (Fo100), *center panel*: very Mg-rich olivine (Fo91: closest compositionally in the lab spectra), *left panel*: fayalite (Fo0). x-axis is wavelength (in μm) y-axis is absorption cross-section/absorptivity in arbitrary units. Vertical dashed lines show positions of observed spectral features of T Cep at long wavelength (20 and 32 μm). The solid lines are the calculated absorption cross-sections while dashed lines (at the top) show the laboratory absorption spectra (data taken from Pitman et al. 2010) [114].

5.7 Summary & Conclusion

We have presented an analysis of the time variations of the IR dust spectrum of optically thin O-rich AGB star, T Cep.

We found that:

1. The inner dust temperature of T Cep is variable.
2. Dust formation is likely to be sporadic, not continuous, and has approximately the same composition all the time.
3. While the observations are consistent with a constant olivine-to-pyroxene ratio, they can accommodate small variations with stellar pulsation. This variation in composition is very subtle and can be explained by selective destruction/processing of the inner most grains with the change in stellar radiation field.
4. The strong correlations between the observed spectral features suggest that they all have same crystalline mineral as a carrier.
5. The structure within the broad 8–14 μm feature with overlapping sub-features at 9.7, 11.3, 13.1 μm is explained by mixtures of crystalline silicates. This confirms the presence of crystalline minerals around low-mass-loss rate O-rich AGB stars.
6. The peak wavelength of the features at 20 and 32 μm suggest the presence of Fe-rich, rather than the expected Mg-rich silicates. This can be explained as occurrence of non-equilibrium condensation mechanism in the outflow of the central star.

The analysis presented here shows that our understanding of the formation of crystalline silicates and the inclusion of iron in those silicates is in its infancy and needs to be revised according to the present findings.

Chapter 6

Investigating the spectral dust features of O-rich AGB stars using spatially resolved spectroscopy

6.1 Introduction

In Chapter 5 we studied the temporal variation of spectral dust features with pulsation cycle for O-rich Mira variable T Cep. We analyzed how the dust formation is related to the pulsation cycle and dust mineralogy. Now in this chapter we will use long slit spectroscopy to investigate the dust shells around seven nearby O-rich AGB stars, in order to see how the spatial structure of the shell changes at different distances from the central star. We will also explore how the spatial variations in spectral dust features can be explained by different competing dust formation hypotheses.

6.2 Purpose of this work

As discussed in § 4.6, the spectra of O-rich AGB stars exhibit a diverse range of IR dust spectral features. In order to understand the IR dust spectra, we need to refer to the three main dust formation hypotheses (as discussed in § 4.4). Different formation hypotheses predict different sequences of solids will form; different solids give rise to different spectral features. Figure 6.1 is a schematic presentation of progression of the spectral feature parameters (peak position, width) as seen observationally in e.g. SE classes (see § 4.6 and Figure 4.14). The observed progression from broad to classic narrow 10 μm silicate features with increasing mass-loss rate is usually interpreted as a progression from dust dominated by oxides to dust dominated by amorphous silicates (Dijkstra et al. 2005, Blommaert et al. 2007) [32, 7].

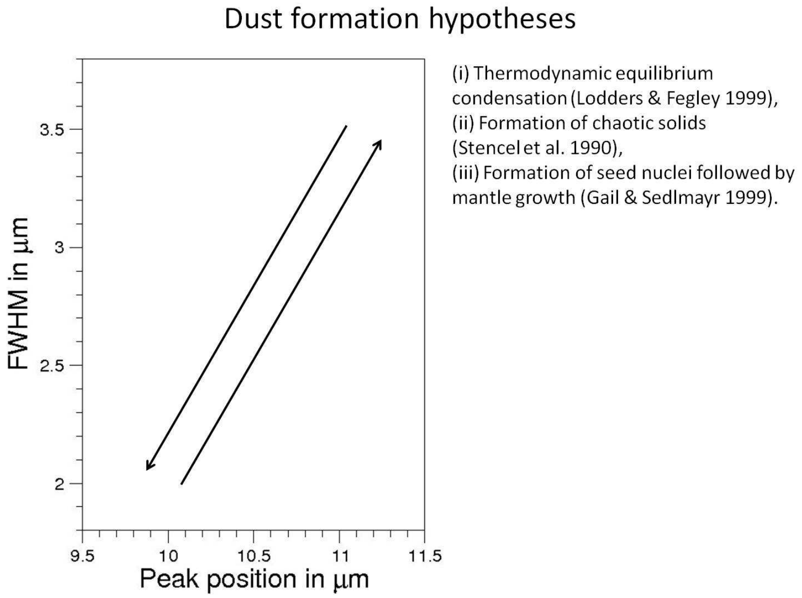
Dust formation hypotheses

Figure 6.1: Schematic presentation of progression of peak positions and widths as seen in SE classes (Sloan et al. 2003) [123].

There are several hypothetical dust formation models that have been developed to explain the trends. These models effectively fall into three competing categories: (i) thermodynamic equilibrium condensation (Lodders & Fegley 1999) [87]; (ii) formation of chaotic solids in a supersaturated gas followed by annealing (Stencel et al. 1990) [133]; (iii) formation of seed nuclei in a supersaturated gas, followed by mantle growth (Gail & Sedlmayr 1999) [42]. The latter should follow thermodynamic equilibrium as long as density is high enough for gas-grain reactions to occur. Both (i) & (iii) are consistent with the oxide to silicate trend as described above and shown schematically in Figure 6.2.

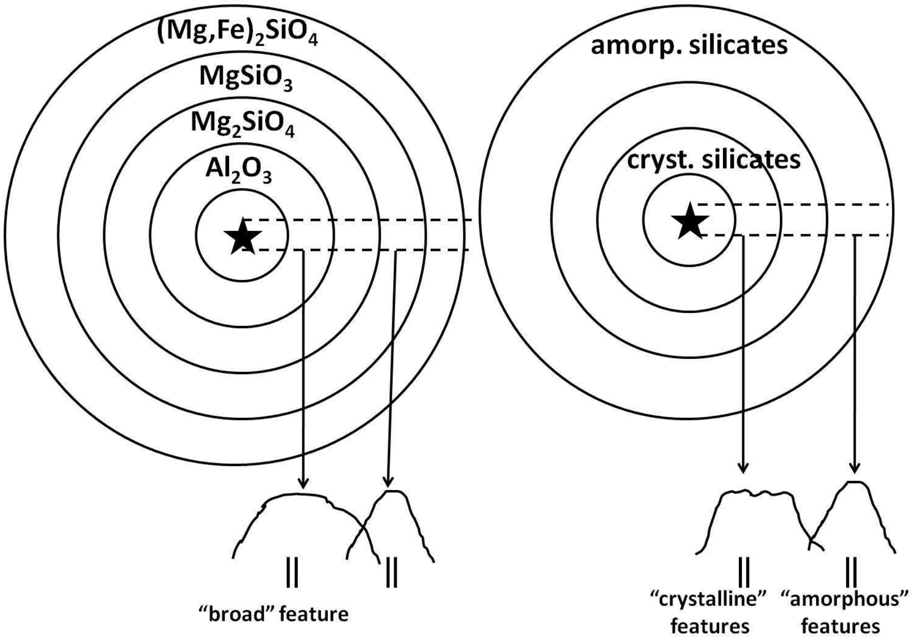

Figure 6.2: Schematic structure of dusts shells. Left panel: Classic dust condensation sequence (Tielens 1990) [137]; Right panel: Dust shell structure suggested by ISO SWS observations of O-rich AGB star T Cep (Guha Niyogi et al. 2011) [49] and for similar type of AGB stars.

In addition to mechanisms (i) and (iii) in Figure 6.1, mechanism (ii) forms chaotic solid grains which have the bulk composition of the gas. In this scenario the grains can anneal if the temperature is high enough. This mechanism predicts that at low C/O ratios, the dust grains would comprise a mixture of olivine, pyroxene, SiO_2, MgO and FeO rather than be dominated by olivine alone. At higher C/O ratios (but still $C/O < 1$), Al-O bonds are predicted to form preferentially; leading to dust dominated by oxides rather than silicates. Several observational studies (Dijkstra et al. 2005, Blommaert et al. 2007) [32, 7] support (i) and (iii), not (ii). However, since chaotic grains can be annealed we may expect to see a spatial trend for the spectral features. Recent studies (see e.g. Guha Niyogi et al. 2011, Pitman et al. 2010; also see Chapter

5) [49, 114] imply that low mass-loss rate objects show crystalline silicates features whereas, higher mass-loss rate objects exhibit amorphous features. This is consistent with the spectral classifications into SE classes with SE1 dominated by crystalline material and SE8 dominated by amorphous material. In terms of chaotic grains, in low-mass loss rate objects dust only forms close to the star where the density is high; higher temperature allow the chaotic grains to be annealed. For higher mass-loss rate objects dust can form further out radially and thus at lower temperatures and so could be dominated by amorphous silicates. The spectral features of T Cep, RX Lac, T Cet and R Hya (see e.g. Guha Niyogi et al. 2011, Pitman et al. 2010) [49, 114], cannot be explained in terms of the classic dust condensation sequence (mechanisms [i] & [iii]). Instead, it suggests that the dust can be best explained by iron-rich crystalline silicate minerals, which may be consistent with the chaotic grain scenario (followed by hypothesis [ii]). This scenario is depicted in Figure 6.2: Right panel.

Spatially resolved spectroscopic data will help us to distinguish between these various dust-formation scenarios as well as other controversial dust grain hypotheses. For example we discuss the 13.0 μm feature in § 4.6. If this feature is due to corundum it should be located close to the central star under mechanisms (i) and (iii), whereas, silica should be co-located with a 9.0 μm feature throughout the shell. For chaotic grains, variation in C/O is expected to dominate the variation in spectral feature shapes and positions. Consequently, in a single object at a single epoch, we should not see these variations.

6.3 Target selection

In order to obtain spatially resolved spectroscopic data, we chose seven targets, which are bright, relatively close by ($\approx$ 200 pc), optically thin and low mass-loss rate O-rich AGB stars. The targets were selected from SE2 and SE3 spectral classes (for

Table 6.1: Target list of nearby O-rich AGB stars observed by Gemini/MICHELLE.

Target	IRAS Name	Right Ascension (RA)	Declination (Dec)	Brightness at $12\,\mu$m (Jy)	Obs. date
R Aur	05132+5331	05:17:17.69	+53:35:10.04	460	28 JAN 2011
R Leo	09448+1139	09:47:33.49	+11:25:43.65	2161	27 JAN 2011
RT Vir	13001+0527	13:02:37.98	+05:11:08.38	462	28 JAN 2011
SW Vir	13114-0232	13:14:04.38	-02:48:25.15	681	28 JAN 2011
R Hya	13269-2301	13:29:42.78	-23:16:52.79	1591	27 JAN 2011
W Hya	13462-2807	13:49:01.49	+28:22:03.49	4200	27 JAN 2011
RX Boo	14219+2555	14:24:11.63	+25:42:13.40	847	28 JAN 2011

Note: The RA and Dec of the targets are used from SIMBAD (FK5 coord. [ep=J2000 eq=2000]); the brightness of the targets at $12\,\mu$m are taken from *IRAS* measurements.

Table 6.2: Classification and physical parameters the targets.

Target	Spectral Type	Spectral Class	Variability Type	Pulsation Periods (days)	Expansion Velocity (km/sec)	Distance (pc)	Mass loss rate $(\dot{M}\mathrm{yr}^{-1})$
R Aur	M6.5–9.5	SE2	M	458	10.0	413	9.8×10^{-7}
R Leo	M6–8	SE2	M	310	8.5	101	1.0×10^{-7}
RT Vir	M8	SE3	SR	155	9.3	138	7.4×10^{-7}
SW Vir	M7	SE3	SR	150	8.9	143	5.7×10^{-7}
R Hya	M6–9	SE2	M	389	8.0	617	1.4×10^{-7}
W Hya*	M7.5–9	SE8	SR	361	8.2	115	8.1×10^{-8}
RX Boo	M6.5–8	SE3	SR	340	10.2	156	8.1×10^{-7}

Note: Spectral types, Spectral classes, pulsation periods (P) are taken from Sloan & Price (1998) [128]; the distances (D) were calculated by using the Parallaxes (from SIMBAD); expansion velocities (v_{exp}), mass-loss rates ($\dot{M}$) are taken from Loup et al. 1993 [88].

$*$ W Hya was misclassified as SE8 and has been subsequently re classified as SE2.

reference see § 4.6: Figure 4.14). Some information about our selected targets are given in Table 6.1 and 6.2.

All objects were previously observed with *IRAS* LRS[1]. In addition three objects (R Hya, W Hya, RX Boo) were observed by *ISO* SWS[2]. We also acquired the visual light curve for each object from the AAVSO database[3]. The positions in the lightcurves at which Gemini data were taken, are indicated by dashed straight lines (see Figure 6.3 through Figure 6.9).

---

[1] http://www.iras.ucalgary.ca/ volk/getlrs_plot.html

[2] http://isc.astro.cornell.edu/ sloan/library/swsatlas/atlas.html

[3] http://www.aavso.org/

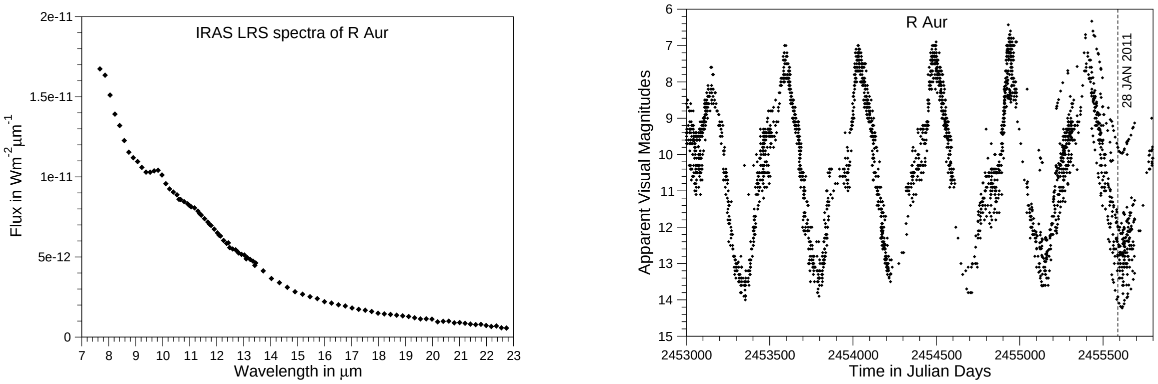

Figure 6.3: Left: IRAS LRS observational data of R Aur, Right: Light curve of R Aur for last seven years. The Gemini observation date is indicated by dashed straight line.

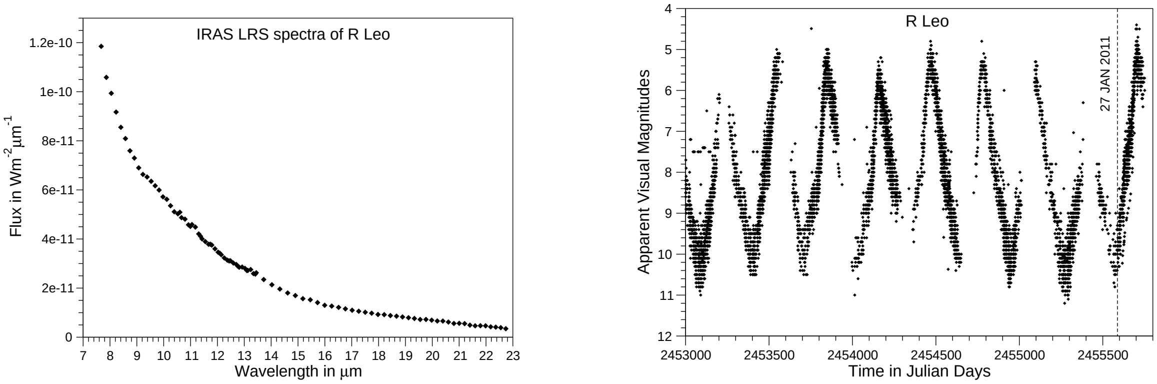

Figure 6.4: Left: IRAS LRS observational data of R Leo, Right: Light curve of R Leo for last seven years. The Gemini observation date is indicated by dashed straight line.

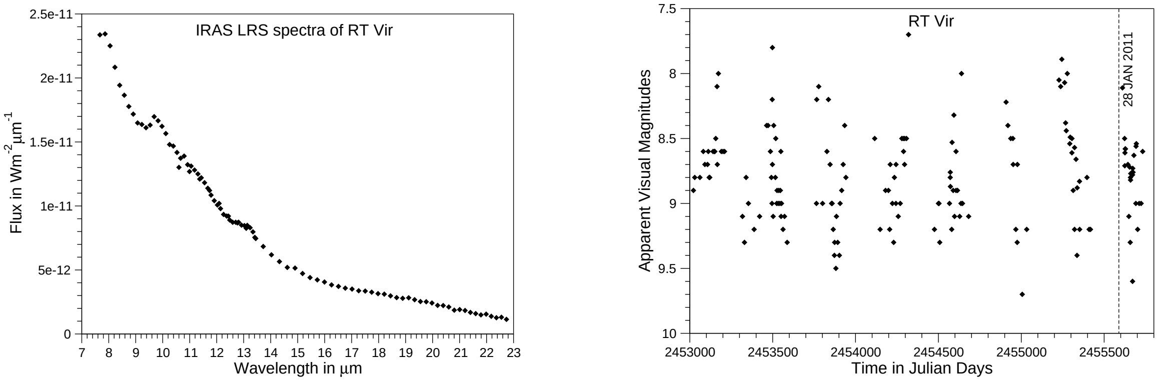

Figure 6.5: Left: IRAS LRS observational data of RT Vir, Right: Light curve of RT Vir for last seven years. The Gemini observation date is indicated by dashed straight line.

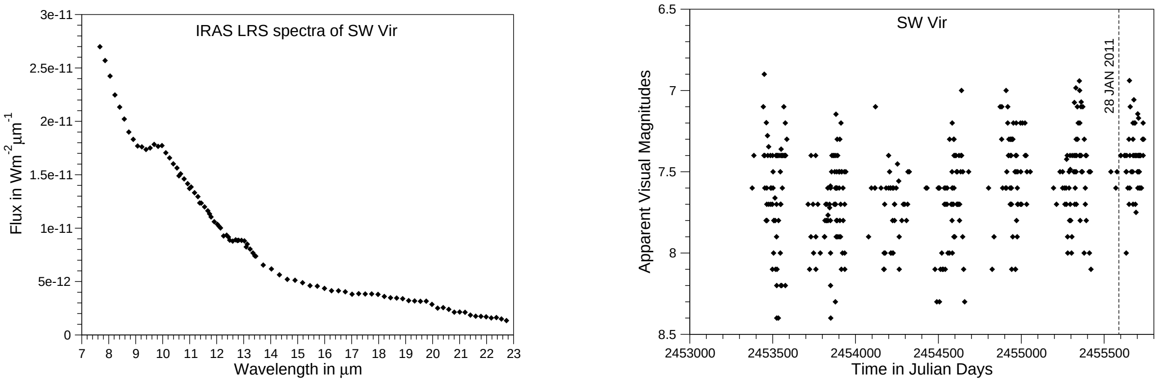

Figure 6.6: Left: IRAS LRS observational data of SW Vir, Right: Light curve of SW Vir for last seven years. The Gemini observation date is indicated by dashed straight line.

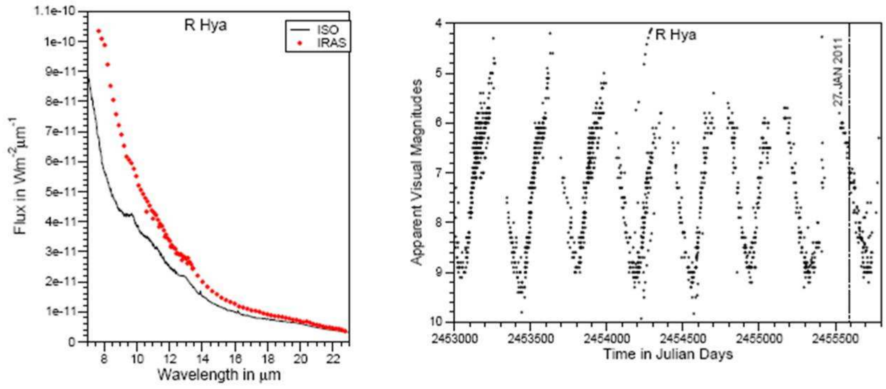

Figure 6.7: Left: IRAS LRS and ISO SWS (TDT # 08200502) observational data of R Hya, Right: Light curve of R Hya for last seven years. The Gemini observation date is indicated by dashed straight line.

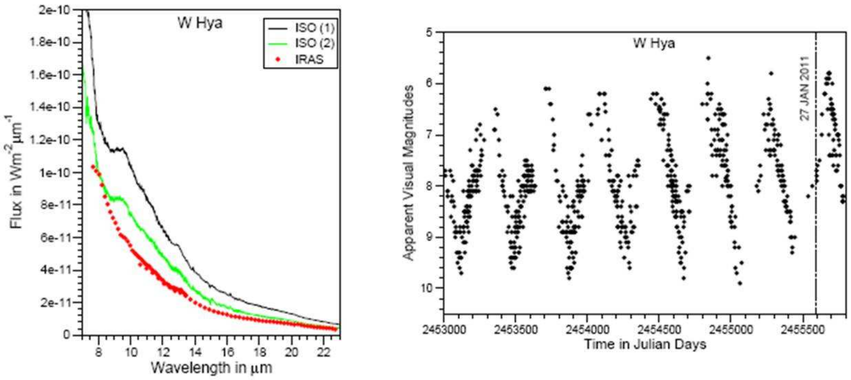

Figure 6.8: Left: IRAS LRS and ISO SWS (TDT # 08902004, 41800303) observational data of W Hya, Right: Light curve of W Hya for last seven years. The Gemini observation date is indicated by dashed straight line.

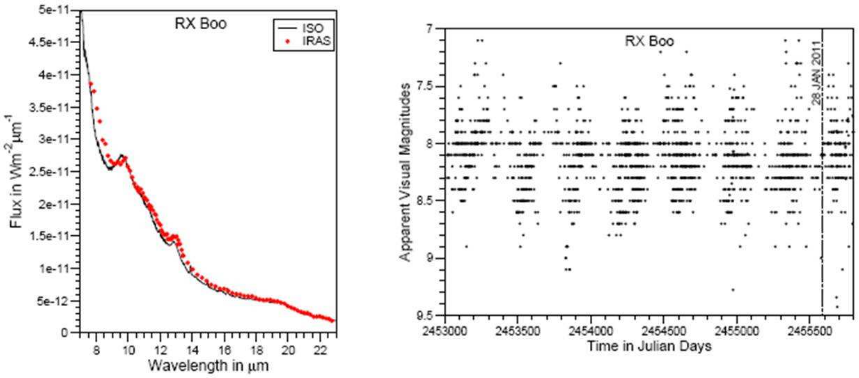

Figure 6.9: Left: IRAS LRS and ISO SWS (TDT # 08201905) observational data of RX Boo, Right: Light curve of RX Boo for last seven years.The Gemini observation date is indicated by dashed straight line.

6.4 Observation

Using the MICHELLE mid-infrared imager/spectrometer attached to the Gemini Observatory's 8.1 m northern telescope at Mauna Kea, Hawaii, we successfully acquired spatially resolved spectra for seven O-rich AGB stars (program ID GN-2010B-C-3).

6.4.1 Long slit spectroscopy

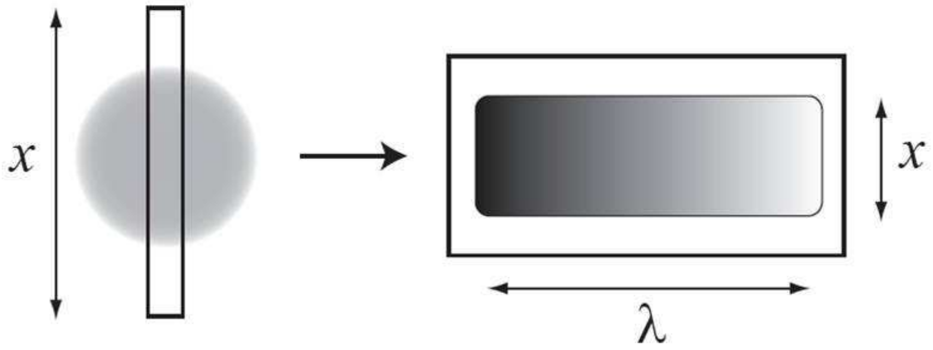

Figure 6.10: A schematic diagram illustrating the technique of long slit spectroscopy. Left: the entrance slit to the spectrometer is placed over the extended source. Right: the resulting spectra on the observing device containing both spatial and spectral information. For an extended source, a long slit spectral image contain several spectra, each correspond to a different part of the source along the slit.

Our observations were acquired using the long slit spectroscopy method, with the MICHELLE spectrometer to resolve the dust shell spatially. It is a technique used to obtain both spatial and spectral information simultaneously (see Figure 6.10). This is not a conventional use of a spectrometer, but very powerful method to analyze the spectral dust features at different distances from the central star at a single epoch.

Each individual 1-D spectrum samples the dust shell at different positions along the slit, and we offset the slit perpendicular to its length to sample the full two-dimensional structure of the object as seen on the sky. The star was first acquired by peaking up the signal on the slit, and then a series of spectra were taken at generally 10 offset positions with respect to the initial peak-up position (which is assumed to be centered on the star). A slit width of $0.36''$ was used for the observations, and the slit offsets were at intervals of $0.3''$ so there is a small amount of overlap between adjacent slit spectra. Figure 6.11 is a schematic representation of how the dust shell has been spatially resolved around the central star (only offset positions 3, 5, and 7 are shown in Figure 6.11).

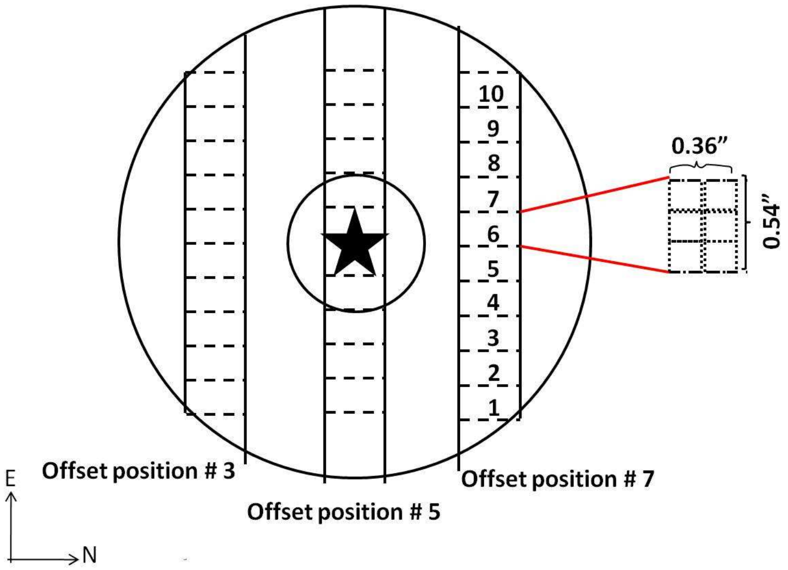

Figure 6.11: A schematic presentation of how the dust shells are spatially resolved. Three different offset positions (3, 5, 7) of the slit are demonstrated; along with how the slit has been sliced. The slit is oriented east-west on the sky for all the observations so the long axis of the sampled region is along the right ascension direction and the offsets are in the declination direction.

At each slit position the spectrum has been extracted in 10 slices along the slit centered on the peak position which is assumed to be the position of the star even for slit positions significantly offset from the star itself. The actual physical size of an individual slice is illustrated in Figure 6.11. Thus we have a set of 100 spectra for all the targets at a 10×10 grid of positions (see Figure 6.12). The total set of spectra samples a roughly $3.6'' \times 5.4''$ region of the sky. The slit is oriented east-west on the sky for all the observations so the long axis of the sampled region is along the right ascension direction and the offsets are in the declination direction. For one of the target (R Aur), we only acquired 6×10 grid of positions because of the limitation of observation time.

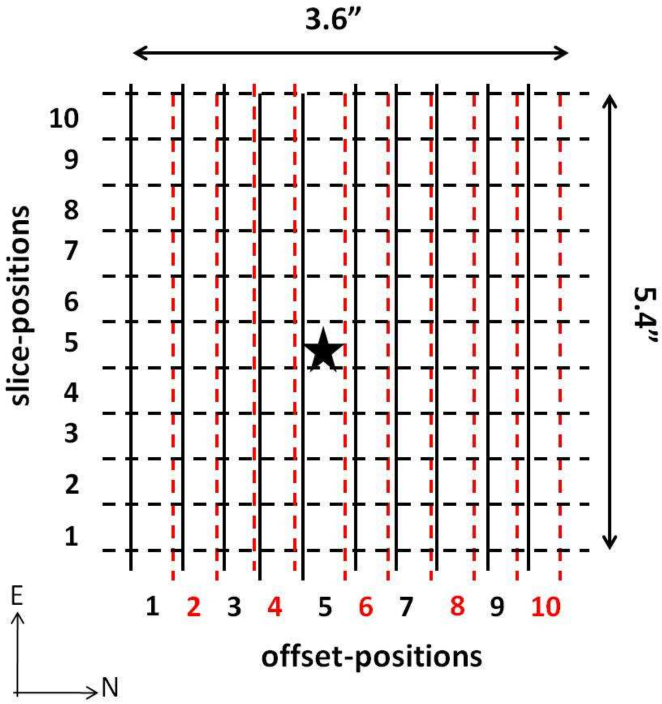

Figure 6.12: A schematic presentation of 10×10 grid of positions, also shown that there is a small amount of overlap between adjacent slits. The total set of spectra samples a roughly 3.6″×5.4″ region of the sky.

6.5 Data reduction process

The data reduction was done in the standard manner using the Gemini Image Reduction and Analysis Facility *IRAF* package[4]. For imaging the raw frames were stacked and the images were calibrated using the observation of the photometric standard star to convert from ADU to Jansky or from ADU to Jansky per square arc-second as appropriate. The expected fluxes of the standard star were taken from Cohen et al. (1999) [24]. For spectroscopy the telluric correction and absolute calibration were carried out by taking the ratio of the object spectrum to the standard star spectrum, with a small wavelength shift and scaling for airmass as required to remove the atmospheric bands, and then multiplying through by the expected spectrum of the standard star, again taken from the spectrophotometric templates of Cohen et al.

---

[4] http://iraf.noao.edu/

(1999) [24]. The slicing of the spectra was carried out using a custom *IRAF* script extension to the Gemini midir package. The best shifting and scaling for the overall extracted science spectrum was determined first and these values were generally applied to the individual spectral slices during a second reduction, since the spectral slices at larger radii from the star have a much lower signal and signal-to-noise ratio which makes the determination of the best telluric correction parameters difficult. Then, the 2-D spectrum was sliced (that is, the 2-D data was reduced to a series of 1-d spectra corresponding to positions in the shell). Ten slices were produced per slit position with a 30 pixel total spectral extraction region along the slit, so each slice samples a sky region [$0.36''$] across the slit and [$0.54''$] in height along the slit (see Figure 6.11).

6.6 Analysis

Having done the data reduction, now we have a set of 10×10 grid positions of spectra for 6 targets and for R Aur, we have 6×10 grid positions of spectra. These data require further analysis in order to understand how the spectral features change with location with respect to the central star, and which dust formation hypotheses can be supported. For each object we have an area covering $3.6''\times5.4''$ of the sky. Using the distance of the targets from Table 6.2, we can convert this angular extent to a physical size. Furthermore, using the expansion velocity (v_{exp}) from Table 6.2, we provide time scale associated with our observations. The physical size of the dust shell we mapped on the sky and the time scales for each individual target will be provided in § 6.7: Table 6.3. The analysis for all the targets are structured in the following order:

In order to understand how the spatial flux distributions change with distance from the central star, we measured the flux intensities at six wavelengths (8.2, 9.0, 10.0, 11.0, 12.0 13.0 μm). In order to maximize the signal to noise ratio, we took the average flux in a wavelength bin covering the range of 8.05–8.35, 8.85–9.15, 9.85–10.15, 10.85–11.15, 11.85–12.15 and 12.85–13.15 μm (each of which contains 11 points) respectively. The spatial flux intensity distributions are presented as 2-D maps (flux intensities as function of X [offset-positions] and Y [slice-positions]) for all the targets.

To extract detailed information about spectral changes, we have to determine the contribution to the continuum for each grid point. Since continuum depends on the grain properties as well as on the temperature distribution (as shown in Eq. 4.2), a 'real' continuum is very difficult to define. Observational constraints (i.e. the atmosphere) mean we have a severely restricted wavelength range (8–14 μm); much narrower than space-based observations. Thus we cannot apply the same method to determine the continuum as applied for T Cep (for reference see § 5.3). Instead we chose two pseudo-continuum points (at 8.2 and 12.0 μm), which will be used as proxy for the underlying continuum at all wavelength. We use two continuum points in order to minimize the effect of a known molecular absorption band $\approx 8.0\,\mu$m (SiO; Tsuji et al. 1997, Speck et al. 2000) [139, 131]. We then take the ratio of the flux intensities [$F_{cont.}(\lambda_1)/F_{cont.}(\lambda_2)$, where $\lambda_1 = 8.2$ and $\lambda_2 = 12.0\,\mu$m] as proxies for continuum and plotted as a 2-D map (an example for an object, SW Vir is shown in Figure 6.13: Left panel).

We can also map the dust continuum by fitting a power-law to the slope of the observed spectrum. Dust temperatures are expected to be ~1000 K (see § 3.2) such that the peak of the Planck curve are always shortward of our data in wavelength space, and thus on the Rayleigh-Jeans regime and the continuum can be approximated as a power-law ($F_\lambda \propto \lambda^{-5-\beta}$; where β is called emissivity). The modification by the emissivity law still yields a power law. Furthermore, in the case of distribution of temperatures the sum of the blackbodies will still give a power-law, but it will now be shallower compare to the Planck-curve alone. We fit a power-law continuum to the

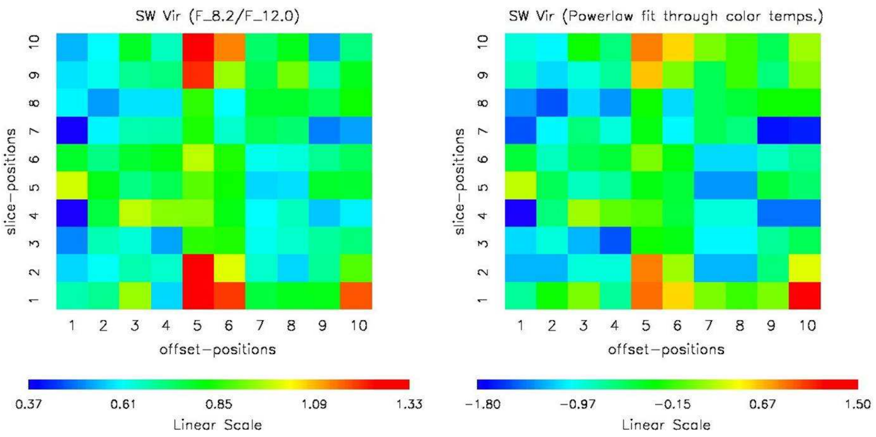

Figure 6.13: Left: 2-D map of the $F_{8.2}/F_{12.0}$, which is used as a proxy for the underlying dust temperature. Right: 2-D map of "β" by fitting power law continua through 8.2 and 12.0 μm.

observed spectra passing through both of the continuum points (at 8.2 and 12.0 μm) and determine the power for each of the hundred spectra. The spatial distribution of β are also plotted as a 2-D map in Figure 6.13: Right panel.

In order to test the validity of using 8.2 and 12.0 μm points as proxies for the continuum, we compare the $F_{8.2}/F_{12.0}$ with the best fit power law for a single object (SW Vir). We then determine the correlation coefficients between the $F_{8.2}/F_{12.0}$ and β. The correlation between the $F_{8.2}/F_{12.0}$ and β is strong ($R^2 = 0.913$, see Figure 6.14), which justifies the use of 8.2 and 12.0 μm continuum points as a proxies for the underlying dust continuum to the other 6 targets. While the two measures of the continuum are well correlated there is no discernable pattern to the spatial distribution of the continuum as seen in Figure 6.13.

Having determined a continuum level we follow an approach similar to that in § 5.4, to determine the temperature independent flux distribution at 9.0, 10.0, 11.0 and 13.0 μm. We calculated the relative flux intensities with respect to continuum points as $F_{peak}(\lambda_1)/F_{cont.}(\lambda_2)$ (where, $\lambda_1 = 9.0$, 10.0, 11.0, 13.0 μm and $\lambda_2 = 8.2\,\mu$m and 12.0 μm). These spatial distribution are plotted as 2-D maps.

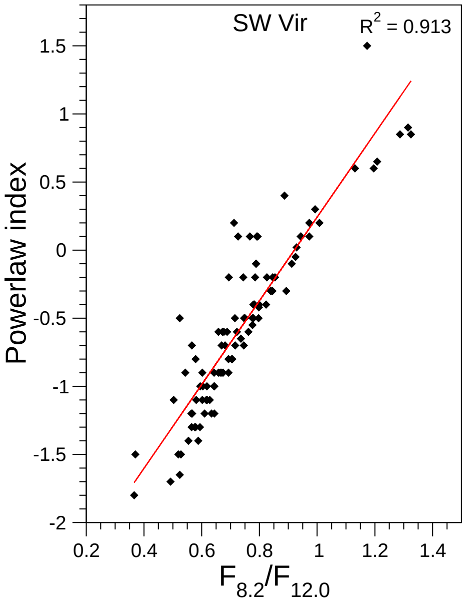

Figure 6.14: Strong correlation between the two measures of the continuum; $F_{8.2}/F_{12.0}$ and power-law.

Since different minerals contribute to the spectra at different wavelengths, we also want to see how much light is emitted at one wavelength relative to another. In this way, we can determine whether these spectral features (at 9.0, 10.0, 11.0, 13.0 μm) can be explained by only one dust component or whether there are mixture of different dust minerals responsible for these features. We calculated the flux intensity ratios as $F_{\lambda_1}/F_{\lambda_2}$ (when $\lambda_1 = 9.0\,\mu$m, then $\lambda_2 = 10.0, 11.0, 13.0\,\mu$m and so on). These spatial distributions of $F_{\lambda_1}/F_{\lambda_2}$ are also plotted as 2-D maps.

As shown in § 6.2 there is a continuous distribution of spectral feature shapes, ranging from the $\approx$ 9–12 μm "broad" feature to the classic 10 μm amorphous silicate feature. Within a single object the spatial changes in the overall shapes and positions of the observed spectral features are subtle, we have also measured the peak positions and Full Width Half Maxima (FWHM) of the "broad" features ($\approx$ 9–12 μm) by the best fitting Gaussian profile for each of the hundred spectra for each target. We determine the spectral feature parameters (i.e peak position, FWHM) by using the NOAO "onedspec" package in IRAF. The spatial distribution of the peak

Table 6.3: A summary of results of all seven targets.

Target	Physical size of 1 grid (A.U.)	Time scale along 1 grid (years)	Observed pattern	Best fitted dust formation hypotheses
	(N-S)×(E-W)	(N-S)×(E-W)		
R Aur	148×223	70×105	unusual	none
R Leo	39×59	22×33	axisymmetric	none
RT Vir	50×74	25×38	axisymmetric	(ii) & (iii)
SW Vir	51×77	27×41	axisymmetric	(ii) & (iii)
R Hya	222×333	131×197	bow-shock	(ii) & (iii)
W Hya	41×62	24×36	two dust shells	(i), (ii) & (iii)
RX Boo	56×84	26×39	asymmetry	none

Note: 1 A.U. = 1.49×10^{11}m.

positions and FWHM are plotted as 2-D maps. To capitalize on the observed and hypothetical correlation between the peak positions and FWHM described in § 6.2 and illustrated in Figure 6.1, we also determined the correlation coefficients between these parameters.

6.7 Results

We discuss the results of our analysis by object. A summary of the results appears in Table 6.3, where the physical size and time scale associated with the pixels are calculated using the distance and expansion velocity (taken from Table 6.2).

6.7.1 R Aur

The O-rich Mira variable R Aur, has been classified as infrared spectral class of SE2 by Sloan & Price (1995, 1998) [127, 128], and as "broad" AGB by Speck et al. (2000) [131]. The calculated physical scales and time scales of R Aur are given in Table 6.3.

Figure 6.16 shows 6×10 grid of the spatially resolved spectra of R Aur. This figure shows weird dust features at grid positions (3,5), (3,6); and (4,5), (4,6). Figure 6.17 shows the 2-D spatial distribution of the monochromatic flux intensities at 8.2, 9.0, 10.0, 11.0, 12.0 13.0 μm. Note that the central star is located at (2,6) coordinate position. In all six cases the overall intensity drops off with distance from the central star, as expected. The 2-D map of the spatial distribution of $F_{8.2}/F_{12.0}$ continuum of R Aur is shown in Figure 6.18. And the 2-D monochromatic maps of spatial distributions of continuum-divided fluxes of R Aur are shown in Figure 6.19 and 6.20. These maps do not show any pattern suggesting that there are not any simple trends with specific spectral features. Finally, we show 2-D maps of the spatial distribution of flux ratios of R Aur to determine how the fluxes at 9.0, 10.0, 11.0 and 13.0 μm vary with respect to one another. These maps are shown in Figure 6.21. These maps show that close to the central star, the amount of light emitted at 9.0 μm is less compare to 10.0 and 11.0 μm along the vertical direction (E-W). And further away from the central star, the light emitted at 10 and 11 μm are week compared to 13.0 μm along the vertical direction.

As can clearly be seen in grid positions (3,5), (3,6); and (4,5), (4,6) this object displays some unusual spectral features. Consequently, framing the analysis in terms of correlation between peak position and FWHM does not make sense. Furthermore, the noisy and apparently featureless spectra in outer slices do not led themselves to the Gaussian fitting. Consequently, we did not measure the spectral feature parameters for R Aur.

Our analysis of the continuum, continuum-divided monochromatic and flux ratios yielded no discernable patterns (see Figure 6.18 through Figure 6.21). The features vary significantly but without the spatial patterns expected from any of the dust formation mechanisms as discussed in § 6.2. This suggests the dust formation may be more turbulent as suggested by the model (Woitke 2006) [154].

Furthermore, while this is the highest resolution spatial observation of dust around this object to date, a single pixel represents 70–105 yrs of mass loss, and thus contains contribution from 56 pulsations. This is shown schematically in Figure 6.15 which is a schematic presentation of how much finer structure could be present inside one

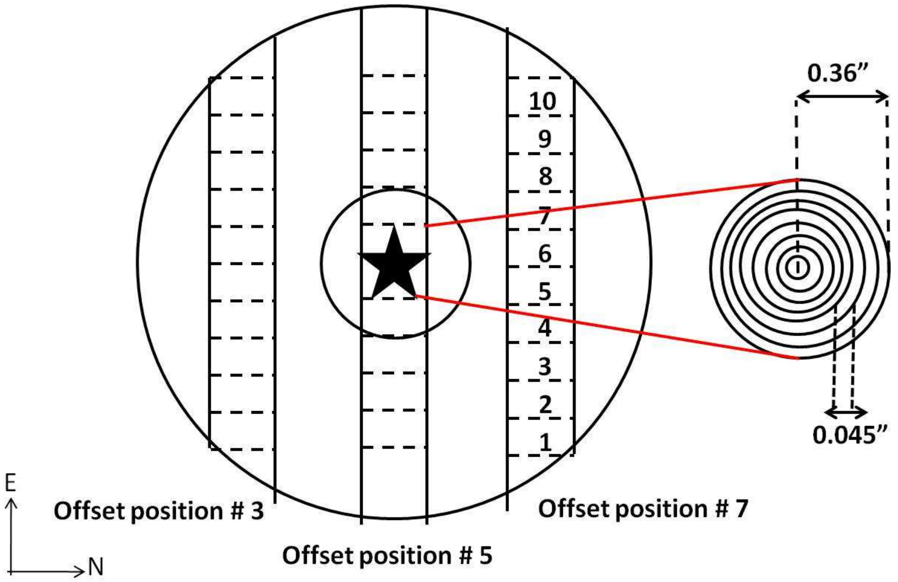

Figure 6.15: A schematic structure of dusts shells showing the finer structure could be present inside one slice. If that is the case, then it would be necessary to obtain spectra of much higher spatial/angular resolution.

slice/offset. This would tend to average out and lose any spatial dependence that the different dust components may have on the structure of the dust shell. Our spatial-resolution is much too low to see variations occurring on the timescale of pulsations (as discussed in § 6.2).

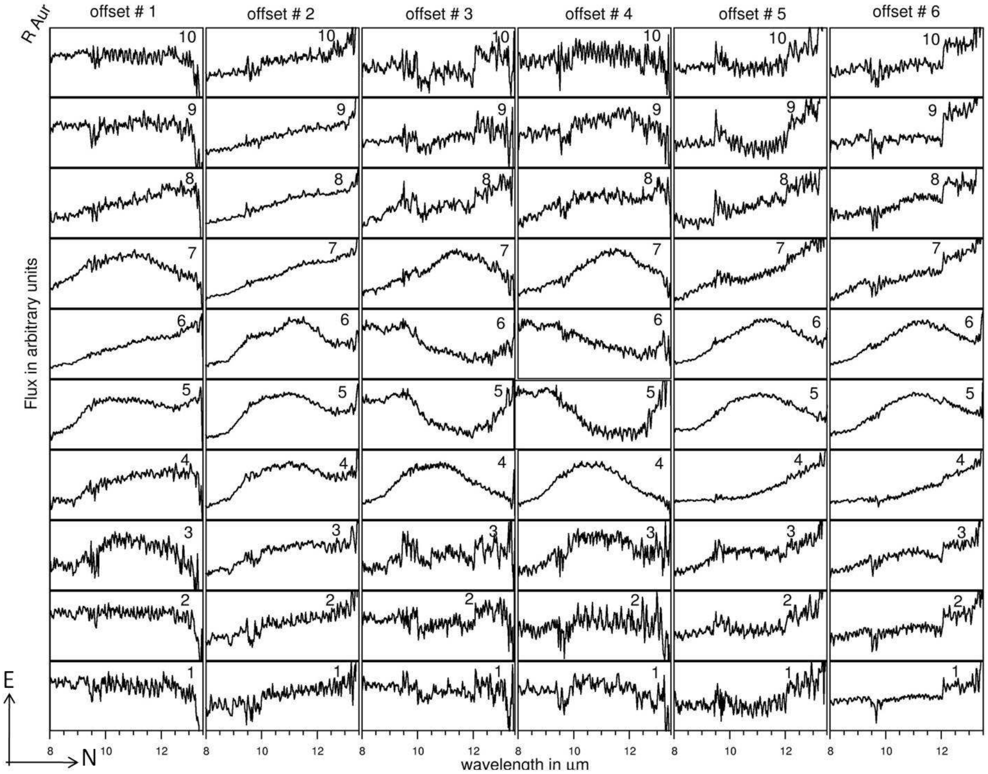

Figure 6.16: Spatially resolved dust spectra of R Aur (Note the telluric ozone may not be completely subtracted out and thus there is an artifact at $\sim 9.7\,\mu$m).

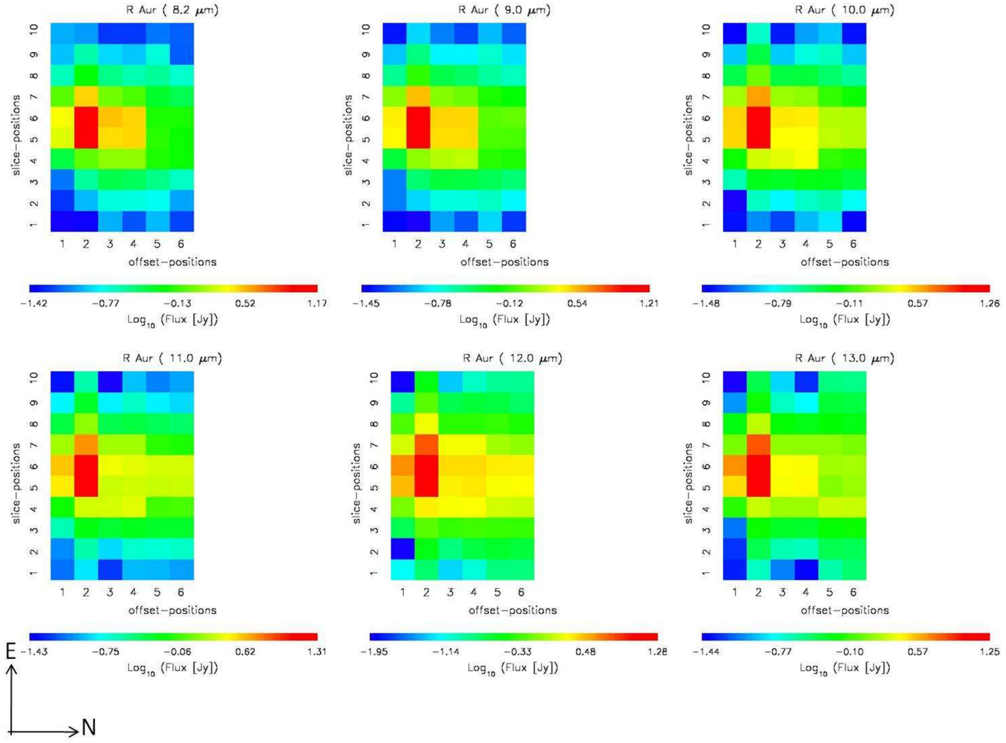

Figure 6.17: 2-D maps of the spatial distribution of the monochromatic flux intensities at 8.2, 9.0, 10.0, 11.0, 12.0 and 13.0 μm of R Aur. The flux intensities are plotted in logarithmic scale. Note the central star is located at (2,6) coordinate position.

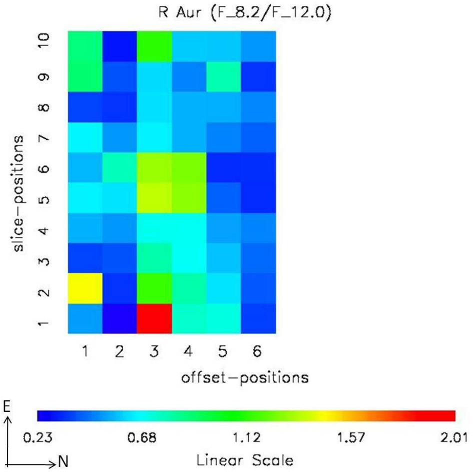

Figure 6.18: 2-D map of the $F_{8.2}/F_{12.0}$ which is used as a proxy for the underlying dust continuum of R Aur. The flux ratios are plotted in linear scale. Note that the central star is located at (2,6) coordinate position.

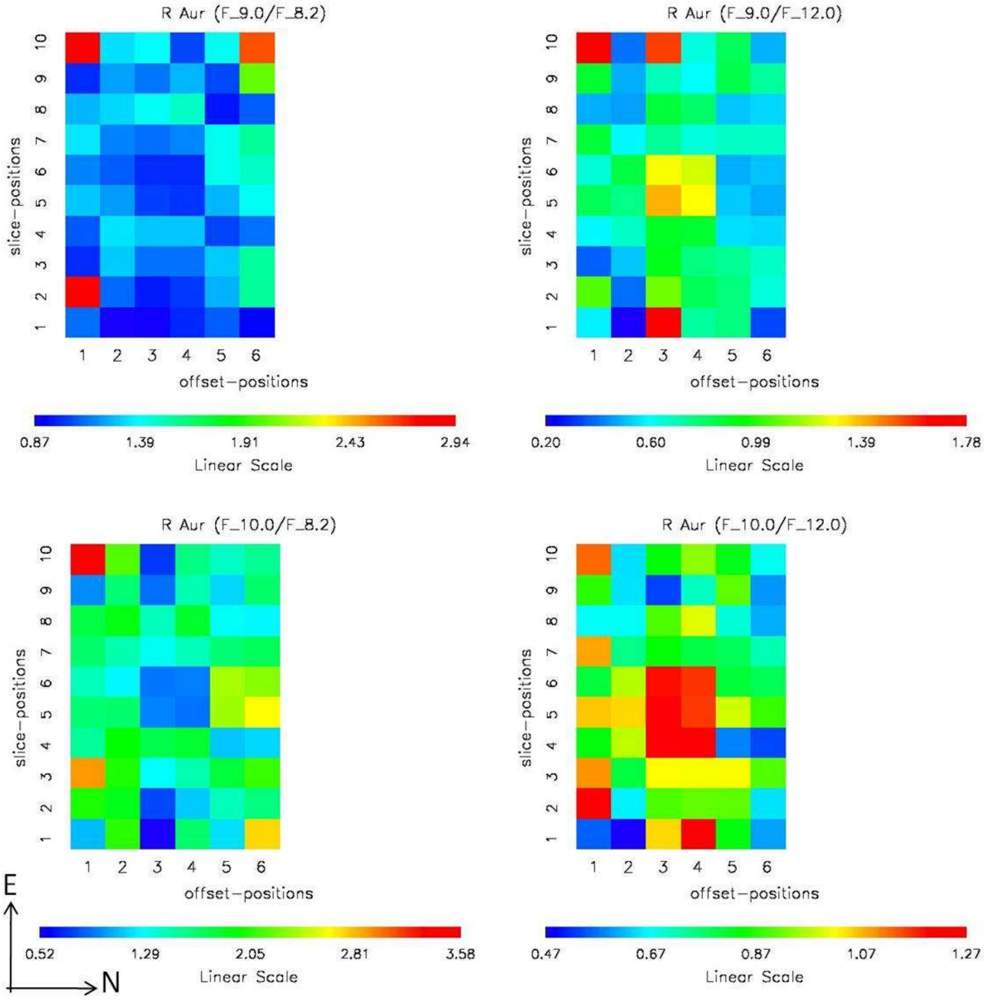

Figure 6.19: 2-D maps of the monochromatic continuum-divided observations at 9.0 and 10.0 μm for R Aur. The flux ratios are plotted in linear scale. Note that the central star is located at (2,6) coordinate position.

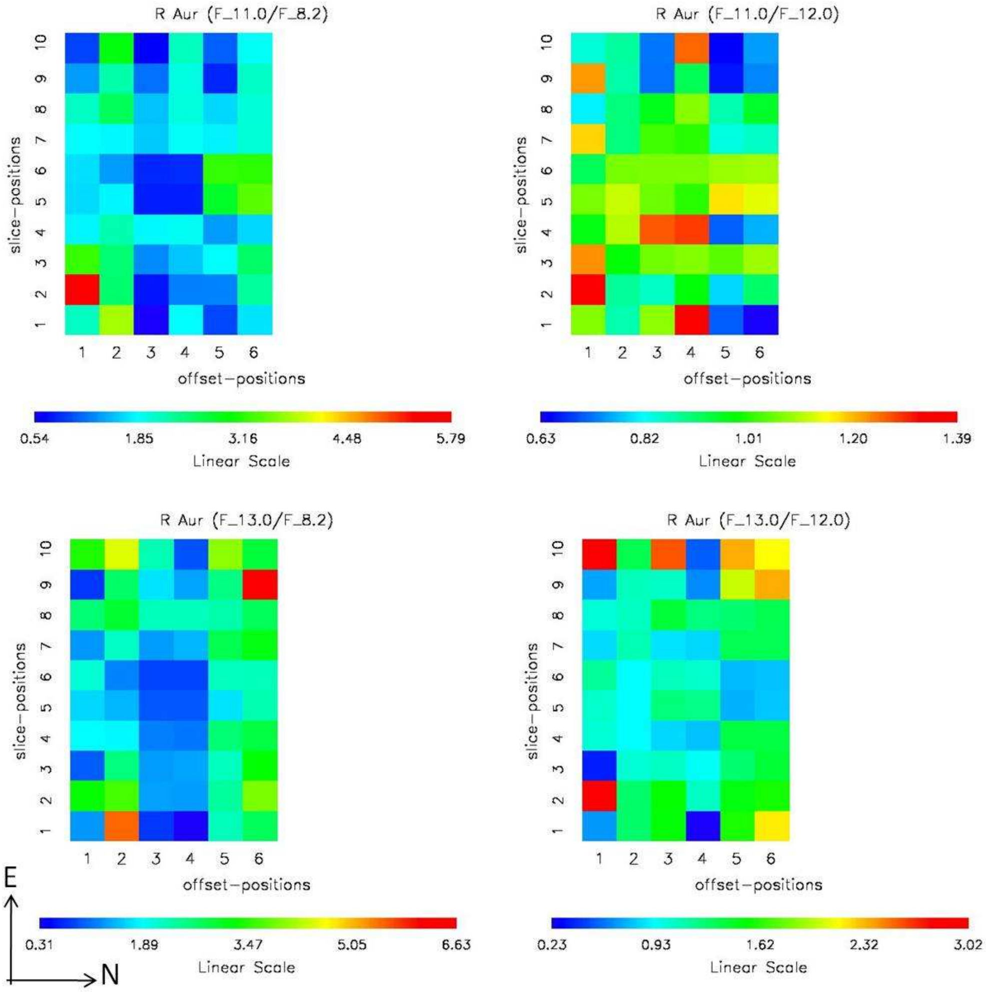

Figure 6.20: 2-D maps of the monochromatic continuum-divided observations at 11.0 and 13.0 μm for R Aur. The flux ratios are plotted in linear scale. Note that the central star is located at (2,6) coordinate position.

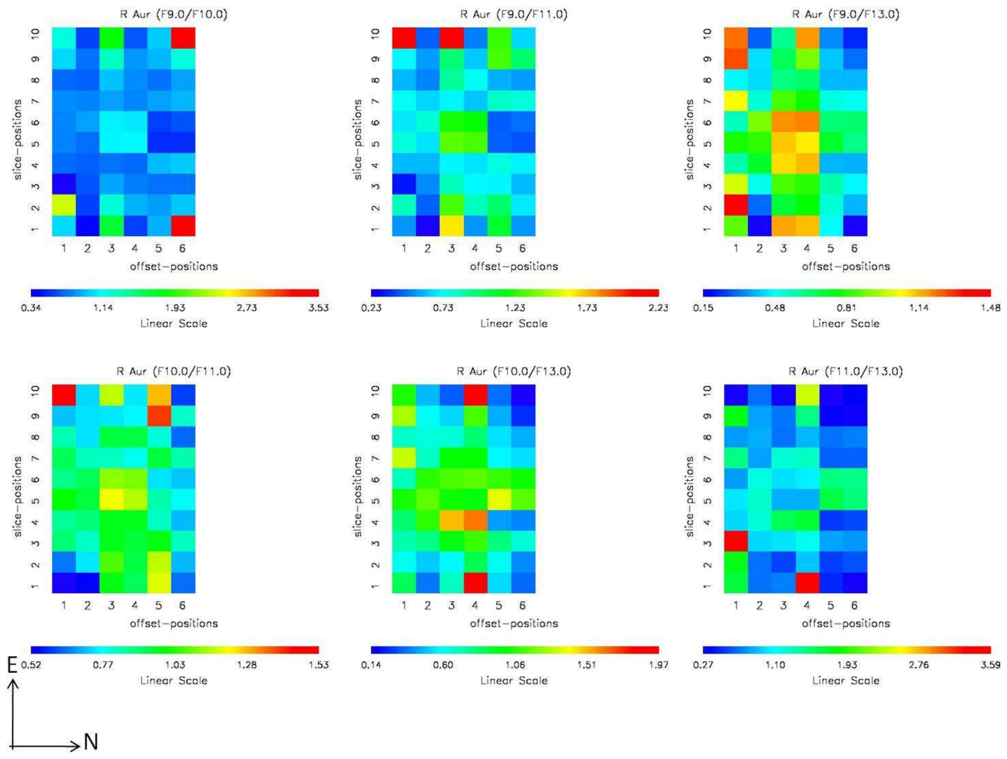

Figure 6.21: 2-D maps of the spatial distribution of the flux ratios at 9.0, 10.0, 11.0 and 13.0 μm with respect to each other of R Aur. The flux ratios are plotted in linear scale. Note that the central star is located at (2,6) coordinate position.

6.7.2 R Leo

The O-rich Mira variable R Leo was discovered by J. A. Koch in 1782. It has been classified as infrared spectral class of SE2 by Sloan & Price (1995, 1998) [127, 128], and as "broad" AGB by Speck et al. (2000) [131]. From previous observation of R Leo, SiO masers (at 43.1 and 42.8 Ghz) have been detected, showing evidence of asymmetric structure (Cotton et al. 2009) [27]. .

Figure 6.22 shows the 10×10 grid of the spatially-resolved spectra of R Leo, which appear to be distributed with an axisymmetric structure. Figure 6.23 shows the 2-D spatial distribution of the monochromatic flux intensities at 8.2, 9.0, 10.0, 11.0, 12.0 13.0 μm. Note that the central star is located at (5,5) coordinate position. In all six cases the overall intensity drops off with distance from the central star, as expected. The 2-D map of the spatial distribution of $F_{8.2}/F_{12.0}$ continuum of R Leo is shown in Figure 6.24 and does not show any trend, suggesting that the temperature distribution is not radially decreasing from the central star. The spatial distributions of continuum-divided fluxes of R Leo are shown in Figure 6.25 and 6.26. Again these maps do not show any pattern, suggesting that there are not any simple trends with specific spectral features. Finally, we show 2-D maps of the spatial distribution of flux ratios of R Leo to determine how the fluxes at 9.0, 10.0, 11.0 and 13.0 μm vary with respect to one another. These maps are shown in Figure 6.27.

As described in § 6.6, we also determine peak positions and FWHMa for best fitting Gaussian to the 9–12 μm broad feature. The spatial distribution of these parameters are shown in Figure 6.28: Top panel. There appears to be a somewhat axisymmetric pattern in the distribution of FWHM, in the offset direction, in slices 4 and 5; no such pattern is seen for the peak position. As discussed in § 6.2, both observations and dust formation hypotheses suggest these parameters should be correlated (see Figure 6.1). Consequently, we sought such correlations shown in Figure 6.28: Bottom panel. We dot not see a strong correlation between these parameters.

Our analysis has not found any discernable patterns in any of the 2-D maps except for the FWHM for the broad feature. As with R Aur the features vary significantly but without the spatial patterns expected from any of the dust formation mechanisms as discussed in § 6.2. This again suggests the dust formation may be more turbulent as suggested by the model (Woitke 2006) [154]. Again the spatial scale is large compared to the time scale for pulsation (see Table 6.3), which would tend to average out and lose any spatial dependence that the different dust components may have on the structure of the dust shell.

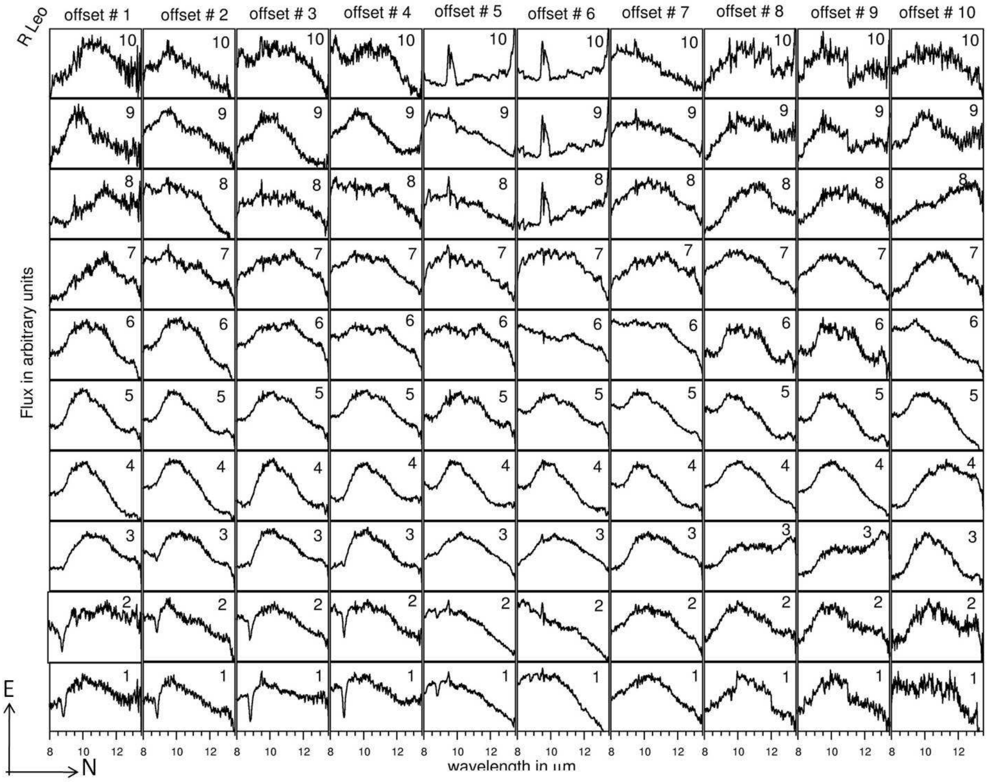

Figure 6.22: Spatially resolved IR spectra of R Leo (Note that the telluric ozone may not be completely subtracted out and thus there is an artifact at $\sim 9.7\,\mu$m).

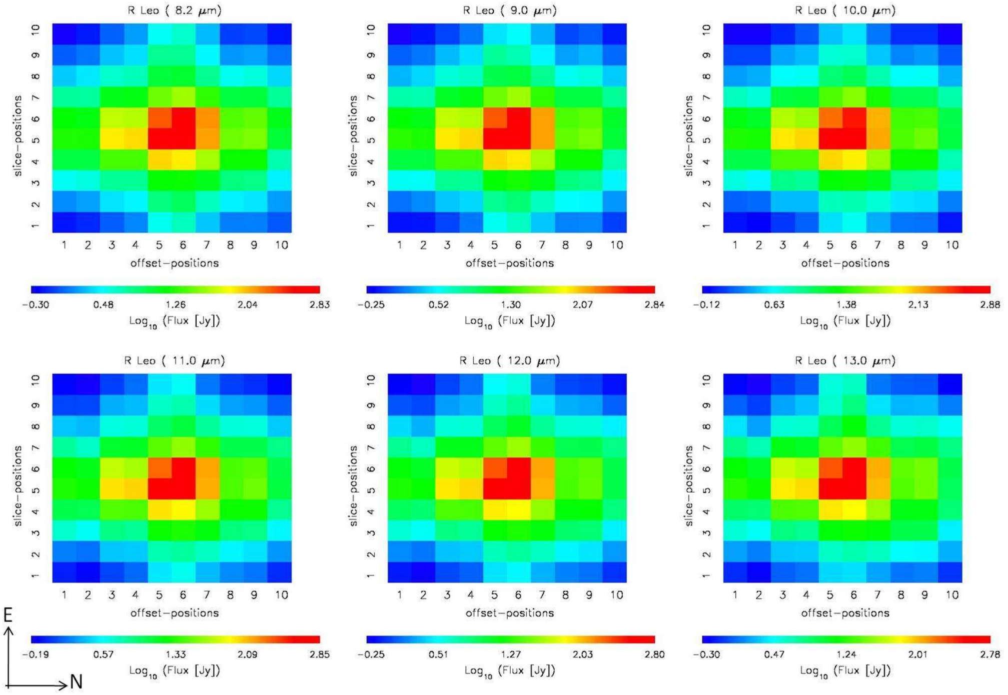

Figure 6.23: 2-D maps of the spatial distribution of the monochromatic flux intensities at 8.2, 9.0, 10.0, 11.0, 12.0 and 13.0 μm of R Leo. The flux intensities are plotted in logarithmic scale. Note that the central star is located at (5,5) coordinate position.

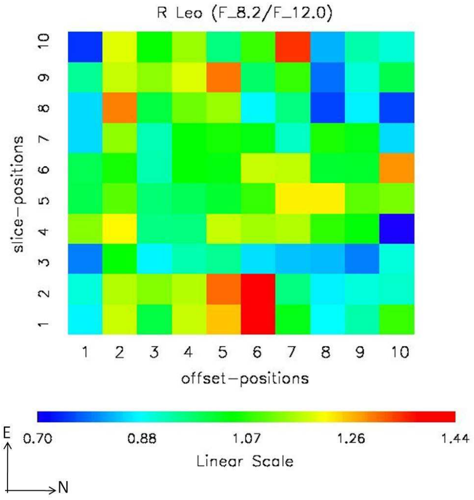

Figure 6.24: 2-D map of the $F_{8.2}/F_{12.0}$ which is used as a proxy for the underlying dust continuum of R Leo. The flux ratios are plotted in linear scale. Note that the central star is located at (5,5) coordinate position.

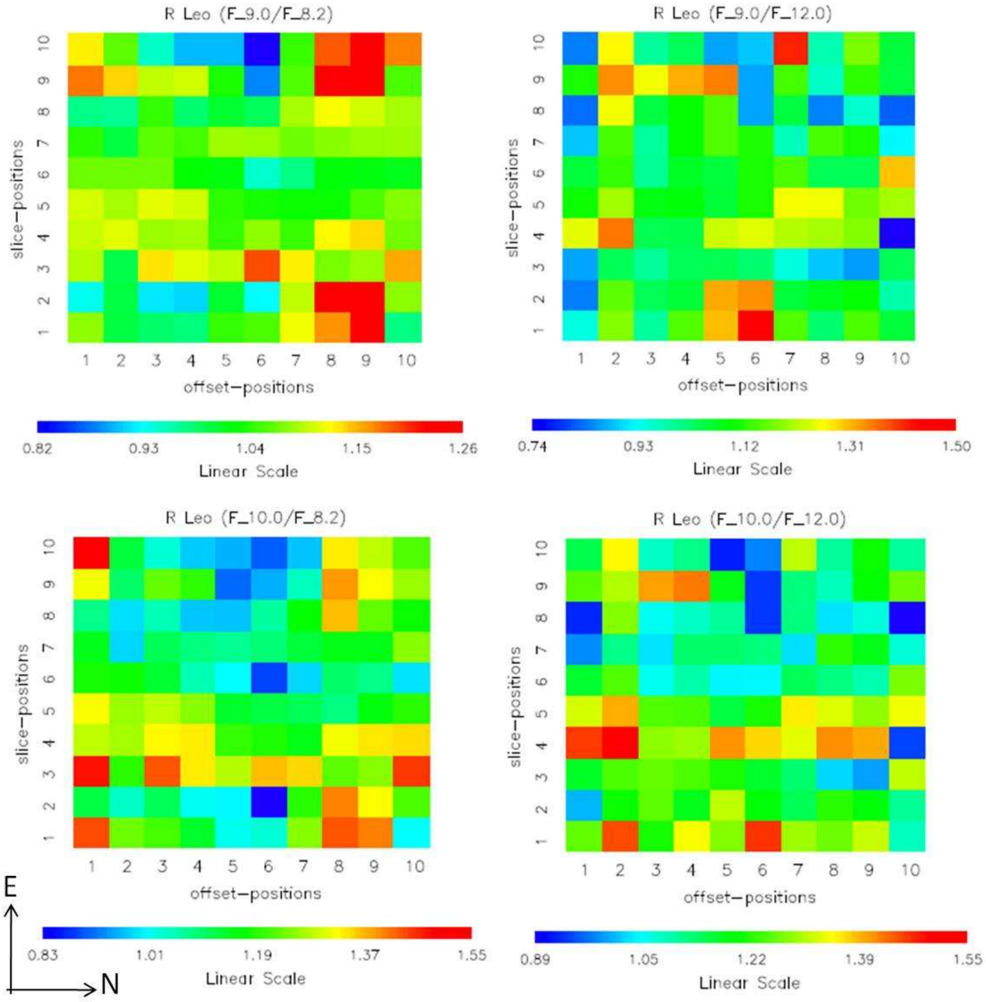

Figure 6.25: 2-D maps of the monochromatic continuum-divided observations at 9.0 and 10.0 μm for R Leo. The flux ratios are plotted in linear scale. Note that the central star is located at (5,5) coordinate position.

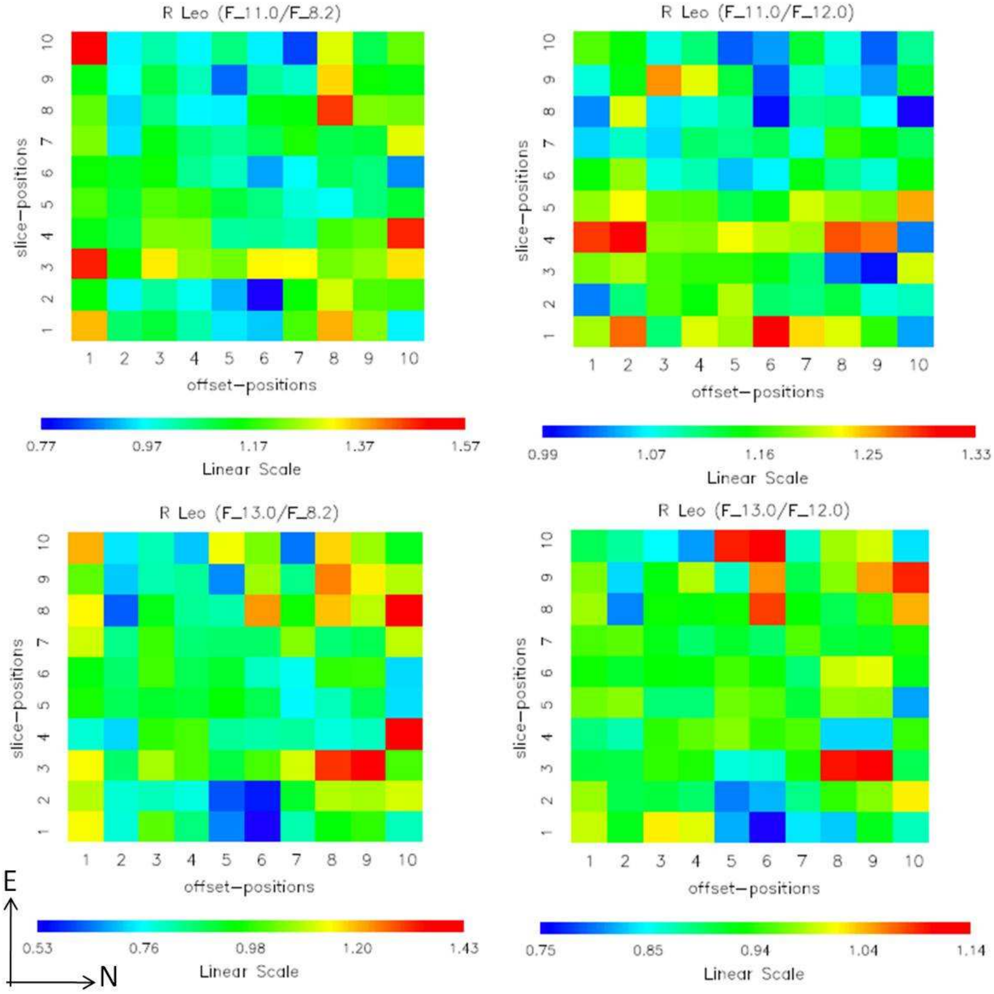

Figure 6.26: 2-D maps of the monochromatic continuum-divided observations at 11.0 and 13.0 μm for R Leo. The flux ratios are plotted in linear scale. Note that the central star is located at (5,5) coordinate position.

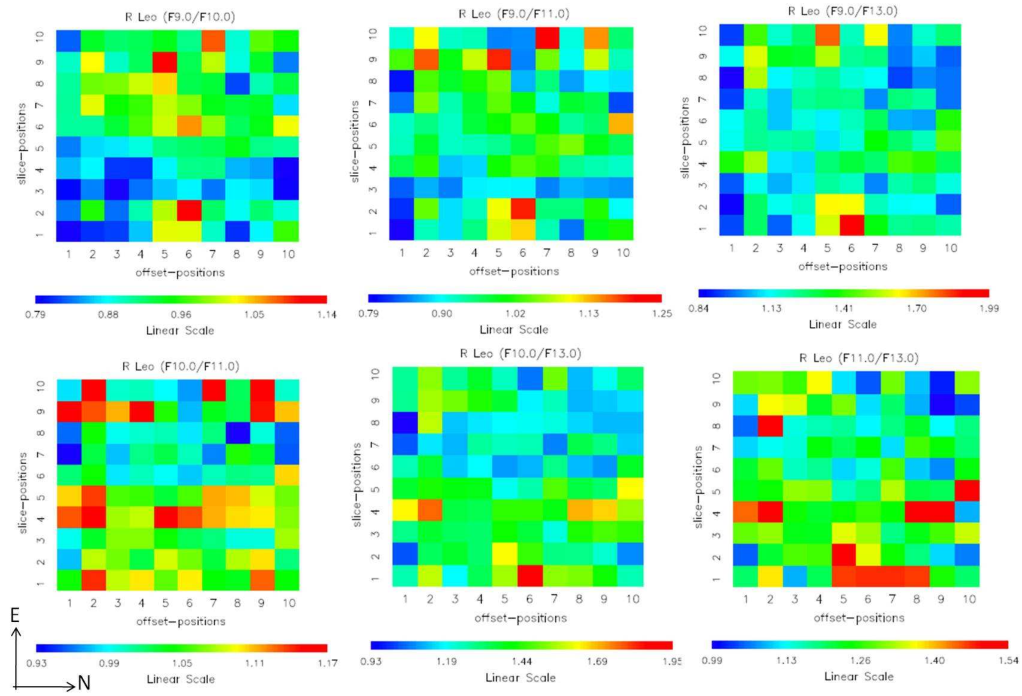

Figure 6.27: 2-D maps of the spatial distribution of the flux ratios at 9.0, 10.0, 11.0 and 13.0 μm with respect to each other of R Leo. The flux ratios are plotted in linear scale. Note that the central star is located at (5,5) coordinate position.

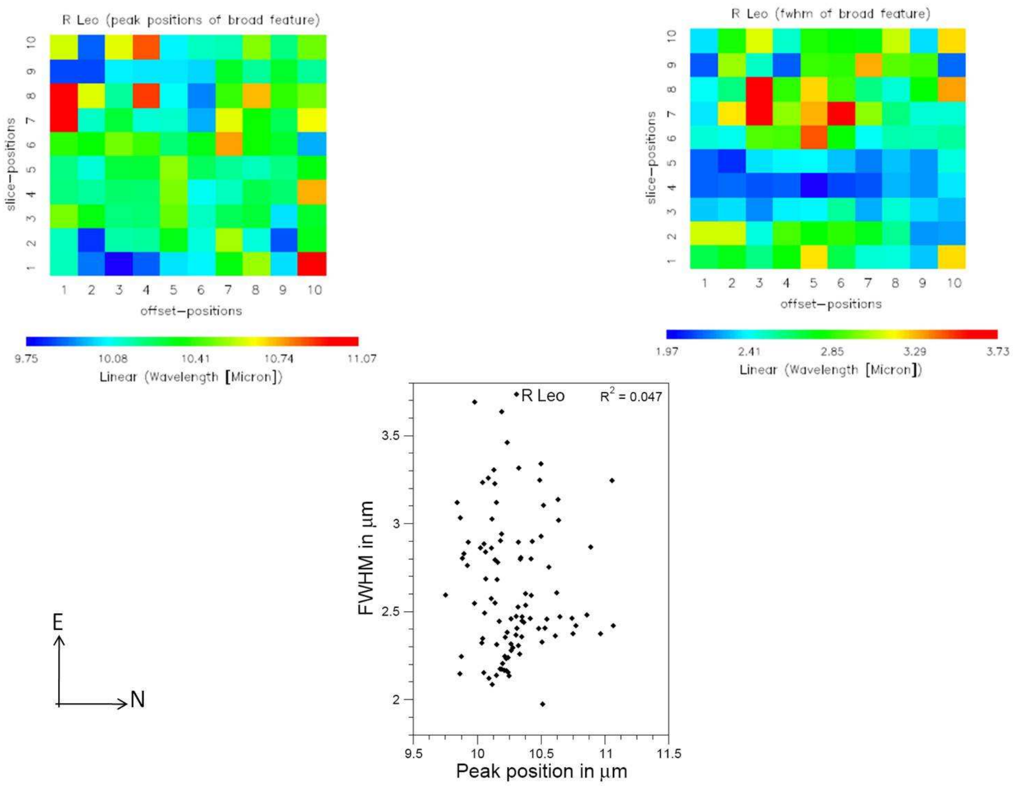

Figure 6.28: Top: 2-D maps of peak position (left) and FWHM (right) of the broad feature of R Leo. Bottom: Correlation between the peak positions and FWHM of the broad features of R Leo.

6.7.3 RT Vir

The O-rich semiregular variable RT Vir, has been classified as infrared spectral class of SE3 by Sloan & Price (1995, 1998) [127, 128]. Active OH (at 1612 MHz) and water (at 22 GHz) masers had been detected around RT Vir (Etoka et al. 2003, Yates et al. 2000) [36, 159]. The latter authors also suggested that RT Vir is a strong candidate for a bipolar or rotating outflow, based on the distribution of water vapor emission. They suspect that a dense cloud around RT Vir is accelerated by radiation pressure without impediment.

Figure 6.29 shows the 10×10 grid of the spatially-resolved spectra of RT Vir, which again appear to be somewhat axisymmetrically distributed. As with the previous objects, we have analyzed these spectra according to the description in § 6.6 to produced several 2-D maps showing how the emission varies across the spatial extent observed. These spatial analyses include monochromatic, continuum-divided, flux-ratio-ed and Gaussian-parameterized maps and are shown in Figures 6.30, 6.31, 6.32, 6.33, 6.34, and 6.35: Top Panels. Note that the central star is located at (6,5) coordinate position in all maps. We also sought correlations between the peak position and FWHM for the "broad" (9–12 μm), which is shown in Figure 6.35: Bottom panel. The only discernable pattern in any of the maps is an apparent N-S band of narrower 9–12 μm features at slices 4 and 5, however, this does not correlate with peak position, as might be expected from Figure 6.1. This could also be described as the 9–12 μm feature is broadening further away from the star along the vertical direction; the feature is narrower close to the central star and in a band along the horizontal direction. This spatial distribution pattern is subtle. One possible explanation is that there is a dense equatorial zone dominated by classic amorphous silicate emission; whereas away from this equatorial density enhancement, chaotic mixtures of oxides and silicates prevail due to lower densities in regions away from the star. This supports hypothesis ([ii] & [iii], as discussed in § 6.2) - i.e. chaotic grain nucleation occurs throughout the shell, but formation of silicate-dominated mantles only occurs where higher densities allow. If the change from narrow classic amorphous silicate feature to "broad" feature is actually due to crystallinity as suggested in Figure 6.2 we would expect to see patterns in the other maps, especially the continuum map, which essentially traces temperature, and there should be a pattern in $F_{10.0}/F_{11.0}$ and correlation between FWHM and peak position; none of these patterns are seen.

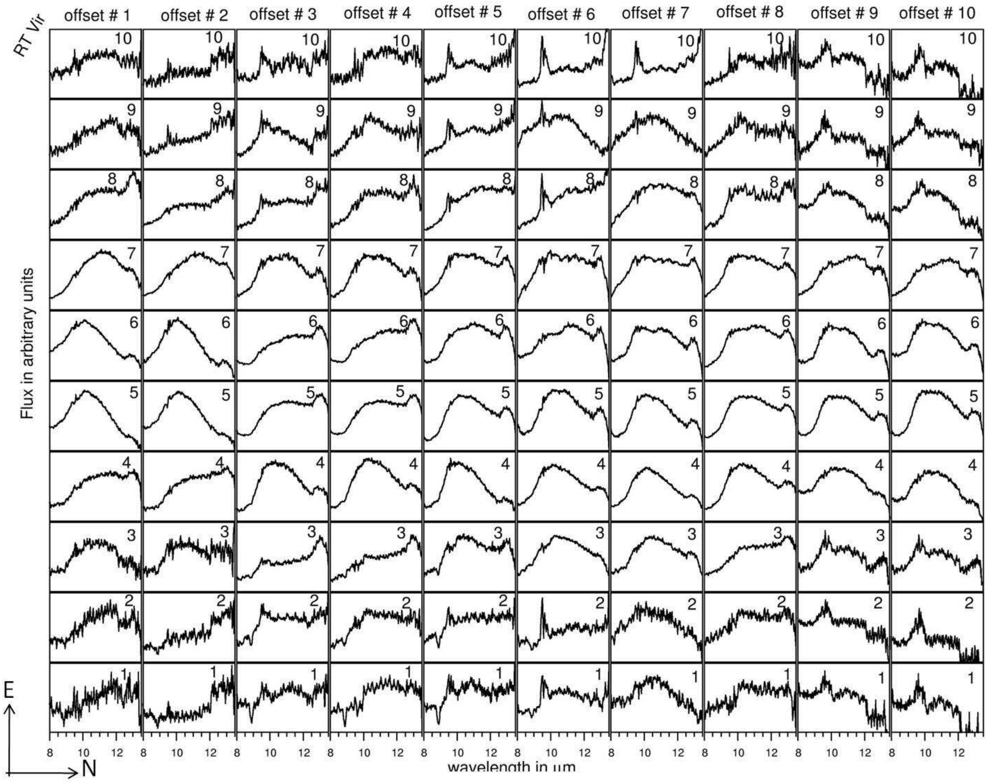

Figure 6.29: Spatially resolved dust spectra of RT Vir. (Note that the telluric ozone may not be completely subtracted out and thus there is an artifact at $\sim 9.7\,\mu$m).

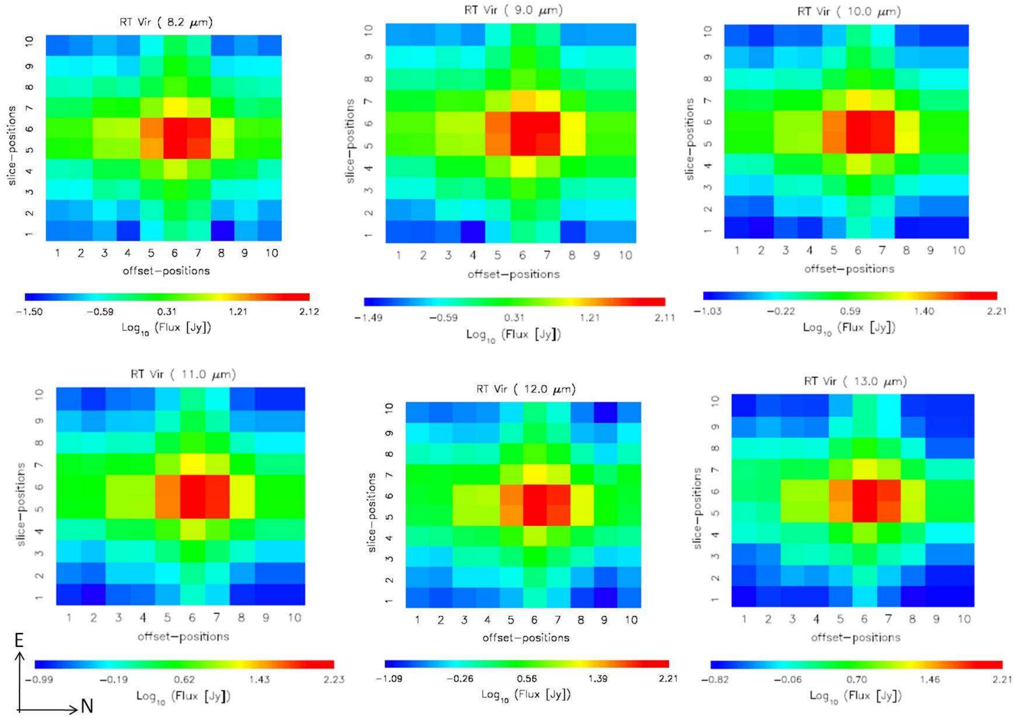

Figure 6.30: 2-D maps of the spatial distribution of the monochromatic flux intensities at 8.2, 9.0, 10.0, 11.0, 12.0 and 13.0 μm of RT Vir. The flux intensities are plotted in logarithmic scale. Note that the central star is located at (6,5) coordinate position.

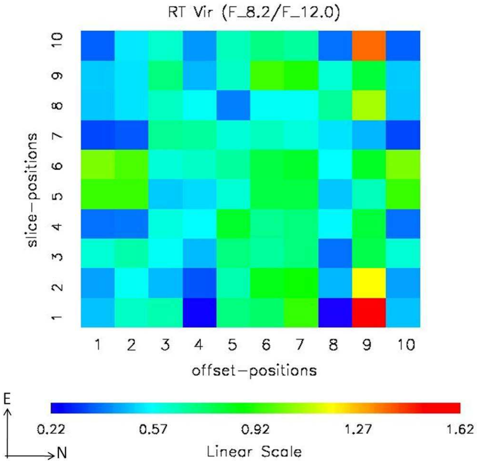

Figure 6.31: 2-D map of the $F_{8.2}/F_{12.0}$ which is used as a proxy for the underlying dust continuum of RT Vir. The flux ratios are plotted in linear scale. Note that the central star is located at (6,5) coordinate position.

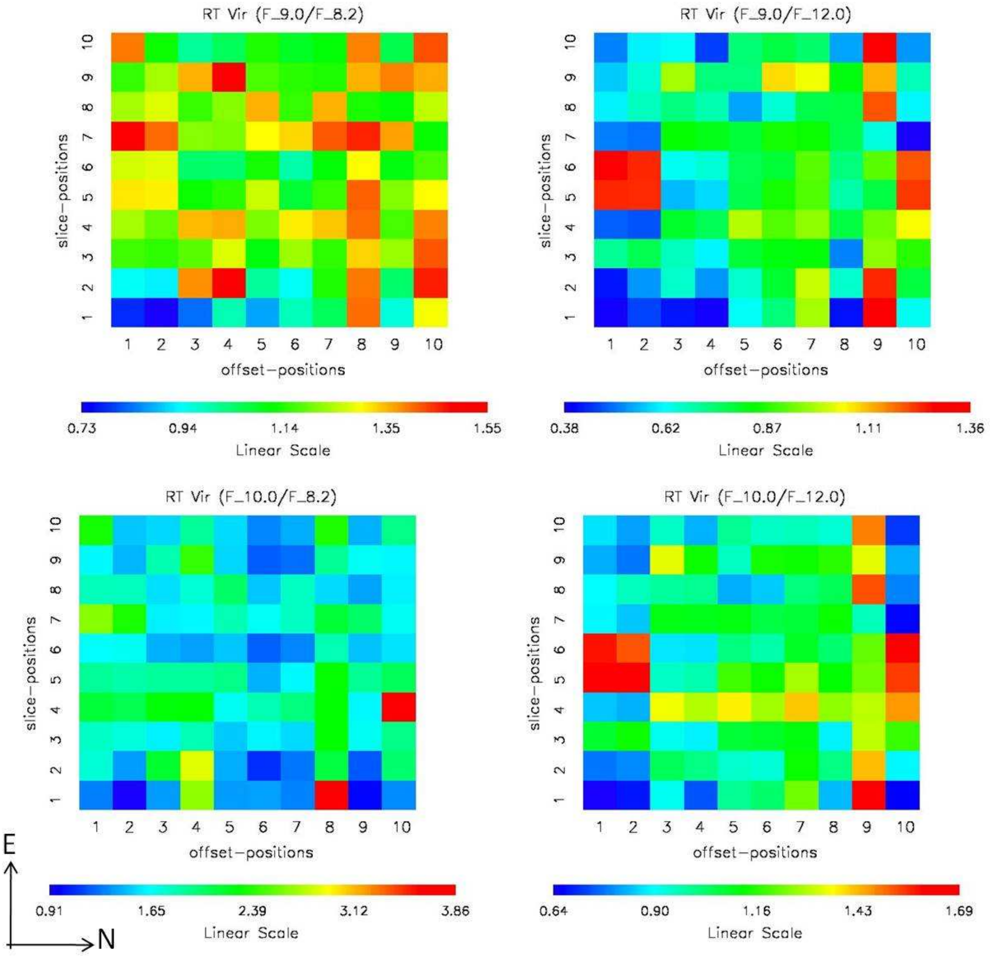

Figure 6.32: 2-D maps of the monochromatic continuum-divided observations at 9.0 and 10.0 μm for RT Vir. The flux ratios are plotted in linear scale. Note that the central star is located at (6,5) coordinate position.

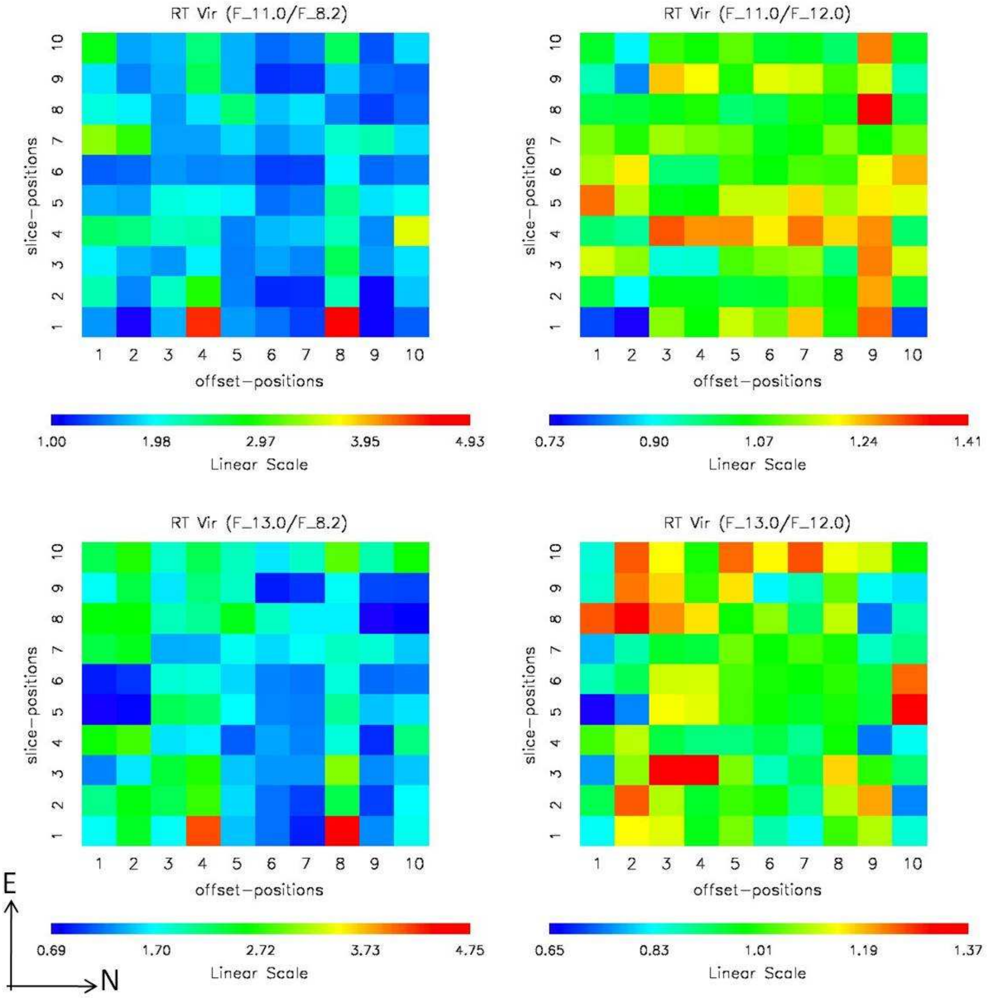

Figure 6.33: 2-D maps of the monochromatic continuum-divided observations at 11.0 and 13.0 μm for RT Vir. The flux ratios are plotted in linear scale. Note that the central star is located at (6,5) coordinate position.

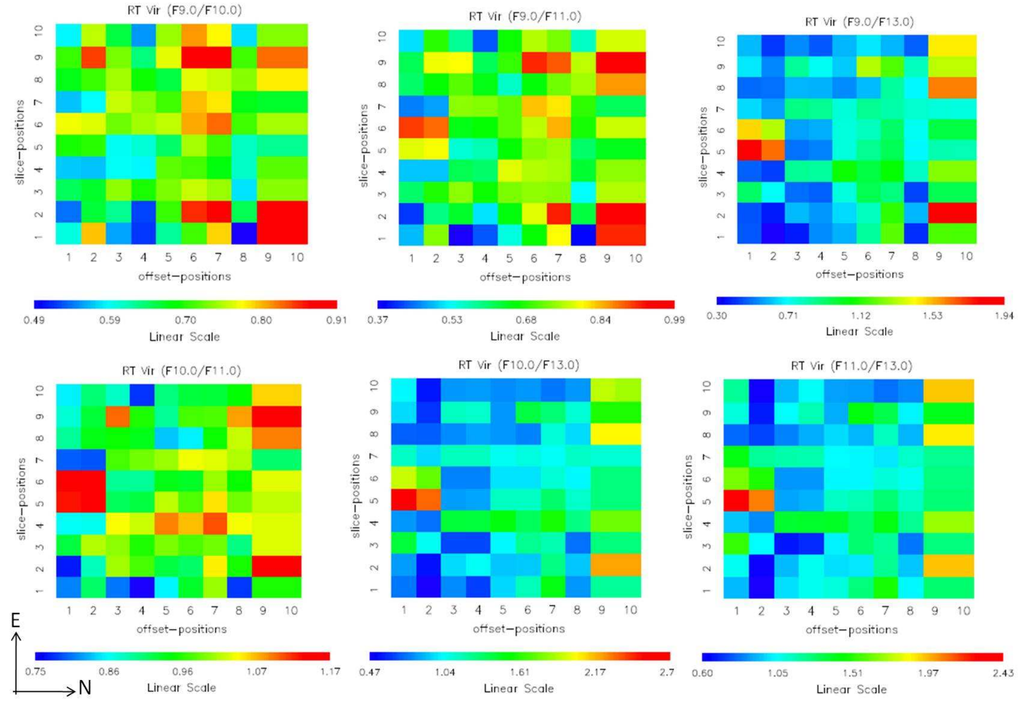
RT Vir (F9.0/F10.0)

RT Vir (F9.0/F11.0)

RT Vir (F9.0/F13.0)

RT Vir (F10.0/F11.0)

RT Vir (F10.0/F13.0)

RT Vir (F11.0/F13.0)

Figure 6.34: 2-D maps of the spatial distribution of the flux ratios at 9.0, 10.0, 11.0 and 13.0 μm with respect to each other of RT Vir. The flux ratios are plotted in linear scale. Note that the central star is located at (6,5) coordinate position.

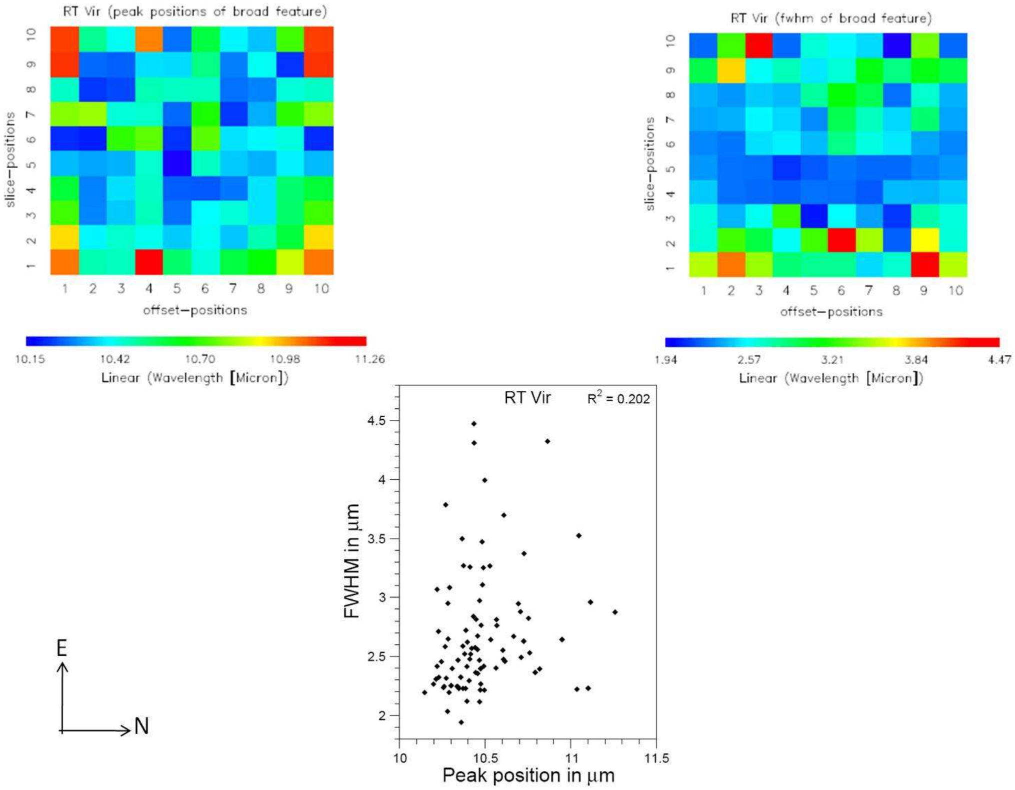

Figure 6.35: Top: 2-D maps of peak position (left) and FWHM (right) of the broad feature of RT Vir. Bottom: Correlation between the peak positions and FWHM of the broad features of RT Vir.

6.7.4 SW Vir

The O-rich semiregular variable SW Vir, has been classified as infrared spectral class of SE3 by Sloan & Price (1995, 1998) [127, 128]. SW Vir is also reported as a suspected binary with a significant radial velocity of 8.5 km/sec by Famaey et al. (2009) [39], while investigating radial velocity data for M-giants belonging to the HIPPARCOS survey.

As with the three previous objects, the data and analysis are represented in several 10×10 grids shown in Figures 6.36, 6.37, 6.38, 6.39, 6.40, 6.41, and 6.42: Top panel. In addition, the correlation between the Gaussian parameters for the 9–12 μm feature are shown in Figure 6.42: Bottom panel. While most of the 2-D maps do not show any discernable patterns, those for the Gaussian parameters show a subtle axisymmetric structure such that the 9–12 μm feature is apparently narrower and bluer in slices 4 through 6. The classic 10.0 μm feature is clear in this horizontal band in spatially-resolved spectra shown in Figure 6.36. These variations in broad feature parameters are consistent with having classic amorphous silicate dominate in a dense torus, and chaotic mixtures of oxides and silicates prevailing in the less-dense regions away from the torus similar to that as RT Vir. This supports hypothesis ([ii] & [iii], as discussed in § 6.2) in that chaotic silicate forms throughout the dust shell but classic silicate dominates in an equatorial density enhancement (Guha Niyogi et al. 2011-b) [50].

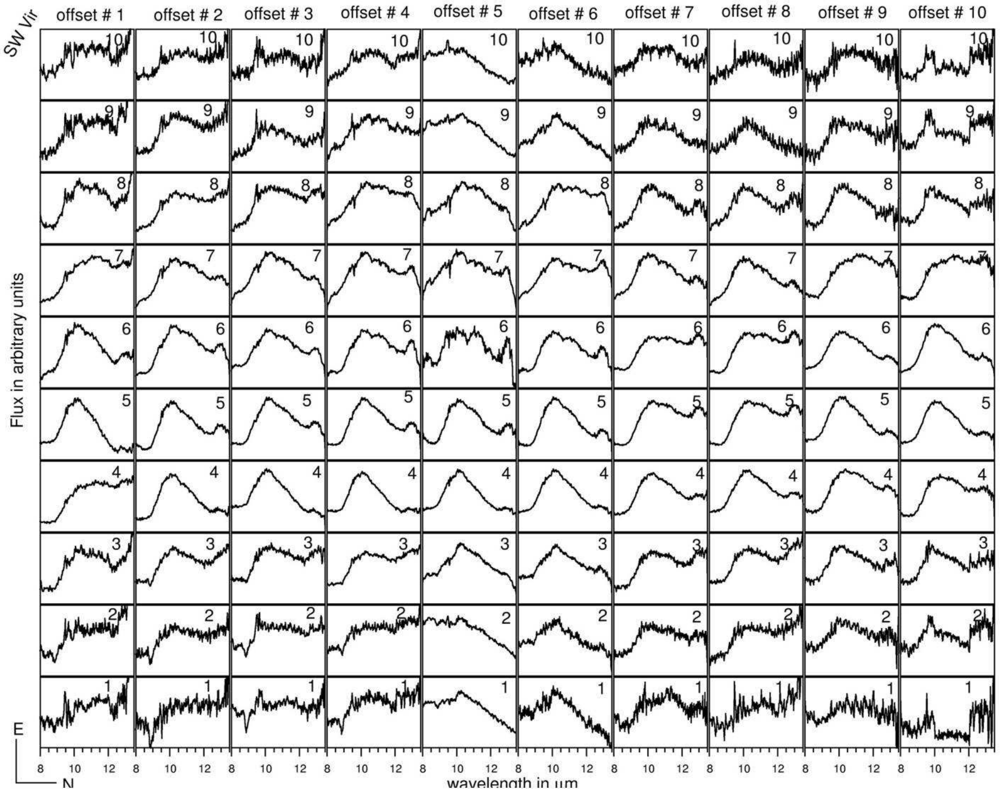

Figure 6.36: Spatially resolved dust spectra of SW Vir. (Note that the telluric ozone may not be completely subtracted out and thus there is an artifact at $\sim 9.7\,\mu$m).

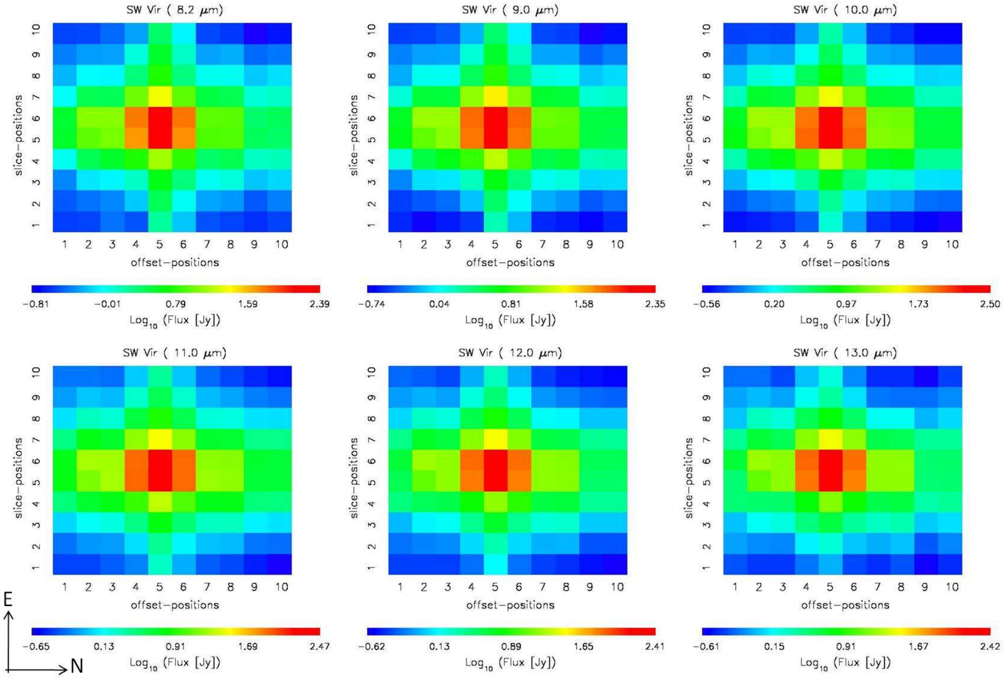

Figure 6.37: 2-D maps of the spatial distribution of the monochromatic flux intensities at 8.2, 9.0, 10.0, 11.0, 12.0 and 13.0 μm of SW Vir. The flux intensities are plotted in logarithmic scale. Note that the central star is located at (5,5) coordinate position.

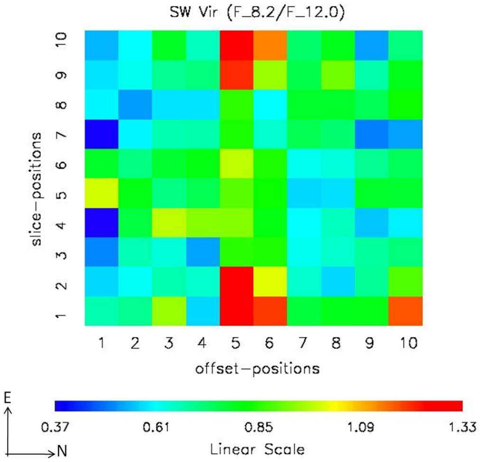

Figure 6.38: 2-D map of the $F_{8.2}/F_{12.0}$ which is used as a proxy for the underlying dust continuum of SW Vir. The flux ratios are plotted in linear scale. Note that the central star is located at (5,5) coordinate position.

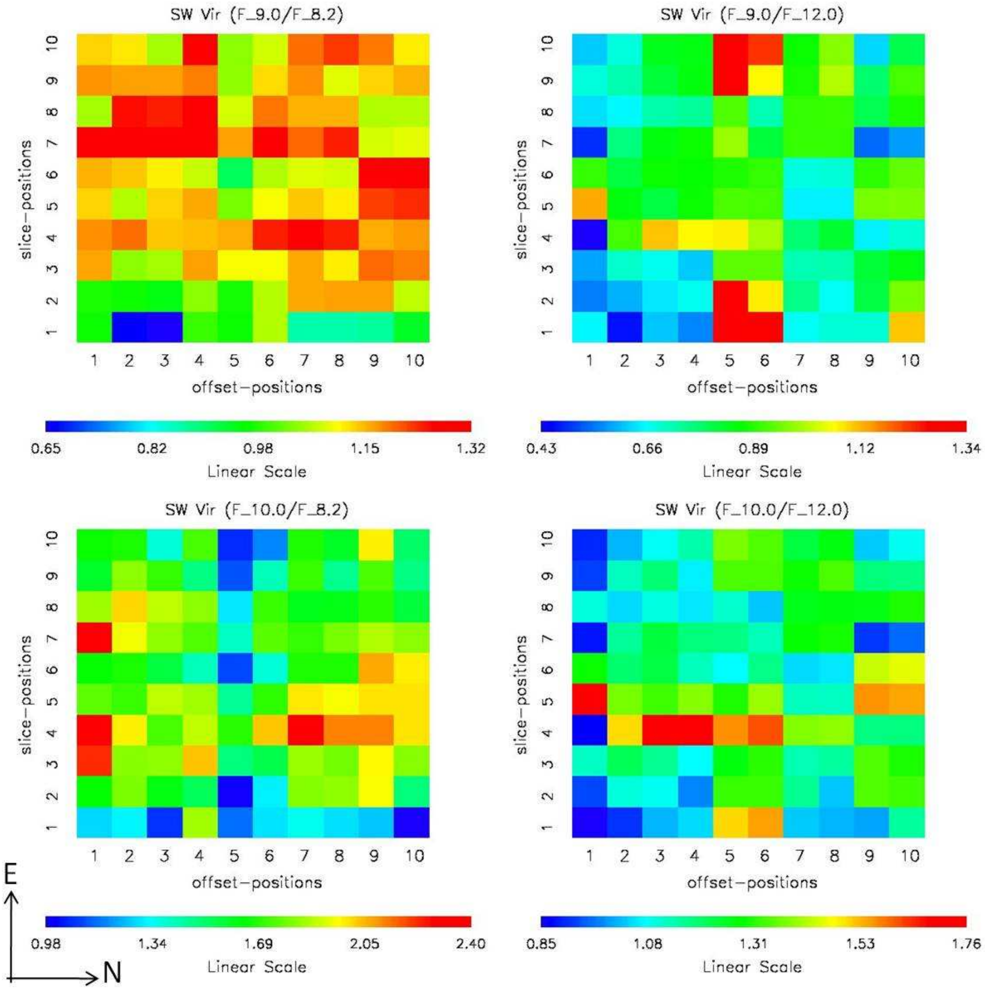

Figure 6.39: 2-D maps of the monochromatic continuum-divided observations at 9.0 and 10.0 μm for SW Vir. The flux ratios are plotted in linear scale. Note that the central star is located at (5,5) coordinate position.

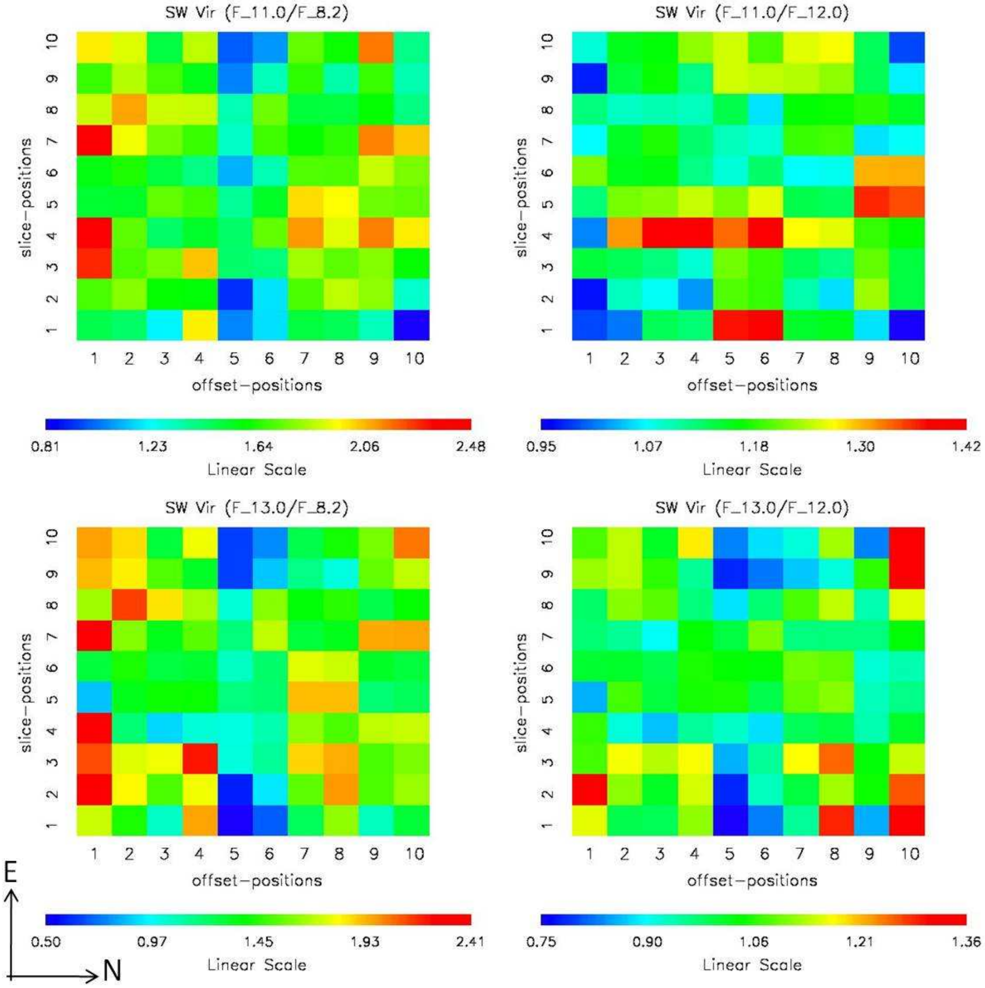

Figure 6.40: 2-D maps of the monochromatic continuum-divided observations at 11.0 and 13.0 μm for SW Vir. The flux ratios are plotted in linear scale. Note that the central star is located at (5,5) coordinate position.

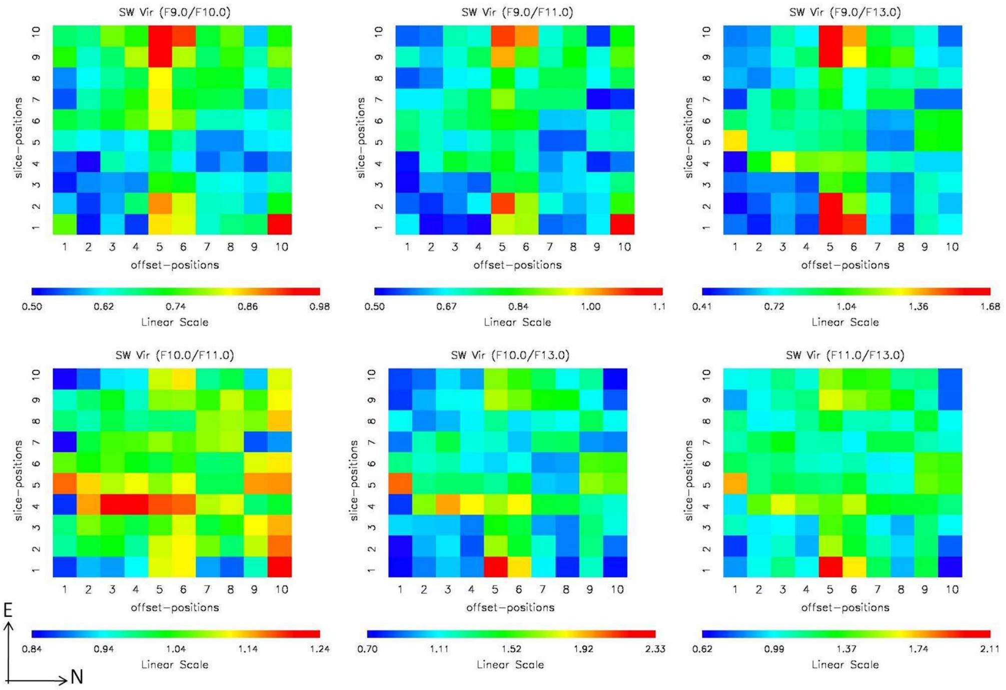

Figure 6.41: 2-D maps of the spatial distribution of the flux ratios at 9.0, 10.0, 11.0 and 13.0 μm with respect to each other of SW Vir. The flux ratios are plotted in linear scale. Note that the central star is located at (5,5) coordinate position.

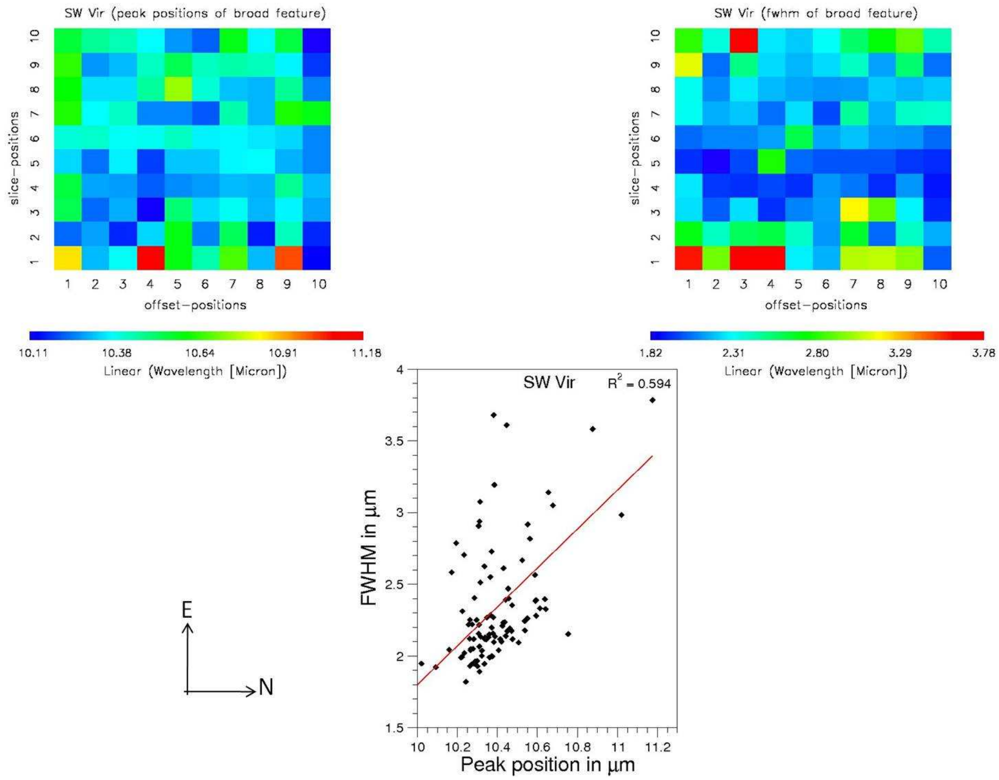

Figure 6.42: Top: 2-D maps of peak position (left) and FWHM (right) of the broad feature of SW Vir. Bottom: Correlation between the peak positions and FWHM of the broad features of SW Vir.

6.7.5 R Hya

The O-rich Mira variable R Hya was discovered by Giacomo Maraldi in 1704, has been classified as infrared spectral class of SE2 by Sloan & Price (1995, 1998) [127, 128], and "featureless" AGB by Speck et al. (2000) [131]. Furthermore, after the *ISO* SWS sky survey, the infrared spectral classification of R Hya had been modified to SE3 by Sloan et al. (2003) [123]. R Hya is known as an "unusual Mira variable" for its declining period between CE 1770 and 1950 (Zijlstra et al. 2002) [162], which has been attributed to a recent possible thermal pulse (Wood & Zarro 1981) [155]. Decin et al. 2008 [30] presented observational data that suggested that the present day mass-loss rate of R Hya is a factor of ≈ 20 lower compare to CE 1770. Moreover, the detection of an AGB-ISM "bow shock" around R Hya at $\approx 400\,''$ to the west by Ueta et al. (2006) [140] shows that the detached shell can be explained by a slowing-down of the stellar wind by surrounding matter.

Following the same structure as used previously in this chapter, the data and analysis are represented in several 10×10 grids shown in Figures 6.43, 6.44, 6.45, 6.46, 6.47, 6.48, and 6.49: Top panel. In addition, the correlation between the Gaussian parameters for the 9–12 μm feature are shown in Figure 6.49: Bottom panel. Note that the central star is located at (6,5) coordinate position. In all six cases the overall intensity drops off with distance from the central star.

Most of these maps show subtle trends in a SE–NW directions. This is especially apparent in the $F_{8.2}/F_{12.0}$ continuum map, where the continuum ratio tends to be low in the SE (top left) corner, and high in the NW (bottom right) corner. This same patterns occurs for $F_{9.0}/F_{12.0}$, $F_{10.0}/F_{8.2}$, $F_{11.0}/F_{8.2}$, $F_{13.0}/F_{8.2}$, $F_{9.0}/F_{10.0}$. Other maps do not show clear trend, but show subtle hints of the same structure. For the maps of the Gaussian parameters we do not see these trends at all, but rather we see the narrowest features closest to the central star, with a possible slight N-S (horizontal) extension. The FWHM may also show this same horizontal structure such that the feature is narrower in offsets 4 through 6. The SE–NW trend is consistent with a temperature effect such that the dust to the S-E is cooler than that in the N-W. It is possible that is structure is attributable to the bow-shock structure discussed above. However, the consistent pattern across all the monochromatic and flux-ratioed maps together with the very different distributions for the Gaussian parameters argue against a mineralogical change in the SE–NW direction. Rather, the Gaussian peak position variations suggest a more classic radial trend in the features with narrow classic silicates close to the central star and more chaotic mixtures of silicates and oxides further out. Again this is consistent with support the chaotic grain hypothesis (ii) together with mantle formation at high densities (iii), as discussed in § 6.2.

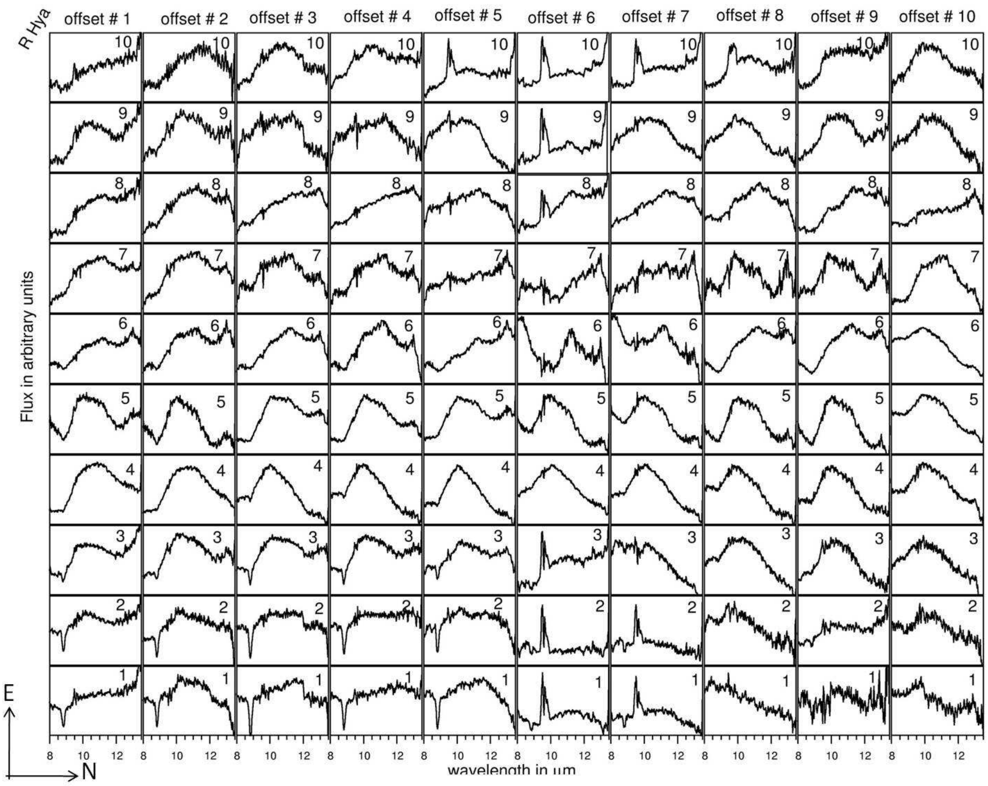

Figure 6.43: Spatially resolved dust spectra of R Hya. (Note that the telluric ozone may not be completely subtracted out and thus there is an artifact at $\sim 9.7\,\mu$m).

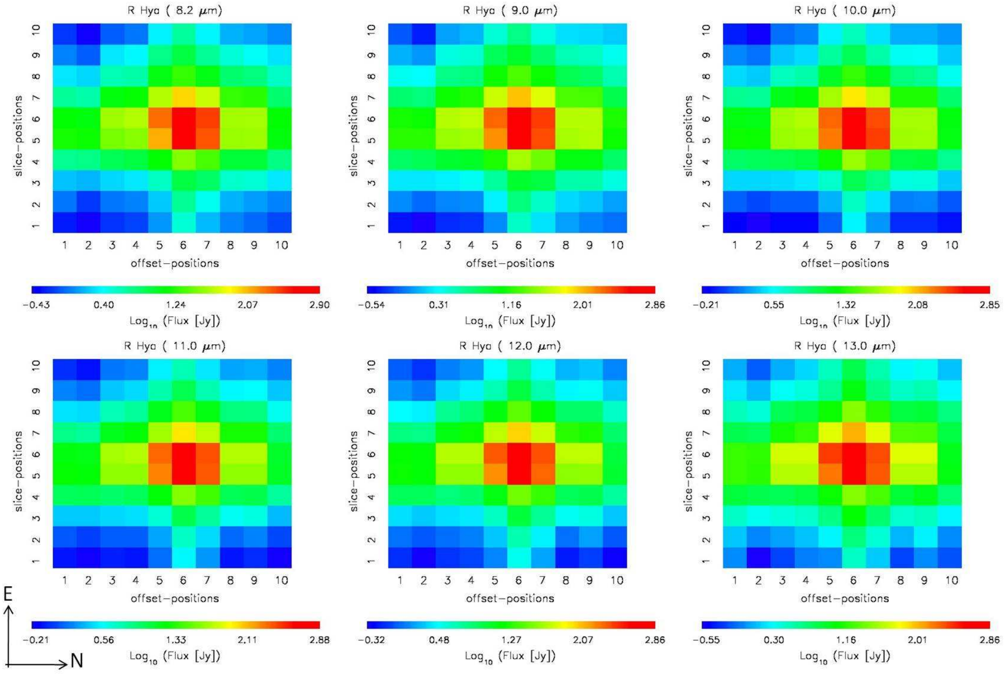

Figure 6.44: 2-D maps of the spatial distribution of the monochromatic flux intensities at 8.2, 9.0, 10.0, 11.0, 12.0 and 13.0 μm of R Hya. The flux intensities are plotted in logarithmic scale. Note that the central star is located at (6,5) coordinate position.

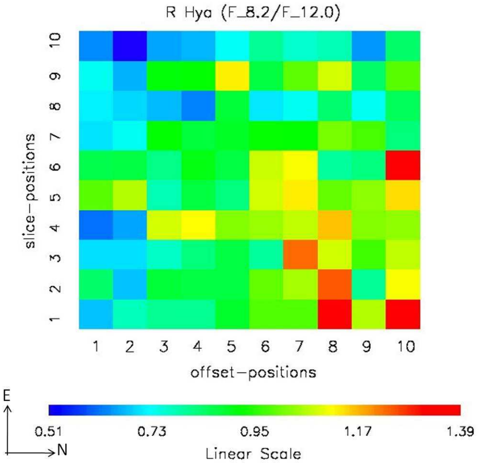

Figure 6.45: 2-D map of the $F_{8.2}/F_{12.0}$ which is used as a proxy for the underlying dust continuum of R Hya. The flux ratios are plotted in linear scale. Note that the central star is located at (6,5) coordinate position.

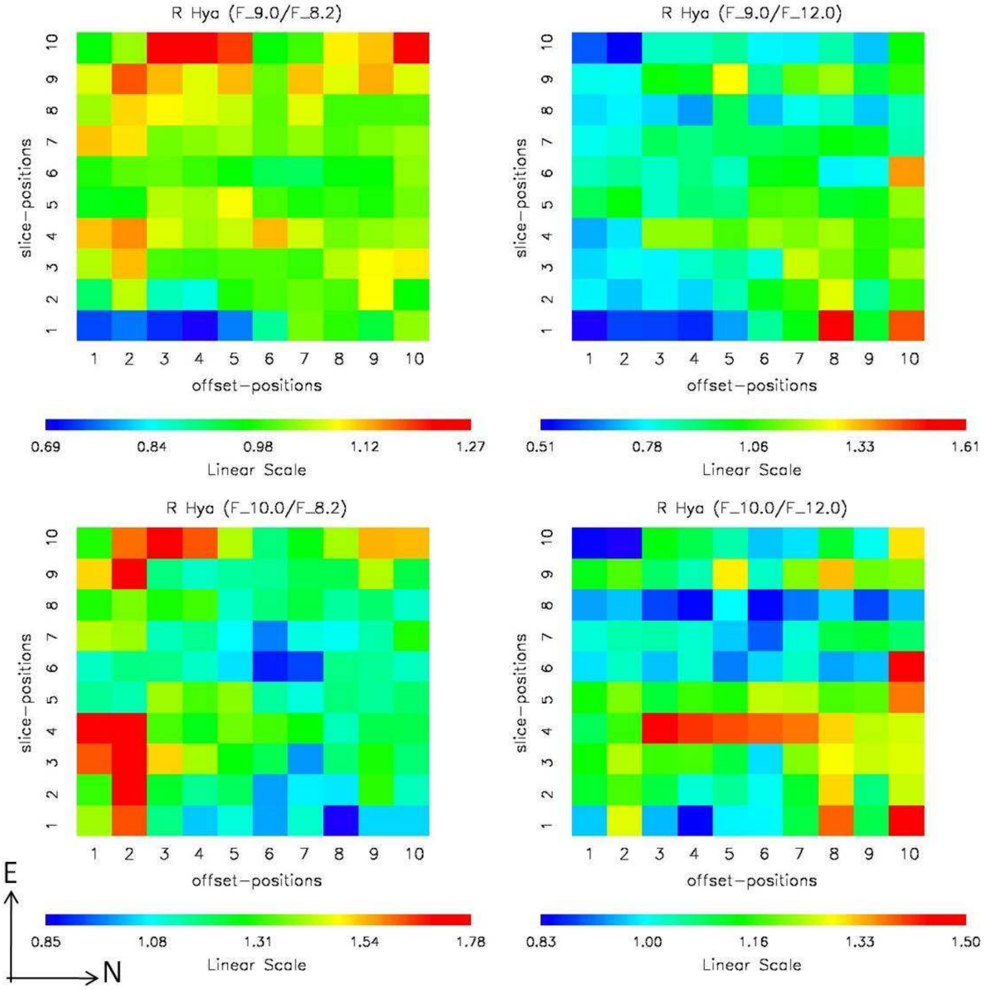

Figure 6.46: 2-D maps of the monochromatic continuum-divided observations at 9.0 and 10.0 μm for R Hya. The flux ratios are plotted in linear scale. Note that the central star is located at (6,5) coordinate position.

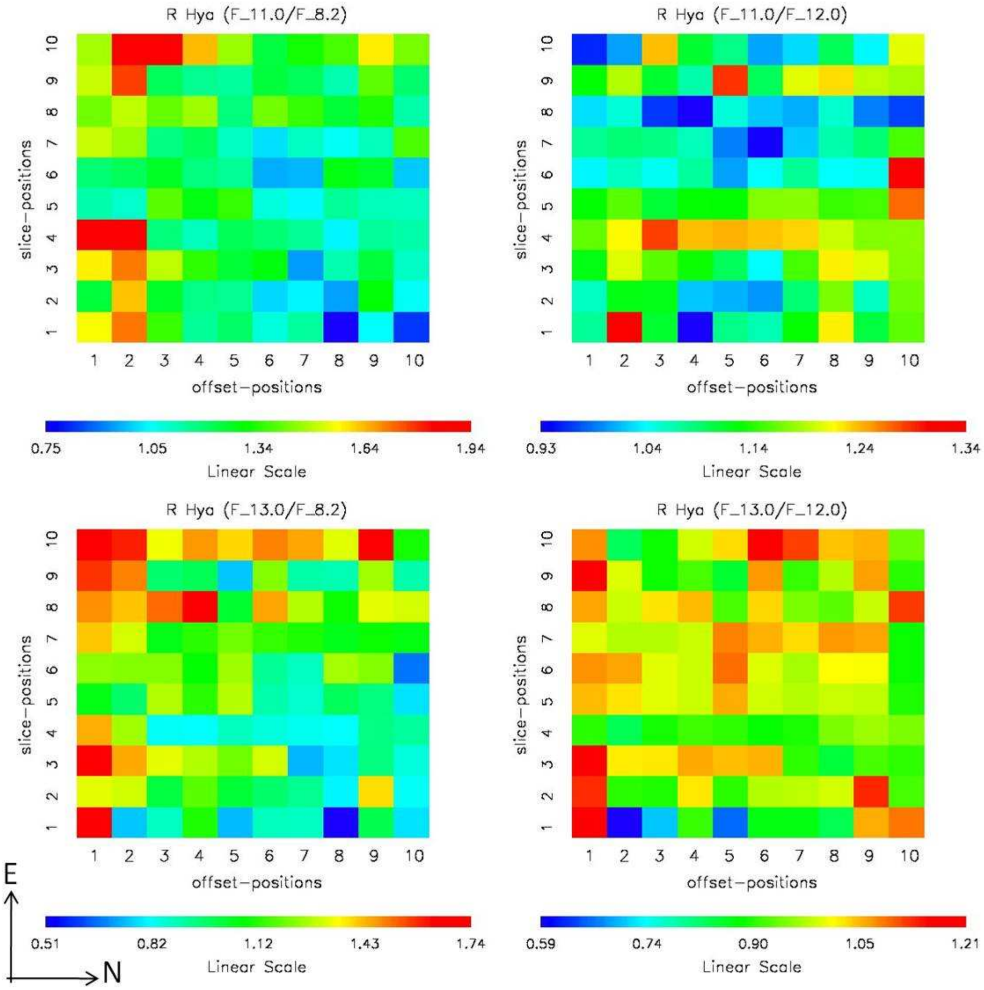

Figure 6.47: 2-D maps of the monochromatic continuum-divided observations at 11.0 and 13.0 μm for R Hya. The flux ratios are plotted in linear scale. Note that the central star is located at (6,5) coordinate position.

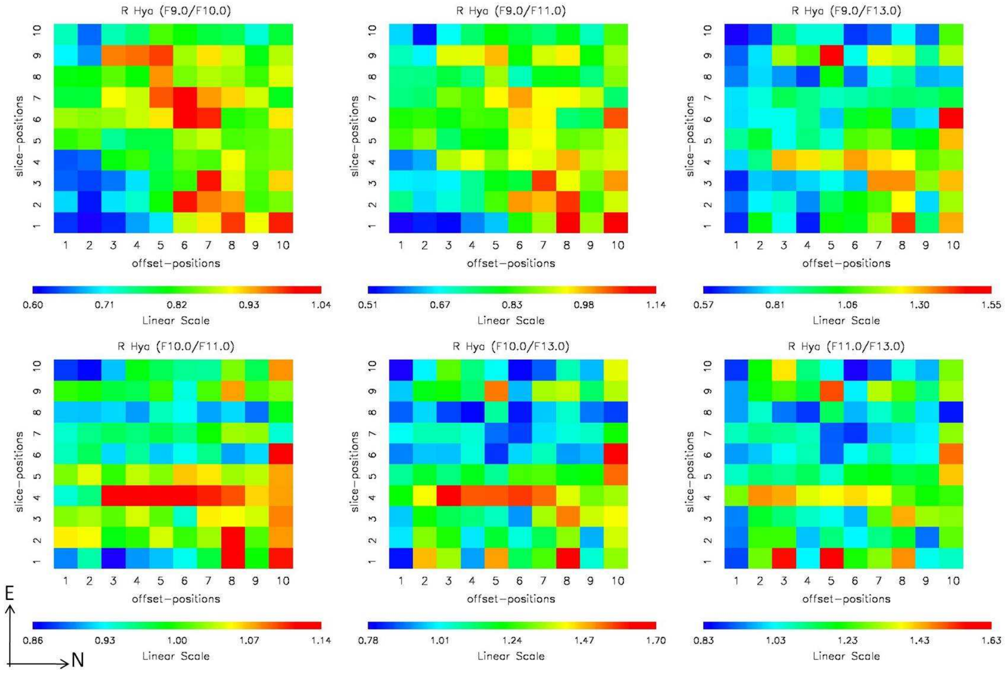

Figure 6.48: 2-D maps of the spatial distribution of the flux ratios at 9.0, 10.0, 11.0 and 13.0 μm with respect to each other of R Hya. The flux ratios are plotted in linear scale. Note that the central star is located at (6,5) coordinate position.

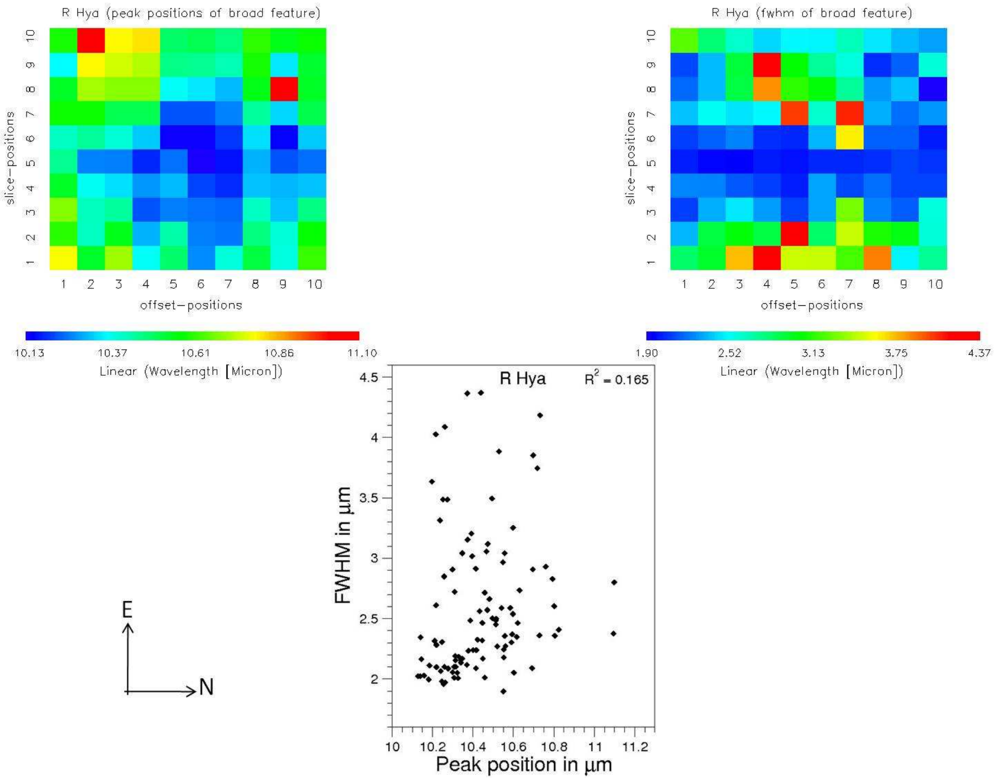

Figure 6.49: Top: 2-D maps of peak position (left) and FWHM (right) of the broad feature of R Hya. Bottom: Correlation between the peak positions and FWHM of the broad features of R Hya.

6.7.6 W Hya

The O-rich semiregular variable W Hya, was classified as infrared spectral class of SE8 by Sloan & Price (1995, 1998) [127, 128], however, this was an automated classification scheme that clearly misclassified this object. Speck et al. (2000) [131] classified W Hya in their "broad" AGB group. Following the re-observation of W Hya with *ISO* SWS, the infrared spectral classification of W Hya was modified to SE3 by Sloan et al. (2003) [123] following the same criteria laid down by Sloan & Price (1995) [127]. W Hya has been known for some time to be surrounded by rather dense gas, dust, and active OH masers (1612 MHz; Etoka et al. 2003) [36]. Wishnow et al. 2010 [153] even reported presence of two dust shells around W Hya.

Following the same structure as used previously in this chapter, the data and analysis are represented in several 6×10 grids. Because of the ozone artifact effect and other obvious artifacts seen in the 10×10 observed grid of spectra in Figure 6.50, we only consider slice position 4, 5, 6 and 7 for the 10 offset positions for further analysis. The remaining 6×10 grid maps are shown in Figures 6.51, 6.52, 6.53, 6.54, 6.55, and 6.56: Top panel. Note that the central star is located at (6,5) coordinate position.

Several of spatial maps shown a SE–NW trend in brightness and flux ratios. This is particularly apparent in the $F_{8.2}/F_{12.0}$ continuum map (Figure 6.52) but also shows up clearly in most of the continuum-divided images, when the continuum is measured at $12.0\,\mu$m but not at $8.2\,\mu$m (see Figures 6.53 and 6.54). For those continuum-divided images using $F_{8.2}$ the spatial distribution seems to be more radial from the central star. This may be related to contamination of the $8.2\,\mu$m flux measurements by the SiO absorption. The SE–NW trend is also seen in the flux-ratio-ed maps especially for $F_{9.0}/F_{10.0}$ and $F_{9.0}/F_{11.0}$. This trend is consistent with a temperature variation such that the dust in the SE corner is coolest and dust in the NW corner is warmest.

The 2-D map of spatial distribution of the peak positions for the "broad" (9–

$12\,\mu$m) seems to follow that of the $8.2\,\mu$m flux, so that it is radially dependent, with a longer wavelength peak measured closest to the central star, and the peak position shifts blue-ward with distance from the central star. This trend is not mimicked in the spatial distribution of FWHMa. The radial trend in peak position can be interpreted in two possible scenarios. Following § 6.2 we have suggested that chaotic silicates form, but those close to the central star get annealed into crystalline grains which would give rise to redder 9–$12\,\mu$m features (see Figure 6.2: Right panel). The chaotic silicates further away do not anneal and therefore look more like classic amorphous silicate features, following dust formation hypotheses (ii). Alternatively, dust dominated by amorphous alumina (aluminium oxide) would also have redder 9–$12\,\mu$m features than the classic amorphous silicate dust. In this case the data supports the classic condensation sequence (see Figure 6.2: Left panel). Consequently our maps of W Hya do not distinguish between the competing dust formation hypotheses (i) and (ii).

Plotting the relationship between the two Gaussian parameters we see two apparent groups (see Figure 6.56: Bottom panel). Previous observations of W Hya have suggested that it is surrounded by two separate, discrete shells (Wishnow et al. 2010) [153]. We may be seeing evidence for those separate shells in the separation of the "broad" feature into two groups. In both cases there is a strong trend of features becoming narrower when then are bluer (or broader when they are redder). However, group 1 has an average peak position around $10.5\,\mu$m and a wide spread of widths, whereas group 2 is redder, peaking closer to $11.3\,\mu$m but with a narrower range of widths. The mostly likely scenario to explain the grouping are that the group 2 features are due to amorphous alumina alone, whereas the group 1 features represent mixtures of amorphous alumina and amorphous silicates (see "broad" group model in Speck et al. 2000) [131]. In this case group 2 represents naked alumina grains close to the central star, while group 1 are grains where silicates has started to form on the alumina seeds. However, formation of silicates is never sufficient to completely hide the spectral contributions from the underlying alumina. Consequently we suggest that our observations of W Hya support dust formation mechanism (iii), forming alumina seeds and silicates mantles - but always at low enough temperatures to be amorphous.

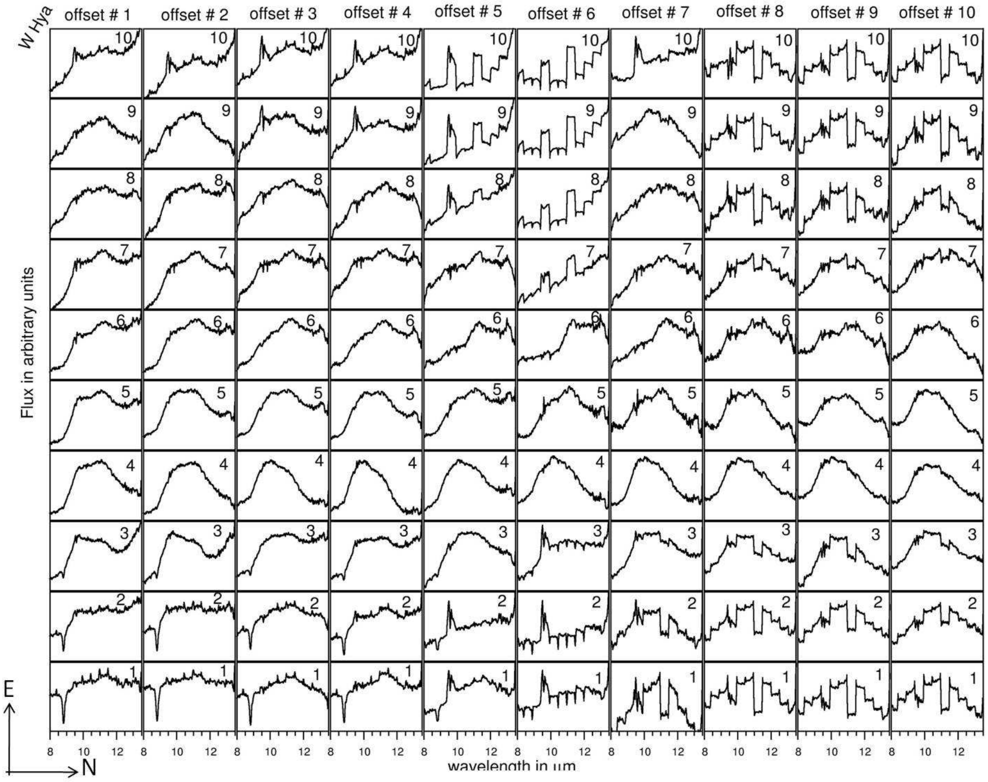

Figure 6.50: Spatially resolved dust spectra of W Hya. (Note that the telluric ozone may not be completely subtracted out and thus there is an artifact at $\sim 9.7\,\mu$m).

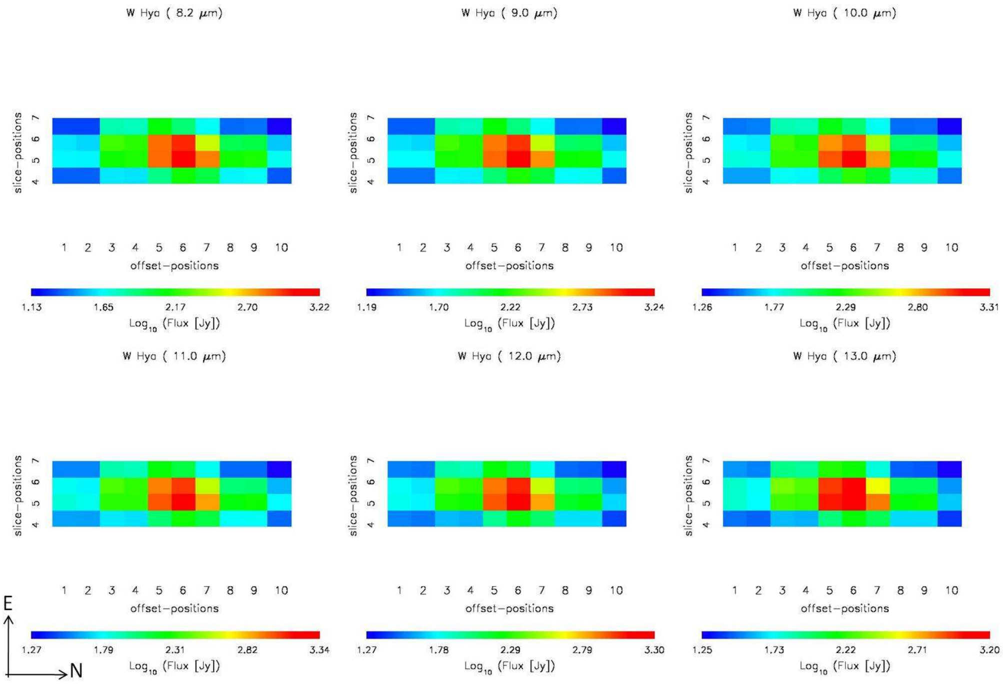

Figure 6.51: 2-D maps of the spatial distribution of the monochromatic flux intensities at 8.2, 9.0, 10.0, 11.0, 12.0 and 13.0 μm of W Hya. The flux intensities are plotted in logarithmic scale. Note that the central star is located at (6,5) coordinate position.

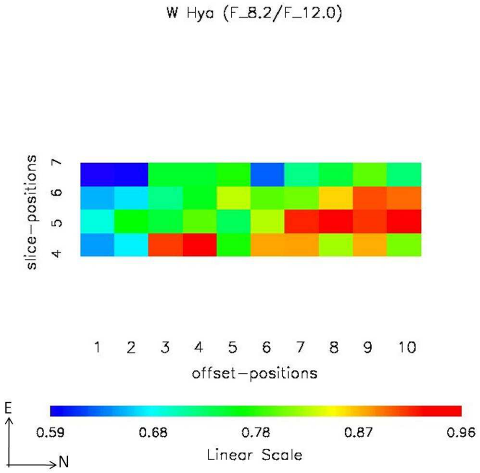

Figure 6.52: 2-D map of the $F_{8.2}/F_{12.0}$ which is used as a proxy for the underlying dust continuum of W Hya. The flux ratios are plotted in linear scale. Note that the central star is located at (6,5) coordinate position.

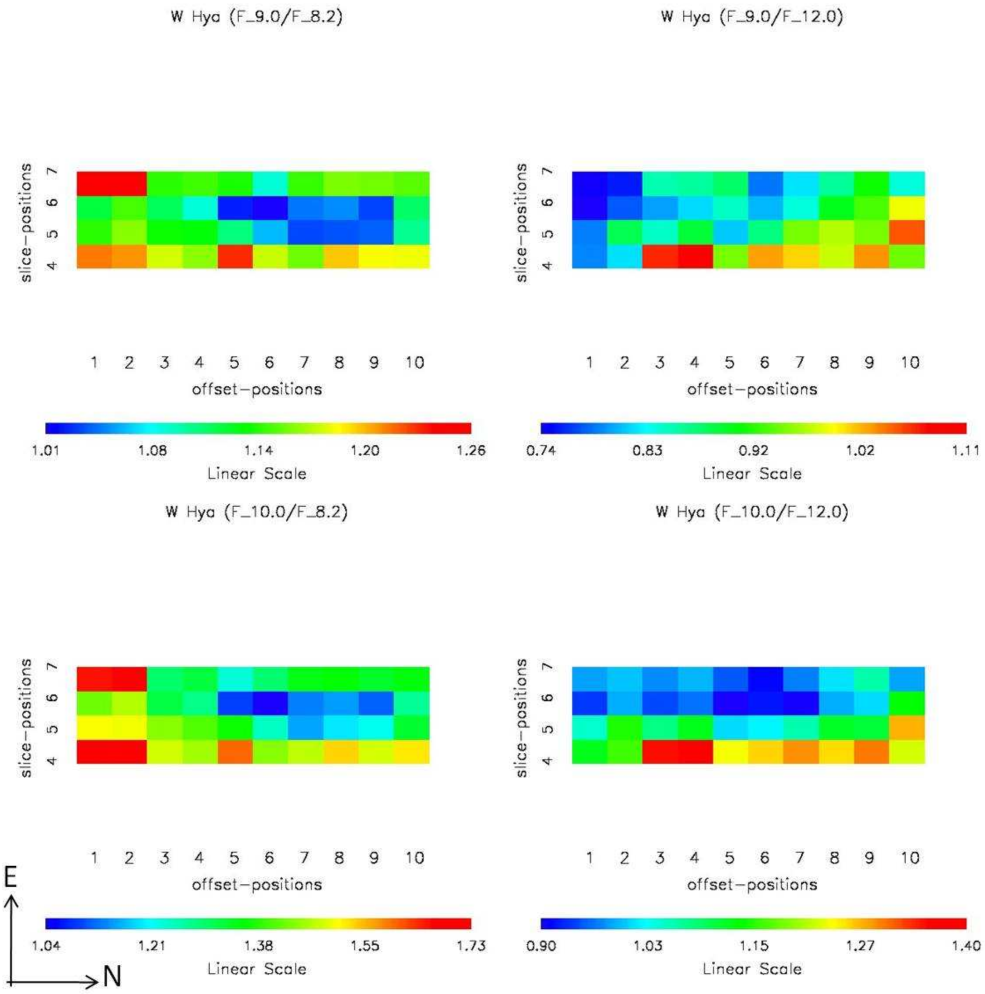

Figure 6.53: 2-D maps of the monochromatic continuum-divided observations at 9.0 and 10.0 μm for W Hya. The flux ratios are plotted in linear scale. Note that the the central star is located at (6,5) coordinate position.

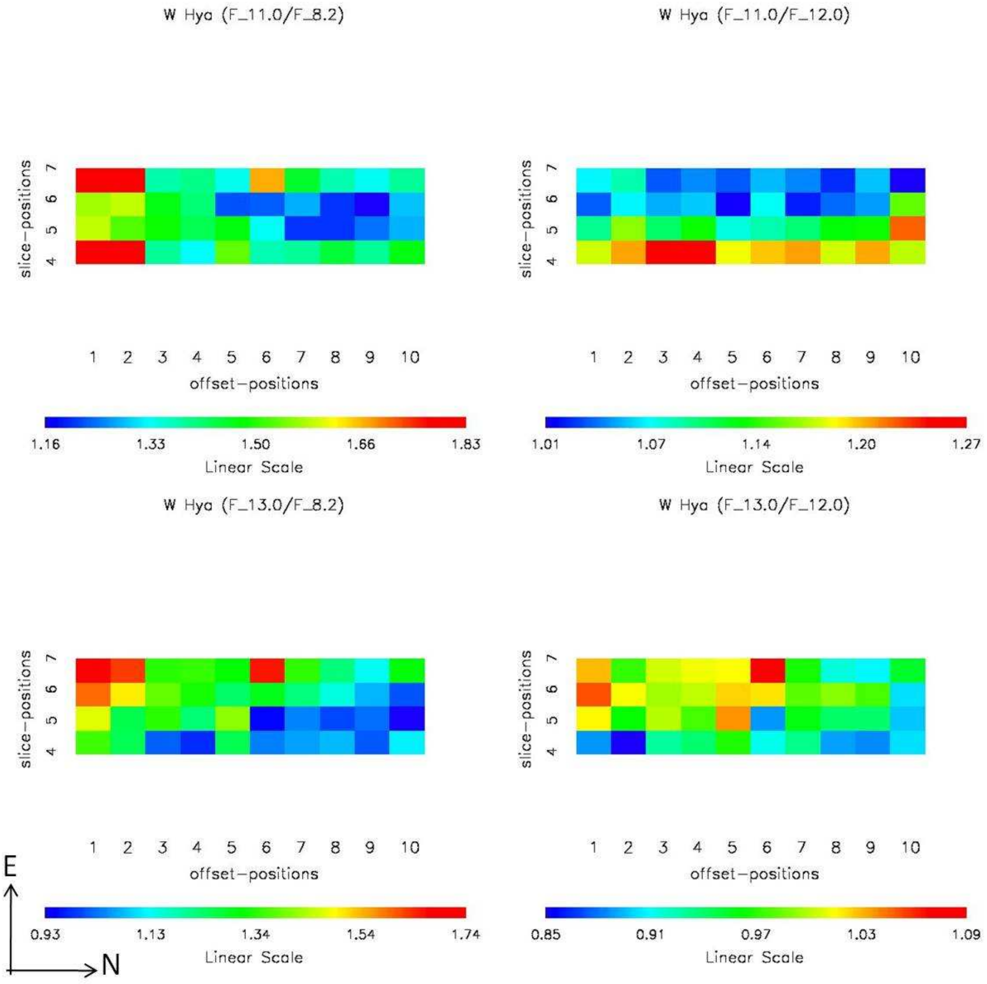

Figure 6.54: 2-D maps of the monochromatic continuum-divided observations at 11.0 and 13.0 μm for W Hya. The flux ratios are plotted in linear scale. Note that the central star is located at (6,5) coordinate position.

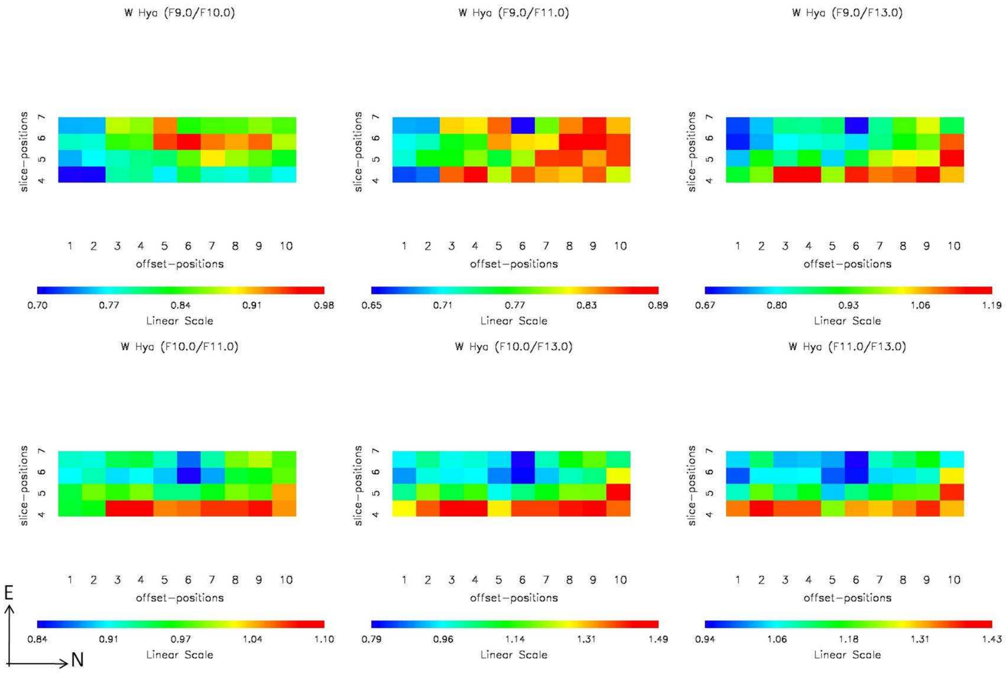

Figure 6.55: 2-D maps of the spatial distribution of the flux ratios at 9.0, 10.0, 11.0 and 13.0 μm with respect to each other of W Hya. The flux ratios are plotted in linear scale. Note that the central star is located at (6,5) coordinate position.

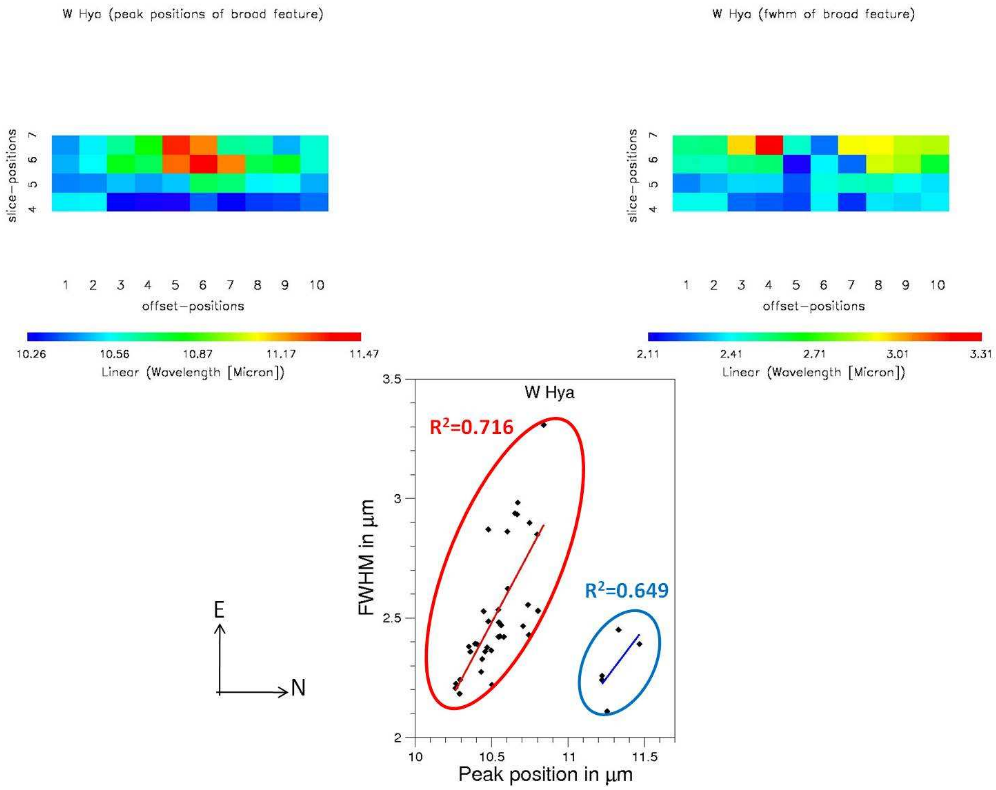

Figure 6.56: Top: 2-D maps of peak position (left) and FWHM (right) of the broad feature of W Hya. Bottom: Correlation between the peak positions and FWHM of the broad features of W Hya.

6.7.7 RX Boo

The O-rich semiregular variable RX Boo, has been classified as infrared spectral class of SE3 by Sloan & Price (1995, 1998) [127, 128], and "broad+sil" AGB by Speck et al. (2000) [131]. RX Boo has been detected to surrounded by water vapor masers by Winnberg et al. (2008) [152]. They also found an evidence of an incomplete ring around RX Boo with an inner radius of 91 milliarcseconds (see Figure 6.57), which may cause spatial asymmetry structure.

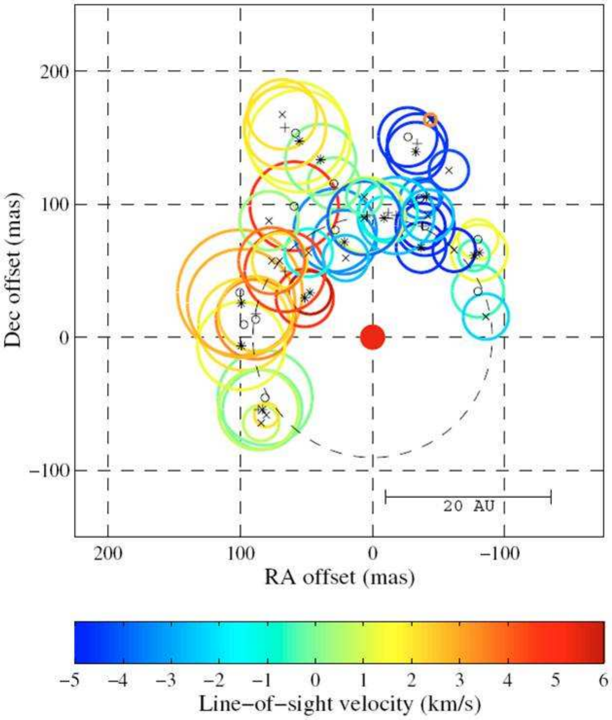

Figure 6.57: The central star is surrounded by incomplete ring with maser components. Figure taken from Winnberg et al. (2008) [152].

Following the same structure as used previously in this chapter, the data and analysis are represented in several 10×10 grids shown in Figures 6.58, 6.59, 6.60, 6.61, 6.62, 6.63, and 6.64: Top panel. Note that the central star is located at (8,5) coordinate position.

Most of the spatial maps do not show any particular patterns. The $F_{8.2}/F_{12.0}$

continuum map shows a hint of a SW–NE trend, but it is not very clear. This same pattern may be present in the flux-ratio-ed map $F_{9.0}/F_{10.0}$, but otherwise the spatial distributions of the monochromatic continuum-divided, flux-ratio-ed and gaussian parameterized data do not show any patterns. Furthermore, their is no correlation between the peak positions and FWHMa for the "broad" (9–12 μm) as shown in Figure 6.64: Bottom panel. The apparent SW–NE trend may be related to the shape of the maser emission ring shown in Figure 6.57. There is a gap on the ring of maser emission to the SW, which may imply a lower density zone, which would, in turn, lead to a difference in the radiation field in that direction. However, the lack of similar structures in most of our maps suggest this is not very important in determining the spatial distribution of mineralogy of the dust.

Our analysis on RX Boo has not found any discernable patterns in any of the 2-D maps. Similar with R Aur and R Leo, the features vary significantly but without the spatial patterns expected from any of the dust formation mechanisms as discussed in § 6.2. This again suggests the dust formation may be more turbulent as suggested by the model (Woitke 2006) [154]. Again the spatial scale is large compared to the time scale for pulsation (see Table 6.3), which would tend to average out and lose any spatial dependence that the different dust components may have on the structure of the dust shell.

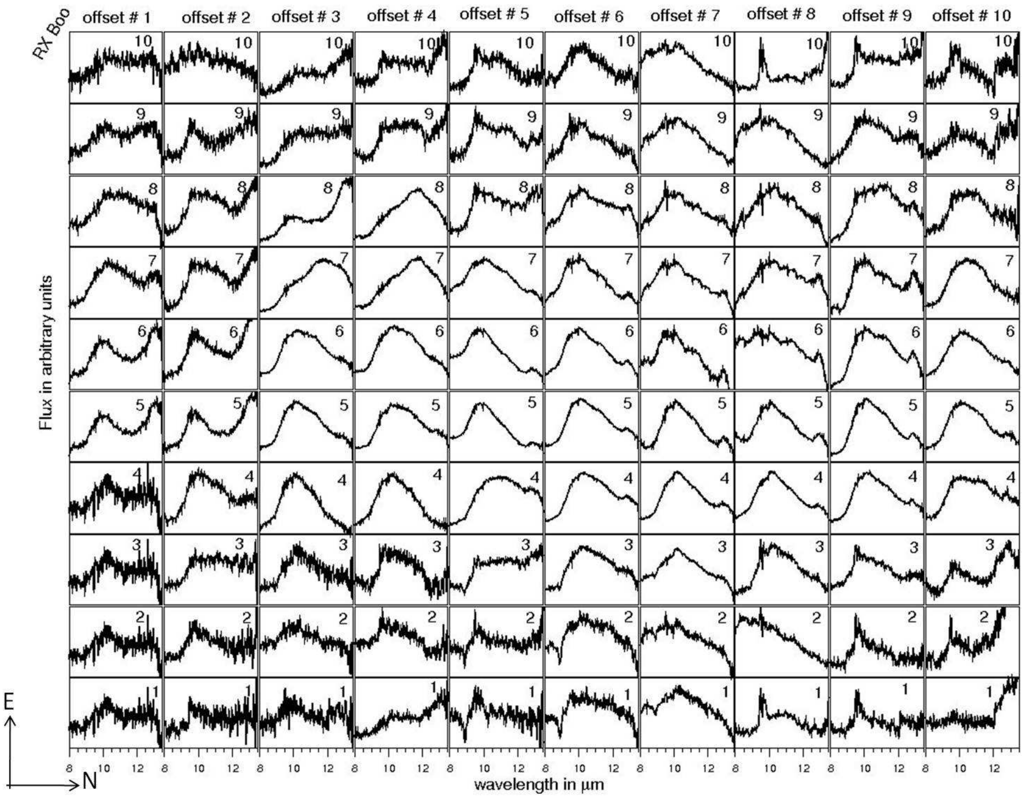

Figure 6.58: Spatially resolved dust spectra of RX Boo. (Note that the telluric ozone may not be completely subtracted out and thus there is an artifact at $\sim 9.7\,\mu$m).

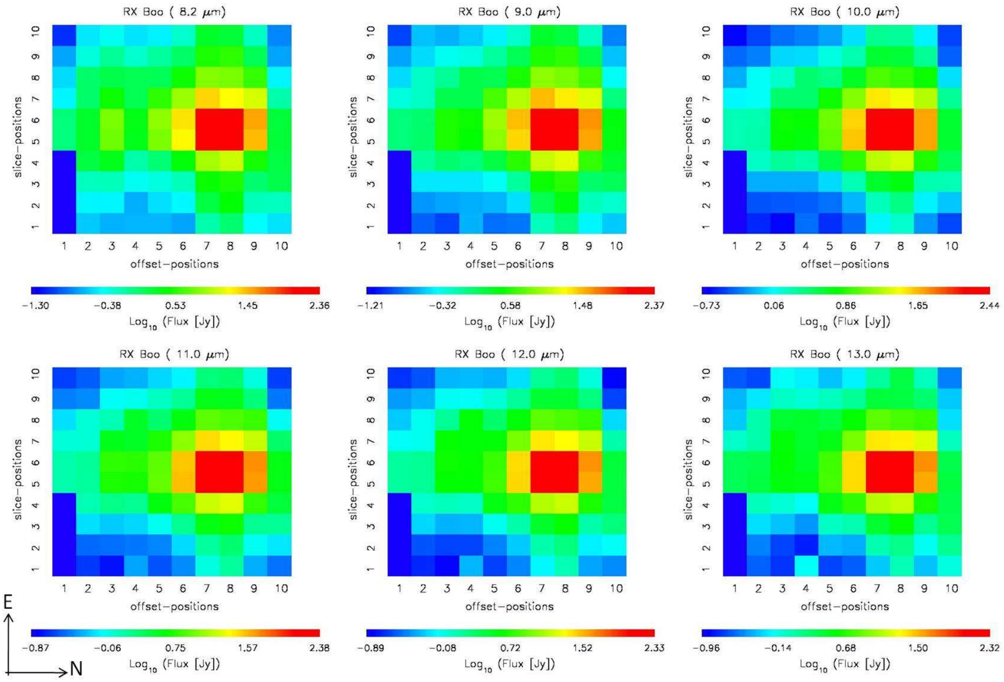

Figure 6.59: 2-D maps of the spatial distribution of the monochromatic flux intensities at 8.2, 9.0, 10.0, 11.0, 12.0 and 13.0 μm of RX Boo. The flux intensities are plotted in logarithmic scale. Note that the central star is located at (8,5) coordinate position.

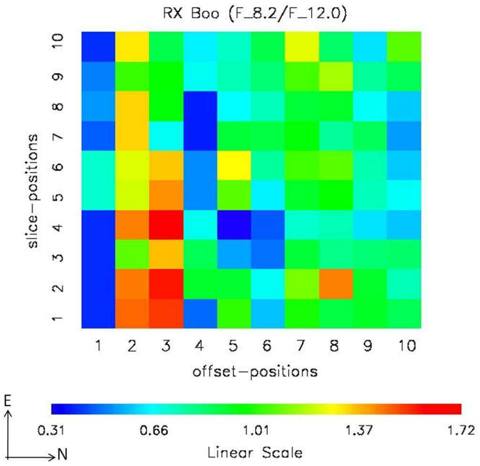

Figure 6.60: 2-D map of the $F_{8.2}/F_{12.0}$ which is used as a proxy for the underlying dust continuum of RX Boo. The flux ratios are plotted in linear scale. Note that the central star is located at (8,5) coordinate position.

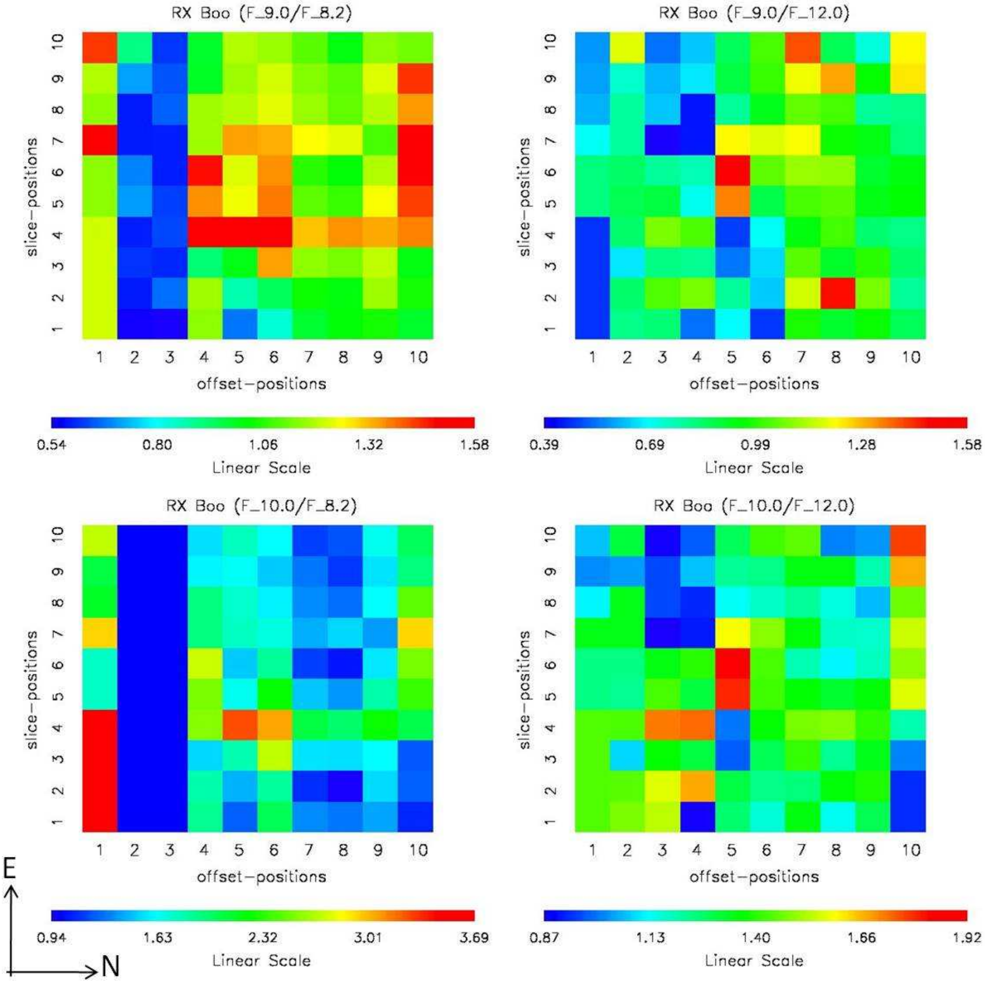

Figure 6.61: 2-D maps of the monochromatic continuum-divided observations at 9.0 and 10.0 μm for RX Boo. The flux ratios are plotted in linear scale. Note that the central star is located at (8,5) coordinate position.

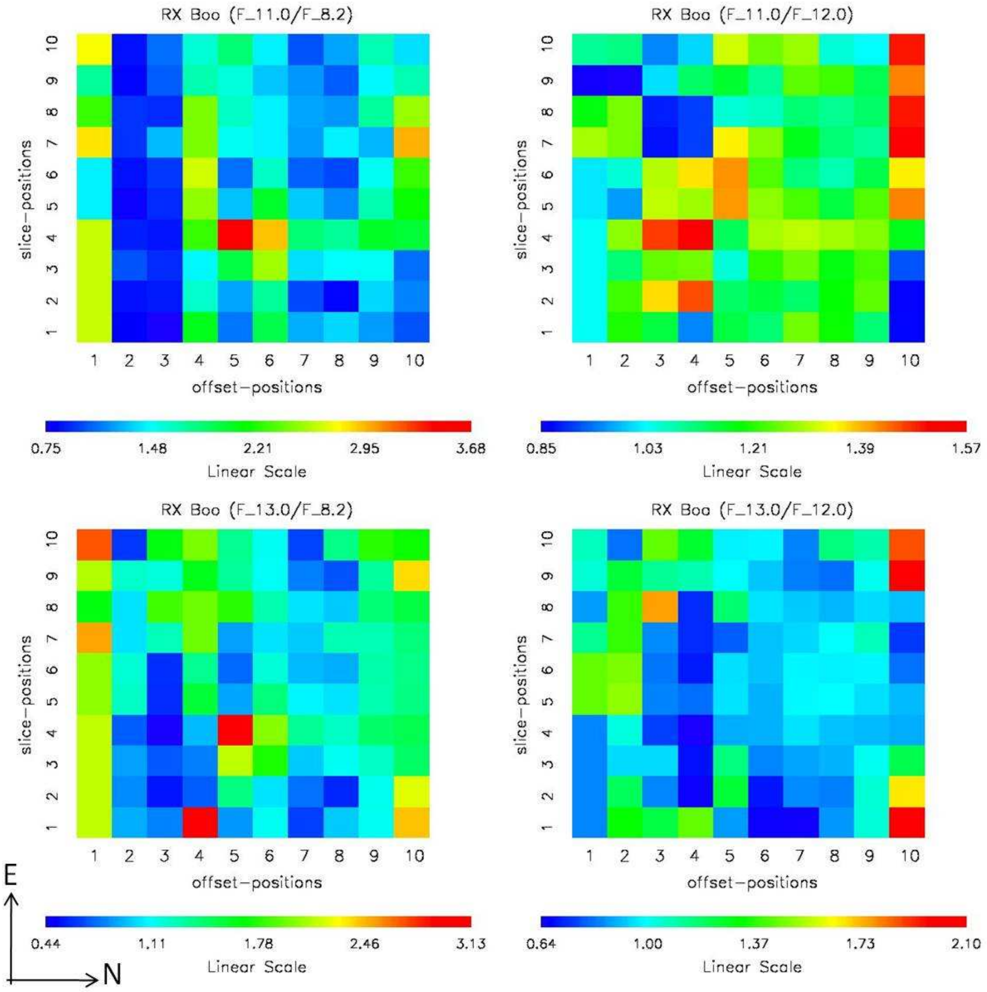

Figure 6.62: 2-D maps of the monochromatic continuum-divided observations at 11.0 and 13.0 μm for RX Boo. The flux ratios are plotted in linear scale. Note that the central star is located at (8,5) coordinate position.

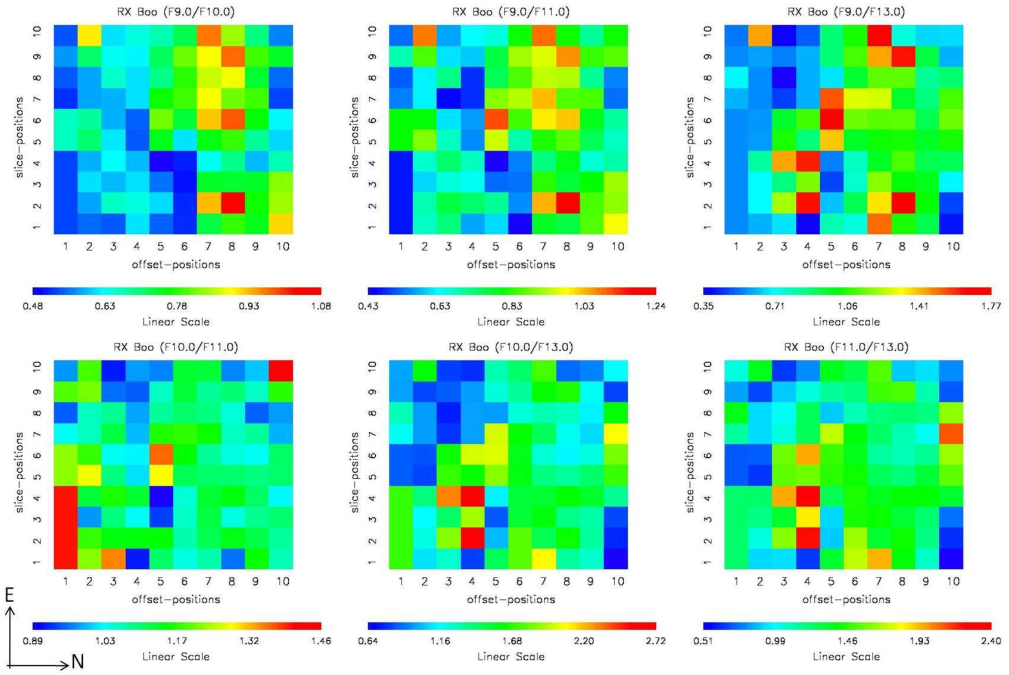

Figure 6.63: 2-D maps of the spatial distribution of the flux ratios at 9.0, 10.0, 11.0 and 13.0 μm with respect to each other of RX Boo. The flux ratios are plotted in linear scale. Note that the central star is located at (8,5) coordinate position.

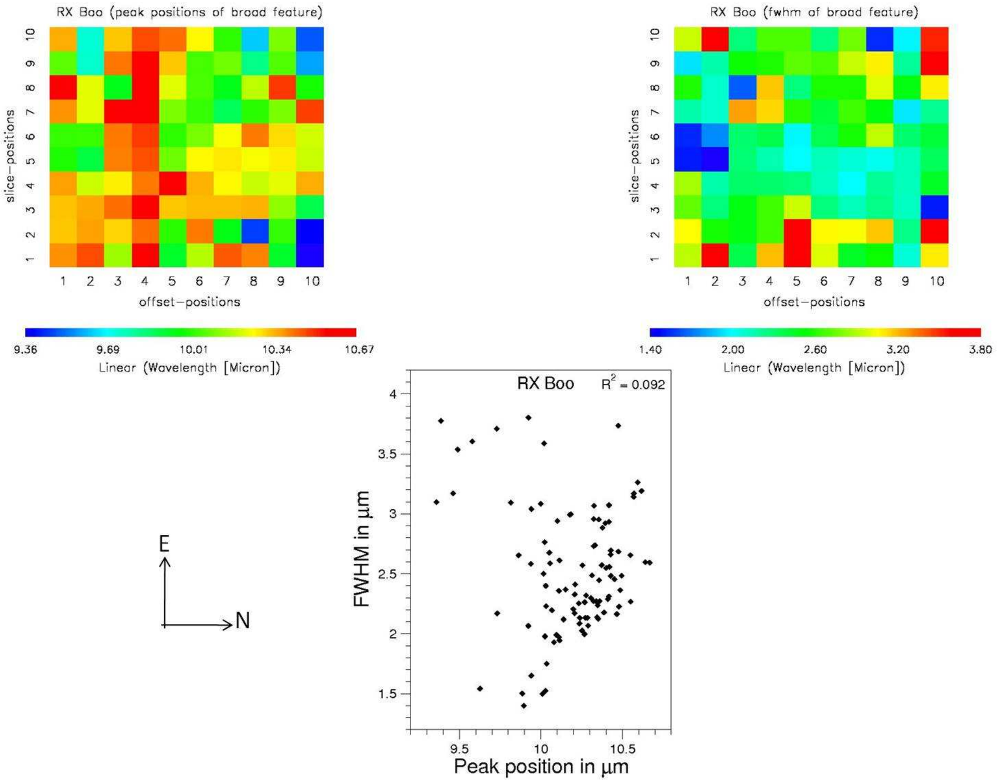

Figure 6.64: Top: 2-D maps of peak position (left) and FWHM (right) of the broad feature of RX Boo. Bottom: Correlation between the peak positions and FWHM of the broad features of RX Boo.

6.8 Summary & Conclusion

From the spatially resolved data of seven O-rich AGB stars, we see that 3 of them (RT Vir, SW Vir and R Hya) support both the “chaotic” grain formation hypothesis (ii) and formation of seed nuclei, followed by mantle growth hypothesis (iii). The spatial distribution of W Hya do not distinguish between the competing dust formation hypotheses ([i], [ii] & [iii]); it supports all three hypotheses. For the other 3 targets (R Aur, R Leo and RX Boo), their spectral features vary significantly but without any spatial trend. These results support none of the hypotheses; similar to what we had predicted for T Cep (see § 5.6). These results suggest that the turbulent dynamics, pulsation shocks in the dust-forming zones around O-rich AGB stars lead to inhomogeneous dust formation, producing fine scale structure in the density of the dust envelope. In this O-rich environment, there are many potential minerals can be formed but their stability is very sensitive to the precise local conditions (as suggested by Woitke 2006) [154].

As discussed in § 6.7 and Figure 6.15, one of the limitation of our observation is that our spatial-resolution is much too low. For future observation purposes, it would be necessary to obtain spectra of much higher spatial resolution in order to resolve the finer structure of the dust shell.

Chapter 7

Effect of composition-temperature-grainshape on the IR laboratory spectra of crystalline silicate minerals

7.1 Introduction

As discussed in § 4.6 that one of the most exciting recent findings in cosmic dust studies was the discovery of crystalline silicate dust by the *ISO* SWS. In order to identify the physical properties (composition, lattice structure, grain size, and shape) of the dust grains around O-rich AGB stars, we use spectroscopy. We compare spectral feature parameters (i.e. peak positions, widths and amplitudes) of the laboratory spectra of different dust species to astronomical observations in order to match and identify the dust species present in space. However, these parameters are significantly influenced by three competing factors (composition, temperature and shape of the dust grains). A change in composition (X) may change the parameters (position, width or amplitude) of a spectral feature (as also shown in Figure 4.1); a simultaneous change in temperature (T) and/or grain-shape (ς) could compensate for a compositional change. Consequently there is a degeneracy such that a given spectral feature may have more than one explanation. This degeneracy problem is exacerbated by a lack of laboratory data covering all possible physical parameters of the dust. In this chapter we investigate the degeneracy space created by two competing factors X and T of dust grains for the simplest predicted crystalline silicate mineral olivine and propose tools for mapping and breaking this degeneracy.

For future follow up, a proposal had been submitted to University of Missouri Research Board, in order to extend this 2-D degeneracy study to include the third dimension (grain shape, ς) and extend it to cover other mineral series (i.e. pyroxenes) and higher temperatures as well. The summary of the proposed plan will be discussed in § 7.4.

7.2 Purpose of this work

In order to identify the true dust carrier in the circumstellar environment of O-rich AGB stars, we need to map the degeneracy space and to determine at what extent the degeneracy can be broken observationally. One of the advantages of looking at crystalline, rather than amorphous dust is that the parameters (position, width and amplitude) of the spectral features are more sensitive to X, T and ς. This allows us to diagnose such quantities in space.

There are several competing hypotheses related to dust grain formation mechanisms, which predict a variety of dust grain structures and compositions (as discussed in § 6.2). Observationally, some spectral features have multiple identifications. A notorious example is the so-called "13μm" feature whose carrier is still not well-constrained (e.g. Sloan et al. 2003 and reference therein) [123]. Another example is RX Lac, whose far-IR features have been attributed to two different crystalline silicates: diopside ($CaMgSi_2O_6$) by Hony et al. (2009) [64] and fayalite (Fe_2SiO_4) by Pitman et al. (2010) [114]; as also shown in Figure 4.1, even though both groups used the same spectroscopic data from *ISO*. Yet another example is T Cep whose *ISO* spectral features have been attributed to Fe-rich crystalline silicate by Guha Niyogi et al. 2011 [49], whereas, Van Malderen (2003) [143] interpreted the dust around T Cep as amorphous and Mg-rich in nature. A more evolved example comes from a planetary nebula. Analysis of the complete *ISO* spectrum of NGC 6302 indicates the presence of the crystalline minerals forsterite (Mg_2SiO_4) and enstatite ($MgSiO_3$) by Molster et al. (2001) [97]. But Kemper et al. (2002) [73] found evidence of diopside [$CaMg(SiO_3)_2$] and also suggested that calcite ($CaCO_3$) and dolomite [$CaMg(CO_3)_2$] are present. However, not all of the sharp peaks observed in the astronomical spectrum have been identified, and carbonates are not expected to form in such environments (e.g. Ferrarotti & Gail 2005) [40]. Hofmeister et al. (2004) [62] compared the spectral features from NGC 6302 to the calcium aluminate minerals, hibonite ($CaAl_{12}O_{19}$) and grossite ($CaAl_4O_7$), and demonstrated excellent peak correlations up to the spectral limits of the *ISO* data. In addition Hofmeister & Bowey (2006) [58] suggested that hydrous silicates may be present (i.e. lizardite [$Mg_{2.95}Fe_{0.05}Si_2O_5(OH)_4$] and saponite [$(Na,Ca/2)_{0.3}(Mg,Fe)_3(Al,Si)_4O_{10}(OH)_2.4H_2O$]).

The discrepancies between the published attributions arise from limiting the parameter space for the astromineralogical data used in interpretations. That is, spectral feature parameters depend on physical parameters of the dust (X, T and ς), but it is difficult to incorporate all these parameters simultaneously. And thus researchers tend to limit the parameter space considered in any given investigation. In this chapter I'll present the effect of two parameter space (X, T) of crystalline olivine minerals on their IR spectra.

7.3 Laboratory studies of crystalline silicate spectra

As the various laboratory data sets had been already introduced in § 3.6, now it is appropriate to discuss their implications. There have been several laboratory studies on crystalline silicate mineral spectra most of which concentrate on olivines and pyroxenes. These simple minerals are expected to form in space, based on various dust condensation models/hypotheses (e.g. Gaustad 1963, Lodders & Fegley 1999) [43, 87]. In this Chapter, I will mainly use the laboratory data from three groups: 1. WashU (e.g. Hofmeister et al. 2007, Pitman et al. 2010) [60, 114], 2. Kyoto (e.g. Chihara et al. 2002, Koike et al. 2003, Koike et al. 2006, Murata et al. 2009, Koike et al. 2010) [23, 76, 78, 104, 77] and 3. Jena (e.g. Fabian et al. 2001, Jaeger et al. 1998) [37, 69] group.

Furthermore, several groups have investigated the effect of grain shape (ς) on spectral properties (see Bohren & Huffman 1983, Fabian et al. 2001, Min et al. 2003, Takigawa et al. 2009) [8, 37, 95, 135].

7.3.1 The effect of composition (X)

The effect of composition (X) on olivine minerals at room temperature have been published by all three research groups and provide a large database of spectroscopic information. Koike et al. (2003) [76] has published a series of opacity (mass absorption coefficients) measurements at 300 K for the olivine series, covering several Fe/[Mg+Fe] ratios from forsterite (Mg_2SiO_4, designated as Fo100) to fayalite (Fe_2SiO_4, designated as Fo0). A finer grid of compositions across the olivine series at 300 K was published by Pitman et al. (2010) [114] as absorbance (a), which agree well with the Kyoto data (see Figure 7.1).

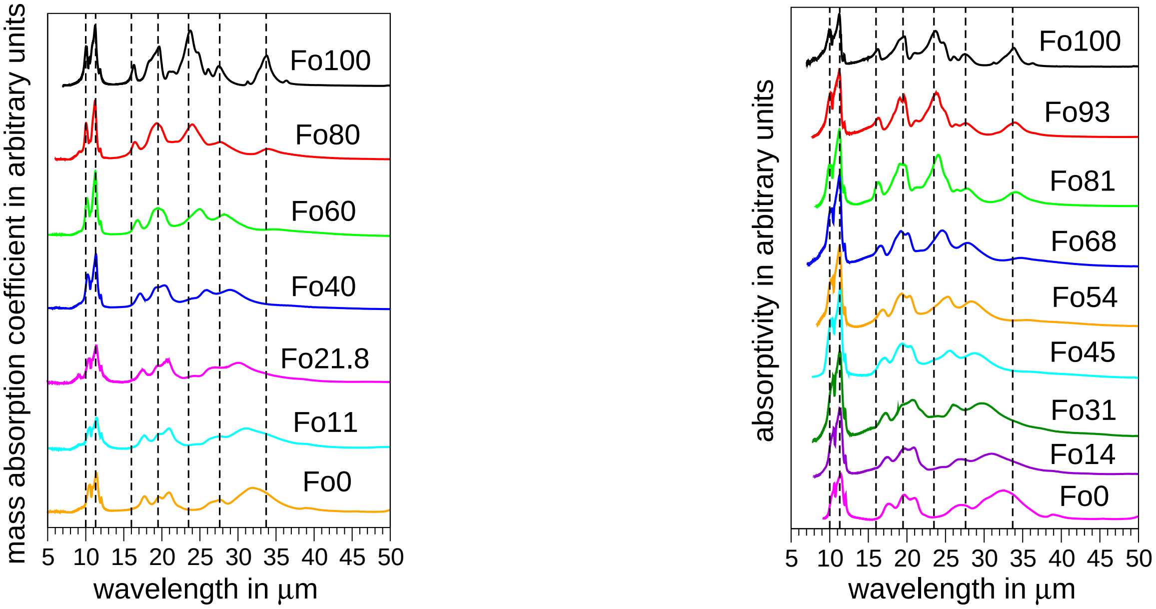

Figure 7.1: Compositional effect on IR spectral features of olivine series members. Left panel: lab data taken from Koike et al. (2003) [76], Right panel: lab data taken from Pitman et al. 2010 [114]. The prominent spectral features of the Mg-endmember are indicated by dashed straight lines. x-axis is wavelength (in μm); y-axis is absorption in arbitrary units.

The Kyoto group Chihara et al. (2002) [23] has also studied the Fe–Mg pyroxene sequence at 300 K from enstatite ($MgSiO_3$, designated as En100) to ferrosilite ($FeSiO_3$, designated as En0); while the WashU group has provided complementary unpublished data on the same series of minerals[1] (see Figure 7.2).

For both olivine and pyroxene minerals, the spectral feature positions shift towards longer wavelengths as the Fe/[Mg+Fe] ratio increases. However, the trends are not simply linear and change for the different types of silicates.

---

[1] We have a longstanding collaboration with Anne Hofmeister at WashU and can access new laboratory data through: http://galena.wustl.edu/~dustspec/info.html

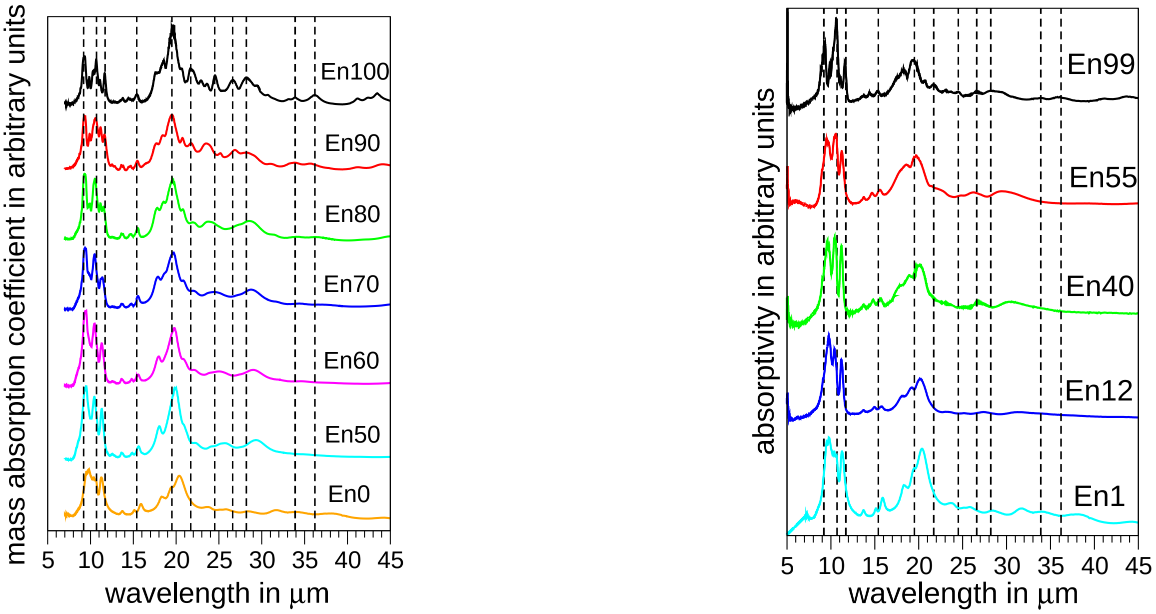

Figure 7.2: Compositional effect on IR spectral features of pyroxene series. Left panel: lab data taken from Chihara et al. (2002) [23], Right panel: lab data taken from Hofmeister et al in prep. [59]. The prominent peak features of En100/En99 are indicated by dashed straight lines. x-axis is wavelength (in μm); y-axis is absorption in arbitrary units.

7.3.2 The effect of temperature (T)

The Kyoto group (Koike et al. 2006) [78] also studied the effect of T (from 8 K to 300 K) on three family members of the olivine series (Mg_2SiO_4, $Mg_{1.8}Fe_{0.2}SiO_4$ and Fe_2SiO_4), but did not study the T effect for intermediate compositions. They are shown in Figure 7.3), 7.4 and 7.5 respectively.

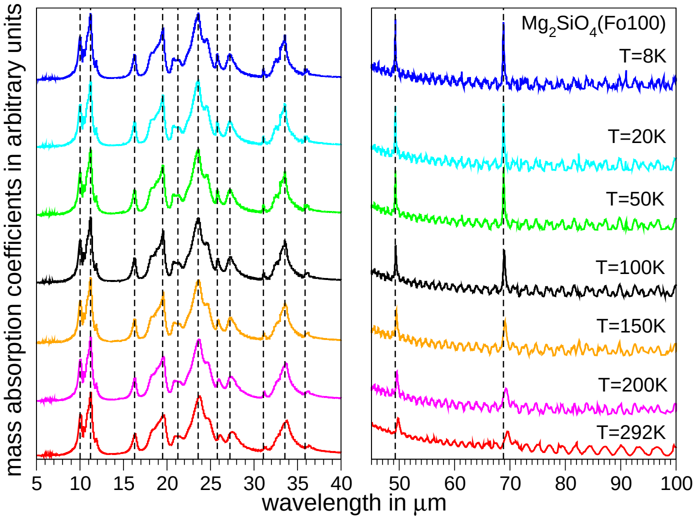

Figure 7.3: Effect of temperature on IR spectral features of the Mg-rich endmember (Mg_2SiO_4). The peak positions for 8 K-spectrum are indicated by dashed straight lines. x-axis is wavelength (in μm); y-axis is absorption in arbitrary units.

In case of all three compositions, it is clear that as the T increases, the spectral features shift towards longer wavelength, the width increases and the amplitude decreases. This effect is very prominent for far-IR (50–100 μm) features.

For the pyroxene series there is less data on the effect of T. Kyoto group (Murata et al. 2009) [104] published T-effect data only for the Mg-rich endmember pyroxene (enstatite: $MgSiO_3$, see Figure 7.6).

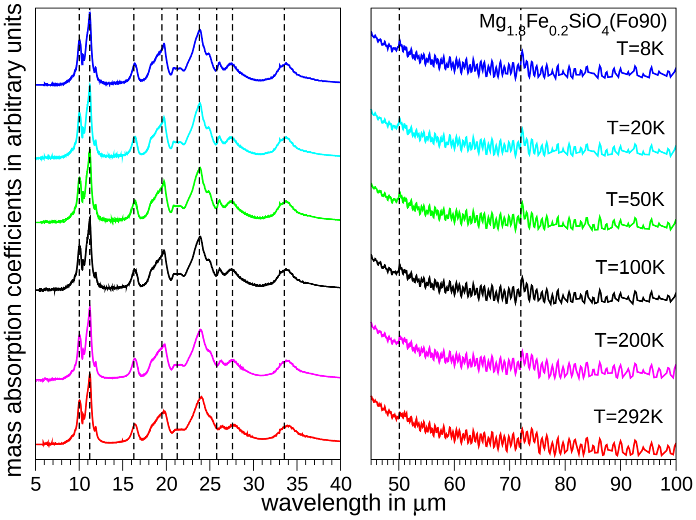

Figure 7.4: Effect of temperature on IR spectral features of the Fe-rich endmember ($Mg_{1.8}Fe_{0.2}SiO_4$). The peak positions for 8 K-spectrum are indicated by dashed straight lines. x-axis is wavelength (in μm); y-axis is absorption in arbitrary units.

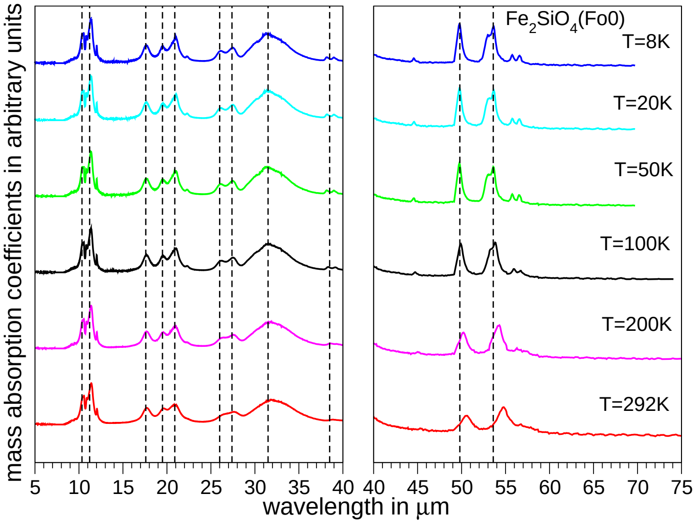

Figure 7.5: Effect of temperature on IR spectral features of the Fe-rich endmember (Fe_2SiO_4). The peak positions for 8 K-spectrum are indicated by dashed straight lines. x-axis is wavelength (in μm); y-axis is absorption in arbitrary units.

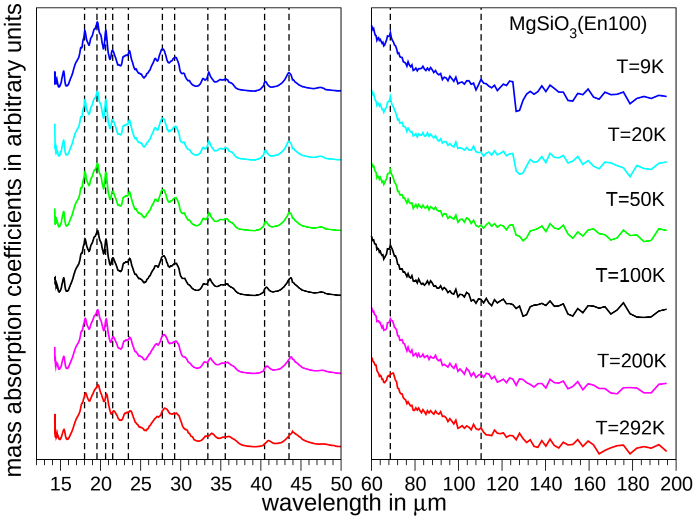

Figure 7.6: Effect of temperature on IR spectral features of the Mg-rich endmember of pyroxene ($MgSiO_3$). The peak positions for 9 K-spectrum are indicated by dashed straight lines. x-axis is wavelength (in μm); y-axis is absorption in arbitrary units.

7.3.3 The effect of grain shape (ς)

A further complication is the effect of grain shape (ς), Since solid particles in astrophysical environments are expected to be very irregular in shape, they are difficult to characterize (as also discussed in § 3.4.2). Traditionally, cosmic dust grains have been assumed to be spherical for simplicity, however, it is becoming increasingly obvious that the use of spherical grains leads to unrealistic spectral features (see e.g. Min et al. 2003, DePew et al. 2006, Hofmeister et al. 2009) [95, 31, 61]. These recent studies suggest that approximating cosmic dust by continuous distributions of simple shapes (e.g. ellipsoids [CDE], spheroids [CDS] and hollow spheres [DHS]) may be sufficient. Consequently we have followed Min et al. 2003 [95] in order to investigate the effect of ς (for e.g. see Figure 5.14), considering the limiting case of particles very small compared to the wavelength of radiation (in Rayleigh domain).

However, these investigations require the complex refractive indices for the minerals. While the data from the WashU and Kyoto groups provide a good sampling for compositional effects, as well as adequate sampling for temperature effects, neither group provides the complex refractive indices or dielectric constants for all compositions or temperatures. As a consequence we cannot use them to analyze the effect of grain shape on dust spectra. However, complex refractive indices have been produced by the Jena group (e.g. Jaeger et al. 1998, Fabian et al. 2001) [69, 37] but again, only for some of the endmember (x= 0 or 1) compositions (e.g. Mg_2SiO_4, Fe_2SiO_4, $MgSiO_3$) and with a limited selection of temperatures.

In addition to these simple grain shape distributions it has been suggested that ς may depend on the formation conditions (Takigawa et al. 2009) [135]. In this case, simple shape distributions centered around spherical grains may not be representative.

7.3.4 Results

In order to investigate the X-T space for the olivine series, we use available/accessible laboratory spectral data (e.g. Pitman et al. 2010, Koike et al. 2003, Koike et al. 2006) [114, 76, 78]. As an example, we have selected 13 prominent spectral features of forsterite (Mg_2SiO_4) mineral in order to study the effect of X-T space simultaneously. The effect of X and T on two well separated spectral features at mid-IR (at 16 μm) and far-IR (at 49 μm) are shown in Figure 7.7 and Figure 7.8.

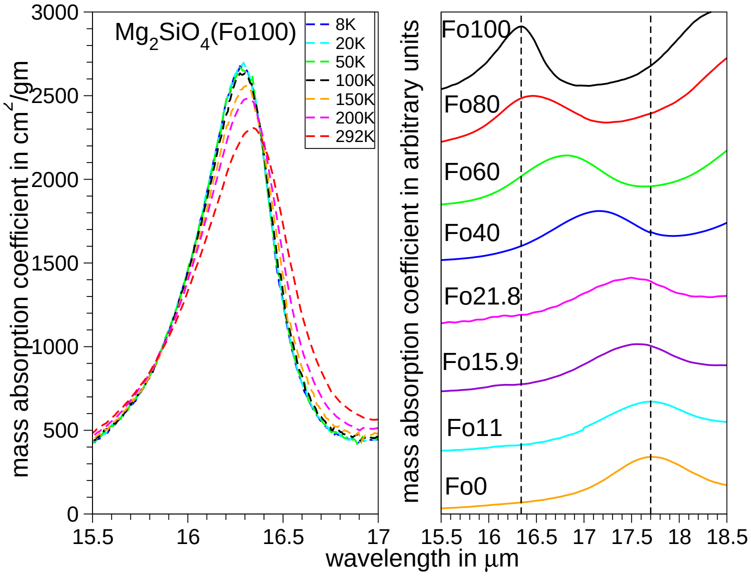

Figure 7.7: Effect of temperature (left panel) & composition (right panel) on 16 μm feature. x-axis is wavelength (in μm); y-axis is absorption in arbitrary units.

It is clear that the X effect is much stronger for the mid-IR feature (16 μm) and on the other hand the T effect is much stronger for the far-IR feature (49 μm). However, 49 μm feature is absent for some of the intermediate compositions in X space.

After selecting the spectral features for different compositions and at 8 different temperatures (ranging from 8 K to 300 K), we determine the three parameters (peak position, width and amplitude) for each spectral feature by fitting Gaussian function. We have developed a code based on the principle of nonlinear least squares fitting in order to fit the Gaussian function not only to the smooth well separated spectral

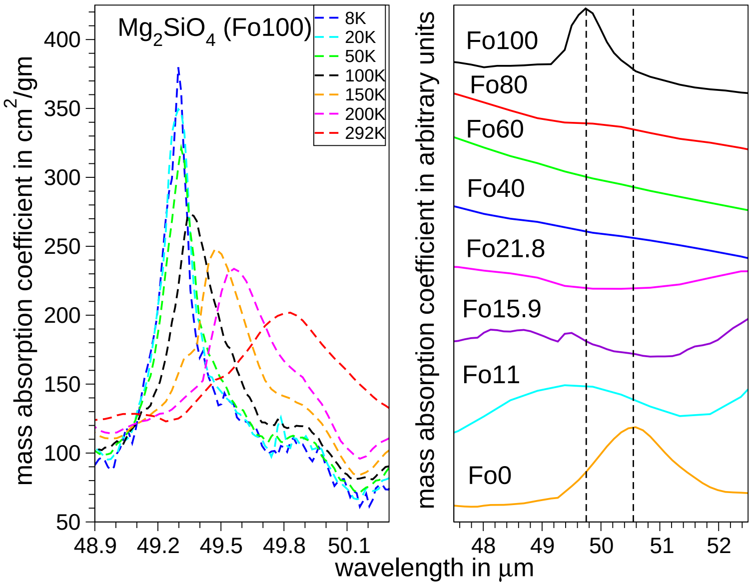

Figure 7.8: Effect of temperature (left panel) & composition (right panel) on 49 μm feature. x-axis is wavelength (in μm); y-axis is absorption in arbitrary units.

features, but also to the noisy spectral features. The code has also been modified for the double peak feature (e.g. the 10 μm feature of forsterite), in order to measure the three parameters.

All these extracted parameters are gathered in a database. This database allows us to study the IR spectral features of crystalline silicate minerals as a combined function of X, T. The database created by all these spectral features are shown in Appendix § B (from Table B.1 through B.16).

Figure 7.9 and 7.10 show how each spectral feature parameter (i.e. peak position, width and amplitude) varies with T and X simultaneously for the 16 & 49 μm features respectively.

It is clear that different combinations of composition and temperature can lead to identical spectral feature parameters (see bold faced numbers in Table B.3 and B.19, note that here we only demonstrating the degeneracy effect of 16 and 49 μm features), which could be misleading when determining the dust composition and temperature simultaneously. For the 16 μm (see Table B.3) feature same spectral feature parameters (peak position, width) are produced by Mg_2SiO_4 at 8, 20 and 50 K; and for $Mg_{1.8}Fe_{0.2}SiO_4$ the same peak position and width are even produced by at higher temperatures at 100 and 200 K; and for Fe_2SiO_4 also same spectral features parameters are produced at 8 and 20 K. For $Mg_{1.11}Fe_{0.89}SiO_4$ at 300 K, we see that the peak is at 17.63 μm; whereas, for Fe_2SiO_4 at 8 and 20 K, the peak is at 17.64 μm. Now if we're able to extrapolate the data for $Mg_{1.11}Fe_{0.89}SiO_4$ at higher temperature (≈ 400 K), that may coincide with the peak positions of Fe_2SiO_4 at low temperature. Thus we see that the degeneracy could be produced by either temperature effect or compositional effect.

7.4 Proposed work

7.4.1 Development of the tool

We propose to extend our 2-D degeneracy study, to include the third dimension (grain shape, ς) and extend it to cover other mineral series (i.e. pyroxenes) and higher temperatures. Laboratory spectra are limited to experimental temperatures <300 K. This is due to radiative transfer considerations. Above ∼300 K emission from the sample will become significant and thus the observed transmission spectrum is a superposition of emission and absorptions. However, in some astrophysical environments we expect dust to be much hotter than 300 K. And to form crystalline grains we expect temperatures above 1000 K (Tielens 1990, Grossman 1972) [137, 48]. Therefore, we also propose to extrapolate the T data for olivine series to higher temperatures. In the case of the olivine series, the T-dependence of the peak positions varies with wavelength and thus the extrapolation will be applied independently for each feature. The extrapolation of T space has not been explored before, but it is a necessary step to consider in order to compare the laboratory data with observational data (further discussed in § 7.4.2).

In addition, we also propose to investigate the pyroxene series by applying the approach developed for the effect of T and X on the olivine series. In this way we will provide a similar 2-D grid of data for pyroxene variations with X and T. This will provide a code that will produce synthetic spectra for any Fe–Mg pyroxene X or T up to 300 K based on data from Kyoto and WashU, which can again be tested against the data from Jena. For pyroxenes the data available is sparser with cruder coverage of the X parameter.

We also propose to extend the degeneracy study to include the effect of ς for both the olivine and pyroxene series based on the approach described in § 3.4 to cover simple shape distributions. Furthermore, recent experimental studies on the evaporation of single crystal of forsterite show that this mineral evaporates anisotropically (Takigawa et al. 2009) [135], which may lead to distinct grain shape distributions which are not centered around spheres. Therefore we will also include weighted distributions of spheroids where the weight is centered at prolate and at oblate spheroids to account for these experimental results.

The final product will be a code which will allow us to specify composition, temperature and grain shape distribution and generate synthetic spectra for olivines and/or Fe–Mg pyroxenes. Furthermore for each spectral feature we will generate contour plots of peak positions, widths and amplitude as a function of X, T and ς in order to allow interpretation of individual observed spectral features.

7.4.2 Application to the astronomical observations

In order to demonstrate the efficacy of this tool, it can be applied to a subset of dusty astrophysical environments, i.e. O-rich AGB stars. The spectral features of SE1 through SE3 classes (for reference see § 4.6: Figure 4.14) objects can be reanalyzed (total of 33 objects; SE1: 4, SE2: 17 and SE3: 12).

To all these objects, we can explore the three physical parameter space (X, T and ς) to find the best fit spectral parameters (peak position, width, amplitude) with the observational data. By using our tool, we can generate synthetic spectra of olivine and/or pyroxene silicates for any value of X or T, and for a range of ς and will be able to determine how well it works. By comparing the degeneracy spaces generated for each spectral feature, the $X - T - \varsigma$ space can be reduced and limits can be placed on the dust grain parameters. This will provide a better understanding of astromineralogy.

7.5 Conclusion & Future work

The varying combinations of composition, temperature and grain shape of crystalline silicate minerals can lead to identical spectral feature parameters, which could be misleading to our understanding of astromineralogy. To break this degeneracy, we developed a database of composition, temperature on observable spectral features. We propose to extend this 2-D degeneracy study to include the third dimension (grain shape) and extend it to cover other mineral series (i.e. pyroxenes) and higher temperatures as well. This tool can be applied to a subset of dusty astrophysical environments (i.e. O-rich stars), in order to improve our understanding on astromineralogy.

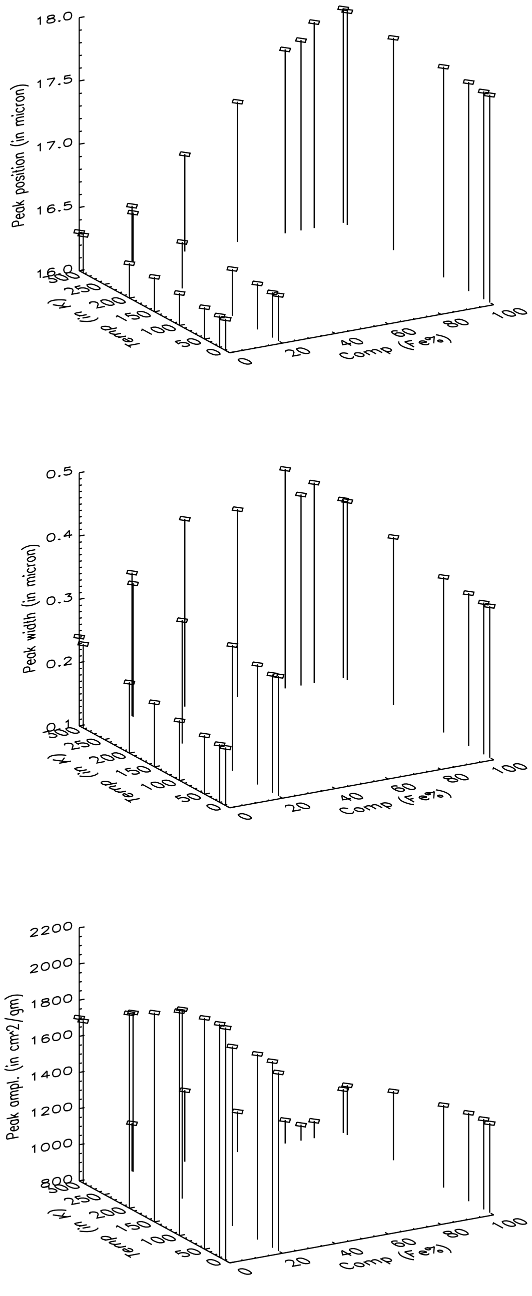

Figure 7.9: 3D plots of peak position, width and amplitude as combined function of composition and temperature of 16 μm feature.

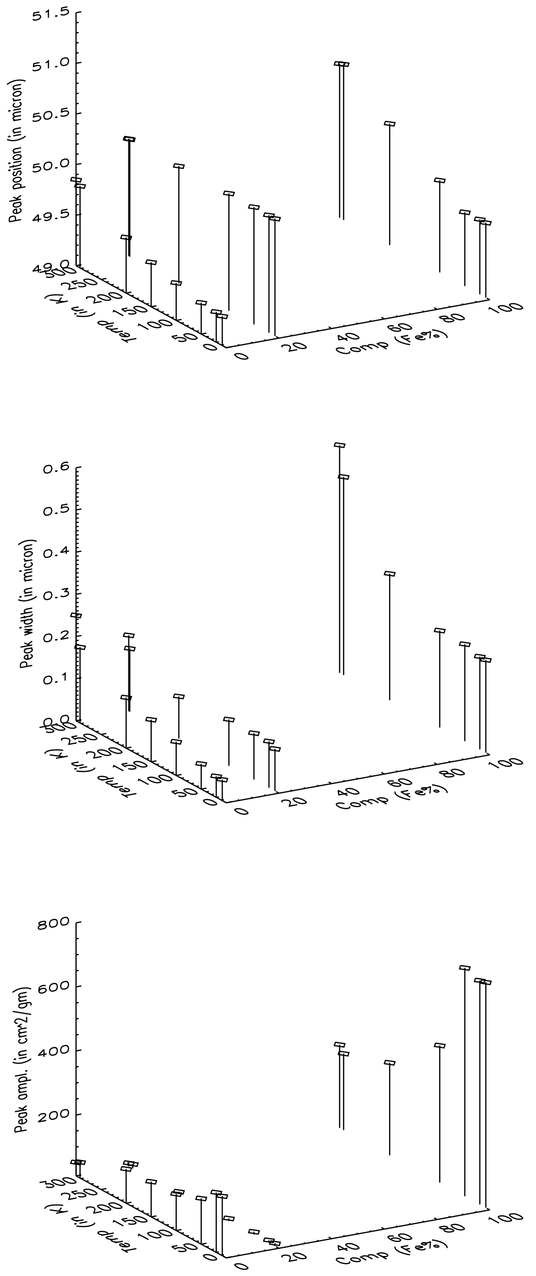

Figure 7.10: 3D plots of peak position, width and amplitude as combined function of composition and temperature of 49 μm feature.

Appendix A

Planck function of blackbody radiation

A blackbody is an ideal object that absorbs all electromagnetic radiation that falls on it. No electromagnetic radiation can pass through it or reflect from it. However, a blackbody emits radiation depending on its temperature (see Figure A.1).

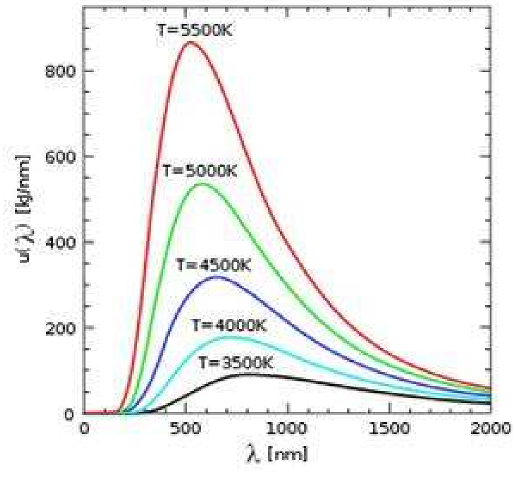

Figure A.1: This plot represents thermal radiation of different objects at different temperature and how the peak wavelength shifts towards short wavelength as the temperature of the object increases.

For an ideal blackbody, Planck's law of blackbody radiation is given by,

$$B_\lambda(T) = \frac{2hc^2}{\lambda^5} \frac{1}{e^{\frac{hc}{\lambda kT}} - 1}, \tag{A.1}$$

where, $B_\lambda(T)$ is energy per unit area per unit wavelength

h is Planck constant (6.626×10^{-34} Js)

k is Boltzmann constant (1.38×10^{-23} JK^{-1})

c is speed of light (2.997×10^{8} ms^{-1})

T is temperature of the blackbody

λ is the wavelength.

Appendix B

Database of crystalline olivine minerals

B.1 Database created by crystalline olivine minerals as a function of composition and temperature

Table B.1: Database of crystalline olivine minerals for 10 μm spectral feature.

Wavelength (μm)	Chemical Composition	Temperature (K)	References (data taken)	peak position (μm)	peak width (μm)	peak ampl. (cm^2/gm)
10.0	Mg_2SiO_4	8	Koike et al.(2006)	10.03	0.17	3713
10.0	Mg_2SiO_4	20	Koike et al.(2006)	10.03	0.18	3719
10.0	Mg_2SiO_4	50	Koike et al.(2006)	10.03	0.18	3732
10.0	Mg_2SiO_4	100	Koike et al.(2006)	10.03	0.18	3822
10.0	Mg_2SiO_4	150	Koike et al.(2006)	10.04	0.19	3979
10.0	Mg_2SiO_4	200	Koike et al.(2006)	10.06	0.20	4186
10.0	Mg_2SiO_4	292	Koike et al.(2006)	10.10	0.23	5127
10.0	Mg_2SiO_4	300	Koike et al.(2003)	10.11	0.24	5549
10.0	$Mg_{1.8}Fe_{0.2}SiO_4$	8	Koike et al.(2006)	10.06	0.20	3795
10.0	$Mg_{1.8}Fe_{0.2}SiO_4$	20	Koike et al.(2006)	10.06	0.20	3801
10.0	$Mg_{1.8}Fe_{0.2}SiO_4$	50	Koike et al.(2006)	10.06	0.20	3784
10.0	$Mg_{1.8}Fe_{0.2}SiO_4$	100	Koike et al.(2006)	10.06	0.20	3702
10.0	$Mg_{1.8}Fe_{0.2}SiO_4$	200	Koike et al.(2006)	10.06	0.20	3795
10.0	$Mg_{1.8}Fe_{0.2}SiO_4$	292	Koike et al.(2006)	10.07	0.21	3825
10.0	$Mg_{1.8}Fe_{0.2}SiO_4$	300	Koike et al.(2003)	10.05	0.16	2630
10.0	$Mg_{1.6}Fe_{0.4}SiO_4$	300	Koike et al.(2003)	10.16	0.40	1195
10.0	$Mg_{1.4}Fe_{0.6}SiO_4$	300	Koike et al.(2003)	10.33	0.40	1025
10.0	$Mg_{1.22}Fe_{0.78}SiO_4$	300	Koike et al.(2003)	10.38	0.45	940
10.0	$Mg_{1.16}Fe_{0.84}SiO_4$	300	Koike et al.(2003)	10.42	0.40	888
10.0	$Mg_{1.11}Fe_{0.89}SiO_4$	300	Koike et al.(2003)	10.48	0.42	896
10.0	Fe_2SiO_4	8	Koike et al.(2006)	10.53	0.30	5996
10.0	Fe_2SiO_4	20	Koike et al.(2006)	10.53	0.30	6388
10.0	Fe_2SiO_4	50	Koike et al.(2006)	10.54	0.31	8849
10.0	Fe_2SiO_4	100	Koike et al.(2006)	10.58	0.35	2137
10.0	Fe_2SiO_4	200	Koike et al.(2006)	10.48	0.18	2952
10.0	Fe_2SiO_4	292	Koike et al.(2006)	10.52	0.24	6923
10.0	Fe_2SiO_4	300	Koike et al.(2003)	10.60	0.36	4792

Table B.2: Database of crystalline olivine minerals for 11 μm spectral feature.

Wavelength (μm)	Chemical Composition	Temperature (K)	References (data taken)	peak position (μm)	peak width (μm)	peak ampl. (cm^2/gm)
11.0	Mg_2SiO_4	8	Koike et al.(2006)	11.16	0.24	4792
11.0	Mg_2SiO_4	20	Koike et al.(2006)	11.16	0.24	4789
11.0	Mg_2SiO_4	50	Koike et al.(2006)	11.17	0.24	4776
11.0	Mg_2SiO_4	100	Koike et al.(2006)	11.17	0.24	4770
11.0	Mg_2SiO_4	150	Koike et al.(2006)	11.17	0.25	4769
11.0	Mg_2SiO_4	200	Koike et al.(2006)	11.18	0.25	4757
11.0	Mg_2SiO_4	292	Koike et al.(2006)	11.19	0.26	4737
11.0	Mg_2SiO_4	300	Koike et al.(2003)	11.19	0.26	4720
11.0	$Mg_{1.8}Fe_{0.2}SiO_4$	8	Koike et al.(2006)	11.17	0.23	5374
11.0	$Mg_{1.8}Fe_{0.2}SiO_4$	20	Koike et al.(2006)	11.17	0.23	5394
11.0	$Mg_{1.8}Fe_{0.2}SiO_4$	50	Koike et al.(2006)	11.17	0.23	5384
11.0	$Mg_{1.8}Fe_{0.2}SiO_4$	100	Koike et al.(2006)	11.17	0.23	5266
11.0	$Mg_{1.8}Fe_{0.2}SiO_4$	200	Koike et al.(2006)	11.17	0.23	5387
11.0	$Mg_{1.8}Fe_{0.2}SiO_4$	292	Koike et al.(2006)	11.18	0.24	5337
11.0	$Mg_{1.8}Fe_{0.2}SiO_4$	300	Koike et al.(2003)	11.18	0.22	5030
11.0	$Mg_{1.6}Fe_{0.4}SiO_4$	300	Koike et al.(2003)	11.24	0.21	5022
11.0	$Mg_{1.4}Fe_{0.6}SiO_4$	300	Koike et al.(2003)	11.31	0.20	3927
11.0	$Mg_{1.22}Fe_{0.78}SiO_4$	300	Koike et al.(2003)	11.39	0.20	2104
11.0	$Mg_{1.16}Fe_{0.84}SiO_4$	300	Koike et al.(2003)	11.39	0.20	2263
11.0	$Mg_{1.11}Fe_{0.89}SiO_4$	300	Koike et al.(2003)	11.43	0.21	1727
11.0	Fe_2SiO_4	8	Koike et al.(2006)	11.37	0.18	2961
11.0	Fe_2SiO_4	20	Koike et al.(2006)	11.37	0.18	2964
11.0	Fe_2SiO_4	50	Koike et al.(2006)	11.37	0.18	2942
11.0	Fe_2SiO_4	100	Koike et al.(2006)	11.37	0.18	2867
11.0	Fe_2SiO_4	200	Koike et al.(2006)	11.39	0.18	2728
11.0	Fe_2SiO_4	292	Koike et al.(2006)	11.41	0.19	2516
11.0	Fe_2SiO_4	300	Koike et al.(2003)	11.41	0.19	2491

Table B.3: Database of crystalline olivine minerals for 16 μm spectral feature.

Wavelength (μm)	Chemical Composition	Temperature (K)	References (data taken)	peak position (μm)	peak width (μm)	peak ampl. (cm^2/gm)
16.0	Mg_2SiO_4	8	Koike et al.(2006)	**16.25**	**0.19**	2090
16.0	Mg_2SiO_4	20	Koike et al.(2006)	**16.25**	**0.19**	2092
16.0	Mg_2SiO_4	50	Koike et al.(2006)	**16.25**	**0.19**	2072
16.0	Mg_2SiO_4	100	Koike et al.(2006)	16.26	0.20	2041
16.0	Mg_2SiO_4	150	Koike et al.(2006)	16.27	0.20	1958
16.0	Mg_2SiO_4	200	Koike et al.(2006)	16.28	0.21	1878
16.0	Mg_2SiO_4	292	Koike et al.(2006)	16.30	0.23	1697
16.0	Mg_2SiO_4	300	Koike et al.(2003)	16.31	0.24	1703
16.0	$Mg_{1.8}Fe_{0.2}SiO_4$	8	Koike et al.(2006)	**16.36**	**0.29**	1788
16.0	$Mg_{1.8}Fe_{0.2}SiO_4$	20	Koike et al.(2006)	**16.36**	**0.29**	1832
16.0	$Mg_{1.8}Fe_{0.2}SiO_4$	50	Koike et al.(2006)	16.36	0.30	1827
16.0	$Mg_{1.8}Fe_{0.2}SiO_4$	100	Koike et al.(2006)	**16.37**	**0.30**	1793
16.0	$Mg_{1.8}Fe_{0.2}SiO_4$	200	Koike et al.(2006)	**16.37**	**0.30**	1848
16.0	$Mg_{1.8}Fe_{0.2}SiO_4$	292	Koike et al.(2006)	16.39	0.31	1682
16.0	$Mg_{1.8}Fe_{0.2}SiO_4$	300	Koike et al.(2003)	16.44	0.33	1086
16.0	$Mg_{1.6}Fe_{0.4}SiO_4$	300	Koike et al.(2003)	16.77	0.40	1195
16.0	$Mg_{1.4}Fe_{0.6}SiO_4$	300	Koike et al.(2003)	17.11	0.40	1025
16.0	$Mg_{1.22}Fe_{0.78}SiO_4$	300	Koike et al.(2003)	17.45	0.45	940
16.0	$Mg_{1.16}Fe_{0.84}SiO_4$	300	Koike et al.(2003)	17.51	0.40	888
16.0	$Mg_{1.11}Fe_{0.89}SiO_4$	300	Koike et al.(2003)	17.63	0.42	896
16.0	Fe_2SiO_4	8	Koike et al.(2006)	**17.64**	**0.34**	1296
16.0	Fe_2SiO_4	20	Koike et al.(2006)	**17.64**	**0.34**	1300
16.0	Fe_2SiO_4	50	Koike et al.(2006)	17.65	0.34	1289
16.0	Fe_2SiO_4	100	Koike et al.(2006)	17.67	0.35	1257
16.0	Fe_2SiO_4	200	Koike et al.(2006)	17.68	0.37	1182
16.0	Fe_2SiO_4	292	Koike et al.(2006)	17.69	0.38	1076
16.0	Fe_2SiO_4	300	Koike et al.(2003)	17.70	0.38	1041

Table B.4: Database of crystalline olivine minerals for 19 μm spectral feature.

Wavelength (μm)	Chemical Composition	Temperature (K)	References (data taken)	peak position (μm)	peak width (μm)	peak ampl. (cm^2/gm)
19.0	Mg_2SiO_4	8	Koike et al.(2006)	19.51	0.19	2090
19.0	Mg_2SiO_4	20	Koike et al.(2006)	19.51	0.19	2092
19.0	Mg_2SiO_4	50	Koike et al.(2006)	19.52	0.19	2072
19.0	Mg_2SiO_4	100	Koike et al.(2006)	19.54	0.20	2041
19.0	Mg_2SiO_4	150	Koike et al.(2006)	19.56	0.20	1958
19.0	Mg_2SiO_4	200	Koike et al.(2006)	19.59	0.21	1878
19.0	Mg_2SiO_4	292	Koike et al.(2006)	19.63	0.23	1697
19.0	Mg_2SiO_4	300	Koike et al.(2003)	19.66	0.24	1703
19.0	$Mg_{1.8}Fe_{0.2}SiO_4$	8	Koike et al.(2006)	19.71	0.29	1788
19.0	$Mg_{1.8}Fe_{0.2}SiO_4$	20	Koike et al.(2006)	19.71	0.29	1832
19.0	$Mg_{1.8}Fe_{0.2}SiO_4$	50	Koike et al.(2006)	19.72	0.30	1827
19.0	$Mg_{1.8}Fe_{0.2}SiO_4$	100	Koike et al.(2006)	19.77	0.30	1793
19.0	$Mg_{1.8}Fe_{0.2}SiO_4$	200	Koike et al.(2006)	19.79	0.30	1848
19.0	$Mg_{1.8}Fe_{0.2}SiO_4$	292	Koike et al.(2006)	19.24	0.31	1682
19.0	$Mg_{1.8}Fe_{0.2}SiO_4$	300	Koike et al.(2003)	19.44	0.33	1086
19.0	$Mg_{1.6}Fe_{0.4}SiO_4$	300	Koike et al.(2003)	19.22	0.30	1695
19.0	$Mg_{1.4}Fe_{0.6}SiO_4$	300	Koike et al.(2003)	19.23	0.32	1525
19.0	$Mg_{1.22}Fe_{0.78}SiO_4$	300	Koike et al.(2003)	19.31	0.35	1440
19.0	$Mg_{1.16}Fe_{0.84}SiO_4$	300	Koike et al.(2003)	19.34	0.38	1388
19.0	$Mg_{1.11}Fe_{0.89}SiO_4$	300	Koike et al.(2003)	19.40	0.40	1396
19.0	Fe_2SiO_4	8	Koike et al.(2006)	19.50	0.16	1896
19.0	Fe_2SiO_4	20	Koike et al.(2006)	19.50	0.16	1900
19.0	Fe_2SiO_4	50	Koike et al.(2006)	19.51	0.17	1889
19.0	Fe_2SiO_4	100	Koike et al.(2006)	19.51	0.17	1857
19.0	Fe_2SiO_4	200	Koike et al.(2006)	19.52	0.18	1782
19.0	Fe_2SiO_4	292	Koike et al.(2006)	19.55	0.18	1676
19.0	Fe_2SiO_4	300	Koike et al.(2003)	19.59	0.20	1641

Table B.5: Database of crystalline olivine minerals for 21 μm spectral feature.

Wavelength (μm)	Chemical Composition	Temperature (K)	References (data taken)	peak position (μm)	peak width (μm)	peak ampl. (cm^2/gm)
21.0	Mg_2SiO_4	8	Koike et al.(2006)	21.05	0.37	1590
21.0	Mg_2SiO_4	20	Koike et al.(2006)	21.05	0.37	1576
21.0	Mg_2SiO_4	50	Koike et al.(2006)	21.05	0.37	1639
21.0	Mg_2SiO_4	100	Koike et al.(2006)	21.08	0.38	1701
21.0	Mg_2SiO_4	150	Koike et al.(2006)	21.06	0.39	1404
21.0	Mg_2SiO_4	200	Koike et al.(2006)	21.09	0.41	1231
21.0	Mg_2SiO_4	292	Koike et al.(2006)	21.11	0.43	1420
21.0	Mg_2SiO_4	300	Koike et al.(2003)	21.13	0.46	1196
21.0	$Mg_{1.8}Fe_{0.2}SiO_4$	8	Koike et al.(2006)	21.02	0.32	1185
21.0	$Mg_{1.8}Fe_{0.2}SiO_4$	20	Koike et al.(2006)	21.02	0.32	1184
21.0	$Mg_{1.8}Fe_{0.2}SiO_4$	50	Koike et al.(2006)	21.03	0.35	1025
21.0	$Mg_{1.8}Fe_{0.2}SiO_4$	100	Koike et al.(2006)	21.05	0.36	983
21.0	$Mg_{1.8}Fe_{0.2}SiO_4$	200	Koike et al.(2006)	21.08	0.37	803
21.0	$Mg_{1.8}Fe_{0.2}SiO_4$	292	Koike et al.(2006)	21.08	0.37	783
21.0	$Mg_{1.8}Fe_{0.2}SiO_4$	300	Koike et al.(2003)	21.10	0.40	750
21.0	$Mg_{1.6}Fe_{0.4}SiO_4$	300	Koike et al.(2003)	20.88	0.42	1539
21.0	$Mg_{1.4}Fe_{0.6}SiO_4$	300	Koike et al.(2003)	20.89	0.44	1418
21.0	$Mg_{1.22}Fe_{0.78}SiO_4$	300	Koike et al.(2003)	20.95	0.46	1222
21.0	$Mg_{1.16}Fe_{0.84}SiO_4$	300	Koike et al.(2003)	20.88	0.43	1210
21.0	$Mg_{1.11}Fe_{0.89}SiO_4$	300	Koike et al.(2003)	20.98	0.45	1047
21.0	Fe_2SiO_4	8	Koike et al.(2006)	20.97	0.36	1624
21.0	Fe_2SiO_4	20	Koike et al.(2006)	20.97	0.36	1619
21.0	Fe_2SiO_4	50	Koike et al.(2006)	20.97	0.36	1622
21.0	Fe_2SiO_4	100	Koike et al.(2006)	20.97	0.38	1519
21.0	Fe_2SiO_4	200	Koike et al.(2006)	20.97	0.41	1288
21.0	Fe_2SiO_4	292	Koike et al.(2006)	20.97	0.45	1014
21.0	Fe_2SiO_4	300	Koike et al.(2003)	20.98	0.44	1085

Table B.6: Database of crystalline olivine minerals for 23 μm spectral feature.

Wavelength (μm)	Chemical Composition	Temperature (K)	References (data taken)	peak position (μm)	peak width (μm)	peak ampl. (cm^2/gm)
23.0	Mg_2SiO_4	8	Koike et al.(2006)	23.50	0.37	3590
23.0	Mg_2SiO_4	20	Koike et al.(2006)	23.50	0.37	3576
23.0	Mg_2SiO_4	50	Koike et al.(2006)	23.51	0.38	3639
23.0	Mg_2SiO_4	100	Koike et al.(2006)	23.54	0.41	3701
23.0	Mg_2SiO_4	150	Koike et al.(2006)	23.56	0.41	3404
23.0	Mg_2SiO_4	200	Koike et al.(2006)	23.59	0.41	3231
23.0	Mg_2SiO_4	292	Koike et al.(2006)	23.69	0.49	3420
23.0	Mg_2SiO_4	300	Koike et al.(2003)	23.67	0.46	3196
23.0	$Mg_{1.8}Fe_{0.2}SiO_4$	8	Koike et al.(2006)	23.76	0.47	3187
23.0	$Mg_{1.8}Fe_{0.2}SiO_4$	20	Koike et al.(2006)	23.76	0.47	3184
23.0	$Mg_{1.8}Fe_{0.2}SiO_4$	50	Koike et al.(2006)	23.76	0.46	3020
23.0	$Mg_{1.8}Fe_{0.2}SiO_4$	100	Koike et al.(2006)	23.78	0.47	2983
23.0	$Mg_{1.8}Fe_{0.2}SiO_4$	200	Koike et al.(2006)	23.85	0.51	2803
23.0	$Mg_{1.8}Fe_{0.2}SiO_4$	292	Koike et al.(2006)	24.00	0.65	3453
23.0	$Mg_{1.8}Fe_{0.2}SiO_4$	300	Koike et al.(2003)	23.98	0.72	1780
23.0	$Mg_{1.6}Fe_{0.4}SiO_4$	300	Koike et al.(2003)	24.86	0.92	1539
23.0	$Mg_{1.4}Fe_{0.6}SiO_4$	300	Koike et al.(2003)	24.50	0.25	1232
23.0	$Mg_{1.22}Fe_{0.78}SiO_4$	300	Koike et al.(2003)	24.17	0.57	1035
23.0	$Mg_{1.16}Fe_{0.84}SiO_4$	300	Koike et al.(2003)	24.25	0.49	1020
23.0	$Mg_{1.11}Fe_{0.89}SiO_4$	300	Koike et al.(2003)	24.21	0.35	987
23.0	Fe_2SiO_4	8	–	–	–	–
23.0	Fe_2SiO_4	20	–	–	–	–
23.0	Fe_2SiO_4	50	–	–	–	–
23.0	Fe_2SiO_4	100	–	–	–	–
23.0	Fe_2SiO_4	200	–	–	–	–
23.0	Fe_2SiO_4	292	–	–	–	–
23.0	Fe_2SiO_4	300	–	–	–	–

Table B.7: Database of crystalline olivine minerals for 26 μm spectral feature.

Wavelength (μm)	Chemical Composition	Temperature (K)	References (data taken)	peak position (μm)	peak width (μm)	peak ampl. (cm^2/gm)
26.0	Mg_2SiO_4	8	Koike et al.(2006)	25.77	0.11	1374
26.0	Mg_2SiO_4	20	Koike et al.(2006)	25.77	0.11	1473
26.0	Mg_2SiO_4	50	Koike et al.(2006)	26.02	0.12	1223
26.0	Mg_2SiO_4	100	Koike et al.(2006)	25.82	0.10	993
26.0	Mg_2SiO_4	150	Koike et al.(2006)	25.86	0.12	985
26.0	Mg_2SiO_4	200	Koike et al.(2006)	25.91	0.13	970
26.0	Mg_2SiO_4	292	Koike et al.(2006)	26.02	0.18	958
26.0	Mg_2SiO_4	300	Koike et al.(2003)	26.08	0.18	868
26.0	$Mg_{1.8}Fe_{0.2}SiO_4$	8	Koike et al.(2006)	26.08	0.16	791
26.0	$Mg_{1.8}Fe_{0.2}SiO_4$	20	Koike et al.(2006)	26.08	0.16	797
26.0	$Mg_{1.8}Fe_{0.2}SiO_4$	50	Koike et al.(2006)	26.09	0.16	756
26.0	$Mg_{1.8}Fe_{0.2}SiO_4$	100	Koike et al.(2006)	26.12	0.18	740
26.0	$Mg_{1.8}Fe_{0.2}SiO_4$	200	Koike et al.(2006)	26.26	0.18	455
26.0	$Mg_{1.8}Fe_{0.2}SiO_4$	292	Koike et al.(2006)	26.40	0.20	305
26.0	$Mg_{1.8}Fe_{0.2}SiO_4$	300	Koike et al.(2003)	26.45	0.22	268
26.0	$Mg_{1.6}Fe_{0.4}SiO_4$	300	Koike et al.(2003)	25.66	0.46	824
26.0	$Mg_{1.4}Fe_{0.6}SiO_4$	300	Koike et al.(2003)	25.78	0.55	665
26.0	$Mg_{1.22}Fe_{0.78}SiO_4$	300	Koike et al.(2003)	26.41	0.79	558
26.0	$Mg_{1.16}Fe_{0.84}SiO_4$	300	Koike et al.(2003)	26.65	0.84	432
26.0	$Mg_{1.11}Fe_{0.89}SiO_4$	300	Koike et al.(2003)	26.96	0.92	530
26.0	Fe_2SiO_4	8	Koike et al.(2006)	26.03	0.32	514
26.0	Fe_2SiO_4	20	Koike et al.(2006)	26.03	0.32	516
26.0	Fe_2SiO_4	50	Koike et al.(2006)	26.03	0.32	520
26.0	Fe_2SiO_4	100	Koike et al.(2006)	26.06	0.34	429
26.0	Fe_2SiO_4	200	Koike et al.(2006)	26.15	0.36	271
26.0	Fe_2SiO_4	292	Koike et al.(2006)	26.18	0.38	245
26.0	Fe_2SiO_4	300	Koike et al.(2003)	26.20	0.41	219

Table B.8: Database of crystalline olivine minerals for 27 μm spectral feature.

Wavelength (μm)	Chemical Composition	Temperature (K)	References (data taken)	peak position (μm)	peak width (μm)	peak ampl. (cm^2/gm)
27.0	Mg_2SiO_4	8	Koike et al.(2006)	27.20	0.35	1672
27.0	Mg_2SiO_4	20	Koike et al.(2006)	27.20	0.34	1613
27.0	Mg_2SiO_4	50	Koike et al.(2006)	27.19	0.40	1899
27.0	Mg_2SiO_4	100	Koike et al.(2006)	27.22	0.38	1708
27.0	Mg_2SiO_4	150	Koike et al.(2006)	27.27	0.36	1450
27.0	Mg_2SiO_4	200	Koike et al.(2006)	27.35	0.42	1569
27.0	Mg_2SiO_4	292	Koike et al.(2006)	27.47	0.44	1373
27.0	Mg_2SiO_4	300	Koike et al.(2003)	27.46	0.44	1390
27.0	$Mg_{1.8}Fe_{0.2}SiO_4$	8	Koike et al.(2006)	27.44	0.52	1019
27.0	$Mg_{1.8}Fe_{0.2}SiO_4$	20	Koike et al.(2006)	27.43	0.53	1043
27.0	$Mg_{1.8}Fe_{0.2}SiO_4$	50	Koike et al.(2006)	27.45	0.53	1003
27.0	$Mg_{1.8}Fe_{0.2}SiO_4$	100	Koike et al.(2006)	27.50	0.51	919
27.0	$Mg_{1.8}Fe_{0.2}SiO_4$	200	Koike et al.(2006)	27.66	0.48	732
27.0	$Mg_{1.8}Fe_{0.2}SiO_4$	292	Koike et al.(2006)	27.81	0.52	675
27.0	$Mg_{1.8}Fe_{0.2}SiO_4$	300	Koike et al.(2003)	27.82	0.76	546
27.0	$Mg_{1.6}Fe_{0.4}SiO_4$	300	Koike et al.(2003)	27.83	0.76	550
27.0	$Mg_{1.4}Fe_{0.6}SiO_4$	300	Koike et al.(2003)	27.84	0.74	523
27.0	$Mg_{1.22}Fe_{0.78}SiO_4$	300	Koike et al.(2003)	27.88	0.79	486
27.0	$Mg_{1.16}Fe_{0.84}SiO_4$	300	Koike et al.(2003)	27.90	0.80	349
27.0	$Mg_{1.11}Fe_{0.89}SiO_4$	300	Koike et al.(2003)	27.93	0.82	319
27.0	Fe_2SiO_4	8	Koike et al.(2006)	27.52	0.35	820
27.0	Fe_2SiO_4	20	Koike et al.(2006)	27.52	0.35	810
27.0	Fe_2SiO_4	50	Koike et al.(2006)	27.52	0.35	810
27.0	Fe_2SiO_4	100	Koike et al.(2006)	27.56	0.37	720
27.0	Fe_2SiO_4	200	Koike et al.(2006)	27.63	0.38	495
27.0	Fe_2SiO_4	292	Koike et al.(2006)	27.69	0.42	321
27.0	Fe_2SiO_4	300	Koike et al.(2003)	27.70	0.44	350

Table B.9: Database of crystalline olivine minerals for 31 μm spectral feature.

Wavelength (μm)	Chemical Composition	Temperature (K)	References (data taken)	peak position (μm)	peak width (μm)	peak ampl. (cm^2/gm)
31.0	Mg_2SiO_4	8	Koike et al.(2006)	31.07	0.04	580
31.0	Mg_2SiO_4	20	Koike et al.(2006)	31.07	0.04	557
31.0	Mg_2SiO_4	50	Koike et al.(2006)	31.07	0.04	484
31.0	Mg_2SiO_4	100	Koike et al.(2006)	31.12	0.05	429
31.0	Mg_2SiO_4	150	Koike et al.(2006)	31.19	0.04	374
31.0	Mg_2SiO_4	200	Koike et al.(2006)	31.18	0.05	406
31.0	Mg_2SiO_4	292	Koike et al.(2006)	31.22	0.04	196
31.0	Mg_2SiO_4	300	Koike et al.(2003)	31.27	0.12	303
31.0	$Mg_{1.8}Fe_{0.2}SiO_4$	8	–	–	–	–
31.0	$Mg_{1.8}Fe_{0.2}SiO_4$	20	–	–	–	–
31.0	$Mg_{1.8}Fe_{0.2}SiO_4$	50	–	–	–	–
31.0	$Mg_{1.8}Fe_{0.2}SiO_4$	100	–	–	–	–
31.0	$Mg_{1.8}Fe_{0.2}SiO_4$	200	–	–	–	–
31.0	$Mg_{1.8}Fe_{0.2}SiO_4$	292	–	–	–	–
31.0	$Mg_{1.8}Fe_{0.2}SiO_4$	300	–	–	–	–
31.0	$Mg_{1.6}Fe_{0.4}SiO_4$	300	Koike et al.(2003)	30.18	0.79	980
31.0	$Mg_{1.4}Fe_{0.6}SiO_4$	300	Koike et al.(2003)	30.29	0.85	962
31.0	$Mg_{1.22}Fe_{0.78}SiO_4$	300	Koike et al.(2003)	30.38	1.07	833
31.0	$Mg_{1.16}Fe_{0.84}SiO_4$	300	Koike et al.(2003)	30.58	0.97	999
31.0	$Mg_{1.11}Fe_{0.89}SiO_4$	300	Koike et al.(2003)	30.88	1.22	827
31.0	Fe_2SiO_4	8	Koike et al.(2006)	31.52	2.00	2949
31.0	Fe_2SiO_4	20	Koike et al.(2006)	31.54	2.01	2954
31.0	Fe_2SiO_4	50	Koike et al.(2006)	31.51	2.00	2943
31.0	Fe_2SiO_4	100	Koike et al.(2006)	31.63	2.00	2785
31.0	Fe_2SiO_4	200	Koike et al.(2006)	31.83	2.00	2400
31.0	Fe_2SiO_4	292	Koike et al.(2006)	32.08	1.97	2022
31.0	Fe_2SiO_4	300	Koike et al.(2003)	32.04	2.15	2353

Table B.10: Database of crystalline olivine minerals for 33 μm spectral feature.

Wavelength (μm)	Chemical Composition	Temperature (K)	References (data taken)	peak position (μm)	peak width (μm)	peak ampl. (cm^2/gm)
33.0	Mg_2SiO_4	8	Koike et al.(2006)	33.56	0.10	1276
33.0	Mg_2SiO_4	20	Koike et al.(2006)	33.56	0.12	1474
33.0	Mg_2SiO_4	50	Koike et al.(2006)	33.57	0.12	1399
33.0	Mg_2SiO_4	100	Koike et al.(2006)	33.50	0.32	2481
33.0	Mg_2SiO_4	150	Koike et al.(2006)	33.54	0.35	2325
33.0	Mg_2SiO_4	200	Koike et al.(2006)	33.61	0.37	2165
33.0	Mg_2SiO_4	292	Koike et al.(2006)	33.71	0.45	2060
33.0	Mg_2SiO_4	300	Koike et al.(2003)	33.72	0.44	1969
33.0	$Mg_{1.8}Fe_{0.2}SiO_4$	8	Koike et al.(2006)	33.64	0.83	1588
33.0	$Mg_{1.8}Fe_{0.2}SiO_4$	20	Koike et al.(2006)	33.64	0.83	1595
33.0	$Mg_{1.8}Fe_{0.2}SiO_4$	50	Koike et al.(2006)	33.65	0.85	1632
33.0	$Mg_{1.8}Fe_{0.2}SiO_4$	100	Koike et al.(2006)	33.67	0.87	1654
33.0	$Mg_{1.8}Fe_{0.2}SiO_4$	200	Koike et al.(2006)	33.77	0.88	1538
33.0	$Mg_{1.8}Fe_{0.2}SiO_4$	292	Koike et al.(2006)	33.87	0.84	1278
33.0	$Mg_{1.8}Fe_{0.2}SiO_4$	300	Koike et al.(2003)	33.94	0.93	558
33.0	$Mg_{1.6}Fe_{0.4}SiO_4$	300	–	–	–	–
33.0	$Mg_{1.4}Fe_{0.6}SiO_4$	300	–	–	–	–
33.0	$Mg_{1.22}Fe_{0.78}SiO_4$	300	–	–	–	–
33.0	$Mg_{1.16}Fe_{0.84}SiO_4$	300	–	–	–	–
33.0	$Mg_{1.11}Fe_{0.89}SiO_4$	300	–	–	–	–
33.0	Fe_2SiO_4	8	–	–	–	–
33.0	Fe_2SiO_4	20	–	–	–	–
33.0	Fe_2SiO_4	50	–	–	–	–
33.0	Fe_2SiO_4	100	–	–	–	–
33.0	Fe_2SiO_4	200	–	–	–	–
33.0	Fe_2SiO_4	292	–	–	–	–
33.0	Fe_2SiO_4	300	–	–	–	–

Table B.11: Database of crystalline olivine minerals for 35 μm spectral feature.

Wavelength (μm)	Chemical Composition	Temperature (K)	References (data taken)	peak position (μm)	peak width (μm)	peak ampl. (cm^2/gm)
35.0	Mg_2SiO_4	8	Koike et al.(2006)	35.87	0.06	710
35.0	Mg_2SiO_4	20	Koike et al.(2006)	35.87	0.06	684
35.0	Mg_2SiO_4	50	Koike et al.(2006)	35.87	0.08	955
35.0	Mg_2SiO_4	100	Koike et al.(2006)	35.91	0.09	735
35.0	Mg_2SiO_4	150	Koike et al.(2006)	35.93	0.10	665
35.0	Mg_2SiO_4	200	Koike et al.(2006)	35.95	0.13	595
35.0	Mg_2SiO_4	292	Koike et al.(2006)	35.98	0.14	542
35.0	Mg_2SiO_4	300	Koike et al.(2003)	35.99	0.15	498
35.0	$Mg_{1.8}Fe_{0.2}SiO_4$	8	–	–	–	–
35.0	$Mg_{1.8}Fe_{0.2}SiO_4$	20	–	–	–	–
35.0	$Mg_{1.8}Fe_{0.2}SiO_4$	50	–	–	–	–
35.0	$Mg_{1.8}Fe_{0.2}SiO_4$	100	–	–	–	–
35.0	$Mg_{1.8}Fe_{0.2}SiO_4$	200	–	–	–	–
35.0	$Mg_{1.8}Fe_{0.2}SiO_4$	292	–	–	–	–
35.0	$Mg_{1.8}Fe_{0.2}SiO_4$	300	–	–	–	–
35.0	$Mg_{1.6}Fe_{0.4}SiO_4$	300	–	–	–	–
35.0	$Mg_{1.4}Fe_{0.6}SiO_4$	300	–	–	–	–
35.0	$Mg_{1.22}Fe_{0.78}SiO_4$	300	–	–	–	–
35.0	$Mg_{1.16}Fe_{0.84}SiO_4$	300	–	–	–	–
35.0	$Mg_{1.11}Fe_{0.89}SiO_4$	300	–	–	–	–
35.0	Fe_2SiO_4	8	–	–	–	–
35.0	Fe_2SiO_4	20	–	–	–	–
35.0	Fe_2SiO_4	50	–	–	–	–
35.0	Fe_2SiO_4	100	–	–	–	–
35.0	Fe_2SiO_4	200	–	–	–	–
35.0	Fe_2SiO_4	292	–	–	–	–
35.0	Fe_2SiO_4	300	–	–	–	–

Table B.12: Database of crystalline olivine minerals for 38 μm spectral feature.

Wavelength (μm)	Chemical Composition	Temperature (K)	References (data taken)	peak position (μm)	peak width (μm)	peak ampl. (cm^2/gm)
38.0	Mg_2SiO_4	8	–	–	–	–
38.0	Mg_2SiO_4	20	–	–	–	–
38.0	Mg_2SiO_4	50	–	–	–	–
38.0	Mg_2SiO_4	100	–	–	–	–
38.0	Mg_2SiO_4	150	–	–	–	–
38.0	Mg_2SiO_4	200	–	–	–	–
38.0	Mg_2SiO_4	292	–	–	–	–
38.0	Mg_2SiO_4	300	–	–	–	–
38.0	$Mg_{1.8}Fe_{0.2}SiO_4$	8	–	–	–	–
38.0	$Mg_{1.8}Fe_{0.2}SiO_4$	20	–	–	–	–
38.0	$Mg_{1.8}Fe_{0.2}SiO_4$	50	–	–	–	–
38.0	$Mg_{1.8}Fe_{0.2}SiO_4$	100	–	–	–	–
38.0	$Mg_{1.8}Fe_{0.2}SiO_4$	200	–	–	–	–
38.0	$Mg_{1.8}Fe_{0.2}SiO_4$	292	–	–	–	–
38.0	$Mg_{1.8}Fe_{0.2}SiO_4$	300	–	–	–	–
38.0	$Mg_{1.6}Fe_{0.4}SiO_4$	300	–	–	–	–
38.0	$Mg_{1.4}Fe_{0.6}SiO_4$	300	–	–	–	–
38.0	$Mg_{1.22}Fe_{0.78}SiO_4$	300	–	–	–	–
38.0	$Mg_{1.16}Fe_{0.84}SiO_4$	300	–	–	–	–
38.0	$Mg_{1.11}Fe_{0.89}SiO_4$	300	–	–	–	–
38.0	Fe_2SiO_4	8	Koike et al.(2006)	38.50	0.12	320
38.0	Fe_2SiO_4	20	Koike et al.(2006)	38.50	0.12	295
38.0	Fe_2SiO_4	50	Koike et al.(2006)	38.50	0.13	270
38.0	Fe_2SiO_4	100	Koike et al.(2006)	38.52	0.15	250
38.0	Fe_2SiO_4	200	Koike et al.(2006)	38.54	0.16	223
38.0	Fe_2SiO_4	292	Koike et al.(2006)	38.56	0.18	206
38.0	Fe_2SiO_4	300	Koike et al.(2003)	38.58	0.20	175

Table B.13: Database of crystalline olivine minerals for 49 μm spectral feature.

Wavelength (μm)	Chemical Composition	Temperature (K)	References (data taken)	peak position (μm)	peak width (μm)	peak ampl. (cm^2/gm)
49.0	Mg_2SiO_4	8	Koike et al.(2006)	49.29	0.05	196
49.0	Mg_2SiO_4	20	Koike et al.(2006)	49.30	0.05	197
49.0	Mg_2SiO_4	50	Koike et al.(2006)	49.31	0.06	153
49.0	Mg_2SiO_4	100	Koike et al.(2006)	49.37	0.08	124
49.0	Mg_2SiO_4	150	Koike et al.(2006)	49.42	0.10	120
49.0	Mg_2SiO_4	200	Koike et al.(2006)	49.55	0.12	117
49.0	Mg_2SiO_4	292	Koike et al.(2006)	49.81	0.18	60
49.0	Mg_2SiO_4	300	Koike et al.(2003)	49.60	0.55	152
49.0	$Mg_{1.8}Fe_{0.2}SiO_4$	8	Koike et al.(2006)	**50.16**	0.10	19
49.0	$Mg_{1.8}Fe_{0.2}SiO_4$	20	Koike et al.(2006)	**50.16**	**0.11**	18
49.0	$Mg_{1.8}Fe_{0.2}SiO_4$	50	Koike et al.(2006)	**50.16**	**0.11**	19
49.0	$Mg_{1.8}Fe_{0.2}SiO_4$	100	Koike et al.(2006)	**50.16**	**0.11**	18
49.0	$Mg_{1.8}Fe_{0.2}SiO_4$	200	Koike et al.(2006)	**50.16**	0.10	16
49.0	$Mg_{1.8}Fe_{0.2}SiO_4$	292	Koike et al.(2006)	50.16	0.15	24
49.0	$Mg_{1.8}Fe_{0.2}SiO_4$	300	Koike et al.(2003)	50.18	0.16	14
49.0	$Mg_{1.6}Fe_{0.4}SiO_4$	300	–	–	–	–
49.0	$Mg_{1.4}Fe_{0.6}SiO_4$	300	–	–	–	–
49.0	$Mg_{1.22}Fe_{0.78}SiO_4$	300	–	–	–	–
49.0	$Mg_{1.16}Fe_{0.84}SiO_4$	300	–	–	–	–
49.0	$Mg_{1.11}Fe_{0.89}SiO_4$	300	Koike et al.(2003)	49.35	1.28	62
49.0	Fe_2SiO_4	8	Koike et al.(2006)	49.74	0.22	714
49.0	Fe_2SiO_4	20	Koike et al.(2006)	49.74	0.23	709
49.0	Fe_2SiO_4	50	Koike et al.(2006)	49.73	0.22	723
49.0	Fe_2SiO_4	100	Koike et al.(2006)	49.91	0.23	438
49.0	Fe_2SiO_4	200	Koike et al.(2006)	50.20	0.30	299
49.0	Fe_2SiO_4	292	Koike et al.(2006)	50.54	0.47	249
49.0	Fe_2SiO_4	300	Koike et al.(2003)	50.52	0.54	270

Table B.14: Database of crystalline olivine minerals for 53 μm spectral feature.

Wavelength (μm)	Chemical Composition	Temperature (K)	References (data taken)	peak position (μm)	peak width (μm)	peak ampl. (cm^2/gm)
53.0	Mg_2SiO_4	8	–	–	–	–
53.0	Mg_2SiO_4	20	–	–	–	–
53.0	Mg_2SiO_4	50	–	–	–	–
53.0	Mg_2SiO_4	100	–	–	–	–
53.0	Mg_2SiO_4	150	–	–	–	–
53.0	Mg_2SiO_4	200	–	–	–	–
53.0	Mg_2SiO_4	292	–	–	–	–
53.0	Mg_2SiO_4	300	–	–	–	–
53.0	$Mg_{1.8}Fe_{0.2}SiO_4$	8	–	–	–	–
53.0	$Mg_{1.8}Fe_{0.2}SiO_4$	20	–	–	–	–
53.0	$Mg_{1.8}Fe_{0.2}SiO_4$	50	–	–	–	–
53.0	$Mg_{1.8}Fe_{0.2}SiO_4$	100	–	–	–	–
53.0	$Mg_{1.8}Fe_{0.2}SiO_4$	200	–	–	–	–
53.0	$Mg_{1.8}Fe_{0.2}SiO_4$	292	–	–	–	–
53.0	$Mg_{1.8}Fe_{0.2}SiO_4$	300	–	–	–	–
53.0	$Mg_{1.6}Fe_{0.4}SiO_4$	300	Koike et al.(2003)	53.05	1.10	165
53.0	$Mg_{1.4}Fe_{0.6}SiO_4$	300	Koike et al.(2003)	53.04	1.02	150
53.0	$Mg_{1.22}Fe_{0.78}SiO_4$	300	Koike et al.(2003)	53.06	1.23	53
53.0	$Mg_{1.16}Fe_{0.84}SiO_4$	300	Koike et al.(2003)	53.60	1.10	100
53.0	$Mg_{1.11}Fe_{0.89}SiO_4$	300	Koike et al.(2003)	54.07	0.94	145
53.0	Fe_2SiO_4	8	Koike et al.(2006)	53.64	0.18	390
53.0	Fe_2SiO_4	20	Koike et al.(2006)	53.67	0.17	368
53.0	Fe_2SiO_4	50	Koike et al.(2006)	53.64	0.16	349
53.0	Fe_2SiO_4	100	Koike et al.(2006)	53.85	0.20	301
53.0	Fe_2SiO_4	200	Koike et al.(2006)	54.22	0.33	361
53.0	Fe_2SiO_4	292	Koike et al.(2006)	54.72	0.48	362
53.0	Fe_2SiO_4	300	Koike et al.(2003)	54.76	0.60	401

Table B.15: Database of crystalline olivine minerals for 69 μm spectral feature.

Wavelength (μm)	Chemical Composition	Temperature (K)	References (data taken)	peak position (μm)	peak width (μm)	peak ampl. (cm^2/gm)
69.0	Mg_2SiO_4	8	Koike et al.(2006)	68.82	0.06	262
69.0	Mg_2SiO_4	20	Koike et al.(2006)	68.82	0.08	236
69.0	Mg_2SiO_4	50	Koike et al.(2006)	68.85	0.10	224
69.0	Mg_2SiO_4	100	Koike et al.(2006)	68.96	0.14	169
69.0	Mg_2SiO_4	150	Koike et al.(2006)	69.10	0.21	110
69.0	Mg_2SiO_4	200	Koike et al.(2006)	69.28	0.46	124
69.0	Mg_2SiO_4	292	Koike et al.(2006)	69.56	0.39	75
69.0	Mg_2SiO_4	300	Koike et al.(2003)	69.63	0.35	33
69.0	$Mg_{1.8}Fe_{0.2}SiO_4$	8	–	–	–	–
69.0	$Mg_{1.8}Fe_{0.2}SiO_4$	20	–	–	–	–
69.0	$Mg_{1.8}Fe_{0.2}SiO_4$	50	–	–	–	–
69.0	$Mg_{1.8}Fe_{0.2}SiO_4$	100	–	–	–	–
69.0	$Mg_{1.8}Fe_{0.2}SiO_4$	200	–	–	–	–
69.0	$Mg_{1.8}Fe_{0.2}SiO_4$	292	–	–	–	–
69.0	$Mg_{1.8}Fe_{0.2}SiO_4$	300	–	–	–	–
69.0	$Mg_{1.6}Fe_{0.4}SiO_4$	300	–	–	–	–
69.0	$Mg_{1.4}Fe_{0.6}SiO_4$	300	–	–	–	–
69.0	$Mg_{1.22}Fe_{0.78}SiO_4$	300	–	–	–	–
69.0	$Mg_{1.16}Fe_{0.84}SiO_4$	300	–	–	–	–
69.0	$Mg_{1.11}Fe_{0.89}SiO_4$	300	–	–	–	–
69.0	Fe_2SiO_4	8	–	–	–	–
69.0	Fe_2SiO_4	20	–	–	–	–
69.0	Fe_2SiO_4	50	–	–	–	–
69.0	Fe_2SiO_4	100	–	–	–	–
69.0	Fe_2SiO_4	200	–	–	–	–
69.0	Fe_2SiO_4	292	–	–	–	–
69.0	Fe_2SiO_4	300	–	–	–	–

Table B.16: Database of crystalline olivine minerals for 72 μm spectral feature.

Wavelength (μm)	Chemical Composition	Temperature (K)	References (data taken)	peak position (μm)	peak width (μm)	peak ampl. (cm^2/gm)
72.0	Mg_2SiO_4	8	–	–	–	–
72.0	Mg_2SiO_4	20	–	–	–	–
72.0	Mg_2SiO_4	50	–	–	–	–
72.0	Mg_2SiO_4	100	–	–	–	–
72.0	Mg_2SiO_4	150	–	–	–	–
72.0	Mg_2SiO_4	200	–	–	–	–
72.0	Mg_2SiO_4	292	–	–	–	–
72.0	Mg_2SiO_4	300	–	–	–	–
72.0	$Mg_{1.8}Fe_{0.2}SiO_4$	8	Koike et al.(2006)	72.24	0.20	105
72.0	$Mg_{1.8}Fe_{0.2}SiO_4$	20	Koike et al.(2006)	72.25	0.20	87
72.0	$Mg_{1.8}Fe_{0.2}SiO_4$	50	Koike et al.(2006)	72.25	0.20	66
72.0	$Mg_{1.8}Fe_{0.2}SiO_4$	100	Koike et al.(2006)	72.26	0.21	48
72.0	$Mg_{1.8}Fe_{0.2}SiO_4$	200	Koike et al.(2006)	72.26	0.22	45
72.0	$Mg_{1.8}Fe_{0.2}SiO_4$	292	Koike et al.(2006)	72.25	0.20	43
72.0	$Mg_{1.8}Fe_{0.2}SiO_4$	300	Koike et al.(2003)	72.26	0.19	41
72.0	$Mg_{1.6}Fe_{0.4}SiO_4$	300	–	–	–	–
72.0	$Mg_{1.4}Fe_{0.6}SiO_4$	300	–	–	–	–
72.0	$Mg_{1.22}Fe_{0.78}SiO_4$	300	–	–	–	–
72.0	$Mg_{1.16}Fe_{0.84}SiO_4$	300	–	–	–	–
72.0	$Mg_{1.11}Fe_{0.89}SiO_4$	300	–	–	–	–
72.0	Fe_2SiO_4	8	–	–	–	–
72.0	Fe_2SiO_4	20	–	–	–	–
72.0	Fe_2SiO_4	50	–	–	–	–
72.0	Fe_2SiO_4	100	–	–	–	–
72.0	Fe_2SiO_4	200	–	–	–	–
72.0	Fe_2SiO_4	292	–	–	–	–
72.0	Fe_2SiO_4	300	–	–	–	–

Bibliography

[1] Asplund, M., Grevesse, N., Sauval, A. J., and Scott, P. The Chemical Composition of the Sun. *Annual Review of Astronomy & Astrophysics 47* (Sept. 2009), 481–522.

[2] Begemann, B., Dorschner, J., Henning, T., and Mutschke, H. Optical Properties of Glassy SiS 2 and the 21 Micron Feature. *Astrophysical Journal Letters 464* (June 1996), L195+.

[3] Begemann, B., Dorschner, J., Henning, T., Mutschke, H., Guertler, J., Koempe, C., and Nass, R. Aluminum Oxide and the Opacity of Oxygen-rich Circumstellar Dust in the 12–17 Micron Range. *Astrophysical Journal 476* (Feb. 1997), 199–+.

[4] Begemann, B., Henning, T., Mutschke, H., and Dorschner, J. Magnesium-iron oxides-astrophysical origin and optical constants. *Planetary and Space Science 43* (Feb. 1995), 1257–1261.

[5] Benitez, P. M., and Vargas, M. J. A photometric study of four semi-regular variable stars. *Journal of the British Astronomical Association 112* (Dec. 2002), 349–352.

[6] Bloecker, T. Stellar evolution of low and intermediate-mass stars. I. Mass loss on the AGB and its consequences for stellar evolution. *Astronomy and Astrophysics 297* (May 1995), 727.

[7] Blommaert, J. A. D. L., Vanhollebeke, E., Cami, J., Groenewegen, M. A. T., Habing, H. J., Markwick-Kember, F., Omont, A., Schultheis, M., Tielens, A. G. G. M., Waters, L. B. F. M., and Wood, P. R. The Dust Sequence along the AGB. In *Why Galaxies Care About AGB Stars: Their Importance as Actors and Probes* (Nov. 2007), F. Kerschbaum, C. Charbonnel, & R. F. Wing, Ed., vol. 378 of *Astronomical Society of the Pacific Conference Series*, pp. 164–+.

[8] Bohren, C. F., and Huffman, D. R. *Absorption and scattering of light by small particles.* 1983.

[9] Bohren, C. F., Huffman, D. R., and Kam, Z. Book-Review - Absorption and Scattering of Light by Small Particles. *Nature 306* (Dec. 1983), 625–+.

[10] Bose, M., Floss, C., and Stadermann, F. J. An Investigation into the Origin of Fe-Rich Presolar Silicates in Acfer 094. *Astrophysical Journal 714* (May 2010), 1624–1636.

[11] Bouwman, J., Meeus, G., de Koter, A., Hony, S., Dominik, C., and Waters, L. B. F. M. Processing of silicate dust grains in Herbig Ae/Be systems. *Astronomy and Astrophysics 375* (Sept. 2001), 950–962.

[12] Bussmann, R. S., Dey, A., Borys, C., Desai, V., Jannuzi, B. T., Le Floc'h, E., Melbourne, J., Sheth, K., and Soifer, B. T. Infrared Luminosities and Dust Properties of z 2 Dust-obscured Galaxies. *Astrophysical Journal 705* (Nov. 2009), 184–198.

[13] Cami, J. *Molecular gas and dust around evolved stars.* PhD thesis, University of Amsterdam, 2002.

[14] Cami, J. Molecules and dust around oxygen-rich AGB stars. In *Mass-Losing Pulsating Stars and their Circumstellar Matter* (Apr. 2003), Y. Nakada, M. Honma, & M. Seki, Ed., vol. 283 of *Astrophysics and Space Science Library*, pp. 209–212.

[15] Cami, J., de Jong, T., Justtannont, K., Yamamura, I., and Waters, L. B. F. M. ISO-SWS Spectra of OH/IR Stars. *Astrophysics and Space Science 255* (1998), 339–340.

[16] Cami, J., van Malderen, R., and Markwick, A. J. SpectraFactory.net: A Database of Molecular Model Spectra. *The Astrophysical Journal Supplement Series 187* (Apr. 2010), 409–415.

[17] Cami, J., Yamamura, I., de Jong, T., Onaka, T., Tielens, A. G. G. M., Justtanont, K., and Waters, L. B. F. M. Warm dioxides around O-rich AGB stars. In *The Universe as Seen by ISO* (Mar. 1999), P. Cox & M. Kessler, Ed., vol. 427 of *ESA Special Publication*, pp. 281–+.

[18] Casassus, S., Roche, P. F., Aitken, D. K., and Smith, C. H. The Galactic disc distribution of planetary nebulae with warm dust emission features - I. *Monthly Notices of the Royal Astronomical Society 320* (Feb. 2001), 424–434.

[19] Castelaz, M. W., Luttermoser, D. G., Caton, D. B., and Piontek, R. A. Phase-dependent Spectroscopy of Mira Variable Stars. *Astronomical Journal 120* (Nov. 2000), 2627–2637.

[20] Cherchneff, I. A chemical study of the inner winds of asymptotic giant branch stars. *Astronomy and Astrophysics 456* (Sept. 2006), 1001–1012.

[21] Chiar, J. E., Ennico, K., Pendleton, Y. J., Boogert, A. C. A., Greene, T., Knez, C., Lada, C., Roellig, T., Tielens, A. G. G. M., Werner, M., and Whittet, D. C. B. The Relationship between the Optical Depth of the 9.7 μm Silicate Absorption Feature and Infrared Differential Extinction in Dense Clouds. *Astrophysical Journal, Letters to the Editor 666* (Sept. 2007), L73–L76.

[22] Chihara, H., Koike, C., and Tsuchiyama, A. Compositional dependence of infrared absorption spectra of crystalline silicates. III. Melilite solid solution. *Astronomy and Astrophysics 464* (Mar. 2007), 229–234.

[23] Chihara, H., Koike, C., Tsuchiyama, A., Tachibana, S., and Sakamoto, D. Compositional dependence of infrared absorption spectra of crystalline silicates. I. Mg-Fe pyroxenes. *Astronomy and Astrophysics 391* (Aug. 2002), 267–273.

[24] Cohen, M., Walker, R. G., Carter, B., Hammersley, P., Kidger, M., and Noguchi, K. Spectral Irradiance Calibration in the Infrared. X. A Self-Consistent Radiometric All-Sky Network of Absolutely Calibrated Stellar Spectra. *The Astronomical Journal 117* (Apr. 1999), 1864–1889.

[25] Corasaniti, P. S. The impact of cosmic dust on supernova cosmology. *Monthly Notices of the Royal Astronomical Society 372* (Oct. 2006), 191–198.

[26] Corman, A. *Carbon stars and silicon carbide.* Phd dissertation, University of Missouri, Department of Physics and Astronomy, 2010.

[27] Cotton, W. D., Ragland, S., Pluzhnik, E., Danchi, W. C., Traub, W. A., Willson, L. A., and Lacasse, M. G. SIO Masers in Asymmetric Miras. I. R Leonis. *Astrophysical Journal 704* (Oct. 2009), 170–182.

[28] Day, K. L. Mid-infrared optical properties of vapor-condensed magnesium silicates. *Astrophysical Journal 234* (Nov. 1979), 158–161.

[29] de Graauw, T., Haser, L. N., Beintema, D. A., Roelfsema, P. R., van Agthoven, H., Barl, L., Bauer, O. H., Bekenkamp, H. E. G., Boonstra, A.-J., Boxhoorn, D. R., Cote, J., de Groene, P., van Dijkhuizen, C., Drapatz, S., Evers, J., Feuchtgruber, H., Frericks, M., Genzel, R., Haerendel, G., Heras, A. M., van der Hucht, K. A., van der Hulst, T., Huygen, R., Jacobs, H., Jakob, G., Kamperman, T., Katterloher, R. O., Kester, D. J. M., Kunze, D., Kussendrager, D., Lahuis, F., Lamers, H. J. G. L. M., Leech, K., van der Lei, S., van der Linden, R., Luinge, W., Lutz, D., Melzner, F., Morris, P. W., van Nguyen, D., Ploeger, G., Price, S., Salama, A., Schaeidt, S. G., Sijm, N., Smoorenburg, C., Spakman, J., Spoon, H., Steinmayer, M., Stoecker, J., Valentijn, E. A., Vandenbussche, B., Visser, H., Waelkens, C., Waters, L. B. F. M., Wensink, J., Wesselius, P. R., Wiezorrek, E., Wieprecht, E., Wijnbergen, J. J., Wildeman, K. J., and Young, E. Observing with the ISO Short-Wavelength Spectrometer. *Astronomy and Astrophysics 315* (Nov. 1996), L49–L54.

[30] Decin, L., Blomme, L., Reyniers, M., Ryde, N., Hinkle, K. H., and de Koter, A. Probing the mass-loss history of the unusual Mira variable ¡ASTROBJ¿R Hydrae¡/ASTROBJ¿ through its infrared CO wind. *Astronomy and Astrophysics 484* (June 2008), 401–412.

[31] DePew, K., Speck, A., and Dijkstra, C. Astromineralogy of the 13 μm Feature in the Spectra of Oxygen-rich Asymptotic Giant Branch Stars. I. Corundum and Spinel. *Astrophysical Journal 640* (Apr. 2006), 971–981.

[32] Dijkstra, C., Speck, A. K., Reid, R. B., and Abraham, P. The 10 μm Feature of M-Type Stars in the Large Magellanic Cloud and the Dust Condensation Sequence. *Astrophysical Journal, Letters to the Editor 633* (Nov. 2005), L133–L136.

[33] Doyle, D., Pilbratt, G., and Tauber, J. The Herschel and Planck Space Telescopes. *IEEE Proceedings 97* (Aug. 2009), 1403–1411.

[34] Draine, B. T. Interstellar Dust Grains. *Annual Review of Astronomy & Astrophysics 41* (2003), 241–289.

[35] Egan, M. P., and Sloan, G. C. The Physical Basis for the Silicate Dust Sequence. *Astrophysical Journal 558* (Sept. 2001), 165–175.

[36] Etoka, S., Le Squeren, A. M., and Gerard, E. Detection of 1612 MHz OH emission in the semiregular variable stars RT Vir, R Crt and W Hya. *Astronomy and Astrophysics 403* (May 2003), L51–L54.

[37] Fabian, D., Henning, T., Jäger, C., Mutschke, H., Dorschner, J., and Wehrhan, O. Steps toward interstellar silicate mineralogy. VI. Dependence of crystalline olivine IR spectra on iron content and particle shape. *Astronomy and Astrophysics 378* (Oct. 2001), 228–238.

[38] Fabian, D., Jäger, C., Henning, T., Dorschner, J., and Mutschke, H. Steps toward interstellar silicate mineralogy. V. Thermal Evolution of Amorphous Magnesium Silicates and Silica. *Astronomy and Astrophysics 364* (Dec. 2000), 282–292.

[39] Famaey, B., Pourbaix, D., Frankowski, A., van Eck, S., Mayor, M., Udry, S., and Jorissen, A. Spectroscopic binaries among Hipparcos M giants,. I. Data, orbits, and intrinsic variations. *Astronomy and Astrophysics 498* (May 2009), 627–640.

[40] Ferrarotti, A. S., and Gail, H.-P. Mineral formation in stellar winds. V. Formation of calcium carbonate. *Astronomy and Astrophysics 430* (Feb. 2005), 959–965.

[41] Ferrarotti, A. S., and Gail, H.-P. Composition and quantities of dust produced by AGB-stars and returned to the interstellar medium. *Astronomy and Astrophysics 447* (Feb. 2006), 553–576.

[42] Gail, H.-P., and Sedlmayr, E. Mineral formation in stellar winds. I. Condensation sequence of silicate and iron grains in stationary oxygen rich outflows. *Astronomy and Astrophysics 347* (July 1999), 594–616.

[43] Gaustad, J. E. The Opacity of Diffuse Cosmic Matter and the Early Stages of Star Formation. *Astrophysical Journal 138* (Nov. 1963), 1050–+.

[44] Gehrz, R. D., and Woolf, N. J. Mass Loss from M Stars. *Astrophysical Journal 165* (May 1971), 285–+.

[45] Gervais, F. *In Handbook of Optical Constants of Solids*, vol. 761. 1991.

[46] Gillett, F. C., Low, F. J., and Stein, W. A. Stellar Spectra from 2.8 to 14 Microns. *Astrophysical Journal 154* (Nov. 1968), 677–+.

[47] Gilman, R. C. On the Composition of Circumstellar Grains. *Astrophysical Journal, Letters to the Editor 155* (Mar. 1969), L185+.

[48] Grossman, L. Condensation in the primitive solar nebula. *Geochimica et Cosmochimica Acta 36* (June 1972), 597–619.

[49] Guha Niyogi, S., Speck, A. K., and Onaka, T. A Temporal Study of the Oxygen-rich Pulsating Variable Asymptotic Giant Branch Star, T Cep: Investigation on Dust Formation and Dust Properties. *Astrophysical Journal 733* (June 2011), 93–+.

[50] Guha Niyogi, S., Speck, A. K., and Volk, K. Investigating spatial distribution of dust around SW Vir. *The Astronomical Review 6*, 8 (Oct. 2011), 080000–38.

[51] Habing, H. J. Circumstellar envelopes and Asymptotic Giant Branch stars. *The Astronomy and Astrophysics Review 7* (1996), 97–207.

[52] Habing, H. J., and Whitelock, P. A. *AGB Stars as Tracers of Stellar Populations.* 2003.

[53] Hackwell, J. A. Interstellar Silicate Absorption Bands. *Nature 227* (Aug. 1970), 822–823.

[54] Hao, L., Spoon, H. W. W., Sloan, G. C., Marshall, J. A., Armus, L., Tielens, A. G. G. M., Sargent, B., van Bemmel, I. M., Charmandaris, V., Weedman, D. W., and Houck, J. R. The Detection of Silicate Emission from Quasars at 10 and 18 Microns. *Astrophysical Journal, Letters to the Editor 625* (June 2005), L75–L78.

[55] Harwit, M., Malfait, K., Decin, L., Waelkens, C., Feuchtgruber, H., and Melnick, G. J. The Infrared Continuum Spectrum of VY Canis Majoris. *Astrophysical Journal 557* (Aug. 2001), 844–853.

[56] Henning, T., Begemann, B., Mutschke, H., and Dorschner, J. Optical properties of oxide dust grains. *Astronomy and Astrophysics Supplement 112* (July 1995), 143–+.

[57] Heras, A. M., and Hony, S. Oxygen-rich AGB stars with optically thin dust envelopes. *Astronomy and Astrophysics 439* (Aug. 2005), 171–182.

[58] Hofmeister, A. M., and Bowey, J. E. Quantitative infrared spectra of hydrosilicates and related minerals. *Monthly Notices of the Royal Astronomical Society 367* (Apr. 2006), 577–591.

[59] Hofmeister, A. M., and Pitman, K. M. Unpublished.

[60] Hofmeister, A. M., and Pitman, K. M. Evidence for kinks in structural and thermodynamic properties across the forsterite-fayalite binary from thin-film IR absorption spectra. *Physics and Chemistry of Minerals 34* (July 2007), 319–333.

[61] Hofmeister, A. M., Pitman, K. M., Goncharov, A. F., and Speck, A. K. Optical Constants of Silicon Carbide for Astrophysical Applications. II. Extending Optical Functions from Infrared to Ultraviolet Using Single-Crystal Absorption Spectra. *Astrophysical Journal 696* (May 2009), 1502–1516.

[62] Hofmeister, A. M., Wopenka, B., and Locock, A. J. Spectroscopy and structure of hibonite, grossite, and CaAl"2O"4: Implications for astronomical environments. *Geochimica et Cosmochimica Acta 68* (Nov. 2004), 4485–4503.

[63] Höfner, S., and Andersen, A. C. Winds of M- and S-type AGB stars: an unorthodox suggestion for the driving mechanism. *Astronomy and Astrophysics 465* (Apr. 2007), L39–L42.

[64] Hony, S., Heras, A. M., Molster, F. J., and Smolders, K. An ISO/SWS study of the dust composition around S stars. A novel view of S-star dust. *Astronomy and Astrophysics 501* (July 2009), 609–617.

[65] Houck, J. R., Roellig, T. L., van Cleve, J., Forrest, W. J., Herter, T., Lawrence, C. R., Matthews, K., Reitsema, H. J., Soifer, B. T., Watson, D. M., Weedman, D., Huisjen, M., Troeltzsch, J., Barry,

D. J., Bernard-Salas, J., Blacken, C. E., Brandl, B. R., Charmandaris, V., Devost, D., Gull, G. E., Hall, P., Henderson, C. P., Higdon, S. J. U., Pirger, B. E., Schoenwald, J., Sloan, G. C., Uchida, K. I., Appleton, P. N., Armus, L., Burgdorf, M. J., Fajardo-Acosta, S. B., Grillmair, C. J., Ingalls, J. G., Morris, P. W., and Teplitz, H. I. The Infrared Spectrograph (IRS) on the Spitzer Space Telescope. *The Astrophysical Journal Supplement Series 154* (Sept. 2004), 18–24.

[66] Huffman, D. R., and Stapp, J. L. Optical Measurements on Solids of Possible Interstellar Importance (presented by D. R. Huffman). In *Interstellar Dust and Related Topics* (1973), J. M. Greenberg & H. C. van de Hulst, Ed., vol. 52 of *IAU Symposium*, pp. 297–+.

[67] Huss, G. R., Fahey, A. J., Russell, S. S., and Wasserburg, G. J. Oxygen Isotopes in Refractory Oxide Minerals from Primitive Chondrites. In *Lunar and Planetary Institute Science Conference Abstracts* (Mar. 1995), vol. 26 of *Lunar and Planetary Institute Science Conference Abstracts*, p. 641.

[68] Isles, J. E., and Saw, D. R. B. Mira stars - II: R Cam, R Cas, W Cas, S Cep, T Cep, U CYG and S Del. *Journal of the British Astronomical Association 99* (June 1989), 121–129.

[69] Jaeger, C., Molster, F. J., Dorschner, J., Henning, T., Mutschke, H., and Waters, L. B. F. M. Steps toward interstellar silicate mineralogy. IV. The crystalline revolution. *Astronomy and Astrophysics 339* (Nov. 1998), 904–916.

[70] Jain, P., and Ralston, J. P. Evidence for Evolution or Bias in Host Extinctions of Type 1a Supernovae at High Redshift. *Astrophysical Journal 637* (Jan. 2006), 91–95.

[71] Kemper, F., de Koter, A., Waters, L. B. F. M., Bouwman, J., and Tielens, A. G. G. M. Dust and the spectral energy distribution of the OH/IR star OH 127.8+0.0: Evidence for circumstellar metallic iron. *Astronomy and Astrophysics 384* (Mar. 2002), 585–593.

[72] Kemper, F., Jäger, C., Waters, L. B. F. M., Henning, T., Molster, F. J., Barlow, M. J., Lim, T., and de Koter, A. Detection of carbonates in dust shells around evolved stars. *Nature 415* (Jan. 2002), 295–297.

[73] Kemper, F., Molster, F. J., Jäger, C., and Waters, L. B. F. M. The mineral composition and spatial distribution of the dust ejecta of NGC 6302. *Astronomy and Astrophysics 394* (Nov. 2002), 679–690.

[74] Kessler, M. F., Steinz, J. A., Anderegg, M. E., Clavel, J., Drechsel, G., Estaria, P., Faelker, J., Riedinger, J. R., Robson, A., Taylor, B. G., and Ximénez de Ferrán, S. The Infrared Space Observatory (ISO) mission. *Astronomy and Astrophysics 315* (Nov. 1996), L27–L31.

[75] Knacke, R. F., Gaustad, J. E., Gillett, F. C., and Stein, W. A. A Possible Identification of Interstellar Silicate Absorption in the Infrared Spectrum of 119 Tauri. *Astrophysical Journal, Letters to the Editor 155* (Mar. 1969), L189+.

[76] Koike, C., Chihara, H., Tsuchiyama, A., Suto, H., Sogawa, H., and Okuda, H. Compositional dependence of infrared absorption spectra of crystalline silicate. II. Natural and synthetic olivines. *Astronomy and Astrophysics 399* (Mar. 2003), 1101–1107.

[77] Koike, C., Imai, Y., Chihara, H., Suto, H., Murata, K., Tsuchiyama, A., Tachibana, S., and Ohara, S. Effects of Forsterite Grain Shape on Infrared Spectra. *Astrophysical Journal 709* (Feb. 2010), 983–992.

[78] Koike, C., Mutschke, H., Suto, H., Naoi, T., Chihara, H., Henning, T., Jäger, C., Tsuchiyama, A., Dorschner, J., and Okuda, H. Temperature effects on the mid-and far-infrared spectra of olivine particles. *Astronomy and Astrophysics 449* (Apr. 2006), 583–596.

[79] Koike, C., Tsuchiyama, A., Shibai, H., Suto, H., Tanabé, T., Chihara, H., Sogawa, H., Mouri, H., and Okada, K. Absorption spectra of Mg-rich Mg-Fe and Ca pyroxenes in the mid- and far-infrared regions. *Astronomy and Astrophysics 363* (Nov. 2000), 1115–1122.

[80] Kraemer, K. E., Sloan, G. C., Price, S. D., and Walker, H. J. Classification of 2.4-45.2 Micron Spectra from the Infrared Space Observatory Short Wavelength Spectrometer. *The Astrophysical Journal Supplement Series 140* (June 2002), 389–406.

[81] Kraetschmer, W., and Huffman, D. R. Infrared extinction of heavy ion irradiated and amorphous olivine, with applications to interstellar dust. *Astrophysics and Space Science 61* (Mar. 1979), 195–203.

[82] Krishna Swamy, K. S. *Dust in the universe : similarities and differences.* 2005.

[83] Krügel, E. *An introduction to the physics of interstellar dust.* 2008.

[84] Kwok, S. The synthesis of organic and inorganic compounds in evolved stars. *Nature 430* (Aug. 2004), 985–991.

[85] Lebzelter, T., Posch, T., Hinkle, K., Wood, P. R., and Bouwman, J. Tracing the Development of Dust around Evolved Stars: The Case of 47 Tuc. *Astrophysical Journal, Letters to the Editor 653* (Dec. 2006), L145–L148.

[86] Little-Marenin, I. R., and Little, S. J. Emission features in IRAS LRS spectra of M Mira variables. *Astronomical Journal 99* (Apr. 1990), 1173–1186.

[87] Lodders, K., and Fegley, Jr., B. Condensation Chemistry of Circumstellar Grains. In *Asymptotic Giant Branch Stars* (1999), T. Le Bertre, A. Lebre, & C. Waelkens, Ed., vol. 191 of *IAU Symposium*, pp. 279–+.

[88] Loup, C., Forveille, T., Omont, A., and Paul, J. F. CO and HCN observations of circumstellar envelopes. A catalogue - Mass loss rates and distributions. *Astronomy and Astrophysics Supplement Series 99* (June 1993), 291–377.

[89] Mann, I., Köhler, M., Kimura, H., Cechowski, A., and Minato, T. Dust in the solar system and in extra-solar planetary systems. *The Astronomy and Astrophysics Review 13* (June 2006), 159–228.

[90] Marsakova, V. I., and Andronov, I. L. Unusual Secondary Variations in the Mira Star T Cep. In *IAU Colloq. 176: The Impact of Large-Scale Surveys on Pulsating Star Research* (2000), L. Szabados & D. Kurtz, Ed., vol. 203 of *Astronomical Society of the Pacific Conference Series*, pp. 131–132.

[91] Matsuura, M., Yamamura, I., Cami, J., Onaka, T., and Murakami, H. The time variation in infrared water-vapour bands in Mira variables. *Astronomy and Astrophysics 383* (Mar. 2002), 972–986.

[92] McDonald, I., Boyer, M. L., van Loon, J. T., and Zijlstra, A. A. Dust Production and Mass Loss in the Galactic Globular Cluster 47 Tucanae. *Astrophysical Journal 730* (Apr. 2011), 71–+.

[93] McDonald, I., Sloan, G. C., Zijlstra, A. A., Matsunaga, N., Matsuura, M., Kraemer, K. E., Bernard-Salas, J., and Markwick, A. J.

Rusty Old Stars: A Source of the Missing Interstellar Iron? *Astrophysical Journal, Letters to the Editor 717* (July 2010), L92–L97.

[94] McDonald, I., van Loon, J. T., Dupree, A. K., and Boyer, M. L. Discovery of long-period variable stars in the very metal-poor globular cluster M15. *Monthly Notices of the Royal Astronomical Society 405* (July 2010), 1711–1722.

[95] Min, M., Hovenier, J. W., and de Koter, A. Shape effects in scattering and absorption by randomly oriented particles small compared to the wavelength. *Astronomy and Astrophysics 404* (June 2003), 35–46.

[96] Molster, F. J. *Crystalline silicates in circumstellar dust shells.* PhD thesis, FNWI: Sterrenkundig Instituut Anton Pannekoek, Postbus 19268, 1000 GG Amsterdam, The Netherlands, 2000.

[97] Molster, F. J., Lim, T. L., Sylvester, R. J., Waters, L. B. F. M., Barlow, M. J., Beintema, D. A., Cohen, M., Cox, P., and Schmitt, B. The complete ISO spectrum of NGC 6302. *Astronomy and Astrophysics 372* (June 2001), 165–172.

[98] Molster, F. J., Waters, L. B. F. M., and Tielens, A. G. G. M. Crystalline silicate dust around evolved stars. II. The crystalline silicate complexes. *Astronomy and Astrophysics 382* (Jan. 2002), 222–240.

[99] Molster, F. J., Waters, L. B. F. M., Tielens, A. G. G. M., and Barlow, M. J. Crystalline silicate dust around evolved stars. I. The sample stars. *Astronomy and Astrophysics 382* (Jan. 2002), 184–221.

[100] Molster, F. J., Waters, L. B. F. M., Tielens, A. G. G. M., Koike, C., and Chihara, H. Crystalline silicate dust around evolved stars. III. A

correlations study of crystalline silicate features. *Astronomy and Astrophysics 382* (Jan. 2002), 241–255.

[101] Molster, F. J., Waters, L. B. F. M., Trams, N. R., Van Winckel, H., Decin, L., van Loon, J. T., Jäger, C., Henning, T., Käufl, H.-U., de Koter, A., and Bouwman, J. The composition and nature of the dust shell surrounding the binary AFGL 4106. *Astronomy and Astrophysics 350* (Oct. 1999), 163–180.

[102] Monnier, J. D., Geballe, T. R., and Danchi, W. C. Temporal Variations of Midinfrared Spectra in Late-Type Stars. *Astrophysical Journal 502* (Aug. 1998), 833–+.

[103] Mukai, T., and Koike, C. Optical constants of olivine particles between wavelengths of 7 and 200 microns. *Icarus 87* (Sept. 1990), 180–187.

[104] Murata, K., Chihara, H., Koike, C., Takakura, T., Imai, Y., and Tsuchiyama, A. Crystallization Experiments on Amorphous Magnesium Silicate. I. Estimation of the Activation Energy of Enstatite Crystallization. *Astrophysical Journal 697* (May 2009), 836–842.

[105] Neugebauer, G., Habing, H. J., van Duinen, R., Aumann, H. H., Baud, B., Beichman, C. A., Beintema, D. A., Boggess, N., Clegg, P. E., de Jong, T., Emerson, J. P., Gautier, T. N., Gillett, F. C., Harris, S., Hauser, M. G., Houck, J. R., Jennings, R. E., Low, F. J., Marsden, P. L., Miley, G., Olnon, F. M., Pottasch, S. R., Raimond, E., Rowan-Robinson, M., Soifer, B. T., Walker, R. G., Wesselius, P. R., and Young, E. The Infrared Astronomical Satellite (IRAS) mission. *Astrophysical Journal, Letters to the Editor 278* (Mar. 1984), L1–L6.

[106] Nittler, L., Alexander, C., Gao, X., Walker, R., and Zinner, E. Interstellar Corundum and Spinel from the Tieschitz Ordinary Chondrite. In *Lunar and Planetary Institute Science Conference Abstracts* (Mar. 1994), vol. 25 of *Lunar and Planetary Institute Science Conference Abstracts*, p. 1005.

[107] Nogami, D. Observational Constraints on the Evolution of Cataclysmic Variables below and in the Period Gap. In *Wild Stars in the Old West* (1998), S. Howell, E. Kuulkers, & C. Woodward, Ed., vol. 137 of *Astronomical Society of the Pacific Conference Series*, pp. 495–+.

[108] Okada, Y., Onaka, T., Kaneda, H., and Sakon, I. Depletion Study of Si And Fe with Mid- and Far-Infrared Imaging Spectroscopy with SPICA. In *The Next-Generation Infrared Space Mission: SPICA* (Dec. 2009), A. M. Heras, B. M. Swinyard, K. G. Isaak, & J. R. Goicoechea , Ed., pp. 3008–+.

[109] Onaka, T., de Jong, T., and Willems, F. J. A study of M Mira variables based on IRAS LRS observations. II - Model FITS and derived parameters for 109 Miras. *Astronomy and Astrophysics Supplement 81* (Dec. 1989), 261–284.

[110] Onaka, T., de Jong, T., and Yamamura, I. Time variation of SWS spectra of M-type Mira variables and its dust optical properties. I. ¡ASTROBJ¿Z Cyg¡/ASTROBJ¿. *Astronomy and Astrophysics 388* (June 2002), 573–586.

[111] Onaka, T., de Jong, T., Yamamura, I., Cami, J., and Tanab'e, T. Time variation observations of ISO SWS spectra of two oxygen-rich Mira variables. In *The Universe as Seen by ISO* (Mar. 1999), P. Cox & M. Kessler, Ed., vol. 427 of *ESA Special Publication*, pp. 381–+.

[112] Perrin, G., Coudé du Foresto, V., Ridgway, S. T., Mariotti, J.-M., Traub, W. A., Carleton, N. P., and Lacasse, M. G. Extension of the

effective temperature scale of giants to types later than M6. *Astronomy and Astrophysics 331* (Mar. 1998), 619–626.

[113] Perryman, M. A. C., Lindegren, L., Kovalevsky, J., Hoeg, E., Bastian, U., Bernacca, P. L., Crézé, M., Donati, F., Grenon, M., van Leeuwen, F., van der Marel, H., Mignard, F., Murray, C. A., Le Poole, R. S., Schrijver, H., Turon, C., Arenou, F., Froeschlé, M., and Petersen, C. S. The HIPPARCOS Catalogue. *Astronomy and Astrophysics 323* (July 1997), L49–L52.

[114] Pitman, K. M., Dijkstra, C., Hofmeister, A. M., and Speck, A. K. Infrared laboratory absorbance spectra of olivine: using classical dispersion analysis to extract peak parameters. *Monthly Notices of the Royal Astronomical Society 406* (July 2010), 460–481.

[115] Pitman, K. M., Hofmeister, A. M., Corman, A. B., and Speck, A. K. Optical properties of silicon carbide for astrophysical applications. I. New laboratory infrared reflectance spectra and optical constants. *Astronomy and Astrophysics 483* (May 2008), 661–672.

[116] Pollack, J. B., Toon, O. B., and Khare, B. N. Optical properties of some terrestrial rocks and glasses. *Icarus 19* (July 1973), 372–389.

[117] Posch, T., Kerschbaum, F., Mutschke, H., Dorschner, J., and Jäger, C. On the origin of the 19.5 μ m feature. Identifying circumstellar Mg-Fe-oxides. *Astronomy and Astrophysics 393* (Oct. 2002), L7–L10.

[118] Posch, T., Kerschbaum, F., Mutschke, H., Fabian, D., Dorschner, J., and Hron, J. On the origin of the 13 mu m feature. A study of ISO-SWS spectra of oxygen-rich AGB stars. *Astronomy and Astrophysics 352* (Dec. 1999), 609–618.

[119] Salpeter, E. E. Formation and flow of dust grains in cool stellar atmospheres. *Astrophysical Journal 193* (Nov. 1974), 585–592.

[120] Schweitzer, E. Introducing the French Association of Variable Star Observers. *Journal of the American Association of Variable Star Observers (JAAVSO) 19* (1990), 122–+.

[121] Sloan, G. C., Devost, D., Bernard-Salas, J., Wood, P. R., and Houck, J. R. The Unusual Silicate Dust around HV 2310, an Evolved Star in the Large Magellanic Cloud. *Astrophysical Journal 638* (Feb. 2006), 472–477.

[122] Sloan, G. C., and Egan, M. P. The structure of the dust shells around IRC +10216. *Astrophysical Journal 444* (May 1995), 452–457.

[123] Sloan, G. C., Kraemer, K. E., Goebel, J. H., and Price, S. D. Guilt by Association: The 13 Micron Dust Emission Feature and Its Correlation to Other Gas and Dust Features. *Astrophysical Journal 594* (Sept. 2003), 483–495.

[124] Sloan, G. C., Levan, P. D., and Little-Marenin, I. R. Sources of the 13 Micron Feature Associated with Oxygen-rich Circumstellar Dust. *Astrophysical Journal 463* (May 1996), 310–+.

[125] Sloan, G. C., Matsunaga, N., Matsuura, M., Zijlstra, A. A., Kraemer, K. E., Wood, P. R., Nieusma, J., Bernard-Salas, J., Devost, D., and Houck, J. R. Spitzer Spectroscopy of Mass-loss and Dust Production by Evolved Stars in Globular Clusters. *Astrophysical Journal 719* (Aug. 2010), 1274–1292.

[126] Sloan, G. C., Matsuura, M., Zijlstra, A. A., Lagadec, E., Groenewegen, M. A. T., Wood, P. R., Szyszka, C., Bernard-Salas, J., and van Loon, J. T. Dust Formation in a Galaxy with Primitive Abundances. *Science 323* (Jan. 2009), 353–.

[127] Sloan, G. C., and Price, S. D. Silicate Emission at 10 Microns in Variables on the Asymptotic Giant Branch. *Astrophysical Journal 451* (Oct. 1995), 758–+.

[128] Sloan, G. C., and Price, S. D. The Infrared Spectral Classification of Oxygen-rich Dust Shells. *The Astrophysical Journal Supplement Series 119* (Dec. 1998), 141–158.

[129] Speck, A. K. *The Mineralogy of Dust Around Evolved Stars.* PhD thesis, PhD Thesis, University College London, 1998 %,F University College London Gower Street, London WC1N 1AS, 1998.

[130] Speck, A. K., Barlow, M. J., and Skinner, C. J. The nature of the silicon carbide in carbon star outflows. *Monthly Notices of the Royal Astronomical Society 288* (June 1997), 431–456.

[131] Speck, A. K., Barlow, M. J., Sylvester, R. J., and Hofmeister, A. M. Dust features in the 10-mu m infrared spectra of oxygen-rich evolved stars. *Astronomy and Astrophysics Supplement 146* (Nov. 2000), 437–464.

[132] Speck, A. K., Whittington, A. G., and Hofmeister, A. M. Disordered Silicates in Space: A Study of Laboratory Spectra of "Amorphous" Silicates. *Astrophysical Journal 740* (Oct. 2011), 93.

[133] Stencel, R. E., Nuth, III, J. A., Little-Marenin, I. R., and Little, S. J. The formation and annealing of circumstellar dust, as gauged by IRAS low-resolution spectra and the microwave maser chronology. *Astrophysical Journal, Letters to the Editor 350* (Feb. 1990), L45–L48.

[134] Stroud, R. M., Nguyen, A. N., Alexander, C. M. O., Nittler, L. R., and Stadermann, F. J. Transmission Electron Microscopy of In Situ Presolar

Silicates in Alan Hills 77307. *Meteoritics and Planetary Science Supplement 43* (Aug. 2008), 5201–+.

[135] Takigawa, A., Tachibana, S., Nagahara, H., Ozawa, K., and Yokoyama, M. Anisotropic Evaporation of Forsterite and Its Implication for Dust Formation Conditions in Circumstellar Environments. *Astrophysical Journal, Letters to the Editor 707* (Dec. 2009), L97–L101.

[136] Thompson, G. D., Corman, A. B., Speck, A. K., and Dijkstra, C. Challenging the Carbon Star Dust Condensation Sequence: Anarchist C Stars. *Astrophysical Journal 652* (Dec. 2006), 1654–1673.

[137] Tielens, A. G. G. M. Towards a circumstellar silicate mineralogy. In *From Miras to Planetary Nebulae: Which Path for Stellar Evolution?* (1990), M. O. Mennessier & A. Omont, Ed., pp. 186–200.

[138] Tielens, A. G. G. M., Waters, L. B. F. M., Molster, F. J., and Justtanont, K. Circumstellar Silicate Mineralogy. *Astrophysics and Space Science 255* (1998), 415–426.

[139] Tsuji, T., Ohnaka, K., Aoki, W., and Yamamura, I. Warm molecular envelope of M giants and Miras: a new molecule forming region unmasked by the ISO SWS. *Astronomy and Astrophysics 320* (Apr. 1997), L1–L4.

[140] Ueta, T., Speck, A. K., Stencel, R. E., Herwig, F., Gehrz, R. D., Szczerba, R., Izumiura, H., Zijlstra, A. A., Latter, W. B., Matsuura, M., Meixner, M., Steffen, M., and Elitzur, M. Detection of a Far-Infrared Bow Shock Nebula around R Hya: The First MIRIAD Results. *The Astrophysical Journal 648* (Sept. 2006), L39–L42.

[141] van de Hulst, H. C. *Light Scattering by Small Particles.* 1957.

[142] van Loon, J. T., Cioni, M.-R. L., Zijlstra, A. A., and Loup, C. An empirical formula for the mass-loss rates of dust-enshrouded red supergiants and oxygen-rich Asymptotic Giant Branch stars. *Astronomy and Astrophysics 438* (July 2005), 273–289.

[143] Van Malderen, R. *On the analysis of the IR spectra of cool giants : model atmospheres and time-dependent behaviour.* Phd dissertation, Katholieke Universiteit Leuven, 2003.

[144] Vardya, M. S., de Jong, T., and Willems, F. J. IRAS Low-Resolution Spectrograph observations of silicate and molecular SiO emission in Mira variables. *Astrophysical Journal, Letters to the Editor 304* (May 1986), L29–L32.

[145] Verhoelst, T., Decin, L., van Malderen, R., Hony, S., Cami, J., Eriksson, K., Perrin, G., Deroo, P., Vandenbussche, B., and Waters, L. B. F. M. Amorphous alumina in the extended atmosphere of α Orionis. *Astronomy and Astrophysics 447* (Feb. 2006), 311–324.

[146] Videen, G., and Kocifaj, M., Eds. *Optics of Cosmic Dust* (2002).

[147] Vollmer, C., Hoppe, P., and Brenker, F. E. Si Isotopic Compositions of Presolar Silicate Grains from Red Giant Stars and Supernovae. *Astrophysical Journal 684* (Sept. 2008), 611–617.

[148] Waelkens, C., Waters, L. B. F. M., de Graauw, M. S., Huygen, E., Malfait, K., Plets, H., Vandenbussche, B., Beintema, D. A., Boxhoorn, D. R., Habing, H. J., Heras, A. M., Kester, D. J. M., Lahuis, F., Morris, P. W., Roelfsema, P. R., Salama, A., Siebenmorgen, R., Trams, N. R., van der Bliek, N. R., Valentijn, E. A., and Wesselius, P. R. SWS observations of young main-sequence stars with dusty circumstellar disks. *Astronomy and Astrophysics 315* (Nov. 1996), L245–L248.

[149] Waters, L. B. F. M., Molster, F. J., de Jong, T., Beintema, D. A., Waelkens, C., Boogert, A. C. A., Boxhoorn, D. R., de Graauw, T., Drapatz, S., Feuchtgruber, H., Genzel, R., Helmich, F. P., Heras, A. M., Huygen, R., Izumiura, H., Justtanont, K., Kester, D. J. M., Kunze, D., Lahuis, F., Lamers, H. J. G. L. M., Leech, K. J., Loup, C., Lutz, D., Morris, P. W., Price, S. D., Roelfsema, P. R., Salama, A., Schaeidt, S. G., Tielens, A. G. G. M., Trams, N. R., Valentijn, E. A., Vandenbussche, B., van den Ancker, M. E., van Dishoeck, E. F., Van Winckel, H., Wesselius, P. R., and Young, E. T. Mineralogy of oxygen-rich dust shells. *Astronomy and Astrophysics 315* (Nov. 1996), L361–L364.

[150] Weigelt, G., Beckmann, U., Blöcker, T., Hofmann, K.-H., Ohnaka, K., Schertl, D., Brewer, M. K., Schloerb, F., Efimov, Y. N., Shenavrin, V., Yudin, B., Berger, J., Lacasse, M., Millan-Gabet, R., Monnier, J., Morel, S., Pedretti, E., Traub, W., Malanushenko, V., Mennesson, B., and Scholz, M. Spectro-interferometry of the Mira Star T Cep with the IOTA Interferometer and Comparison with Models. *Astronomische Nachrichten Supplement 324* (July 2003), 71–+.

[151] Werner, M. W., Roellig, T. L., Low, F. J., Rieke, G. H., Rieke, M., Hoffmann, W. F., Young, E., Houck, J. R., Brandl, B., Fazio, G. G., Hora, J. L., Gehrz, R. D., Helou, G., Soifer, B. T., Stauffer, J., Keene, J., Eisenhardt, P., Gallagher, D., Gautier, T. N., Irace, W., Lawrence, C. R., Simmons, L., Van Cleve, J. E., Jura, M., Wright, E. L., and Cruikshank, D. P. The Spitzer Space Telescope Mission. *The Astrophysical Journal Supplement Series 154* (Sept. 2004), 1–9.

[152] Winnberg, A., Engels, D., Brand, J., Baldacci, L., and Walmsley, C. M. Water vapour masers in long-period variable stars. I. RX Bootis and SV Pegasi. *Astronomy and Astrophysics 482* (May 2008), 831–848.

[153] Wishnow, E. H., Townes, C. H., Walp, B., and Lockwood, S. The Dust Surrounding W Hydrae. *The Astrophysical Journal Letters 712* (Apr. 2010), L135–L138.

[154] Woitke, P. Too little radiation pressure on dust in the winds of oxygen-rich AGB stars. *Astronomy and Astrophysics 460* (Dec. 2006), L9–L12.

[155] Wood, P. R., and Zarro, D. M. Helium-shell flashing in low-mass stars and period changes in mira variables. *Astrophysical Journal 247* (July 1981), 247–256.

[156] Woolf, N. J. Circumstellar Infrared Emission. I the Circumstellar Origin of Interstellar Dust (review). In *Interstellar Dust and Related Topics* (1973), J. M. Greenberg & H. C. van de Hulst, Ed., vol. 52 of *IAU Symposium*, pp. 485–+.

[157] Woolf, N. J., and Ney, E. P. Circumstellar Infrared Emission from Cool Stars. *Astrophysical Journal, Letters to the Editor 155* (Mar. 1969), L181+.

[158] Yamamura, I., de Jong, T., Onaka, T., Cami, J., and Waters, L. B. F. M. Detection of warm SO_2 gas in oxygen-rich AGB stars. *Astronomy and Astrophysics 341* (Jan. 1999), L9–L12.

[159] Yates, J. A., Richards, A. M. S., Gledhill, T. M., and Bains, I. Is the Outflow from RT Vir Bipolar or Rotating? In *Asymmetrical Planetary Nebulae II: From Origins to Microstructures* (2000), J. H. Kastner, N. Soker, & S. Rappaport, Ed., vol. 199 of *Astronomical Society of the Pacific Conference Series*, pp. 79–+.

[160] Zijlstra, A. A., and Bedding, T. R. Period Evolution in Mira Variables. *Journal of the American Association of Variable Star Observers (JAAVSO) 31* (2002), 2–10.

[161] Zijlstra, A. A., Bedding, T. R., Markwick, A. J., Loidl-Gautschy, R., Tabur, V., Alexander, K. D., Jacob, A. P., Kiss, L. L., Price, A., Matsuura, M., and Mattei, J. A. Period and chemical evolution of SC stars. *Monthly Notices of the Royal Astronomical Society 352* (July 2004), 325–337.

[162] Zijlstra, A. A., Bedding, T. R., and Mattei, J. A. The evolution of the Mira variable R Hydrae. *Monthly Notices of the Royal Astronomical Society 334* (Aug. 2002), 498–510.

VITA

Suklima Guha Niyogi was born on December 10, 1979 in Calcutta, India. Her parents are Debabrata and Sukriti Guha Niyogi. She attended Calcutta University and graduated with Bachelor degree in Physics with honors in 2002. She earned her Masters Degree in Physics (with a specialization in Astronomy) in 2004 from University of Pune, India. After completing her Masters degree, she joined University of Missouri to pursue her Ph.D. degree in 2006. She decided to work in Astronomy with Prof. Angela Speck, and started working in her group from June, 2008. She received her Ph.D. degree in Physics from University of Missouri in December, 2011.

She is engaged with Rien Dijkstra, who is currently a postdoctoral research fellow in the Netherlands. Her future plan is to move there with her fiance in early 2012. She currently accepted a job at an IT company, PW Consulting B.V. in the Netherlands.